

DISS. ETH No. 29625

**Grid-forming hybrid angle control for power
converters in low-inertia power systems**

A thesis submitted to attain the degree of
DOCTOR OF SCIENCES OF ETH ZURICH
(Dr. Sc. ETH Zurich)

presented by

ALI TAYYEBI KHAMENEH

MSc, Università degli Studi dell'Aquila, Italy
Master, Universidad de Oviedo, Spain

born on 2. December 1987 in Tehran
citizen of Iran

accepted on the recommendation of

Prof. Dr. Florian Dörfler, examiner (ETH Zurich)
Prof. Dr. Janusz Bialek, co-examiner (Imperial College London)
Dr. Adolfo Anta, co-examiner (Austrian Institute of Technology)

2023

ETH Zurich
IfA - Automatic Control Laboratory
ETL, Physikstrasse 3
8092 Zurich, Switzerland

© Ali Tayyebi, 2023
All Rights Reserved

To Alexandra, my family and friends.

At the end of the day, what matters is a shared narrative, the one that evolves beyond our journey and lives forever.

Anonymous

Acknowledgements

I would like to thank Florian for his inspiration, guidance, and support since day one and along the journey. Thank you for teaching me how to be passionate about research. Further, thank you for all the exciting moments of brainstorming, tackling the open problems, and breaking the deadlocks. Finally, thank you for your friendship and teaching me what true leadership is all about.

I would like to thank Adolfo for sharing his experiences with me. Thank you for all the exciting discussions on topics spanning from the depth of control theory to modern power systems. Thank you for reviewing all my papers and reading the countless pages of unpublished sketches and proofs. Finally, thank you for your friendship and all the coffee breaks in Vienna.

I would like to thank Prof. Janusz Bialek for his interest in my research and joining the doctoral examination committee. Further, thank you for sharing your inspiring insights on the future power system challenges with me in Champery and Porto.

I would like to thank Dominic for his valuable insights, help, and support during the initial stage of my doctoral research.

I would like to thank Verena for her help with the translation of thesis abstract, exciting discussions, and allowing me to take a small part in her research journey.

I would like to thank all the former and current members of the complex systems control group of the Automatic Control Lab (IfA) at ETH for their support and help. Special thanks to Miguel, Catalin, Taouba, Irina, Linbin, Jeremy, Marcello, and Saverio for their friendship, support, and sharing their knowledge with me. Further, thanks to all the members of the IfA for welcoming me into an inspiring research environment. Last, I would like to thank Eduardo and Meng for the fruitful research collaborations.

I would like to thank my former colleagues at the Austrian Institute of Technology (AIT) for their help and support. Special thanks to Denis and Alessandro for their excellent thesis works and generous contributions to my research. Further, I would like to thank the management team at AIT, Friederich and Wolfgang for establishing this exciting research collaboration with ETH.

I would like to thank my colleagues at the Hitachi Energy Research for their help and support during the final stage of my doctoral research. Special thanks to Aleksander, Alberto, Helen, Frans, and Bertil for their motivating words. Further, I would like to thank the management team at the Hitachi Energy Research center in Sweden, Nan and

Alireza for their generous support.

I would like to thank Andrea, Alan, and Carim for their excellent thesis works and helping me to gain experience, improve, and grow as a mentor.

I would like to thank my family, friends, and Dr. Mahmood Amirinia for their motivating words and kind support along the journey.

Last, I would like to thank Alexandra for being there for me no matter what. I am not sure if this journey would be possible without your love and support.

Ali Tayyebi
Zürich, December 10, 2023

Abstract

This thesis investigates the comparative system-level performance of classic grid-forming converter control strategies in different low-inertia power system models, i.e., the IEEE 9-bus test system and Hydro-Quebec transmission grid models. The extensive electromagnetic transients simulation-based case studies highlight the positive influence of the grid-forming converters on frequency stability. Further, the behavioral differences of several state-of-the-art grid-forming control techniques are uncovered. Moreover, the interactions of grid-forming converters and synchronous machines in low-inertia power systems are explored. Thus, it is observed that the choice of converter control design i.e., a grid-forming or grid-following control concept plays a critical role in achieving high levels of converter-based generation integration. Further, the post-contingency evolution of frequency stability metrics and their effectiveness in low-inertia power systems are discussed. Subsequently, on the basis of several observations made via simulation case studies, a new grid-forming converter control strategy is designed, i.e., the hybrid angle control. A detailed nonlinear stability analysis of the proposed grid-forming control concept is presented that establishes the almost global asymptotic stability of the closed-loop converter dynamics. The almost global asymptotic stability of the grid-connected converter is proved under parametric existence and stability conditions that are solely met by an appropriate choice of control parameters. In addition, a complementary current-limiting controller is designed that is compatible with the hybrid angle control and preserves the closed-loop stability. Next, from a control-theoretic viewpoint, the application and scalability of the hybrid angle control for the interlinking converters in non-synchronous hybrid AC/DC power grids is investigated. It is observed that not only the stability guarantees of the hybrid angle control are fully scalable in hybrid AC/DC power grids, but also they do not require strong assumptions on the underlying dc interconnections. Moreover, the system-level and device-level control concept performances are respectively verified via electromagnetic transients simulation-based case studies and controller-hardware-in-the-loop simulation approach. Additionally, guidelines on the stability analysis of a two-converter system under the hybrid angle control and recommendations on designing several other multivariable grid-forming controls are presented. Finally, this thesis is concluded by presenting the summary and outlook of this doctoral research, and listing the remaining open problem in this research area.

Zusammenfassung

Diese Arbeit untersucht die vergleichbare systemweite Leistung klassischer netzbildender Umrichtersteuerungsstrategien in verschiedenen Stromnetzmodellen mit geringer Trägheit, nämlich dem IEEE-9-Bus-Testsystem und den Übertragungsnetzmodellen von Hydro-Quebec. Die umfangreichen Fallstudien basierend auf elektromagnetischen transienten Simulationen verdeutlichen den positiven Einfluss der netzbildenden Umrichter auf die Frequenzstabilität. Des Weiteren werden die Verhaltensunterschiede mehrerer hochmoderner netzbildender Steuerungstechniken aufgedeckt. Darüber hinaus werden die Wechselwirkungen zwischen netzbildenden Umrichtern und synchrongekoppelten Maschinen in Stromnetzen mit geringer Trägheit untersucht. Es wird beobachtet, dass die Wahl des Umrichtersteuerungsdesigns, also ein netzbildendes oder netzfolgendes Steuerungskonzept, eine entscheidende Rolle bei der Integration von Umrichter-basierter Stromerzeugung spielt. Weiterhin werden die Auswirkungen der Frequenzstabilitätsmetriken nach einer Netzstörung und deren Effektivität in Stromnetzen mit geringer Trägheit diskutiert. Im Anschluss daran wird auf Grundlage mehrerer Beobachtungen durch Simulationen eine neue netzbildende Umrichtersteuerungsstrategie entwickelt, nämlich die hybride Winkelsteuerung. Es wird eine detaillierte nichtlineare Stabilitätsanalyse des vorgeschlagenen netzbildenden Steuerungskonzepts vorgestellt, die die nahezu globale asymptotische Stabilität der geschlossenen Regelkreis-Dynamik des Umrichters nachweist. Die nahezu globale asymptotische Stabilität des netzgekoppelten Umrichters wird unter parametrischen Existenz- und Stabilitätsbedingungen bewiesen, die allein durch eine geeignete Wahl der Steuerungsparameter erfüllt werden. Darüber hinaus wird ein komplementärer Strombegrenzungsregler entworfen, der mit der hybriden Winkelsteuerung kompatibel ist und die Stabilität des geschlossenen Regelkreises bewahrt. Anschliessend wird aus Sicht der Regelungstechnik die Anwendung und Skalierbarkeit der hybriden Winkelsteuerung für die verbindenden Umrichter in nichtsynchrone Hybrid-AC/DC-Stromnetze untersucht. Es wird beobachtet, dass die Stabilitäts Garantien der hybriden Winkelsteuerung nicht nur in Hybrid-AC/DC-Stromnetzen vollständig skalierbar sind, sondern auch keine starken Annahmen über die zugrunde liegenden Gleichstromverbindungen erfordern. Darüber hinaus werden die Leistungen des Steuerungskonzepts auf Systemebene und Geräteebene jeweils durch elektromagnetische transiente Simulationen und einem simulationsbasierten Ansatz für die Hardware-in-the-Loop-Steuerung verifiziert. Zusätzlich werden Richtlinien zur Stabilitätsanalyse eines Zwei-Umrichter-Systems unter hybrider Winkelsteuerung vorgestellt und Empfehlungen zur Gestaltung mehrerer anderer multi-variabler netzbildender Steuerungen gegeben. Abschliessend wird eine Zusammenfassung

und ein Ausblick auf die Doktorforschung einhergehend mit einer Auflistung der verbleibenden offenen Probleme in diesem Forschungsbereich gegeben.

Contents

Acknowledgements	i
Abstract	iii
Zusammenfassung	v
I Introduction	1
1 Introduction, structure, and contributions	3
1.1 Background and motivation	3
1.2 State of the art	7
1.3 Structure and contributions	9
1.4 Publications	11
II Frequency stability of the low-inertia power systems	15
2 Frequency stability of synchronous machines and grid-forming power converters	17
2.1 Introduction	17
2.2 Model description	19
2.3 Grid-forming control architectures	23
2.4 Network case study	32
2.5 Qualitative analysis	42
2.6 Summary and further work	46
2.7 Appendix A: tuning criteria	47
3 Beyond low-inertia systems: massive integration of grid-forming power converters in transmission grids	51
3.1 Introduction	51

3.2	Model description	54
3.3	Results	56
3.4	Conclusions and outlook	62
III	Grid-forming hybrid angle control	65
4	Grid-forming hybrid angle control and almost global stability of the DC-AC power converter	67
4.1	Introduction	67
4.2	Model description	69
4.3	Closed-loop analysis	75
4.4	Dynamic grid and current-limiting control	80
4.5	Implementation, robustness, practical aspects	86
4.6	Numerical examples	92
4.7	Summary and outlook	99
4.8	Appendix A: proof of the technical results	100
4.9	Appendix B: transformations and identities	105
5	Hybrid angle control and almost global stability of non-synchronous hybrid AC/DC power grids	107
5.1	Introduction	107
5.2	Hybrid AC/DC grid model description	108
5.3	Hybrid angle control and stability analysis	112
5.4	Numerical verification	116
5.5	Outlook	117
5.6	Appendix A: proof of the technical results	117
5.7	Appendix B: mathematical identities	124
6	System-level performance and robustness of the grid-forming hybrid angle control	125
6.1	Introduction	125
6.2	Modeling description	127
6.3	Grid-forming frequency controls	129
6.4	Numerical case studies	134
6.5	Conclusions and outlook	144

6.6	Appendix A: dynamic inverse droop control augmentation	144
6.7	Appendix B: stability analysis of the interconnected converters	145
7	Grid-forming hybrid angle control: behavior, stability, variants, and verification	149
7.1	Introduction	149
7.2	Converter connected to a stiff grid	150
7.3	Closed-loop stability analysis	157
7.4	Converter connected to a weak grid	160
7.5	Experimental verification	165
7.6	Conclusion	169
IV	Conclusion	175
8	Summary, outlook, and open problems	177
8.1	Summary and outlook	177
8.2	Open problems	179
	Bibliography	192
	Curriculum Vitae	193

List of Figures

1.1	An example of energy generation landscape in the past and future power system scenarios.	3
1.2	An example of grid-following (GFL) converter control architecture.	5
1.3	The timescales of different frequency controls provides by the synchronous machines (SMs) and converters.	6
1.4	An example of grid-forming (GFM) converter control architecture.	7
1.5	A potential classification of grid-forming (GFM) controls based on the design approaches.	8
1.6	A potential classification of grid-forming (GFM) controls based on the nature of feedback signals.	8
1.7	The thesis structure and connections between different chapters.	10
2.1	Converter model in $\alpha\beta$ -coordinates with detailed dc energy source model based on (2.1)-(2.3).	20
2.2	IEEE 9-bus test system with a synchronous machine, two large-scale multi-converter systems (i.e., aggregate GFCs), and constant impedance loads.	22
2.3	Equivalent model of an individual converter module (left), large-scale multi-converter system consisting of n identical modules (middle), and aggregate model (right).	23
2.4	Grid-forming control architecture with reference models described in subsections 2.3.3 to 2.3.6.	24
2.5	Block diagram of the low-level cascaded control design (2.6)-(2.8) in dq-coordinates rotating with the angle θ provided by the reference model.	25
2.6	Droop control frequency and ac voltage control block diagrams based on (2.11) and (2.12).	27
2.7	Block diagram of a grid-forming VSM based (2.13)-(2.15).	29
2.8	Matching control block diagram based on (2.16)-(2.18).	30

2.9	Block diagram of dVOC in polar coordinates corresponding to (2.22). Note that singularity at $\ \hat{\mathbf{v}}_{dq}\ = 0$ only appears in the dVOC implementation in polar coordinates but not in the implementation in rectangular coordinates, i.e., (2.21).	31
2.10	Post-event frequency nadir and RoCoF.	33
2.11	Normalized distribution of the RoCoF $ \dot{\omega}_i / \Delta p_i $ of the synchronous machine frequency at node 1 for load disturbances Δp_i ranging from 0.2 p.u. to 0.9 p.u. at node 7. For each load disturbance, $ \dot{\omega}_i / \Delta p_i $ is normalized by the maximum value corresponding to the all-SMs configuration.	35
2.12	Normalized distribution of the nadir $\ \Delta\omega_i\ _\infty/ \Delta p_i $ of the synchronous machine frequency at node 1 for load disturbances Δp_i ranging from 0.2 p.u. to 0.9 p.u. at node 7. For each load disturbance, $\ \Delta\omega_i\ _\infty/ \Delta p_i $ is normalized by the maximum value corresponding to the all-SMs configuration.	35
2.13	Frequency of the system with two VSMS after a 0.75 pu load increase. The converters quickly synchronize with each other and then slowly synchronize with the machine.	36
2.14	DC current demand of the converter at node 2 (top) and its dc voltage (bottom) after a 0.9 pu load disturbance.	36
2.15	DC current demand and saturated dc current (top), frequency of the converter (using matching control) at node 2 and SM after a 0.9 pu load disturbance (bottom).	37
2.16	DC voltage of the converter at node 2 after a 0.9 pu load disturbance when both dc and ac limitation schemes (2.3) and (2.7) are active and $\tau_g = 5s$	37
2.17	DC voltage (top) and dc current demand (bottom) of the converter at node 2 after a 0.9 pu load disturbance when all the limitation schemes i.e., (2.3), (2.7) and (2.24) are active and $\tau_g = 5s$	38
2.18	DC voltage (top) and dc current demand (bottom) of the converter at node 2 after a 0.9 pu load disturbance when both dc and ac limitation schemes (2.3) and (2.7) are active and $\tau_g = 1s$	40
2.19	DC current demand (top) and dc voltage (bottom) of the converter at node 2 after loss of the SM at node 1.	41
2.20	DC current demand (top) and dc voltage (bottom) after a 0.9 pu load disturbance in an all-GFC system.	42
2.21	Change in averaged RoCoF and frequency nadir when transitioning from a system with 3 SMs to a system with one SM and two GFCs.	46

3.1	Quebec grid model consisting of 7 generation nodes (line length in km).	53
3.2	Converter model (see [94, Section II-A] for the parameters definition and further details of the converter modeling).	55
3.3	Droop control block diagram [94, Section III-C].	55
3.4	Frequency evolution of the SM 2 following the loss of SM-GFC 1. When the GFC integration level is set to 80% and 90%, the PSS controllers for the remaining SMs have been identically retuned.	58
3.5	The SM and GFC frequencies for two extreme integration levels, across the grid, following the loss of SM-GFC 1. Regardless of the integration level and the source of frequency signal (i.e., SM or GFC), units in the Northwest region - where contingency occurs - exhibit the largest oscillation.	59
3.6	Normalized frequency nadir vs RoCoF (calculated over two distinct time window) for different integration levels for all the SMs across the grid. The event corresponds to the loss of 2 GW generation due to the disconnection of the HVDC link in Figure 3.1. All data points are normalized against the corresponding metric values of the baseline all-SMs system.	60
3.7	Frequency time series for all units in an all-GFC grid.	63
4.1	Schematic of the closed-loop system (4.7); see Figure 4.5 for the control diagram defining $i_{dc,r}$ and $m(\mu_r, \theta)$, and the Section 4.4.1 for the description of the closed-loop system with the COI grid model.	70
4.2	The boundary of the Möbius strip represents the angle space of (4.7). The arcs contained in the boundary segments colored in blue and red respectively represent the angles in $[-2\pi, 0]$ and $[0, 2\pi]$	74
4.3	Illustration of the Lyapunov function (4.15) under the simplifying assumption that $\tilde{\gamma}, \tilde{\theta} \in \mathbb{R}$, $P = 1$, and $\lambda = 1$	79
4.4	Illustration of normalized μ in (4.33) and Δ_μ in (4.36). For clarity of presentation, here $\beta = 2$ and $\mathcal{D} \in \mathbb{R}_{(0,1,0.9)}$. For small \mathcal{D} (i.e., a severe event) Δ_μ results in the modulation magnitude decay at a lower current compared to a scenario with large \mathcal{D}	85
4.5	Block diagram of the feedback controls (4.3) and (4.5) with implementation (4.39) combined with the feedforward controls (4.52) and (4.53).	93
4.6	Post-event frequency of the system (4.25) under different hybrid angle control (HAC) tuning (top), corresponding normalized RoCoF values (bottom).	95
4.7	Current-limiting control performance with respect to (w.r.t) a three-phase-to-ground fault; output/fault node voltage (top), modulation magnitude (middle), and filter current (bottom).	96
4.8	IEEE 9-bus test system including SM and power converters.	97

4.9	Post-disturbance SM frequency evolution in IEEE 9-bus test system with power converters under different control strategies.	98
4.10	SM and converters' frequency evolution (for three different SM-converter pairs) following a large load disturbance that stresses the converters beyond their current limits.	99
5.1	The overview of the high voltage dc (HVDC) links and North Sea wind power hub (NSWPH) concept that connect the regional groups (RGs) in the Northern Europe and Baltic regions [124].	108
5.2	The hybrid ac/dc grid model comprised of the dynamic dc interconnections, j -th dc node, ILC, transmission line, and ac grid.	109
5.3	The figure-8 immersion of the Klein bottle [129]. The Klein bottle can be decomposed into two Möbius strips (e.g., the ones above and below the colored path) with identical compact boundaries representing M [3]. The merged boundaries of the underlying Möbius strips (e.g., the colored closed curve) represents the angle manifold $M^2 =] - 2\pi, 2\pi[\times] - 2\pi, 2\pi[$ where $-2\pi \equiv 2\pi$	113
5.4	The phase portrait of relative angle errors ($\hat{\delta}_1, \hat{\delta}_2$) (left) and angular frequency errors ($\hat{\omega}_{g,1}, \hat{\omega}_{g,2}$) (right).	118
6.1	DC-AC power converter model schematic with ac quantities represented in stationary $\alpha\beta$ -coordinates [1], [73].	128
6.2	Block diagram of the hybrid angle control (HAC) (6.3) based on the dc voltage and the output ac voltage measurements in Figure 6.1.	135
6.3	IEEE 9-bus test system including SMs and grid-forming converters (GFCs); depending on the choice of the generation technology at nodes 1, 2, and 3 this network model represents: 1) a conventional system (i.e., all-SMs), 2) a SM-dominated system (2SMs-1GFC), 3) a low-inertia system (i.e., 1SM-2GFCs), and 4) a purely converter-based system (i.e., all-GFCs).	137
6.4	Frequency response of the all-GFCs IEEE 9-bus system configuration under hybrid angle control (HAC) strategy following a load disturbance (top), the active power time-evolution associated with the GFCs at node 1, 2, and 3 (bottom).	137
6.5	rate of change of frequency (RoCoF) evolution of the SM at node 1 in 1SM-2GFCs system configuration under different controls and with respect to variations in network load disturbance (top), maximum frequency deviation (bottom).	138
6.6	The post-event frequency time-evolution of the SM at node 1 in 2SMs-1GFC system configuration under different controls for the GFC.	138

6.7	Frequency evolution of SM at node 1 when the GFCs are controlled by HAC strategy with 5 different LPF cutoff frequency and without a LPF.	139
6.8	The PSS-free response of the SM at node 1 when the GFCs are controlled by either HAC or droop control while considering two different LPF cutoff frequencies.	139
6.9	Synthetic two-area low-inertia system configuration.	143
6.10	Frequencies of the two-area system following a grid split scenario.	144
6.11	The simplified two-converter system configuration where $i_{x,j} := m(\mu_j, \theta_j)^\top i_\ell$ and $v_{x,j} := m(\mu_j, \theta_j)v_{dc,j}$ for $j = 1$ and 2 .	148
7.1	The circuit diagram associated with the open-loop dynamics of the grid-connected converter model as in (7.1).	151
7.2	Conceptual illustration of the energy-based stability analysis; here it is assumed that the energy function is only function of the relative angle and dc voltage, i.e., $V(\hat{\delta}, \hat{v}_{dc}) = 2(1 - \cos \hat{\delta}/2) + (1/2)\hat{v}_{dc}^2$.	161
7.3	The circuit diagram of the converter model connected to a weak grid model in abc-coordinates system.	161
7.4	The circuit diagram of the converter model with LC output filter connected to a weak grid model in abc-coordinates system; this model also represents the case of a LCL filter consideration in which the grid-side filter inductance is merged with the grid impedance.	162
7.5	The overall control architecture of a grid-connected converter system including the dc-side controls, ac-side grid-forming (GFM), voltage, and current controls.	164
7.6	C-HiL testbed that includes three external control cards connected to Opal-RT OP5700. The host PC is used to automatically run controller-hardware-in-the-loop (C-HiL) simulations and collect the results.	166
7.7	C-HiL testbed architecture. The controller-hardware-in-the-loop (C-HiL) framework (on the left side) is developed in Python and its main functionality is to coordinate the RT-simulator and control cards. The control cards (on the right side) are connected to the RT-simulator via physical cables.	166
7.8	The time-evolution of normalized frequency (top), active power (middle), and dc voltage (bottom) of an islanded grid-forming (GFM) converter under hybrid angle control (HAC) with respect to (w.r.t) a load disturbance scenario in offline and controller-hardware-in-the-loop (C-HiL) simulations.	170

7.9	The time-evolution of normalized frequency (top), active power (middle), and dc voltage (bottom) of a grid-connected grid-forming (GFM) converter under hybrid angle control (HAC) with respect to (w.r.t) a power set-point change scenario in controller-hardware-in-the-loop (C-HiL) simulations.	171
7.10	The time-evolution of normalized frequency (top), active power (middle), and dc voltage (bottom) of a grid-connected grid-forming (GFM) converter under hybrid angle control (HAC) with respect to (w.r.t) a grid frequency variation scenario in controller-hardware-in-the-loop (C-HiL) simulations.	172
7.11	The time-evolution of normalized frequency (top), active power (middle), and dc voltage (bottom) of two coupled grid-forming (GFM) converters under hybrid angle control (HAC) (with slightly different droop gains) with respect to (w.r.t) a load disturbance scenario in controller-hardware-in-the-loop (C-HiL) simulations.	173

List of Tables

1.1	Key characteristics of synchronous machine (SM)-based and converter-based energy generation.	4
2.1	Case study model and control parameters [71].	48
4.1	The parameters of converter-COI system (4.25).	94
6.1	Case study model and control parameters [71].	136
7.1	Grid-connected converter model and control parameters.	168

Part I

Introduction

Introduction, structure, and contributions

This chapter presents the motivation behind this doctoral research, outlines the state-of-the-art solutions, highlights the structure of this thesis, summarizes the technical contributions, and lists the publications related to this project.

1.1 Background and motivation

The electric power system consisting of the energy generation, transmission, and distribution sectors is the largest machine operated by humans. This complex system includes a diverse combination of mechanical, electrical, electronic, digital, and communication subsystems. The foundation of power system operation and control relies on the design and properties of the legacy synchronous machines (SMs). So far, the well-established SM technology accompanied by robust stabilizing control mechanisms has been ensuring the power system stability. However, due to the global industrial electrification and digitalization trends, emergence of e-mobility technologies, climate change and energy security concerns, need for bulk power transmission, and emergence of various energy storage technologies, the power system is undergoing paradigm-shifting transformations.

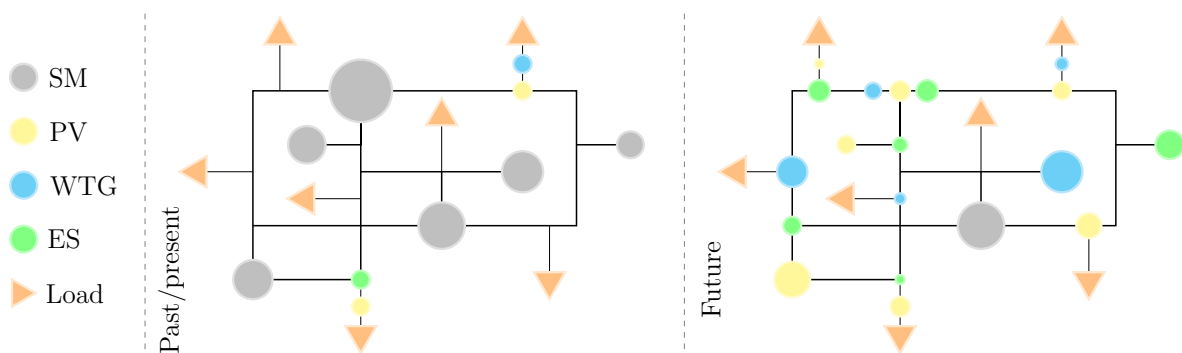


Figure 1.1: An example of energy generation landscape in the past and future power system scenarios.

From the generation perspective, a conceptual power system transformation is illustrated in Figure 1.1. The past/present scenario is highlighted by the central presence of relatively bulk SMs, and insignificant amount of energy storage renewable energy source (RES) integration. However, the distributed energy generation, e.g., via photovoltaic (PV) and wind turbine generator (WTG) technologies is dominantly present in the future power system scenario. Furthermore, the future scenario integrates significant levels of energy storage (ES) due to the intermittency of the RESs and, thus, the need for flexibility. Aside from the central-to-distributed and bulk-to-granular generation transformation, this transition is strongly highlighted by the replacement of the SM technology, its rotational inertia (acting as a global energy buffer for the system), and stabilizing control mechanisms. The combination of these transitional factors leads to the emergence of a low-inertia power system that coincides with the future system scenario. In a low-inertia power system that is characterized by the large levels of RES integration, the majority of generation units are interfaced to the grid via power converters. Thus, the power converters are the key technologies in the future power system scenario. However, the energy generation and power system operation based on the SMs and power converters exhibit pronounced differences that are summarized in Table 1.1.

The overview provided in Table 1.1 uncovers potential critical stability and control challenges associated with the converter-dominated power systems. Therefore, the power converter design and control play a critical role in addressing these challenges (akin to the role of the SM in conventional power systems). More precisely, the converter control design must support load-sharing, drooping, black-start, inertial response, and hierarchical frequency/voltage regulation functionality. However, these requirements originate from the control framework constructed on the basis of SM design. In the converter-dominated power systems the same set of control objectives may not be relevant. It is

Table 1.1: Key characteristics of SM-based and converter-based energy generation.

SM-based generation features	Converter-based generation features
Bulk centralized units	Modular generation units
Robust frequency and voltage control	Fragile frequency and voltage control
Dispatchable generation	Variable generation
Distinct slow and fast timescales	Adjacent fast timescales
Large available rotating inertia	Negligible inertia and inherent storage
Slow actuation and control	Fast actuation and control
Unsustainable generation	Sustainable generation

noteworthy that while the power system transitions to a converter-dominated state, SMs and converters must effectively interact to ensure system stability. In what follows, the control aspect of the story is further investigated and the state-of-the-art power converter control paradigms and design approaches are discussed.

The classic converter control design architecture, i.e., grid-following (GFL) synthesis that is shown in Figure 1.2 relies on an explicit synchronization mechanism, e.g., phase-locked loop (PLL). In a GFL control design, the frequency and phase angle of the point of common coupling (PCC) voltage measurement is extracted by the PLL. Subsequently, the rest of control architecture is constructed on the basis of the information provided by the PLL. Typically, the high-level control loop accounts for the system-level specifications, e.g., active and reactive power set-point tracking, virtual inertia provision, or other ancillary services. On the other hand, the low-level controls (that are typically designed in a rotating rectangular coordinates), e.g., ac voltage and current tracking controllers, and/or virtual impedance/admittance control loops ensure robust device-level performance such that the high-level requirements are met. Next, the modulation algorithm bridges the gap between the converter control and physical subsystems. It is worth mentioning that in GFL architectures, the dc control design ensures stable dc power exchange between the energy source and the converter. In the case of a local energy source connection, e.g., PV or ES the objective of the dc control is the robust regulation of the dc-link voltage. Further, if high voltage direct current (HVDC) link connection is considered, the control objectives are either stabilizing the dc-link voltage or regulating the dc power flow. Nonetheless, in GFL control architecture the dc control design is often decoupled from the converter control design. Finally, a GFL converter

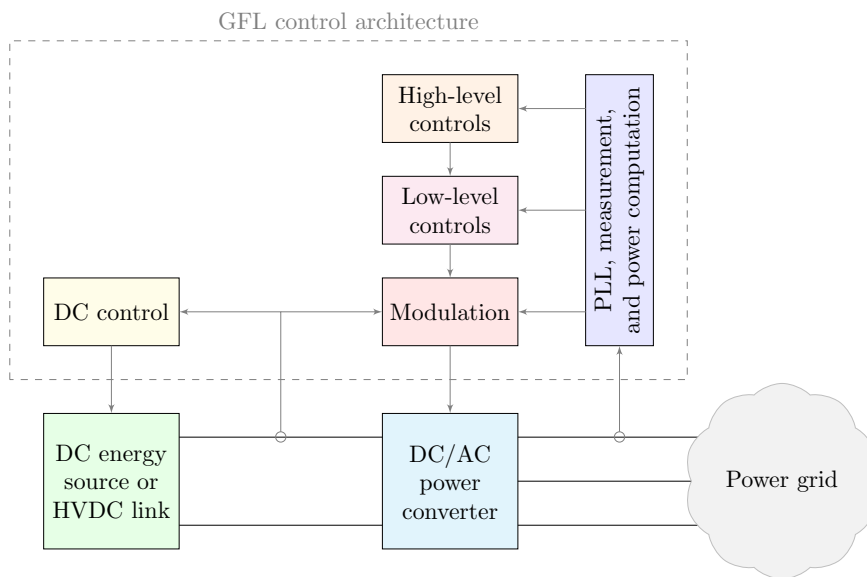


Figure 1.2: An example of grid-following (GFL) converter control architecture.

operating mode can be interpreted as a controllable ac current source that locks onto the grid frequency and injects the desired active and reactive power flows.

The timescales of different frequency controls in a low-inertia power system incorporating SMs and GFL converters is illustrated in Figure 1.3. It is noteworthy that although the converter-based generation achieves faster primary frequency control timescales in contrast to the SM-based generation, the SM inertial response is still the fastest control mechanism that is naturally and immediately activated after a contingency. The delay associated with the PLL in a GFL control design hinders the realization of a true inertial response behavior for the power converters. This drawback of the GFL devices can lead to critical frequency stability challenges in systems where the rotating inertia is reduced below a critical level.

The grid-forming (GFM) control design is envisioned to address the aforementioned limitation of the GFL devices. Further, a GFM converter is expected to behave as a controllable voltage source that creates an independent ac voltage and frequency reference, thus, allowing an islanded and fully converter-based operation, as well as exhibiting a grid-connected operation mode and interoperability with the SMs. A typical GFM control architecture is shown in Figure 1.4. The main difference with respect to (w.r.t) the GFL architecture in Figure 1.2 is the elimination of PLL. The GFM control achieves an implicit synchronization with respect to the power grid that is often implemented through the high-level GFM layer in Figure 1.4. Further, some GFM controls can also operate without the need for explicit low-level ac and dc controls.

To this date, the definition GFM control concept widely varies across different power system sectors, converter-based technologies, and applications. Therefore, a clear and universally accepted definition is not available. On the other hand, the system operators often expect a wide range of control and stability challenges associated with the converter-dominated power systems to be addressed by GFM power converters. In the author’s opinion the key desired characteristics of a GFM control design are: 1) enabling

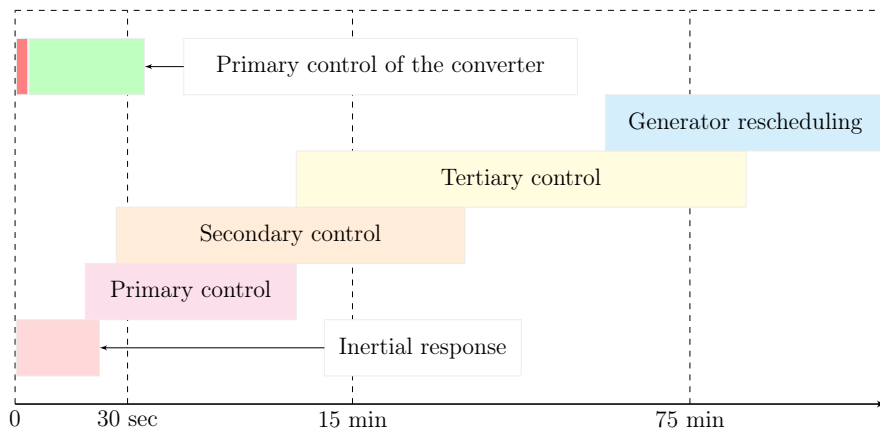


Figure 1.3: The timescales of different frequency controls provides by the SMs and converters.

fast inertial response timescale for power converters, 2) set-point tracking behavior, 3) islanded and grid-connected operation and seamless mode transition capabilities, and 4) compatibility with diverse SM/converter-based generation mixtures.

1.2 State of the art

The GFM control design is currently subject to extensive research in academia, industry, and by the system operators that has led to a plethora of control solutions and performance requirements, e.g., see [1]–[33]. However, it is possible to consider a few potential classifications. From the control design approach perspective, a possible classification is presented in Figure 1.5 and described as it follows.

- * Linear and nonlinear design [34]–[37]: this class includes controllers that replicate the behavior of certain control mechanisms of the SM. The most celebrated solution of this form is the active power – frequency droop control that mimics the behavior of the turbine speed governor. This family of solutions serves as a powerful yet simple and intuitive baseline control candidate.
- * Machine emulation and matching [38]–[44]: the emulation-based techniques mimic the physical dynamics and control of the SMs up to various degrees of accuracy. On the other hand, the model-matching based techniques exploit the dynamic structural similarities of the SM and converter to design controllers, thus, establishing strong duality between the states and parameters of SM and GFM converter. The

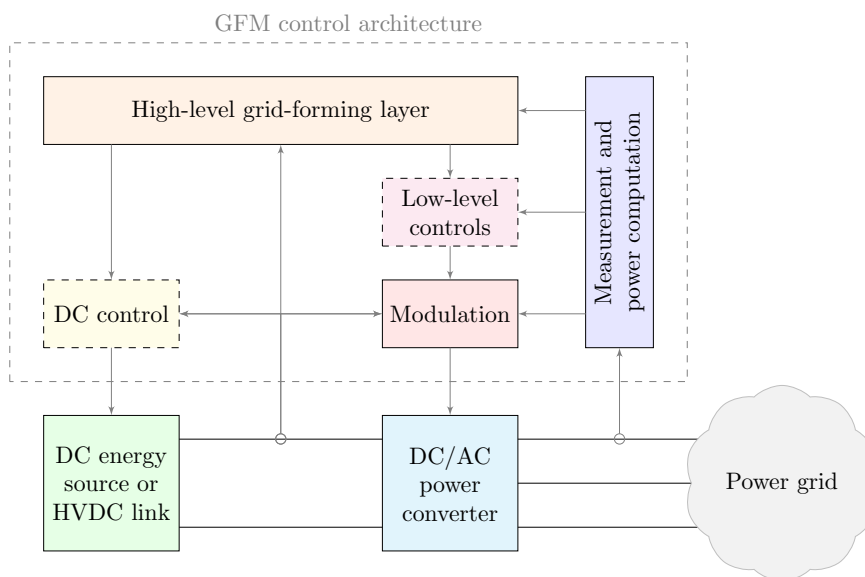


Figure 1.4: An example of GFM converter control architecture.

key advantage of these solutions is the excellent backward compatibility with the SMs.

- * Oscillator-based [45]–[54]: this class of controllers exploits different nonlinear oscillator dynamics for a GFM control design. The oscillator-based methods (under simplifying modeling assumptions) often provide strong global stability guarantees while considering interconnected power converters.
- * Multivariable control [3], [6], [8], [9], [13], [55]–[57]: this class of solutions blends several dc and ac feedback signals into a unifying GFM control. These solutions do not necessarily distinguish between the dc and ac controls, thus, taking into account the natural physical coupling of the dc and ac converter dynamics. However, due to the multivariable nature of these solutions providing an intuitive parameter tuning guideline is not straightforward.
- * Data-driven and optimization-based [58]–[60]: the data-driven and optimization-based methods have been recently employed for a GFM control design. This class of solutions either solely relies on the sampled input-output trajectories of the converter system or requires partial model information to formulate the underlying optimization problem. These solutions often exhibit excellent performance, however, the controller behavior and tuning procedure is not fully intuitive.

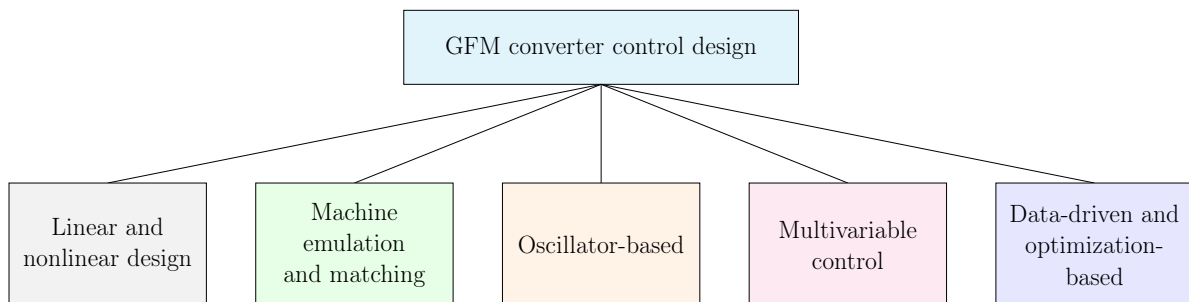


Figure 1.5: A potential classification of GFM controls based on the design approaches.

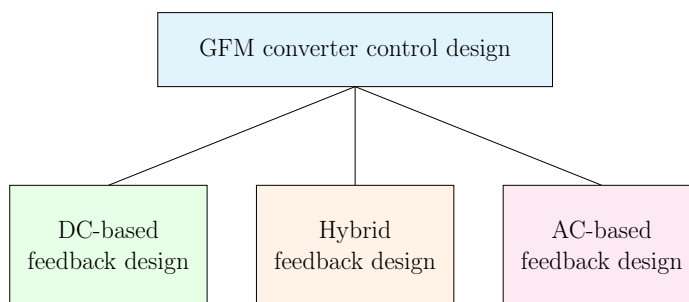


Figure 1.6: A potential classification of GFM controls based on the nature of feedback signals.

Another possible classification based on the nature of the feedback signals exploited in the GFM control design is presented in Figure 1.6 and described as follows.

- * DC-based feedback design [40], [41], [43], [44]: this class of solutions exploits the converter dc states measurements for a GFM control design. The findings presented in Chapter 2 highlight the enhanced robustness of such control solutions.
- * Hybrid feedback design [3], [6], [8], [55]–[57]: this family of solutions combines the dc and ac converter states into a GFM frequency control design that exhibits enhanced small-signal stability and robustness; see Chapters 2 and 6.
- * AC-based feedback design [38], [39], [42], [45], [52]: finally, some GFM controls only rely on the ac converter states and exhibit enhanced small-signal frequency stability; see Chapter 2.

This thesis explores the performance of several control candidates (sampled from the aforementioned classifications) and presents a new grid-forming control design. The next section highlights the structure and summarizes the contributions of this work.

1.3 Structure and contributions

The overall thesis structure and connections between different chapters is shown in Figure 1.7. The remainder of this thesis is divided into three parts. To begin with, Part II includes two chapters and presents findings on the frequency stability of low-inertia power systems.

- * Chapter 2 provides a high-fidelity implementation and comparative performance study of the baseline GFM control strategies in a low-inertia power system model. The employed benchmark is the IEEE 9-bus test system where the simulation models are publicly available. This chapter uncovers the positive influence of the GFM converters on the frequency stability of the low-inertia system, in contrast to the conventional system scenario that is purely based on the SMs. Further, an adverse interaction between the fast GFM converter and slow SM timescales is uncovered that can potentially destabilize certain GFM strategies. Finally, this chapter highlights the enhanced 1) small-signal frequency stability performance of the GFM control strategies that rely on ac feedback signals, and 2) robustness of the GFM control candidates that rely on dc feedback signals w.r.t certain nonlinear phenomena, e.g., current saturation.
- * Chapter 3 provides the results of electromagnetic transients (EMT) simulation case studies on the Hydro-Quebec transmission grid model under different penetration levels of converter-based generation. A key finding is the fact that under the GFL

control strategies, it is not possible to operate the transmission grid purely based on the converter-based devices. However, it is possible to achieve 100% converter-based generation penetration under GFM control strategies. Further, it is observed that on certain penetration levels, the low-inertia system exhibits instability. However, retuning the power system stabilizers (PSSs) for the remaining SMs in the grid counteracts the instability and allows further integration of the converter-based generation. Finally, new insights on the frequency stability metrics definitions and their post-contingency evolution in such low-inertia power systems are provided.

The results of Part II serve as the preliminary design insights for Part III that includes four chapters on the hybrid angle control (HAC) design, stability analysis, theoretic extensions, applications, and verification.

- * Chapter 4 presents the control design of a new GFM control strategy that is the HAC. A detailed nonlinear stability analysis is presented that results in almost

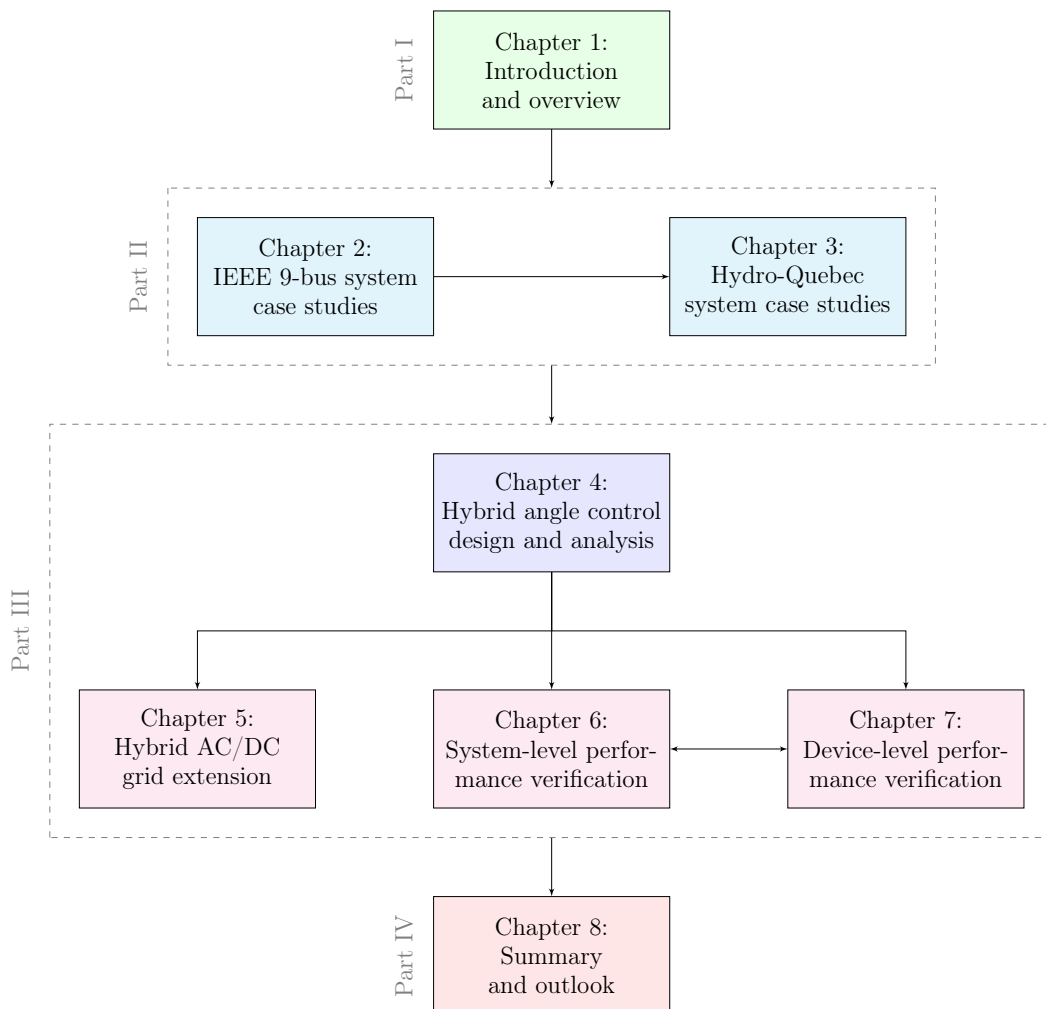


Figure 1.7: The thesis structure and connections between different chapters.

global asymptotic stability (AGAS) of the closed-loop converter dynamics while considering either infinite bus (IB) or dynamic center-of-inertia (COI) grid model. Furthermore, a new bivariate current-limiting control design is presented that is compatible with HAC and preserves the closed-loop stability. Next, a robustness analysis is presented that establishes an ultimate boundedness result under imperfect control implementation. Finally, the numerical verification of the theoretic results are presented.

- * Chapter 5 investigates the application of the HAC for the interlinking converters (ILCs) in non-synchronous hybrid AC/DC power grids. A detailed dynamic modeling of the hybrid AC/DC power grids is presented that includes nonlinear converter models and COI representation non-synchronous areas. Further, the presented stability analysis confirms the applicability of the HAC in such a system and shows the scalability of the previously established stability results, i.e., AGAS. Last but not least, the stabilization of the hybrid AC/DC grid via ILCs under HAC does not require any assumption on the ac power flow or connectivity of the underlying dc interconnections.
- * Chapter 6 presents detailed guidelines on the implementation of the HAC on the benchmark presented in Chapter 2 to facilitate HAC performance comparison w.r.t the baseline GFM control candidates. The extended EMT simulation case studies suggest that the HAC combines the complementary benefits of the baseline GFM control solutions investigated in Chapter 2. Furthermore, theoretic insight on the nonlinear stability analysis of a simplified two-converter system under the HAC is presented.
- * Chapter 7 provides the extended behavioral properties of the GFM HAC. Further, it uncovers that the combination of a new dc voltage control with HAC allows to omit the existence assumption in Chapter 4 while resulting in identical stability guarantees. Moreover, this chapter discloses several control variants for the HAC that can be subject to further research. Finally, several controller-hardware-in-the-loop (C-HiL) test scenarios are presented that verify the device-level control concept performance.

Finally, Part IV presents the conclusions and outlook of this thesis and describes several practical and theoretic open problems.

1.4 Publications

This thesis includes the following papers that respectively appear in Chapters 2-7:

- [1] **A. Tayyebi**, D. Groß, A. Anta, F. Kupzog, and F. Dörfler. “Frequency stability of synchronous machines and grid-forming power converters”. In: *IEEE Journal of Emerging and Selected Topics in Power Electronics* 8.2 (2020), pp. 1004–1018.
- [2] A. Crivellaro, **A. Tayyebi**, C. Gavriluta, D. Groß, A. Anta, F. Kupzog, and F. Dörfler. “Beyond low-inertia systems: Massive integration of grid-forming power converters in transmission grids”. In: *IEEE Power and Energy Society General Meeting (PESGM)*. (Best paper award) 2020.
- [3] **A. Tayyebi**, A. Anta, and F. Dörfler. “Grid-forming hybrid angle control and almost global stability of the DC-AC power converter”. In: *IEEE Transactions on Automatic Control* 68.7 (2022), pp. 3842–3857.
- [4] **A. Tayyebi** and F. Dörfler. “Hybrid angle control and almost global stability of non-synchronous hybrid AC/DC power grids”. In: *IEEE Conference on Decision and Control (CDC)*. 2022.
- [5] **A. Tayyebi**, A. Magdaleno, D. Vettoretti, M. Chen, E. Prieto-Araujo, A. Anta, and F. Dörfler. “System-level performance and robustness of the grid-forming hybrid angle control”. In: *Electric Power Systems Research* 212 (2022), p. 108503.
- [6] **A. Tayyebi**, D. Vettoretti, A. Anta, and F. Dörfler. “Grid-forming hybrid angle control: Behavior, stability, variants and verification”. In: *IEEE Transactions on Smart Grid* (2023). submitted, <https://arxiv.org/abs/2307.09398>.

Next, the following publications are directly/indirectly related to the conducted doctoral research, however, are not presented in this thesis:

- [7] **A. Tayyebi**, F. Dörfler, F. Kupzog, Z. Miletic, and W. Hribernik. “Grid-forming converters – inevitability, control strategies and challenges in future grid applications”. In: *International conference on electricity distribution (CIRED)*. 2018.
- [8] **A. Tayyebi**, A. Anta, and F. Dörfler. “Almost globally stable grid-forming hybrid angle control”. In: *IEEE Conference on Decision and Control (CDC)*. 2020.
- [9] M. Chen, D. Zhou, **A. Tayyebi**, E. Prieto-Araujo, F. Dörfler, and F. Blaabjerg. “Generalized multivariable grid-forming control design for power converters”. In: *IEEE Transactions on Smart Grid* 13.4 (2022), pp. 2873–2885.
- [10] M. Chen, D. Zhou, **A. Tayyebi**, E. Prieto-Araujo, F. Dörfler, and F. Blaabjerg. “Augmentation of generalized multivariable grid-forming control for power converters with cascaded controllers”. In: *IEEE International Power Electronics Conference (IPEC)*. 2022.

- [11] V. Häberle, E. Prieto-Araujo, **A. Tayyebi**, and F. Dörfler. “Grid-forming control design of dynamic virtual power plants”. In: *IFAC Conference on Networked Systems (NecSys)*. 2022.
- [12] V. Häberle, **A. Tayyebi**, X. He, E. Prieto-Araujo, and F. Dörfler. “Grid-forming and spatially distributed control design of dynamic virtual power plants”. In: *IEEE Transactions on Smart Grid* (2022). submitted, <https://arxiv.org/abs/2202.02057>.
- [13] M. Chen, D. Zhou, **A. Tayyebi**, E. Prieto-Araujo, F. Dörfler, and F. Blaabjerg. “On power control of grid-forming converters: modeling, controllability, and full-state feedback design”. In: *IEEE Transactions on Sustainable Energy* (2023), pp. 1–12.

Finally, the following thesis projects were supervised in the course of the doctoral research:

- [14] A. Gattiglio. “Multivariable arctan hybrid angle control and global stability of grid-forming power converters”. 2021.
- [15] A. Magdaleno. “System-level performance evaluation of the hybrid angle control for grid-forming power converters”. 2021.
- [16] C.-C. Jimenez. “Large-scale analysis of massive deployment of converter-based generation equipped with grid-forming strategies”. 2020.
- [17] A. Crivellaro. “Simulation-based study of novel control strategies for inverters in low-inertia system: Grid-forming and followings”. 2019.
- [18] D. Vettoretti. “Validation platform for grid-forming control strategies of power inverters: From component to system-level validation”. 2019.

Part II

Frequency stability of the low-inertia power systems

Frequency stability of synchronous machines and grid-forming power converters

Published in the IEEE Journal of Emerging and Selected Topics in Power Electronics 2020.

Authors – Ali Tayyebi, Dominic Groß, Adolfo Anta, Friederich Kupzog, and Florian Dörfler.

Abstract – An inevitable consequence of the global power system transition towards nearly 100% renewable-based generation is the loss of conventional bulk generation by synchronous machines, their inertia, and accompanying frequency and voltage control mechanisms. This gradual transformation of the power system to a low-inertia system leads to critical challenges in maintaining system stability. Novel control techniques for converters, so-called grid-forming strategies, are expected to address these challenges and replicate functionalities that so far have been provided by synchronous machines. This article presents a low-inertia case study that includes synchronous machines and converters controlled under various grid-forming techniques. In this work 1) the positive impact of the grid-forming converters on the frequency stability of synchronous machines is highlighted, 2) a qualitative analysis which provides insights into the frequency stability of the system is presented, 3) we explore the behavior of the grid-forming controls when imposing the converter dc and ac current limitations, 4) the importance of the dc dynamics in grid-forming control design as well as the critical need for an effective ac current limitation scheme are reported, and lastly 5) we analyze how and when the interaction between the fast grid-forming converter and the slow synchronous machine dynamics can contribute to the system instability.

2.1 Introduction

At the heart of the energy transition is the change in generation technology; from fossil fuel based generation to converter interfaced renewable generation [33]. One of the major consequences of this transition towards a nearly 100% renewable system is the gradual

loss of synchronous machines (SMs), their inertia, and control mechanisms. This loss of the rotational inertia changes the nature of the power system to a low-inertia network resulting in critical stability challenges [33], [61], [62]. On the other hand, low-inertia power systems are characterized by large-scale integration of generation interfaced by power converters, allowing frequency and voltage regulation at much faster time-scales compared to SMs [7], [33].

Indeed, power converters are already starting to provide new ancillary services, modifying their active and reactive power output based on local measurements of frequency and voltage. However, because of the dependency on frequency measurements these *grid-following* control techniques only replicate the instantaneous inertial response of SMs after a contingency with a delay and result in degraded performance on the time scales of interest [63]. To resolve this issue, *grid-forming converters* (GFCs) are envisioned to be the cornerstone of future power systems. Based on the properties and functions of SMs, it is expected that grid-forming converters must support load-sharing/drooping, black-start, inertial response, and hierarchical frequency/voltage regulation. While these services might not be necessary in a future converter-based grid, a long transition phase is expected, where SMs and GFCs must be able to interact and ensure system stability.

Several grid-forming control strategies have been proposed in recent years [7]. *Droop control* mimics the speed droop mechanism present in SMs and is a widely accepted baseline solution [35]. As a natural further step, the emulation of SM dynamics and control led to so-called *virtual synchronous machine* (VSM) strategies [38], [39], [64]. Recently, *matching* control strategies that exploit structural similarities of converters and synchronous machine and *match* their dynamic behavior have been proposed [40], [41], [43], [65]. In contrast, virtual oscillator control (VOC) uses GFCs to mimic the synchronizing behavior of Liénard-type oscillators and can globally synchronize a converter-based power system [46]. However, the nominal power injection of VOC cannot be specified. This limitation is overcome by *dispatchable virtual oscillator control* (dVOC) [45], [47], [48] that ensures synchronization to a pre-specified operating point that satisfies the ac power flow equations.

In this article, the dynamics of the converter dc-link capacitor, the response time of the dc power source, and its current limits is explicitly considered. We review four different grid-forming control strategies and combine them with standard low-level cascaded control design accounting for the ac voltage control and the ac current limitation and control [66]. We explore the various performance aspects of GFC control techniques in an electromagnetic transients (EMT) simulation of the IEEE 9-bus test system, namely: 1) the impact of GFCs on the frequency performance metrics e.g., nadir and rate of change of frequency (RoCoF) [67]–[70], 2) the response of GFCs under large load disturbances, 3) their behavior when imposing dc and ac current limitations, and 4) their response to the loss of SM and performance in a pure converter-based system. Furthermore, we provide an insightful qualitative analysis of the simulation results. The models used in

this work are available online [71].

This study highlights the positive impact of GFCs on improving the standard power system frequency stability metrics. Moreover, we observe that limiting the GFCs dc or ac current accompanied by the interaction of fast converters and slow synchronous machine dynamics can destabilize some grid-forming controls. This observation, highlights the importance of the dc dynamics in grid-forming control design as well as the critical need for an ac current limiting mechanism. Furthermore, we reveal a potentially destabilizing interaction between the fast synchronization of GFCs and the slow response of SMs (see [47], [72] for a similar observation on the interaction of GFCs and line dynamics). Lastly, this study shows that an all-GFCs (i.e., no-inertia) system can exhibit more resilience than a mixed SM-GFCs (i.e., low-inertia) system with respect to the large load variations.

The remainder of this article is structured as follows: Section 2.2 reviews the modeling approach. Section 2.3 presents the system dynamics and adopted grid-forming control techniques. The simulation-based analysis of the study is discussed in Section 2.4. Section 2.5 presents a qualitative analysis of the observations made in case studies. The concluding statements and agenda of future work are reported in Section 2.6. And the choice of control parameters is described in Appendix 2.7.

2.2 Model description

Throughout this study, we use a test system comprised of power converters and synchronous machines. This section describes the models of the individual devices and components [71].

2.2.1 Converter model

To begin with, we consider the converter model illustrated in Figure 2.1 in $\alpha\beta$ -coordinates [40], [73]

$$C_{dc}\dot{v}_{dc} = i_{dc} - G_{dc}v_{dc} - i_x, \quad (2.1a)$$

$$L\dot{\mathbf{i}}_{s,\alpha\beta} = \mathbf{v}_{s,\alpha\beta} - R\mathbf{i}_{s,\alpha\beta} - \mathbf{v}_{\alpha\beta}, \quad (2.1b)$$

$$C\dot{\mathbf{v}}_{\alpha\beta} = \mathbf{i}_{s,\alpha\beta} - \mathbf{i}_{\alpha\beta}, \quad (2.1c)$$

where C_{dc} denotes the dc-link capacitance, G_{dc} models dc losses, and, L , C , and R respectively denote the filter inductance, capacitance, and resistance. Moreover, v_{dc} represents the dc voltage, i_{dc} is the current flowing out of the controllable dc current source, $\mathbf{m}_{\alpha\beta}$ denotes the modulation signal of the full-bridge averaged switching stage model, $i_x := (1/2)\mathbf{m}_{\alpha\beta}^T\mathbf{i}_{s,\alpha\beta}$ denotes the net dc current delivered to the switching stage,

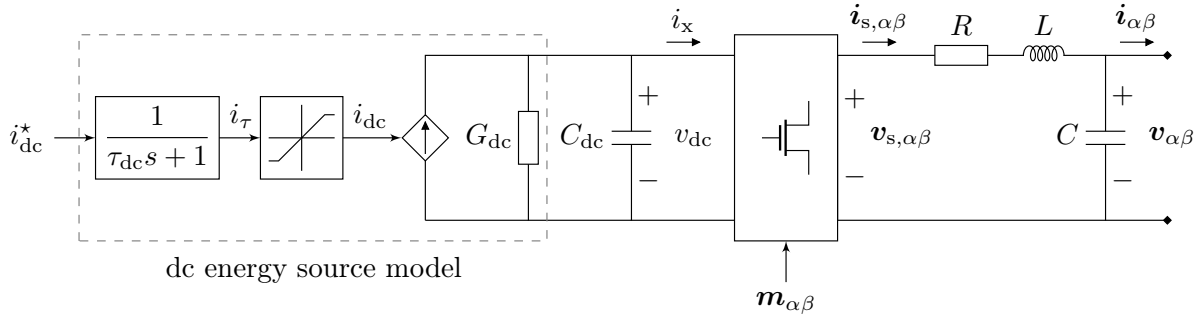


Figure 2.1: Converter model in $\alpha\beta$ -coordinates with detailed dc energy source model based on (2.1)-(2.3).

and $\mathbf{i}_{s,\alpha\beta}$ and $\mathbf{v}_{s,\alpha\beta} := (1/2)\mathbf{m}_{\alpha\beta}v_{dc}$ respectively are the ac switching node current and voltage (i.e., before the output filter), $\mathbf{i}_{\alpha\beta}$ and $\mathbf{v}_{\alpha\beta}$ are the output current and voltage.

To obtain a realistic model of the dc energy source, we model its response time by a first order system

$$\tau_{dc}\dot{i}_\tau = i_{dc}^* - i_\tau, \quad (2.2)$$

where i_{dc}^* is the dc current reference, τ_{dc} is the dc source time constant, and i_τ denotes the current provided by the dc source. Moreover, the dc source current limitation is modeled by the saturation function

$$i_{dc} = \text{sat} \left(i_\tau, i_{\max}^{\text{dc}} \right) = \begin{cases} i_\tau & \text{if } |i_\tau| < |i_{\max}^{\text{dc}}|, \\ \text{sgn}(i_\tau) i_{\max}^{\text{dc}} & \text{if } |i_\tau| \geq |i_{\max}^{\text{dc}}|, \end{cases} \quad (2.3)$$

where i_{\max}^{dc} is the maximum dc source current. Note that we implicitly assume that some storage element is present so that the dc source can support bidirectional power flow. In practice, the limit imposed by (2.3) corresponds to current limits of a dc-dc converter, current limits of an energy storage system, or PV / wind power generation limits. The impact of the dc source limitation (2.3) is investigated in Section 2.4. It is noteworthy that the converter must also limit its ac current to protect its semiconductor switches [74]. This ac current limitation is typically imposed via converter control design (see Section 2.3 for details).

2.2.2 Synchronous machine model

In this work we adopt an 8th order (i.e., including six electrical and two mechanical states), balanced, symmetrical, three-phase SM with a field winding and three damper

windings on the rotor [61, Figure 3.1]

$$\dot{\theta} = \omega, \quad (2.4a)$$

$$J\dot{\omega} = T_m - T_e - T_f, \quad (2.4b)$$

$$\dot{\boldsymbol{\psi}}_{s,dq} = \mathbf{v}_{s,dq} - r_s \mathbf{i}_{s,dq} - \mathcal{J}_2 \boldsymbol{\psi}_{s,dq}, \quad (2.4c)$$

$$\dot{\psi}_{f,d} = v_{f,d} - r_{f,d} i_{f,d}, \quad (2.4d)$$

$$\dot{\boldsymbol{\psi}}_D = \mathbf{v}_D - \mathcal{R}_D \mathbf{i}_D, \quad (2.4e)$$

where θ denotes the rotor angle, J is the inertia constant, ω is the rotor speed, T_m , T_e and T_{fw} denote the mechanical torque, electrical torque, and the friction windage torque (see [61, Section 5.7]). Moreover, $\boldsymbol{\psi}_{s,dq} = [\psi_{s,d} \ \psi_{s,q}]^\top$, $\mathbf{v}_{s,dq} = [v_{s,d} \ v_{s,q}]^\top$, and $\mathbf{i}_{s,dq} = [i_{s,d} \ i_{s,q}]^\top$ denote the stator winding flux, voltage, and current in dq-coordinates (with angle θ as in (2.4a)), $\mathcal{J}_2 = \begin{bmatrix} 0 & -1 \\ 1 & 0 \end{bmatrix}$ denotes the 90° rotation matrix, $\psi_{f,d}$, $v_{f,d}$, and $i_{f,d}$ denote the d-axis field winding flux, voltage and current. Furthermore, r_s and $r_{f,d}$ denote the stator and field winding resistances, $\boldsymbol{\psi}_D = [\psi_{1d} \ \psi_{1q} \ \psi_{2q}]^\top$, $\mathbf{v}_D = [v_{1d} \ v_{1q} \ v_{2q}]^\top$ and $\mathbf{i}_D = [i_{1d} \ i_{1q} \ i_{2q}]^\top$ are the linkage flux, voltage and current associated with three damper windings and $\mathcal{R}_D = \text{diag}(r_{1d}, r_{1q}, r_{2q})$ denotes the diagonal matrix of the damper winding resistances. Note that the windage friction (i.e., modeling friction between the rotor and air) term is commonly expressed as a speed dependent term e.g., $T_f = D_f \omega$ [61, Section 5.7] it is typically negligible for system-level studies and is included here for the sake of completeness and to highlight structural similarities of the SM and two-level voltage source converter with the control presented in Section 2.3.5. Furthermore, the damping torque associated with the damper windings is included in the SM model (2.4) via the damper winding dynamics (2.4e). For more details on the SM modeling and parameters computation the reader is referred to [61, Section 3.3],[62, Chapter 4].

We augment the system (2.4) with a ST1A type excitation dynamics with built-in automatic voltage regulator (AVR) [75, Figure 21]. To counteract the well-known destabilizing effect of the AVR on the synchronizing torque, we equip the system with a simplified power system stabilizer comprised of a two-stage lead-lag compensator [62, Section 12.5]. Lastly, the governor and turbine dynamics are respectively modeled by proportional speed droop control and first order turbine dynamics

$$p = p^* + d_p (\omega^* - \omega), \quad (2.5a)$$

$$\tau_g \dot{p}_\tau = p - p_\tau, \quad (2.5b)$$

where p^* denotes the power set-point, p is the governor output, d_p denotes the governor speed droop gain, and ω^* and ω denote nominal and measured frequency, respectively. Furthermore, τ_g denotes the turbine time constant and p_τ denotes the turbine output power. We refer the reader to [72, Figure 2] for an illustration of the interplay between the SM model, the excitation dynamics, the PSS and governor dynamics. Lastly, the

Matlab/Simulink implementation of the SM model can be found in [71].

2.2.3 Network model

To study the transmission level dynamics of a low-inertia power system, we use Sim Power Systems to perform an EMT simulation of the IEEE 9-bus test system shown in Figure 2.2 [7], [76]. We model the lines via nominal π sections (i.e., with RLC dynamics), model the transformers via three-phase linear transformer models, and consider constant impedance loads (see Table 2.1 for the parameters). We emphasize that the line dynamics cannot be neglected in the presence of grid-forming converters due to potential adverse interactions between their fast response and the line dynamics [47], [72], [77].

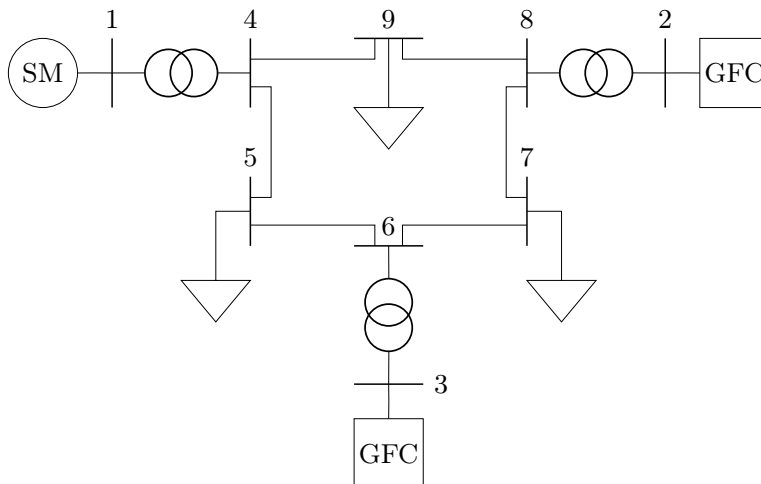


Figure 2.2: IEEE 9-bus test system with a synchronous machine, two large-scale multi-converter systems (i.e., aggregate GFCs), and constant impedance loads.

Remark 1 (Aggregate converter model). *In this case study, each GFC in Figure 2.2 is an aggregate model of 200 commercial converter modules (see Table 2.1 for the parameters). Each module is rated at 500 kVA and the aggregate model is rated at 100 MVA, which is equal to the SM rating. Each module is interfaced to a medium voltage line via a LV-MV transformer (see Figure 2.3). We derive the parameters of the aggregate transformer model by assuming a parallel connection of 100 commercial transformers rated at 1.6 MVA (see Table 2.1). A detailed presentation and derivation of the model aggregation is out of the scope of this work, but we follow developments analogous to [78]–[80] in deriving the equivalent aggregate converter parameters.*

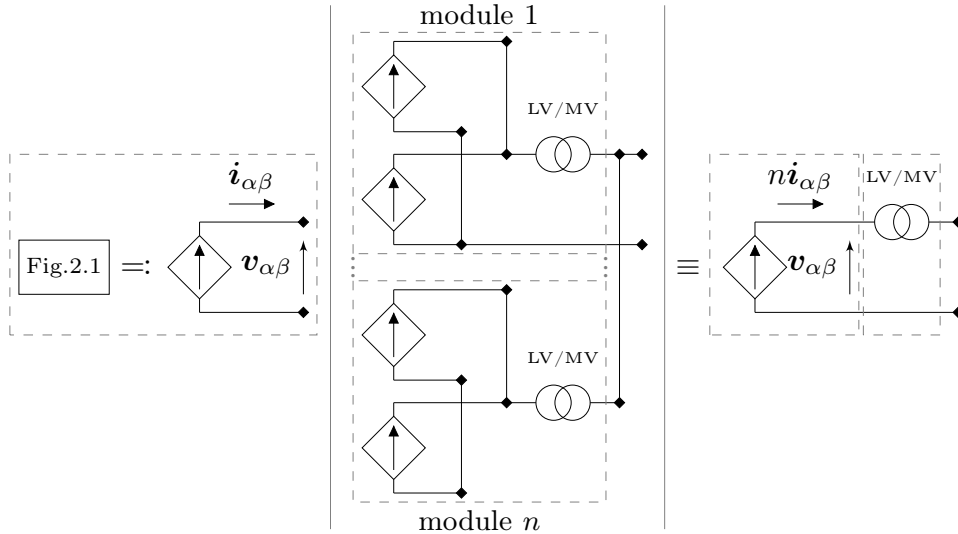


Figure 2.3: Equivalent model of an individual converter module (left), large-scale multi-converter system consisting of n identical modules (middle), and aggregate model (right).

2.3 Grid-forming control architectures

Grid-forming control strategies control (see Figure 2.4) a converter through the reference current i_{dc}^* for the dc energy source (2.1a) and the modulation signal $\mathbf{m}_{\alpha\beta}$ for the dc-ac conversion stage (2.1) (see Figure 2.1). In the following, we briefly review the low-level cascaded control design (i.e., ac voltage control, current limitation and control) for two-level voltage source converters that tracks a voltage reference provided by a reference model (i.e., grid-forming control). Moreover, we propose a controller for the converter dc voltage which defines the reference dc current. Because their design is independent of the choice of the reference model, we first discuss the cascaded voltage / current control and the dc-side control. Subsequently, we review four common grid-forming control strategies. For each strategy, we describe the angle dynamics, frequency dynamics and ac voltage magnitude regulation. Throughout this section we will employ the three phase abc, $\alpha\beta$ and dq-coordinates (see [73, Sections 4.5 and 4.6] for details on the transformations). We remind the reader that the Simulink implementation of the controls presented in the forthcoming subsections is available online [71].

2.3.1 Low-level cascaded control design

AC voltage control

We employ a standard converter control architecture that consists of a reference model providing a reference voltage $\hat{\mathbf{v}}_{dq}$ with angle $\angle \hat{\mathbf{v}}_{dq} = \theta$ and magnitude $\|\hat{\mathbf{v}}_{dq}\|$. The modulation signal $\mathbf{m}_{\alpha\beta}$ is determined by cascaded proportional-integral (PI) controllers

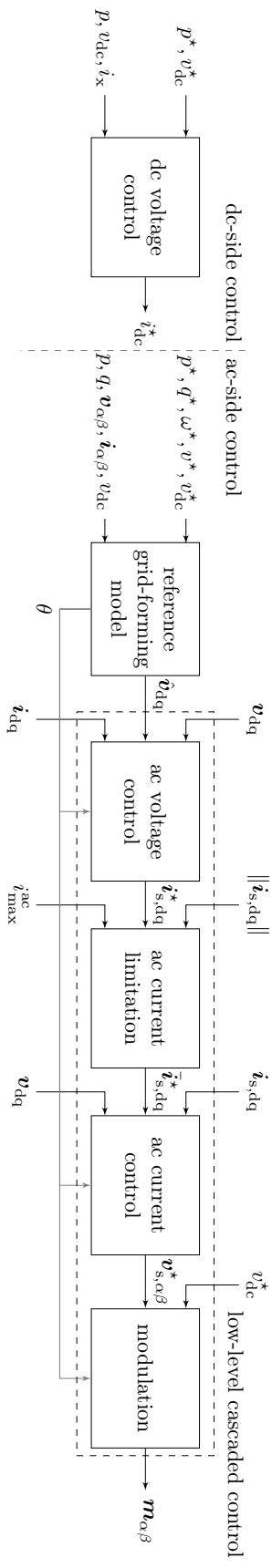


Figure 2.4: Grid-forming control architecture with reference models described in subsections 2.3.3 to 2.3.6.

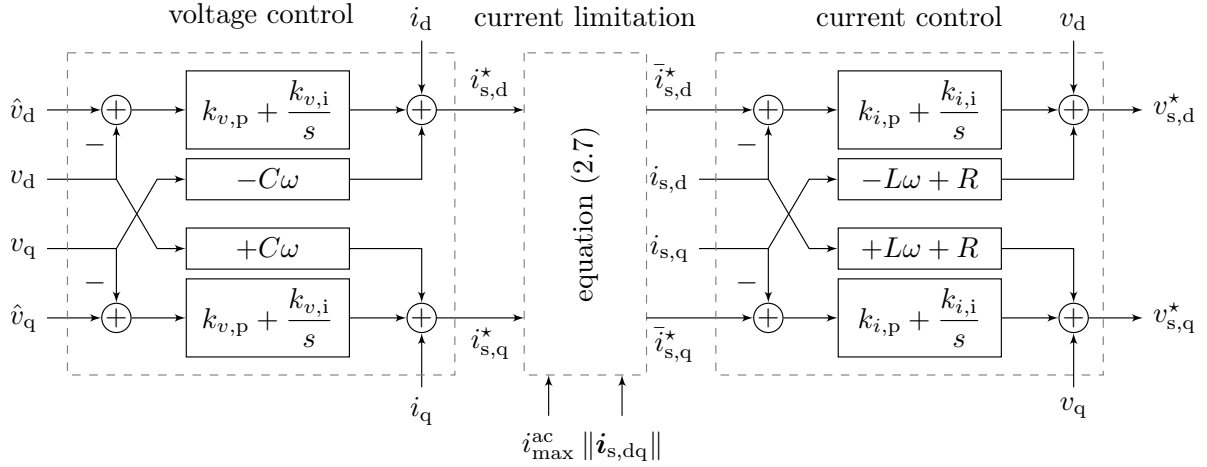


Figure 2.5: Block diagram of the low-level cascaded control design (2.6)-(2.8) in dq-coordinates rotating with the angle θ provided by the reference model.

that are implemented in dq-coordinates (rotating with the reference angle θ) and track the voltage reference $\hat{\mathbf{v}}_{dq}$ (see [66]). The voltage tracking error $\hat{\mathbf{v}}_{dq} - \mathbf{v}_{dq}$ is used to compute the reference $\mathbf{i}_{s,dq}^* = [i_{sd}^* \ i_{sq}^*]^\top$ for the switching node current $\mathbf{i}_{s,dq}$

$$\dot{\mathbf{x}}_{v,dq} = \hat{\mathbf{v}}_{dq} - \mathbf{v}_{dq}, \quad (2.6a)$$

$$\mathbf{i}_{s,dq}^* := \underbrace{\mathbf{i}_{dq} + C\omega \mathcal{J}_2 \mathbf{v}_{dq}}_{\text{feed-forward terms}} + \underbrace{\mathcal{K}_{v,p} (\hat{\mathbf{v}}_{dq} - \mathbf{v}_{dq}) + \mathcal{K}_{v,i} \mathbf{x}_{v,dq}}_{\text{PI control}} \quad (2.6b)$$

here $\mathbf{x}_{v,dq} = [x_{v,d} \ x_{v,q}]^\top$ denotes the integrator state, $\mathbf{v}_{dq} = [v_d \ v_q]^\top$ denotes the output voltage measurement, $\hat{\mathbf{v}}_{dq} = [\hat{v}_d \ 0]^\top$ denotes the reference voltage, $\mathbf{i}_{dq} = [i_d \ i_q]^\top$ denotes the output current, \mathcal{I}_2 is the 2-D identity matrix, $\mathcal{K}_{v,p} = k_{v,p} \mathcal{I}_2$ and $\mathcal{K}_{v,i} = k_{v,i} \mathcal{I}_2$ denote diagonal matrices of proportional and integral gains, respectively.

AC current limitation

We assume that the underlying current controller or low-level protections of the converter limit the ac current. We model this in abstraction by scaling down the reference current $\|\mathbf{i}_{s,dq}^*\|$ if it exceeds the pre-defined converter current limit i_{\max}^{ac} [81, Section III], i.e.,

$$\bar{\mathbf{i}}_{s,dq}^* := \begin{cases} \mathbf{i}_{s,dq}^* & \text{if } \|\mathbf{i}_{s,dq}^*\| \leq i_{\max}^{\text{ac}}, \\ \gamma_i \mathbf{i}_{s,dq}^* & \text{if } \|\mathbf{i}_{s,dq}^*\| > i_{\max}^{\text{ac}}, \end{cases} \quad (2.7)$$

where $\bar{\mathbf{i}}_{s,dq}^*$ denotes the limited reference current that preserves the direction of $\mathbf{i}_{s,dq}^*$ and $\gamma_i := \left(i_{\max}^{\text{ac}} / \|\mathbf{i}_{s,dq}^*\| \right)$. We emphasize that limiting the ac current can have a strong

impact on the stability margins and dynamics of grid-forming power converters [82]. While numerous different strategies have been proposed to limit the ac current injection of voltage source converters with grid-forming controls [74], [81], [83]–[87] the problem of designing a robust ac current limitation strategy that effectively reacts to the load-induced over-current and grid faults is an open research problem. Moreover, complex current limitation strategies typically require careful tuning of the controllers. Therefore, to provide a clear and concise investigation of the behavior of the existing grid-forming control solutions, we use the simple ac current limiting strategy (2.7).

AC current control

In order to implement this scheme, a PI controller for the current $\mathbf{i}_{s,dq} = [i_{s,d} \ i_{s,q}]^\top$ is used to track $\bar{\mathbf{i}}_{s,dq}^*$

$$\dot{\mathbf{x}}_{i,dq} = \bar{\mathbf{i}}_{s,dq}^* - \mathbf{i}_{s,dq}, \quad (2.8a)$$

$$\mathbf{v}_{s,dq}^* := \underbrace{\mathbf{v}_{dq} + \mathcal{Z}\mathbf{i}_{s,dq}}_{\text{feed-forward terms}} + \underbrace{\mathcal{K}_{i,p} \left(\bar{\mathbf{i}}_{s,dq}^* - \mathbf{i}_{s,dq} \right) + \mathcal{K}_{i,i} \mathbf{x}_{i,dq}}_{\text{PI control}}, \quad (2.8b)$$

where $\mathcal{Z} = L\omega\mathcal{J}_2 + R\mathcal{I}_2$, $\mathbf{v}_{s,dq}^* = [v_{s,d}^* \ v_{s,q}^*]^\top$ is the reference for the switching node voltage (i.e., before output filter in Figure 2.1), $\mathbf{x}_{i,dq} = [x_{i,d} \ x_{i,q}]^\top$ denotes the integrator state, and $\mathcal{K}_{i,p} = k_{p,i}\mathcal{I}_2$ and $\mathcal{K}_{i,i} = k_{i,i}\mathcal{I}_2$ denote the diagonal matrices of proportional and integral gains, respectively. Note that the first two terms of the right hand side of (2.6b) and (2.8b) are feed-forward terms. Finally, the modulation signal $\mathbf{m}_{\alpha\beta}$ is given by

$$\mathbf{m}_{\alpha\beta} = \frac{2\mathbf{v}_{s,\alpha\beta}^*}{v_{dc}^*}, \quad (2.9)$$

where $\mathbf{v}_{s,\alpha\beta}^*$ is the $\alpha\beta$ -coordinates image of $\mathbf{v}_{s,dq}^*$ defined in (2.8) and v_{dc}^* denotes the nominal converter dc voltage.

2.3.2 DC voltage control

The dc current reference i_{dc}^* that is tracked by the controllable dc source (2.2) is given by a proportional control for the dc voltage and feed-forward terms based on the nominal ac active power injection p^* and the filter losses

$$i_{dc}^* = \underbrace{k_{dc}(v_{dc}^* - v_{dc})}_{\text{proportional control}} + \underbrace{\frac{p^*}{v_{dc}^*} + \left(G_{dc}v_{dc} + \frac{v_{dc}i_x - p}{v_{dc}^*} \right)}_{\text{power injection and loss feed-forward}}, \quad (2.10)$$

where $v_{dc}i_x$ is the dc power flowing into the switches, p is the ac power injected into the grid, and the last term on the right hand side of (2.10) implements a feed-forward power control that compensates the filter losses. The loss compensation is required to ensure exact tracking of the power reference by matching control (see Section 2.3.5) and also improves the dc voltage regulation for the other control strategies considered in this study. Thus, to employ an identical dc voltage control, we apply (2.10) for all control strategies discussed throughout this work.

2.3.3 Droop control

Droop control resembles the speed droop property (2.5a) of the SM governor [35] and trades off deviations of the power injection (from its nominal value p^*) and frequency deviations (from ω^*)

$$\dot{\theta} = \omega, \quad (2.11a)$$

$$\omega = \omega^* + d_\omega (p^* - p), \quad (2.11b)$$

where d_ω denotes the droop gain. To replicate the service provided by the automatic voltage regulator (AVR) of synchronous machines we use a PI controller acting on the output voltage error

$$\hat{v}_d = k_p (v^* - \|\mathbf{v}_{dq}\|) + k_i \int_0^t (v^* - \|\mathbf{v}_{dq}(\tau)\|) d\tau. \quad (2.12)$$

to obtain the direct axis reference \hat{v}_d for the underlying voltage loop (v^* and $\|\mathbf{v}_{dq}\|$ are the reference and measured voltage magnitude). We remark that $\hat{v}_q = 0$ and the reactive power injection varies such that exact voltage regulation is achieved.

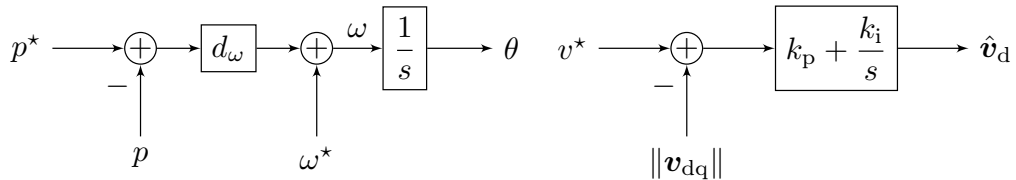


Figure 2.6: Droop control frequency and ac voltage control block diagrams based on (2.11) and (2.12).

2.3.4 Virtual synchronous machine

Many variations of virtual synchronous machines (VSMs) have been proposed [38], [64]. In this work, we consider the frequency dynamics induced by the synchronverter [64]

$$\dot{\theta} = \omega, \quad (2.13a)$$

$$J_r \dot{\omega} = \frac{1}{\omega^*} (p^* - p) + D_p (\omega^* - \omega), \quad (2.13b)$$

where $D_p (\omega^* - \omega)$ is commonly referred to as (virtual) damping [64, Section II-B] and is inspired by the speed droop response of a synchronous machine. Note that the speed dependent term in (2.13b) has no exact analogue in a synchronous machine. The response of SM damper windings and its turbine governor are on different time scales and the SM damper windings do not act relative to the nominal frequency. In contrast, the speed dependent term in (2.13b) provides both instantaneous damping and at steady-state (i.e., the equivalent to SM turbine governor droop) relative to the nominal frequency. Moreover, J_r is the virtual rotor's inertia constant. Note that the dynamics (2.13) reduce to droop control (2.11) when using $J_r/D_p \approx 0$ as recommended in [64]. These angle dynamics capture the main salient features of virtual synchronous machines, but do not suffer from drawbacks of more complicated implementations (see [7] for a discussion). The three-phase voltage induced by the VSM is given by

$$\hat{\mathbf{v}}_{\text{abc}} = 2\omega M_f i_f \left(\sin(\theta) \quad \sin\left(\theta - \frac{2\pi}{3}\right) \quad \sin\left(\theta - \frac{4\pi}{3}\right) \right)^\top, \quad (2.14)$$

where M_f and i_f are respectively the virtual mutual inductance magnitude and excitation current. Similar to (2.12), we utilize input i_f to achieve exact ac voltage regulation via PI control and thereby replicate the function of the AVR of a synchronous machine

$$i_f = \frac{k_p}{M_f} \left(v^* - \|\mathbf{v}_{\text{dq}}\| \right) + \frac{k_i}{M_f} \int_0^t \left(v^* - \|\mathbf{v}_{\text{dq}}(\tau)\| \right) d\tau. \quad (2.15)$$

Transforming $\hat{\mathbf{v}}_{\text{abc}}$ to dq-coordinates with θ and ω as in (2.13), the voltage and current loops and modulation signal generation remain the same as (2.6)–(2.9).

2.3.5 Matching control

Matching control is a grid-forming control strategy that exploits structural similarities between power converters and SMs [40], [41], [43], [44], [65] and is based on the observation that the dc-link voltage - similar to the synchronous machine frequency - indicates power imbalances. Hence, the dc voltage, up to a constant factor, is used to drive the converter frequency. This control technique structurally matches the differential equa-

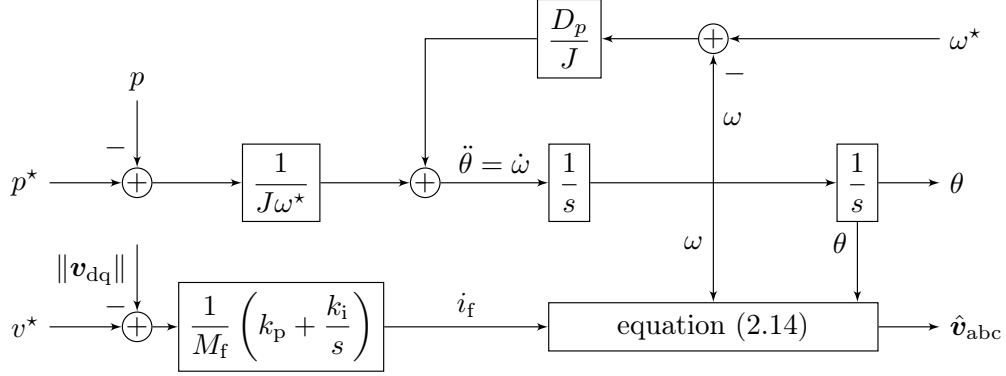


Figure 2.7: Block diagram of a grid-forming VSM based (2.13)-(2.15).

tions of a converter to those of a SM. Furthermore, analogous to the machine input torque, the dc current is used to control the ac power. The angle dynamics of matching control are represented by

$$\dot{\theta} = k_{\theta} v_{\text{dc}}, \quad (2.16)$$

where $k_{\theta} := \omega^*/v_{\text{dc}}^*$. Finally, the ac voltage magnitude is controlled through the modulation magnitude μ by a PI controller

$$\mu = k_p \left(v^* - \|\mathbf{v}_{\text{dq}}\| \right) + k_i \int_0^t \left(v^* - \|\mathbf{v}_{\text{dq}}(\tau)\| \right) d\tau. \quad (2.17)$$

The reference voltage for the voltage controller in $\alpha\beta$ -coordinates is given by:

$$\hat{\mathbf{v}}_{\alpha\beta} = \mu [-\sin \theta \quad \cos \theta]^{\top}. \quad (2.18)$$

Transforming $\hat{\mathbf{v}}_{\alpha\beta}$ to dq-coordinates with θ and ω as in (2.16), the voltage and current loops and modulation signal generation remain the same as (2.6)–(2.9).

To further explain the matching concept, we replace v_{dc} in (2.1a) by ω/k_{θ} from (2.16) resulting in

$$\dot{\theta} = \omega, \quad (2.19a)$$

$$C_{\text{dc}} \dot{\omega} = k_{\theta} i_{\text{dc}} - k_{\theta} i_x - G_{\text{dc}} \omega. \quad (2.19b)$$

Recalling the SM's angle and frequency dynamics (2.4a)-(2.4b) and replacing T_f by $D_f \omega$ results in

$$\dot{\theta} = \omega, \quad (2.20a)$$

$$J \dot{\omega} = T_m - T_e - D_f \omega, \quad (2.20b)$$

Comparing (2.19) and (2.20) reveals the structural matching of GFC dynamics to that of SM. Dividing (2.19b) by k_θ^2 to obtain the same units as in (2.20b) and matching variables results in $J_r = C_{dc}/k_\theta^2$, $D_f = G_{dc}/k_\theta^2$, $T_m = i_{dc}/k_\theta$, and $T_e = i_x/k_\theta$. In other words, using matching control the inertia constant of the GFC is linked to its internal energy storage, the dc-side losses $G_{dc}\omega$ are linked to the machine windage friction losses $D_f\omega$, and the frequency droop response is provided through the proportional dc voltage control $k_{dc}(v_{dc}^* - v_{dc}) = (k_{dc}/k_\theta)(\omega^* - \omega)$ (cf. (2.10)). The structural matching induced by (2.16) also extends to the converter ac filter and generator stator dynamics (see [40], [65] for a detailed derivation).

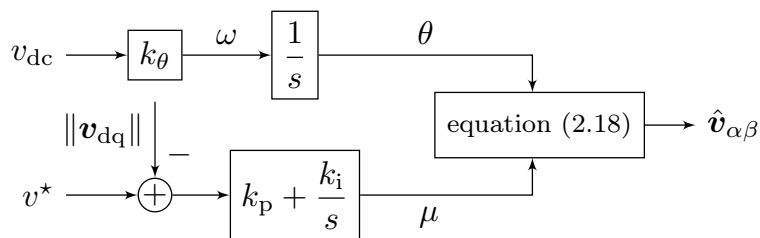


Figure 2.8: Matching control block diagram based on (2.16)-(2.18).

2.3.6 Dispatchable virtual oscillator control

Dispatchable virtual oscillator control (dVOC) [45], [47], [48] is a decentralized grid-forming control strategy that guarantees almost global asymptotic stability for interconnected GFCs with respect to nominal voltage and power set-points [45], [47]. The analytic stability conditions for dVOC explicitly quantify the achievable performance and include the dynamics and transfer capacity of the transmission network [47].

The dynamics of dVOC in $\alpha\beta$ -coordinates are represented by

$$\dot{\hat{\mathbf{v}}}_{\alpha\beta} = \omega^* \mathcal{J}_2 \hat{\mathbf{v}}_{\alpha\beta} + \eta \left(\mathcal{K} \hat{\mathbf{v}}_{\alpha\beta} - \mathcal{R}_2(\kappa) \mathbf{i}_{\alpha\beta} + \phi(v^*, \hat{\mathbf{v}}_{\alpha\beta}) \right), \quad (2.21)$$

where $\phi(v^*, \hat{\mathbf{v}}_{\alpha\beta}) = (\alpha/v^{*2}) \left(v^{*2} - \|\hat{\mathbf{v}}_{\alpha\beta}^2\| \right) \hat{\mathbf{v}}_{\alpha\beta}$, $\hat{\mathbf{v}}_{\alpha\beta} = [\hat{v}_\alpha \ \hat{v}_\beta]^\top$ is the reference voltage, $\mathbf{i}_{\alpha\beta} = [i_\alpha \ i_\beta]^\top$ is current injection of the converter, the angle $\kappa := \tan^{-1}(l\omega^*/r)$ models the network inductance to resistance ratio, and η, α are positive control gains. Furthermore we have

$$\mathcal{R}_2(\kappa) := \begin{pmatrix} \cos \kappa & -\sin \kappa \\ \sin \kappa & \cos \kappa \end{pmatrix}, \mathcal{K} := \frac{1}{v^{*2}} \mathcal{R}_2(\kappa) \begin{pmatrix} p^* & q^* \\ -q^* & p^* \end{pmatrix},$$

where $\mathcal{R}_2(\kappa)$ is the 2-D rotation by κ . As shown in [47] the dynamics (2.21) reduce to a harmonic oscillator if phase synchronization is achieved (i.e., $\mathcal{K} \hat{\mathbf{v}}_{\alpha\beta} - \mathcal{R}_2(\kappa) \mathbf{i}_{\alpha\beta} = 0$) and

$\|\hat{\mathbf{v}}_{\alpha\beta}\| = v^*$ (i.e., $(v^{*2} - \|\hat{\mathbf{v}}_{\alpha\beta}\|^2) \hat{\mathbf{v}}_{\alpha\beta} = 0$). Rewriting (2.21) in polar coordinates for an inductive network (i.e., $\kappa = \pi/2$) reveals the droop characteristics (see [45], [47], [48]) of dVOC as

$$\dot{\theta} = \omega^* + \eta \left(\frac{p^*}{v^{*2}} - \frac{p}{\|\hat{\mathbf{v}}_{dq}\|^2} \right), \quad (2.22a)$$

$$\|\dot{\hat{\mathbf{v}}}_{dq}\| = \eta \left(\frac{q^*}{v^{*2}} - \frac{q}{\|\hat{\mathbf{v}}_{dq}\|^2} \right) \|\hat{\mathbf{v}}_{dq}\| + \eta\phi(v^*, \|\hat{\mathbf{v}}_{dq}\|), \quad (2.22b)$$

where $\phi(v^*, \|\hat{\mathbf{v}}_{dq}\|) = (\alpha/v^{*2})(v^{*2} - \|\hat{\mathbf{v}}_{dq}\|^2)\|\hat{\mathbf{v}}_{dq}\|$. In other words, for a high voltage network and near the nominal steady state (i.e., $\|\hat{\mathbf{v}}_{dq}\| \approx v^*$) the relationship between frequency and active power resemble that of standard droop control given in (2.11) with $d_\omega = \eta/v^{*2}$. Moreover, when choosing the control gain α to obtain post-fault voltages consistent with the other control algorithms described above, the first term in (2.22b) is negligible and (2.22b) reduces to the voltage regulator $\|\dot{\hat{\mathbf{v}}}_{dq}\| \approx -2\eta\alpha(\|\hat{\mathbf{v}}_{dq}\| - v^*)$ near the nominal steady state.

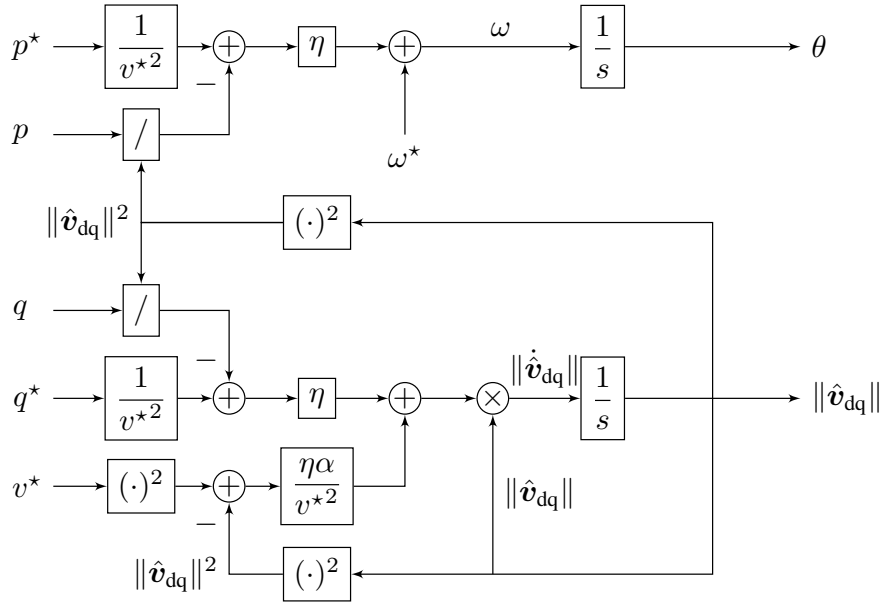


Figure 2.9: Block diagram of dVOC in polar coordinates corresponding to (2.22). Note that singularity at $\|\hat{\mathbf{v}}_{dq}\| = 0$ only appears in the dVOC implementation in polar coordinates but not in the implementation in rectangular coordinates, i.e., (2.21).

2.4 Network case study

In this section, we explore various performance aspects of the grid-forming control techniques in the presence of synchronous machines. In the forthcoming discussion, we use the test system shown in Figure 2.2. The parameters and control gains are given in Table 2.1. The implementation in Simulink is available online [71].

In order to avoid the delay associated with the frequency measurement and signal processing introduced by standard synchronous reference frame phase-locked loop (SRF-PLL)[70], we use the mechanical frequency of the SM at node 1 in Figure 2.2 to evaluate the post-disturbance system frequency (e.g., in Figures 2.11-2.12). For the grid-forming converters we use the internal controller frequencies defined by (2.11), (2.13), (2.16) and (2.22). We remark that, in a real-world system and in an EMT simulation (in contrast to a phasor simulation), there is no well-defined frequency at the voltage nodes during transients, whereas the internal frequencies of the grid-forming converters are always well-defined [33, Section II-J],[88]. Lastly, we note that in all the forthcoming case studies we assume that the system is in steady-state at $t = 0$.

2.4.1 Performance metrics

We adopt the standard power system frequency performance metrics i.e., maximum frequency deviation $\|\Delta\omega\|_\infty$ (i.e., frequency nadir/zenith) and RoCoF $|\dot{\omega}|$ (i.e., the slope of line tangent to the post-event frequency trajectory) defined by

$$\|\Delta\omega\|_\infty := \max_{t \geq t_0} |\omega^* - \omega(t)|, \quad (2.23a)$$

$$|\dot{\omega}| := \frac{|\omega(t_0 + T) - \omega(t_0)|}{T}, \quad (2.23b)$$

where $t_0 > 0$ is the time when the disturbance is applied to the system, and $T > 0$ is the RoCoF calculation window [33], [70]. See Figure 2.10 for visual representation of the metrics described by (2.23). In this work, we use $T = 250\text{ms}$, which is in line with values suggested for protection schemes (see [69, Table 1]). Dividing the metrics (2.23) by the size of the magnitude of the disturbance results in a measure of the system disturbance amplification.

2.4.2 Test network configuration and tuning criteria

In order to study the performance of the control approaches introduced in Section 2.3, we apply the same strategy (with identical tuning) for both converters (i.e., at nodes 2 and 3 in Figure 2.2), resulting in four different SM-GFC paired models. As a benchmark, we also consider an all-SMs system with three identical SMs (i.e., at nodes 1-3). Selecting fair

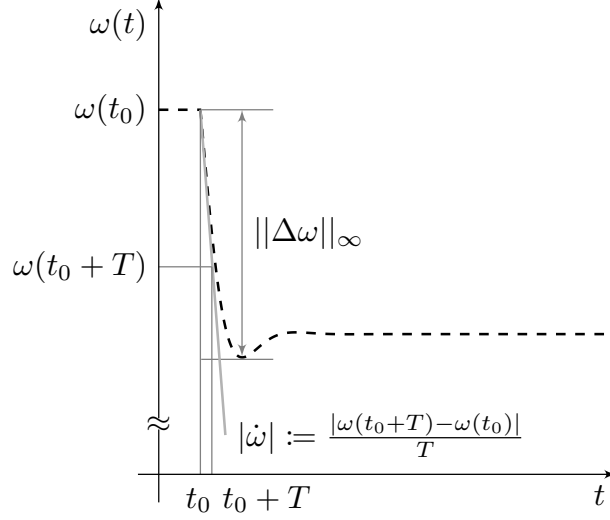


Figure 2.10: Post-event frequency nadir and RoCoF.

tuning criteria for the different control strategies is a challenging task. For this study, we tune the control parameters such that all generation units exhibit identical proportional load sharing behavior. Appendix 2.7 presents the tuning criteria and derivation of some control parameters.

2.4.3 Impact of grid-forming control on frequency metrics

In this section, we test the system behavior for different load disturbances Δp_i . The network base load p_l is constant and uniformly distributed between nodes 5, 7 and 9 while Δp_i is only applied at node 7. For each disturbance input we calculate $\|\Delta\omega_i\|_\infty$ and $|\dot{\omega}_i|$ for the SM at node 1 and normalize these quantities by dividing by $|\Delta p_i|$. Figures 2.11 and 2.12 illustrate the distribution of system disturbance input/output gains associated with introduced frequency performance metrics. Note that the network base load p_l is 2 pu and the elements of the load disturbance sequence $\Delta p_i \in [0.2, 0.9]$, $i = 1, \dots, 100$ are uniformly increasing by 0.007 pu starting from $p_1 = 0.2$ pu.

All the grid-forming controls presented in Section 2.3 are originally designed without consideration of the converter dc and ac current limitation. Thus, to explore the intrinsic behavior of the GFCs and their influence on frequency stability the network loading scenarios described above are selected such that the GFCs dc and ac currents do not exceed the limits imposed by (3) and (7). However, in practice, GFCs are subject to strict dc and ac current limits and are combined with current limiting strategies in a modular fashion. The impact of the dc and ac current limits on the performance of GFCs is explored in Subsections 2.4.4 to 2.4.6.

Figures 2.11 and 2.12 suggest that, regardless of the choice of control strategy, the

presence of grid-forming converters improves the metrics compared to the all-SM system. This possibly observation can be explained by the fast response of converters compared to the slow turbine dynamics, i.e., τ_g in (2.5) is larger than τ_{dc} in (2.2). Because of this, the converters reach frequency synchronization at a faster time-scale and then synchronize with the SM (see Figure 2.13). Overall, for any given disturbance input, the converters are able to react faster than the SM and the remaining power imbalance affecting the SM is smaller than in the all-SM system. This result highlights that the fast response of GFCs should be exploited instead of designing the controls of a converter (fast physical system) to emulate the slow response of synchronous machines [33]. We observe that droop control and dVOC exhibit very similar performance confirming the droop-like behavior of dVOC in predominantly inductive networks (see (2.22)). Moreover, the difference between droop control and VSM arises from the inertial (derivative control) term in (2.13) and the RoCoF is considerably higher when using matching control. This can be explained by the fact that VSM, droop control, and dVOC ignore the dc voltage and aggressively regulate the ac quantities to reach angle synchronization, thus requiring higher transient peaks in dc current to stabilize the dc voltage (see Section 2.4.4). Although improving RoCoF, this approach can lead to instability if the converter is working close to the rated power of the dc source (but far away from its ac current limit), as shown in the next section. On the other hand, matching control regulates the dc link voltage both through the dc source and by adjusting its ac signals.

We selected the RoCoF calculation window according to the guideline [69], which accounts for noise and possible oscillations in the frequency signal. However, these guidelines were derived for a power system fully operated based on SMs. Given that grid-forming converters introduce faster dynamics, machines are expected to reach the frequency nadir faster. Hence, a smaller RoCoF windows might need to be considered in a low-inertia power system to properly assess system performance (the reader is referred to [2, Section III-C] for further insights on the choice of RoCoF window in a low-inertia system). We note that the performance of the different grid-forming control strategies shown in Figure 2.11 and 2.12 is sensitive to the tuning of control gains and choice of RoCoF computation window. However, due to the comparably slow response of conventional generation technology the performance improvements for the system with grid-forming converters over the all-SM system persist for a wide range of parameters. Moreover, using comparable tuning (see Section 2.4.2) the differences between the different grid-forming techniques observed in this section are expected to remain the same.

2.4.4 Response to a large load disturbance

In this subsection we analyze the response of the grid-forming converters to large disturbances when the dc source is working close to its maximum rated values. Specifically, we focus on the implications of the dc current limit (3) to highlight the response of GFCs

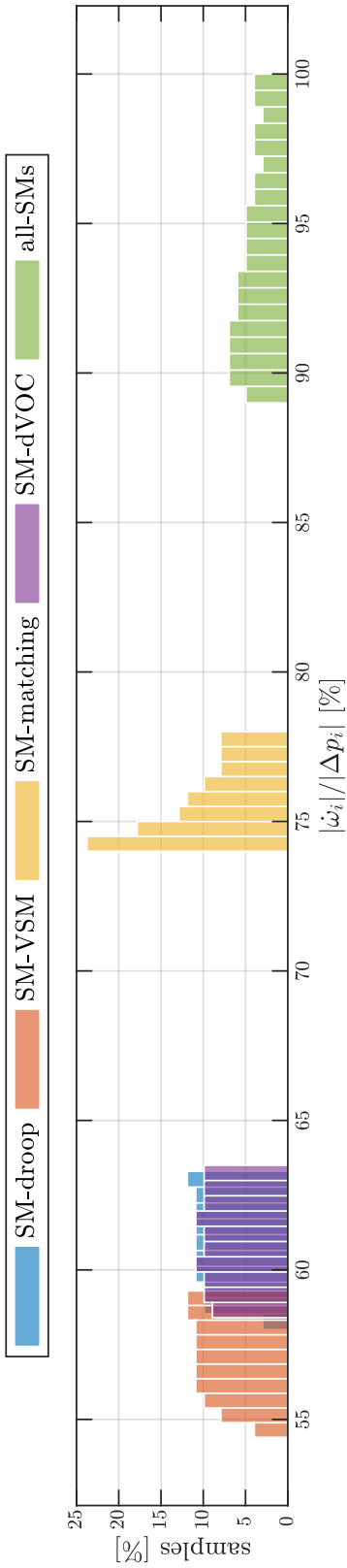


Figure 2.11: Normalized distribution of the RoCoF $|\dot{\omega}_i|/|\Delta p_i|$ of the synchronous machine frequency at node 1 for load disturbances Δp_i ranging from 0.2 p.u. to 0.9 p.u. at node 7. For each load disturbance, $|\dot{\omega}_i|/|\Delta p_i|$ is normalized by the maximum value corresponding to the all-SMs configuration.

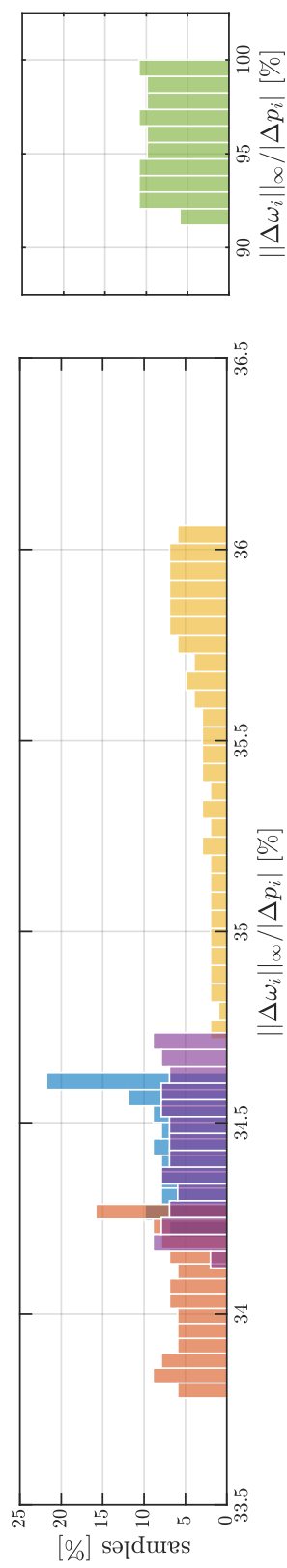


Figure 2.12: Normalized distribution of the nadir $\|\Delta\omega_i\|_\infty/|\Delta p_i|$ of the synchronous machine frequency at node 1 for load disturbances Δp_i ranging from 0.2 p.u. to 0.9 p.u. at node 7. For each load disturbance, $\|\Delta\omega_i\|_\infty/|\Delta p_i|$ is normalized by the maximum value corresponding to the all-SMs configuration.

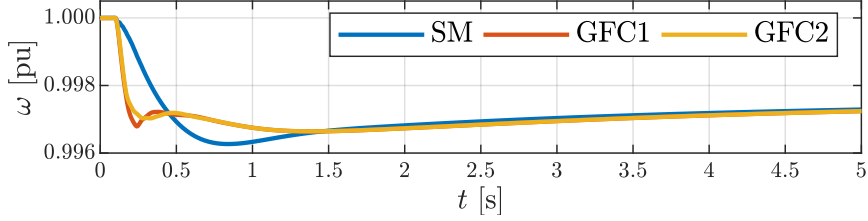


Figure 2.13: Frequency of the system with two VSMs after a 0.75 pu load increase. The converters quickly synchronize with each other and then slowly synchronize with the machine.

when interfacing curtailed renewable generation with low headroom (i.e., PV / wind) or a converter system with an undersized dc-dc converter stage. In such scenarios, the dc current limit can be activated independently of the ac current limit. For clarity of representation we first focus exclusively on the matching control as its angle dynamic (2.16) explicitly considers the dc voltage. Droop control, which does not consider the dc voltage, is solely presented to emphasize the need for an ac current limitation mechanism to implicitly stabilize the dc voltage.

To begin with, we set the network base load p_l and load change Δp to 2.25 and 0.9 pu respectively (i.e., a total network load after the disturbance of 3.15 pu) which is equally shared by the SM and the GFCs. We expect a post-disturbance converter power injection of 1.05 pu and i_{dc} close to the dc current limit $i_{max}^{dc} = \pm 1.2$ pu. Figure 2.14 shows the dc voltage and delayed dc current before saturation for the converter at node 2. For sufficiently large disturbance magnitude, i_{dc}^* and consequently i_τ exceed the current limit, i.e., the dc current $i_{dc} = i_{max}^{dc}$ is saturated. Figures 2.14 and 2.15 highlight that

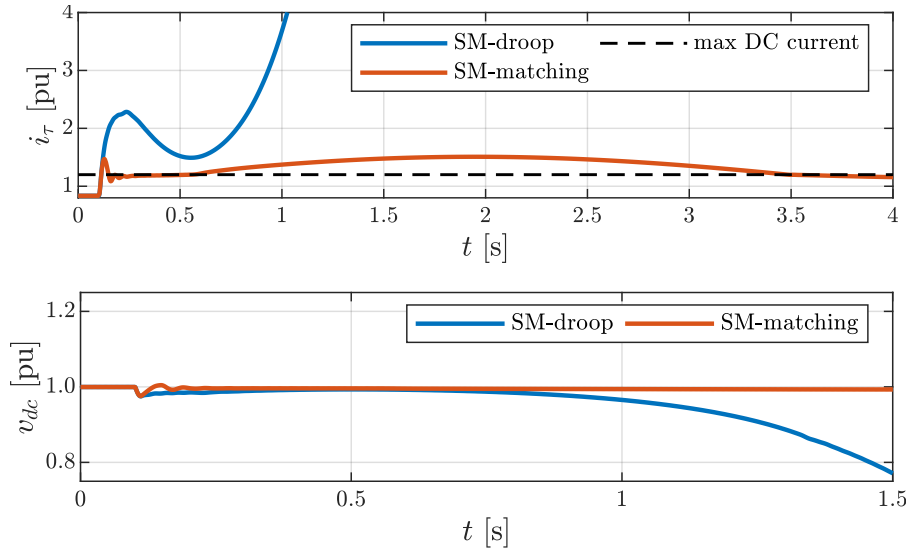


Figure 2.14: DC current demand of the converter at node 2 (top) and its dc voltage (bottom) after a 0.9 pu load disturbance.

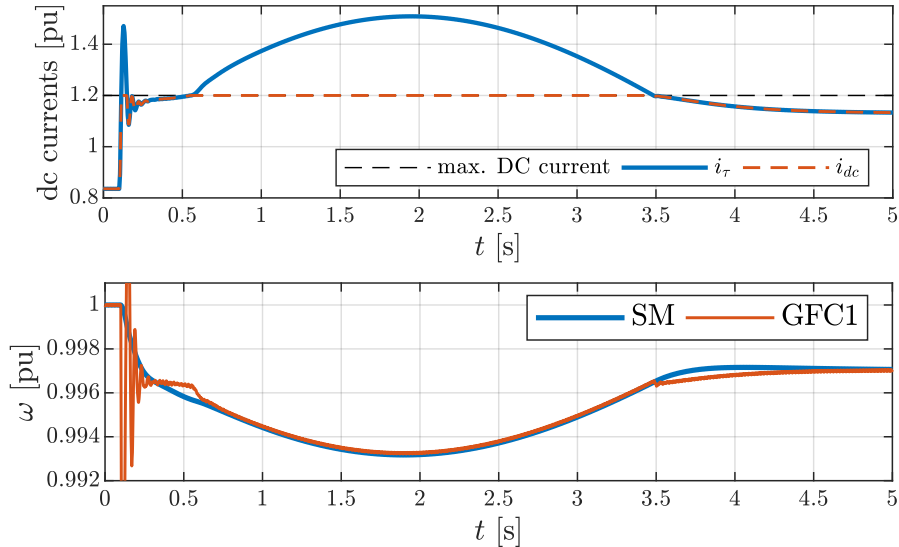


Figure 2.15: DC current demand and saturated dc current (top), frequency of the converter (using matching control) at node 2 and SM after a 0.9 pu load disturbance (bottom).

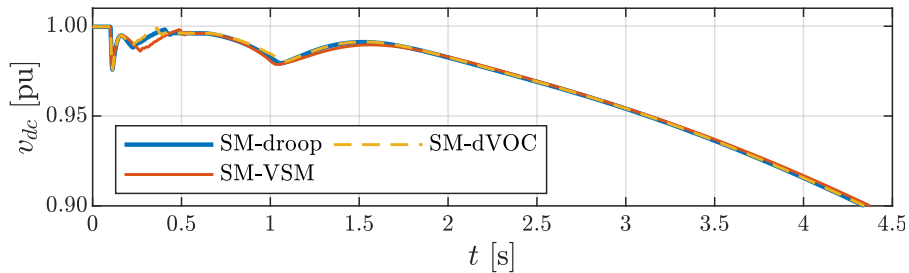


Figure 2.16: DC voltage of the converter at node 2 after a 0.9 pu load disturbance when both dc and ac limitation schemes (2.3) and (2.7) are active and $\tau_g = 5s$.

the matching control succeeds to stabilize the dc voltage despite the saturation of the dc source. The nature of matching control - which accounts for the dc-side dynamics while regulating the ac dynamics i.e., (2.16) - results in increased robustness with respect to large disturbances. From a circuit-theoretic point of view this is possible only if the sum of the ac power injection and filter losses equals the approximately constant dc power inflow $v_{dc}i_{max}^{dc}$. The converter can inject constant ac power into the network only if its angle difference with respect to the remaining devices in the network is constant. In the presence of the slow SM angle and frequency dynamics this implies that the GFCs need to synchronize their frequencies to the SM so that the relative angle $\theta_{GFC} - \theta_{SM} = \theta_{max}$ is constant (see the frequency of GFC 1 following the dc source saturation at $t = 0.5s$ in Figure 2.15). Note that the behavior for the matching controlled GFCs is similar to that of the SM (see Section 2.3.5 and [40], [43], [65]), i.e., it achieves synchronization both under controlled or constant mechanical input power (i.e., dc current injection).

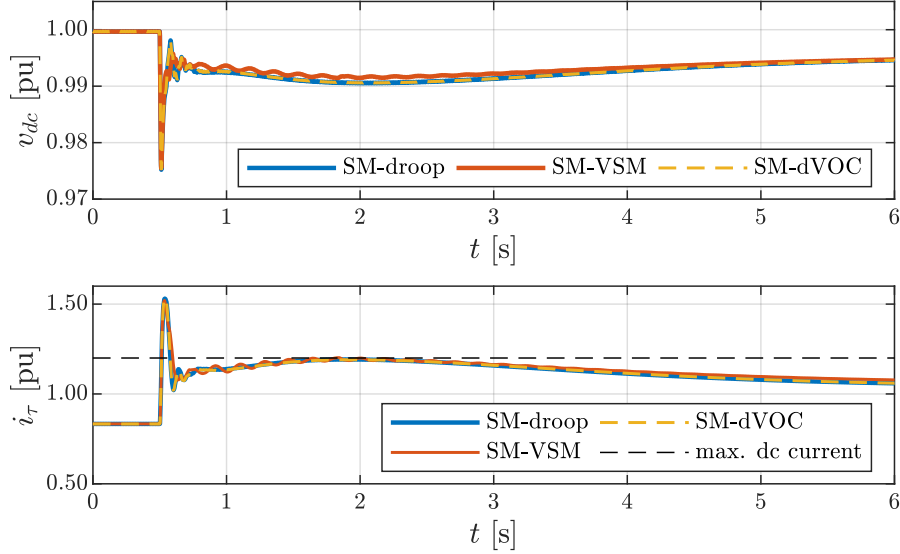


Figure 2.17: DC voltage (top) and dc current demand (bottom) of the converter at node 2 after a 0.9 pu load disturbance when all the limitation schemes i.e., (2.3), (2.7) and (2.24) are active and $\tau_g = 5s$.

Figure 2.14 shows that for the GFCs controlled by droop control the dc-link capacitors discharge to provide $i_\tau - i_{\max}^{\text{dc}}$ (i.e., the portion of current demand which is not provided due to the saturation (2.3)). Because the angle and frequency dynamics (i.e., (2.11), (2.13), and (2.22a)) of droop control, VSM, and dVOC purely rely on ac measurements they are agnostic to the dc dynamics and source saturation. Consequently, a prolonged duration of dc source saturation results in a collapse of the dc voltage. A potential remedy is to incorporate an ac current limitation scheme to prevent the GFC from depleting the dc-link capacitor. This observation motivates the discussion in the next subsection with restricted focus on droop control, VSM, and dVOC techniques.

2.4.5 Incorporating the ac current limitation

In this subsection, we investigate if the ac current limitation (2.7) presented in Section 2.3.1 can mitigate the instabilities of the GFCs controlled by droop control, VSM and dVOC under dc source saturation. To this end, we consider the same base load and disturbance as in the previous test case, i.e., $p_l = 2.25$ and $\Delta p = 0.9$ pu. For this scenario, the GFCs dc transient current demand i_τ and the switching node current magnitude $\|\mathbf{i}_{s,dq}\|$ exceeds the limits (i.e., $i_{\max}^{\text{dc}} = i_{\max}^{\text{ac}} = 1.2$ pu) imposed by (2.3) and (2.7).

We observe that using the ac current limiter does not stabilize the dc voltage of the GFCs controlled by droop control, VSM, and dVOC. Figure 2.16 illustrates the behavior

of the GFC at node 2. Specifically, the current limitation imposed by (2.7) results in integrator windup, a loss of ac voltage control and, ultimately, instability of the grid-forming control [82] and dc voltage. We remark that GFCs exhibit the same instability behavior when the ac current limit is smaller than that of the dc-side i.e., $i_{\max}^{\text{ac}} < i_{\max}^{\text{dc}}$.

To mitigate this load-induced instability, we explore a current limitation scheme that modifies the active power set-point when $\|\mathbf{i}_{\text{s,dq}}\|$ exceeds a certain threshold value, i.e.,

$$\Delta p^* := \begin{cases} 0 & \text{if } \|\mathbf{i}_{\text{s,dq}}\| \leq i_{\text{th}}^{\text{ac}}, \\ \gamma_p \left(\|\mathbf{i}_{\text{s,dq}}\| - i_{\text{th}}^{\text{ac}} \right) & \text{if } \|\mathbf{i}_{\text{s,dq}}\| > i_{\text{th}}^{\text{ac}}, \end{cases} \quad (2.24)$$

and Δp^* is added to p^* in (2.10), (2.11), (2.13b) and (2.21), γ_p denotes a proportional control gain, and $i_{\text{th}}^{\text{ac}} < i_{\max}^{\text{ac}}$ is the activation threshold. Note that the control law (2.24) implicitly manipulates the grid-forming dynamics through their set-points such that the ac current magnitude stays within the admissible limits for large increases in load. We emphasize that this strategy aims at mitigating instabilities induced by large load increases and that the resulting GFC response to grid faults needs to be carefully studied.

For a 0.9 pu load increase, the current limitation strategy (2.24) is able to stabilize the system with $i_{\text{th}}^{\text{ac}} = 0.9$ pu and $\gamma_p = 2.3 (p_b/i_b^{\text{ac}})$ where p_b and i_b^{ac} denote the converter base power and current, respectively. Figure 2.17 depicts the response of the same GFC as in Figure 2.16. Note that (2.24) effectively stabilizes the dc voltage for droop control, VSM, and dVOC. Moreover, in contrast to Figure 2.14, after the post-disturbance transient the dc source is no longer in saturation. Broadly speaking, this strategy succeeds to stabilize the system by steering the GFC power injection away from the critical limits. However, this also influences the post-disturbance operating point of the GFCs due to the threshold value being below the rated value.

Finally, we observe that the different time-scales in a low-inertia system contribute to the instabilities observed in the previous section. In particular, if the SM's turbine responds faster, GFCs with the standard limitation strategy (2.7) preserve stability - without the need to implement (2.24) - despite the fact that transient dc and ac currents exceed the limits. Figure 2.18 shows the GFCs responses when the SM turbine delay τ_g is 1s (cf. Figure 2.16 where $\tau_g = 5$ s). It can be seen that the slow SM turbine dynamics again contribute to the system instability when dc and ac currents are saturated. We conclude that the presence of different time-scales in a low-inertia system - often neglected in the literature [74], [81]–[87] - must be considered in designing a robust ac current limitation mechanism for the GFCs.

Remark 2 (DC and AC measurements). *We observe that using ac measurements to drive the angle dynamics - e.g., VSMs use active power measurements in (2.13) - improves the frequency performance of GFCs (see Figures 2.11 and 2.12). On the other*

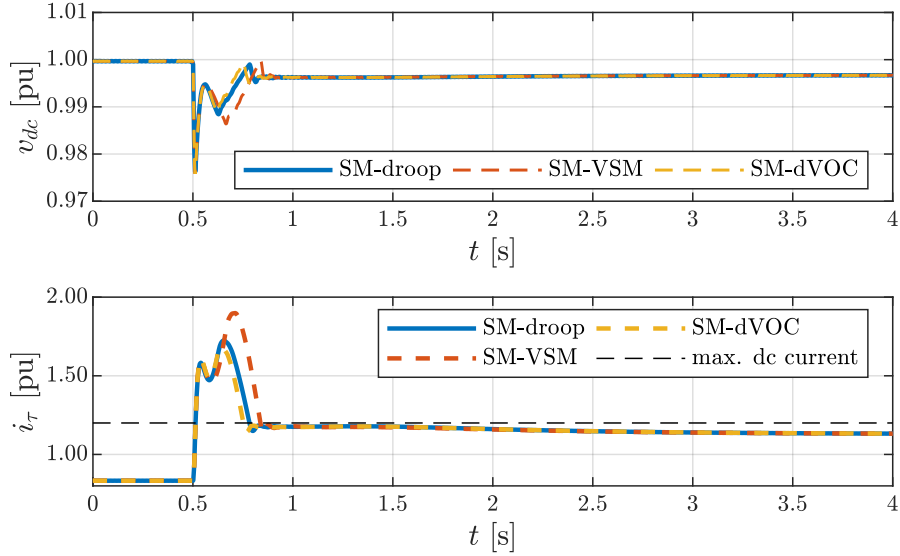


Figure 2.18: DC voltage (top) and dc current demand (bottom) of the converter at node 2 after a 0.9 pu load disturbance when both dc and ac limitation schemes (2.3) and (2.7) are active and $\tau_g = 1$ s.

hand, using dc voltage measurements - e.g., matching control (2.16) - results in robustness with respect to dc current limits. Further research is required to combine these complementary benefits by using both dc and ac measurements in grid-forming control.

2.4.6 Interaction of GFC and SM dynamics

The forthcoming discussion highlights that the interplay between the fast GFC and slow SM dynamics influences the system stability. The following case studies are tightly related to the scenarios in previous subsections.

Loss of synchronous machine

We study the response of GFCs when disconnecting the SM at node 1, that is, the system turns into an all-GFCs network. The implications of such a contingency are threefold. First, the power injected by the machine, which partially supplies the base load, is no longer available. Second, the stabilizing dynamics associated with the machine's governor, AVR, and PSS are removed from the system. Third, the slow dynamics of the SM no longer interact with the fast dynamics of the GFCs.

For this test, we set the base load to 2.1 pu, and the SM and GFCs set-points are set to 0.6 and 0.75 pu respectively. Note that when the SM at node 1 is disconnected, the converters increase their power output according to the power sharing behavior inherent to all four grid-forming controls (see Appendix 2.7). The resulting increase in the con-

verter power injection to roughly 1.05 pu is similar to the load disturbance scenario used to illustrate the instability behavior of droop control in Figure 2.14. Figure 2.19 shows

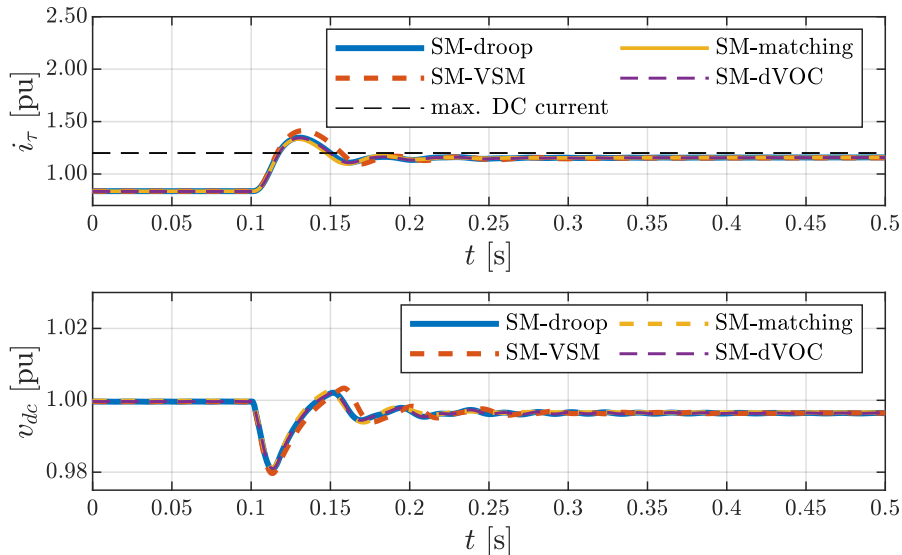


Figure 2.19: DC current demand (top) and dc voltage (bottom) of the converter at node 2 after loss of the SM at node 1.

i_τ and v_{dc} for the converter at node 2. Although the disturbance magnitude affecting the converters is similar to the one in studied in Subsection 2.4.4, all GFCs remain stable after the loss of the SM without the need to incorporate (2.24). In particular, due to the absence of the slow turbine dynamics and fast synchronization of the converters i_τ exceeds the limit i_{\max}^{dc} for around 50ms while it remains above the limit for a prolonged period of time in Figure 2.14.

This highlights the problematic interaction between the fast response of the GFCs and the slow response of the SM. While the synchronous machine perfectly meets classic power system control objectives on slower time scales, the dominant feature of GFCs is their fast response. However, the fast response of GFCs can also result in unforeseen interactions with other parts of the system such as the slow SM response (shown here), line dynamics (see [47], [77]), and line limits [89].

Low-inertia vs. no-inertia systems

Considering the same load disturbance scenario as in Subsection 2.4.4, we observe the same instability of droop control when the test system contains one GFC and two SMs, i.e., the instability cannot be prevented by adding more inertia to the system.

Figure 2.20 shows the dc current demand i_τ (i.e., before saturation) and dc voltage in an all-GFCs (i.e., no-inertia) system for a load increase of $\Delta p = 0.9$ pu. In this case, the GFCs quickly synchronize to the post-event steady state, which does not exceed the

maximum dc current, saturate the dc source for only approximately 200ms, and remain stable. In contrast, in the system with two GFCs and one SM, the SM does not reach its increased post-event steady-state power injection for several seconds. During this time the response of droop control results in a power injection that exceeds the limits of the dc source and collapses the dc voltage. In other words, the slow response of the SM due to the large turbine time constant prolongs the duration of dc source saturation for the GFCs which results in depleting the dc-link if the converter ac current is not limited. We conclude this subsection by remarking that in the mixed SM-GFCs system in the

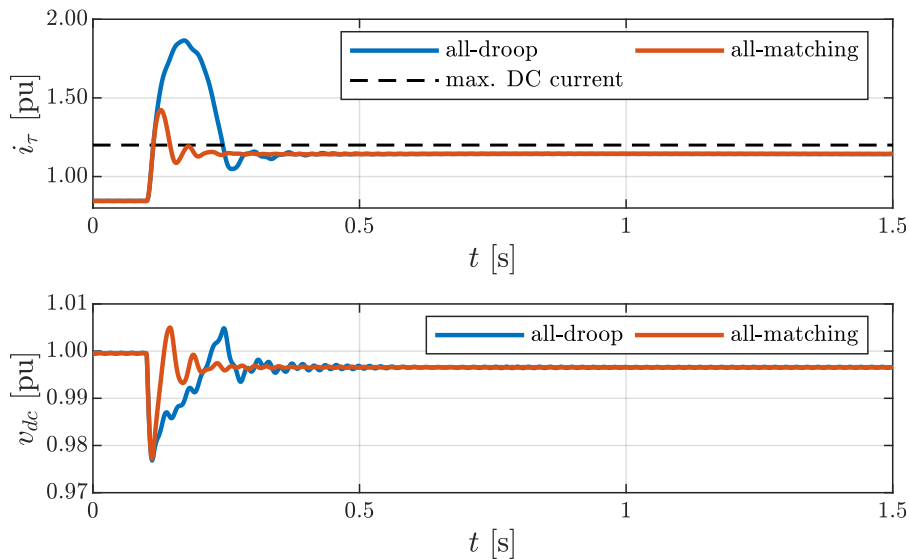


Figure 2.20: DC current demand (top) and dc voltage (bottom) after a 0.9 pu load disturbance in an all-GFC system.

Subsections 2.4.4 and 2.4.5, it is vital to account for dc side limits (either through ac current limits or dc voltage measurements) to stabilize the GFCs in presence of SMs. However, in an all-GFC system - either by default or due to the loss of SM - the dc side is only limited briefly and the system remains stable. This observation highlights that the interaction of the fast GFC dynamics and slow SM dynamics can potentially contribute to system instability.

2.5 Qualitative analysis

In this section, we provide a qualitative but insightful analysis that explains the results observed in Section 2.4.3 and Section 2.4.4. To this end, we develop simplified models that capture the small-signal frequency dynamics of synchronous machines and grid-forming converters. Applying arguments from singular perturbation theory [41], [90] results in a model that highlights the main salient features of the interaction of synchronous machines and grid-forming converters.

2.5.1 Frequency dynamics incorporating GFCs

To obtain a simplified model of the frequency dynamics of the GFCs, we assume that the cascaded ac voltage and ac current control (see (2.6) and (2.8)) achieve perfect tracking (i.e., $\mathbf{v}_{dq} = \hat{\mathbf{v}}_{dq}$). Assuming that the system operates near the nominal steady-state (i.e., $\|\mathbf{v}_{dq}\| \approx v^*$, $\omega \approx \omega^*$) and $p^* = 0$, $q^* = 0$, we rewrite the remaining dynamics in terms of the voltage angle and power injection at every bus. This results in a simplified model of the angle $\underline{\theta}$ and the frequency $\underline{\omega}$ of a GFC or SM relative to a frame rotating at the nominal frequency ω^* .

Droop control and dVOC

For a converter controlled by droop control or dVOC, we obtain

$$\dot{\underline{\theta}} = -d_\omega p, \quad (2.25)$$

where p is the power flowing out of the converter and d_ω is the droop control gain and given by $d_\omega = \eta/v^{*2}$ for dVOC.

Synchronous machine, VSM, and matching control

For a synchronous machine, a VSM, and a converter controlled by matching control we obtain

$$\dot{\underline{\theta}} = \underline{\omega}, \quad (2.26a)$$

$$2H\dot{\underline{\omega}} = -D\underline{\omega} + \text{sat}(p_\tau, p_{\max}) - p, \quad (2.26b)$$

$$\tau\dot{p}_\tau = -p_\tau - d_p\underline{\omega}. \quad (2.26c)$$

For a SM the parameters directly correspond to the parameters of the machine model presented in Section 2.2.2, i.e., H , d_p , and $\tau = \tau_g$, are the machine inertia constant, governor gain, and turbine response time, and the model does not capture SM losses (i.e., $D = 0$) or damper winding torques. Throughout this work we have not considered a limit on the turbine power output (i.e., $p_{\max} = \infty$) because a synchronous machine, in contrast to a GFC, typically has sufficient reserves to respond to the load changes and faults considered in this work. For the VSM presented in Section 2.3.4, we obtain $\tau = 0$, $p_\tau = 0$, $H = 1/2J\omega^*$, and $D = D_p\omega^*$, i.e., the VSM does not emulate a turbine and implements no saturation of the damping term in its frequency dynamics (2.13b). Finally, for matching control we obtain $\tau = \tau_{dc}$, $p_{\max} = v_{dc}^* i_{\max}^{dc}$, $H = 1/2C_{dc}/k_\theta^2$, $d_p = k_{dc}/k_\theta$ (see Section 2.3.5) and $D = 0$, i.e., by linking frequency and dc voltage, matching control clarifies that the dc source plays the role of the turbine in a machine and the proportional dc voltage control plays the role of a governor.

2.5.2 Reduced-order model

For brevity of the presentation we will now restrict our attention to the case of one SM and one GFC. The equivalent inertia constants and turbine time constants for the different grid-forming converter control strategies are either zero or negligible compared to typical inertia constants and turbine time constants for machines (see Table 2.1). We therefore assume that the states of the synchronous machine are slow variables, while the states of the GFC are fast and apply ideas from singular perturbation theory [41], [90].

Using the dc power flow approximation and $p_{d,\text{GFC}}$ and $p_{d,\text{SM}}$ to denote a disturbance input, we obtain $p_{\text{GFC}} = b(\underline{\theta}_{\text{GFC}} - \underline{\theta}_{\text{SM}}) + p_{d,\text{GFC}}$ and $p_{\text{SM}} = b(\underline{\theta}_{\text{SM}} - \underline{\theta}_{\text{GFC}}) + p_{d,\text{SM}}$, where b is the line susceptance. Neglecting the frequency dynamics and dc source dynamics, i.e., letting $\tau \rightarrow 0$ and $H \rightarrow 0$, the dynamics of the relative angle $\delta = \underline{\theta}_{\text{SM}} - \underline{\theta}_{\text{GFC}}$ are given by $\dot{\delta} = \underline{\omega}_{\text{SM}} - (D_{\text{GFC}} + d_p) (b\delta - p_{d,\text{GFC}})$ if $|d_{p,\text{GFC}}| < |p_{\text{max}}|$, $\dot{\delta} = \underline{\omega}_{\text{SM}} - D_{\text{GFC}} (b\delta - p_{d,\text{GFC}} \pm p_{\text{max}})$ if the dc source is saturated, and D_{GFC} denotes the damping provided by the GFC. For typical droop gains and network parameters, the relative angle dynamics are fast compared to the machine dynamics. Letting $\dot{\delta} \rightarrow 0$, we obtain the reduced-order model

$$2H\dot{\underline{\omega}}_{\text{SM}} = -\text{sat}(D_{\text{GFC}}\underline{\omega}_{\text{SM}}, p_{\text{max}}) + p_{\tau,\text{SM}} + p_d, \quad (2.27a)$$

$$\tau\dot{p}_{\tau,\text{SM}} = -p_{\tau,\text{SM}} - d_p\underline{\omega}_{\text{SM}}. \quad (2.27b)$$

where $p_d = p_{d,\text{GFC}} + p_{d,\text{SM}}$, H , d_p , and τ are the inertia constant, governor gain, and turbine time constant of the synchronous machine, D_{GFC} is the damping provided by the GFC, i.e., $D_{\text{GFC}} = 1/d_\omega$ (droop, dVOC, VSM) or $D_{\text{GFC}} = d_p$ (matching). Moreover, droop control, dVOC, and the VSM implement no saturation of their power injection in their respective angle / frequency dynamics (i.e., (2.11b), (2.22a), and (2.13b)) resulting in $p_{\text{max}} = \infty$. In contrast, for matching control the saturation of the dc source results in $p_{\text{max}} = v_{\text{dc}}^* i_{\text{max}}^{\text{dc}}$.

We note that for the case of under damped dynamics (2.27) and without saturation, a closed-form expression for the the step response and frequency nadir (2.27) can be found in [67, Section V-A]. However, even for the seemingly simple model (2.27) the dependence of the nadir on the parameters is very involved and does not provide much insight. By neglecting the damping term in (2.27a) and the feedback term $-p_{\tau,\text{SM}}$ in (2.27b) an insightful expression for the nadir is obtained in [91]. However, the key feature of the GFCs is that they contribute damping, which is not captured by analysis in [91]. Nonetheless, the model (2.27) provides several insights that we discuss in the next section.

2.5.3 Impact of grid-forming control on frequency stability

A system with three synchronous machines as in Section 2.4 can be modeled by (2.27) with $H = 3H_{\text{SM}}$, $d_p = 3d_{p,\text{SM}}$, $\tau = \tau_{\text{SM}}$ and $D_{\text{GFC}} = 0$. This corresponds to the well known *center of inertia* frequency model with first-order turbine dynamics (see [62], [67]). In contrast, if two SMs are replaced by GFCs with equal droop setting we obtain $H = H_{\text{SM}}$, $d_p = d_{p,\text{SM}}$, $\tau = \tau_{\text{SM}}$ and $D_{\text{GFC}} = 2d_{p,\text{SM}}$.

This highlights that, on the time-scales of the SM, the GFCs provide fast acting frequency control. After an increase in load the machine inertia serves as buffer until the relatively slow turbine provides additional power to the machine. In contrast, the converters respond nearly instantaneously to any imbalance and therefore the need for inertia is decreased. Intuitively, this increase in fast primary frequency control should result in lower nadir values. Similarly, the additional damping provided by the converter in (2.27) can be interpreted as a filter acting on the power imbalance, i.e., the GFCs are providing $D_{\text{GFC}}\omega_{\text{SM}}$ or p_{max} and the power imbalance affecting the machine is reduced, therefore resulting in smaller average RoCoF.

To validate the model (2.27) and our interpretation, we compute the frequency nadir and averaged RoCoF (see (2.23)) for the machine parameters and disturbance used in Section 2.4, and $H = \nu 3H_{\text{SM}}$, $d_p = \nu 3d_{p,\text{SM}}$, $\tau = \tau_{\text{SM}}$ and $D_{\text{GFC}} = (1 - \nu)d_{p,\text{SM}}$ and $D = 0$, where $\nu \in [1/3, 1]$ is a scalar parameter that interpolates the parameters between the two cases (all SM, one SM and two GFCs). The average RoCoF and frequency nadir according to (2.27) are shown in Figure 2.21. The case with $p_{\text{max}} = 1.2$ corresponds to matching control, the one with $p_{\text{max}} = \infty$ to droop control, dVOC, and VSMs. It can be seen that the GFCs result in an improvement compared to the all SM scenario, that the implicit saturation of the power injection by matching control results in a smaller improvement compared to droop control, dVOC and VSMs, and that the reduction in the average RoCoF and frequency nadir is line with the corresponding results in Figure 2.11 and Figure 2.12.

2.5.4 Instability in the presence of large load disturbance

The instabilities of droop control, dVOC, and the VSM observed in Section 2.4.4 can qualitatively be investigated using a simplified model of the dc-side. To compute the power $v_{\text{dc}}i_x$ flowing out of the dc-link capacitor, we assume that the controlled converter output filter dynamics are fast and can be neglected (i.e., $\dot{\mathbf{i}}_{s,\alpha\beta} = 0$, $\dot{\mathbf{v}}_{\alpha\beta} = 0$) and that the ac output filter losses are negligible. This results in $v_{\text{dc}}i_x = \mathbf{v}_{s,\alpha\beta}^\top \mathbf{i}_{s,\alpha\beta} = \mathbf{v}_{\alpha\beta}^\top \mathbf{i}_{\alpha\beta} = p$. Moreover, we neglect the dc source dynamics to obtain the simplified dc voltage dynamics

$$C_{\text{dc}}\dot{v}_{\text{dc}} = -G_{\text{dc}}v_{\text{dc}} + \text{sat} \left(k_{\text{dc}}(v_{\text{dc}}^* - v_{\text{dc}}), i_{\text{max}}^{\text{dc}} \right) - \frac{p}{v_{\text{dc}}}, \quad (2.28)$$

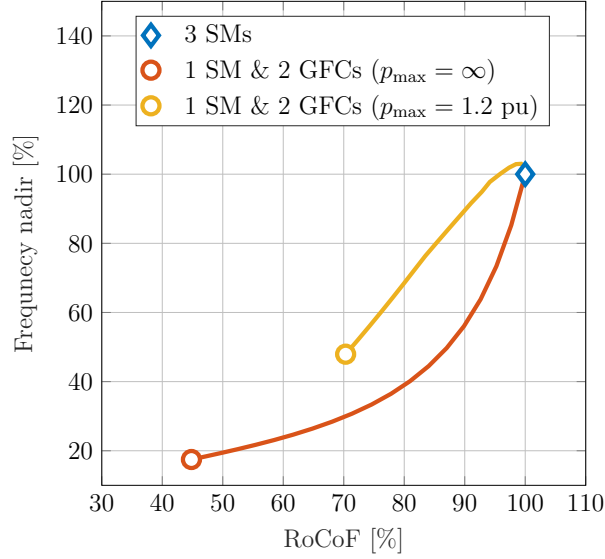


Figure 2.21: Change in averaged RoCoF and frequency nadir when transitioning from a system with 3 SMs to a system with one SM and two GFCs.

i.e., the active power p flowing into the grid is drawn from the dc-link capacitor that is stabilized by a proportional control (see (2.10)) if the dc current i_r is not saturated. For a large enough constant perturbation $p > 0$ the dc current in (2.28) becomes saturated and controllability of the voltage v_{dc} is lost and the dc voltage becomes unstable.

In other words, if the dc source is saturated the power p has to be controlled to stabilize the dc voltage. Matching control achieves this through the angle dynamics $\dot{\theta} = k_{\theta} v_{dc}$ which converge to a constant angle difference (i.e., $\underline{\omega}_{SM} = \underline{\omega}_{GFC}$) and power injection when the dc source is saturated and the SM has enough reserves to maintain $\underline{\omega}_{SM} \approx \omega^*$ with the GFC providing its maximum output power. Moreover, for matching control it can be verified that $(\omega_{GFC} - \omega^*)/\omega^* = (v_{dc} - v_{dc}^*)/v_{dc}^*$. Therefore, the dc voltage deviation is proportional to the frequency deviation and the GFC with matching control remains stable for the scenario shown in Section 2.4.4.

2.6 Summary and further work

In this paper we provided an extensive review of different grid-forming control techniques. Subsequently, we used the IEEE 9-bus test system incorporating high-fidelity GFC and SM models to investigate the performance of different control techniques and their interaction with SM.

Our case studies revealed that 1) the presence of the GFCs improves the frequency stability metrics compared to the baseline all-SMs system, 2) under a sufficiently large load disturbance, it is vital to implement an ac current limiting scheme to stabilize the

grid-forming techniques which only rely on the ac measurements, 3) matching control exhibits robustness to the dc source saturation since its angle dynamics takes into account the dc quantities, 4) we explored the stabilizing influence of the ac current limitation, and 5) we investigated the behavior of GFCs in response to the loss of SM and in all-GFCs system highlighting a potentially destabilizing interaction between the GFCs and SMs dynamics. Moreover, we provided a qualitative analysis of GFCs impact on the frequency stability. Topics for the future works include 1) further exploration of the impacts of dc and ac current limitations on the GFCs behavior and providing a formal stability analysis, 2) proposing a complete ac current limitation strategy which is robust to load-induced over-current as well as grid faults, 3) the seamless transition between grid-forming and grid-following operation, and 4) blending of the different control strategies into a controller that achieves their complementary benefits.

2.7 Appendix A: tuning criteria

The load-sharing capability of the control techniques presented in Section 2.3 is investigated in [7], [38], [45]. Considering a heterogeneous network consisting of several GFCs (with different control) and SMs, we tune the control parameters such that all the units exhibit identical proportional load-sharing in steady-state. For the SM and droop controlled GFC, (2.5a) and (2.11b) can be rearranged to

$$\omega^* - \omega = \frac{1}{d_p} (p - p^*), \quad (2.29a)$$

$$\omega^* - \omega = d_\omega (p - p^*). \quad (2.29b)$$

For VSM, assuming steady-state frequency and setting $\ddot{\theta} = \dot{\omega} = 0$ in (2.13b) results in

$$\omega^* - \omega = \frac{1}{D_p \omega^*} (p - p^*). \quad (2.30)$$

For matching control, we assume that in steady-state $i_{dc} \approx i_{dc}^*$ and $v_{dc}/v_{dc}^* \approx 1$. Setting $\dot{\omega} = 0$ in (2.19b) and replacing i_{dc} by the expression from (2.10) yields

$$\omega^* - \omega = \frac{k_\theta}{k_{dc} v_{dc}} (p - p^*). \quad (2.31)$$

Lastly for dVOC, assuming $\|\hat{\mathbf{v}}_{dq}\| \approx v^*$ in steady-state, the angle dynamics (2.22a) becomes

$$\omega^* - \omega = \frac{\eta}{v^{*2}} (p - p^*). \quad (2.32)$$

Hence, for any given droop gain d_p , if d_ω , D_p , k_{dc} and η are selected such that the slopes of (2.29)-(2.32) are equal, all the GFC control techniques and SM perform equal-load

Table 2.1: Case study model and control parameters [71].

IEEE 9-bus test system base values					
S_b	100 MVA	v_b	230 kV	ω_b	$2\pi 50$ rad/s
MV/HV transformer					
S_r	210 MVA	v_1	13.8 kV	v_2	230 kV
$R_1 = R_2$	0.0027 pu	$L_1 = L_2$	0.08 pu	$R_m = L_m$	500 pu
Single LV/MV transformer module in Figure 2.3					
S_r	1.6 MVA	v_1	1 kV	v_2	13.8 kV
$R_1 = R_2$	0.0073 pu	$L_1 = L_2$	0.018 pu	R_m, L_m	347, 156 pu
Synchronous machine					
S_r	100 MVA	v_r	13.8 kV	D_f	0
H	3.7 s	d_p	1 %	τ_g	5 s
Single converter module in Figure 2.3					
S_r	500 kVA	G_{dc}, C_{dc}	0.83, 0.008 Ω^{-1} , F	v_{dc}^*, u_{ll-rms}^*	2.44, 1 kV
R	0.001 Ω	L	200 μ H	C	300 μ F
n	100	τ_{dc}	50 ms	i_{max}^{dc}	1.2 pu
AC current, ac voltage, and dc voltage control					
$k_{v,p}, k_{v,i}$	0.52, 232.2	$k_{i,p}, k_{i,i}$	0.73, 0.0059	k_{dc}	1.6×10^3
Droop control					
d_ω	$2\pi 0.05$ rad/s	ω^*	$2\pi 50$	k_p, k_i	0.001, 0.5
Virtual synchronous machine					
D_p	10^5	J	2×10^3	k_p, k_i	0.001, 0.0021
Matching control					
k_θ	0.12	k_{dc}	1.6×10^3	k_p, k_i	0.001, 0.5
Dispatchable virtual oscillator control					
η	0.021	α	6.66×10^4	κ	$\pi/2$

sharing. Moreover, by selecting k_{dc} based on this criteria, the dc voltage control gain in (2.10) is automatically set which is identical for all GFC implementation [71].

Regarding the ac voltage regulation, the control gains in (2.12), (2.15), (2.17), and (2.22b) are selected to regulate the ac voltage at approximately equal time-scales. We refer to [92] for details on tuning the cascaded inner loops presented in Subsection 2.3.1. It is noteworthy that the time-scale of the reference model (i.e., grid-forming dynamics) must be slower than ac voltage control shown in Figure 2.4 to ensure optimal performance. Similarly, the ac current control must be faster than the outer voltage controller. Lastly, the choice of virtual inertia constant in (2.13b) can largely influence VSM's dynamic behavior. We adopted the recommendation $J/D_p = 0.02$ proposed in [64]. The parameters used in the implementation [71] are reported in Table 2.1.

Beyond low-inertia systems: massive integration of grid-forming power converters in transmission grids

Presented at the IEEE Power and Energy Society General Meeting (PESGM) 2020.

Authors – Alessandro Crivellaro*, Ali Tayyebi*, Catalin Gavrilita, Dominic Groß, Adolfo Anta*, Friederich Kupzog, and Florian Dörfler.

(*equal contributions; the thesis author contributed to the model development, control implementations, benchmark model preparation, test case definition, and writing the paper.)

Abstract – As renewable sources increasingly replace existing conventional generation, the dynamics of the grid drastically changes, posing new challenges for transmission system operations, but also arising new opportunities as converter-based generation is highly controllable in faster timescales. This paper investigates grid stability under the massive integration of grid-forming converters. We utilize detailed converter and synchronous machine models and describe frequency behavior under different penetration levels. First, we show that the transition from 0% to 100% can be achieved from a frequency stability point of view. This is achieved by retuning power system stabilizers at high penetration values. Second, we explore the evolution of the nadir and RoCoF for each generator as a function of the amount of inverter-based generation in the grid. This work sheds some light on two major challenges in low and no-inertia systems: defining novel performance metrics that better characterize grid behavior, and adapting present paradigms in PSS design.

3.1 Introduction

The demand for the reduction of the carbon footprint has led to an increasing integration of renewable sources. The replacement of conventional power plants, interfacing the grid via synchronous machines (SMs), with wind and solar generation results in significant

changes in power system dynamics. Specifically, as these new converter-based sources replace SMs, the amount of rotational inertia in power systems decreases, accompanied with the loss of stabilizing control mechanisms that are present in SMs.

As a result of this transition, low-inertia power systems encounter critical stability challenges [33]; EirGrid and SONI, for instance, limited the instantaneous penetration of variable renewable energy sources to 55% [27] and recently increased the limit to 67% and set a goal of 75% of fuel-free generation [93]. As of now, certain grids need to preserve a minimum amount of inertia, which implies higher cost and hinders the penetration of renewable generation. New converter control strategies can potentially address these low-inertia system stability issues. These approaches can be split in two categories [33], [70]: grid-following control, where the converter *follows* the measured frequency and voltage magnitude in the grid (via a synchronizing mechanism such as phase locked loop), and grid-forming control, where the converter *defines* the voltage magnitude and frequency. Given the fact that the first strategy relies on the existence of a well-defined voltage waveform, it cannot fully replace the functionality of the SMs. In this work, we focus on grid-forming converters (GFCs) and their critical role in the transition towards a 100% converter-based grid.

Different GFC control strategies have been proposed, such as droop control [35], virtual synchronous machine [64], dispatchable virtual oscillator control [45] and matching control [65], among others. To the best of our knowledge, various aspects of the integration of GFCs (e.g., the consequent gradual inertia reduction) in a realistic transmission grid model and in an electromagnetic transient (EMT) simulation environment have not been thoroughly explored. In [94] and [72], different grid-forming and grid-following techniques have been tested in simple network models. However, these studies rely on the IEEE 9-bus system that lacks sufficient granularity and complexity to fully analyze the transition scenario to GFCs.

The objective of this work is to explore the limits of GFC integration at the transmission level, using an EMT simulation of a realistic grid model that fully reflects the existing dynamics. Previous studies suggest that systems exhibit instability [72], [93], [95] when the penetration of non-synchronous generation increases to roughly 70%. The study in [95] only considers grid-following converters, and the work in [72] shows that instability can be caused by adverse interactions of GFCs with the power system stabilizer (PSS) and automatic voltage regulator (AVR). Our work suggests that, given the right control strategies for converter-based generation, a minimum amount of inertia might not be required for grid operation, from a frequency stability perspective. Nonetheless, some controllers can no longer be agnostic to the amount of converter-based generation, as the grid dynamics varies drastically depending on the generation mix. Moreover, we question the suitability of standard frequency metrics, such as nadir and rate-of-change-of-frequency (RoCoF), for converter-dominated grids. This paper does not analyze other critical aspects in low-inertia systems such as voltage control, responsiveness to faults,

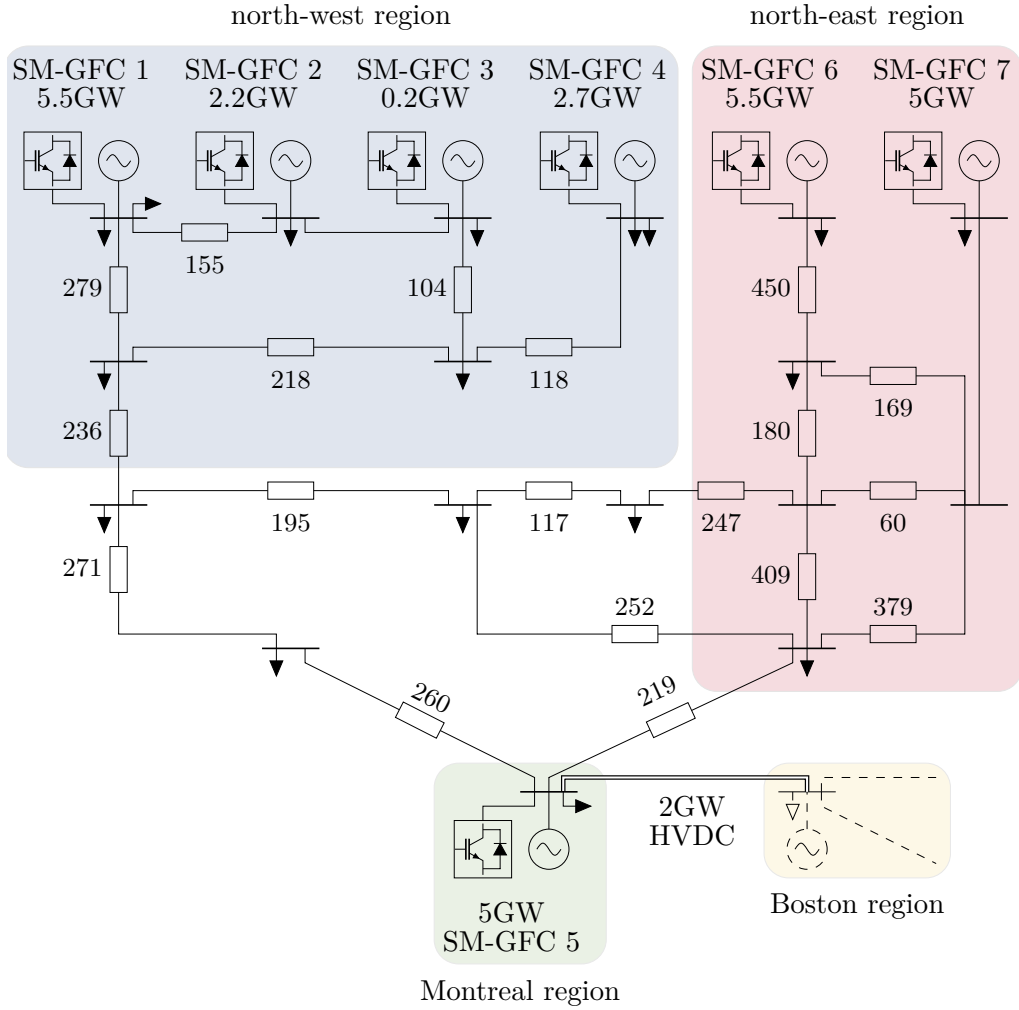


Figure 3.1: Quebec grid model consisting of 7 generation nodes (line length in km).

etc.

The main contributions of this paper are: first, to show that, from a frequency stability perspective and for a particular grid, it is possible to transition from 0 to 100% converter-based generation. Second, we remark the need for PSS retuning based on the continuously changing amount of non-synchronous penetration. Third, we explore how the nadir and RoCoF, measured over different time windows, evolve as a function of the penetration of converter-based generation. These results expose new challenges that have been so far overlooked in the mainstream literature and calls for further research to address many open points, such as: are nadir and RoCoF still good descriptors of grid stability? How relevant are fast transients in frequency? Can decentralized PSS structures provide adequate damping under different converter-dominated scenarios?

3.2 Model description

We start with the description of the grid, SMs, and GFCs models.

3.2.1 Transmission grid model

In this work we adopt the transmission grid model from [96], representing a simplified model of the Quebec region, with a total generation capacity of 26.2 GVA consisting of seven SMs. This grid is characterized by three distinct regions which are interconnected via long transmission lines. Most of the generation can be found in the North and most of the load in the southern part. Even though the generation is mainly characterized by hydro-power plants, it has been selected for this study as the relevant information and the EMT simulation model are publicly available, as provided by Hydro-Quebec. Moreover, it has the right degree of complexity, i.e., being complex enough to explore the interactions of GFCs and SMs at different levels of inertia, and simple enough to understand the system behavior. Specifically, inside the model there are 7 SMs of different sizes, ranging from 5.5 GW to 200 MW. Each SM is represented by a set of 8th order, 3-phase dynamical model coupled with a hydraulic turbine, governor, an AVR, and multi-band PSS (type 4B). Note that only primary frequency control is implemented in the SM model, and the droop constant of each SM is set to 5%. As explained later in the Section 3.2.3, we extend the model with an HVDC link of 2 GW (existing in the original Hydro-Quebec grid but not in [96]), modeling a contingency that is independent of the penetration level of GFCs. For simplicity, we only consider constant impedance loads in our model. A simplified version of the grid model is depicted in Figure 3.1.

3.2.2 Grid-forming converter model

The converter-based generation is implemented by means of two-level voltage source converters, stacked in parallel to form large-scale generation units [94, Remark 1]. The converter dc energy source is a controllable current source, connected in parallel with a resistance (which models the dc losses) and the dc-link capacitance. The switching stage is modelled using a full-bridge 3-phase average model, ac output filter (see Figure 3.2), and coupled to the medium voltage via a LV/MV transformer. Each converter is controlled as a grid-forming unit defining the angle, frequency and voltage. For simplicity, in this work we focus on grid-forming droop control (see [35], [94, Section III-C]). It is noteworthy that - under a realistic tuning and for a wide range of contingencies - other techniques such as virtual synchronous machine (VSM) [64], matching controlled GFCs [65] and dispatchable virtual oscillator control (dVOC) [45] exhibit similar behavior to that of the converters controlled by droop control [94, Section IV]. The control block diagrams of the droop strategy appear in Figure 3.3. For the sake of compactness we refer

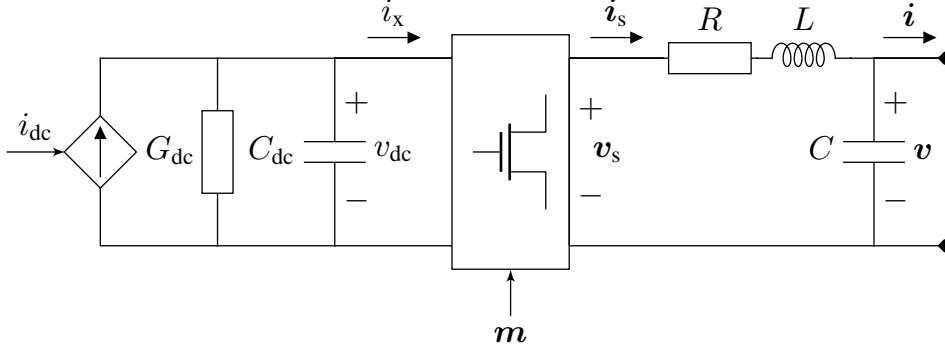


Figure 3.2: Converter model (see [94, Section II-A] for the parameters definition and further details of the converter modeling).

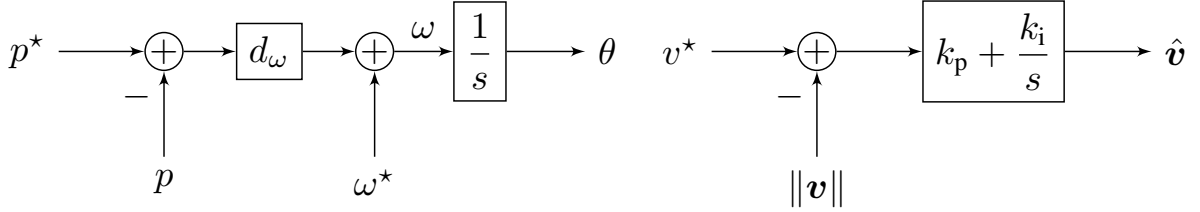


Figure 3.3: Droop control block diagram [94, Section III-C].

the reader to [94, Section III] and [71] for further details on the converter control design. The droop gain is selected in order to provide the same load sharing capabilities as of the SMs in the system (see [94, Appendix A] for details). Lastly, a proportional controller regulates the dc-link voltage via dc source current actuation [94, Section III-B].

3.2.3 Modeling the SM-GFC generation transition

Given that the original model is an aggregated model, the generation transition in this study is carried out in a uniform, gradual way. Each SM is replaced by a collocated combination of SM and GFC, where the ratings of each generation unit is defined according to the penetration level¹. Formally speaking, the ratio of converter-based generation $\eta \in [0, 1]$ is defined as:

$$\eta = \frac{\sum_{i=1}^7 S_{\text{GFC}_i}}{\sum_{i=1}^7 (S_{\text{GFC}_i} + S_{\text{SM}_i})}. \quad (3.1)$$

where S_{SM_i} denotes the rating of the i -th SM in the combined model and S_{GFC_i} denotes the rating for the i -th converter. The individual ratings of the combined SM-GFC model

¹For a more granular grid model where each individual generator is included, it might be more realistic to represent this transition in a more discrete manner, where each SM is fully replaced by converter-based generation, one at a time.

replacing the original SM are then adjusted as a function of η :

$$S_{\text{GFC}_i} = \eta S_{\text{SM}_i}^0, \quad (3.2a)$$

$$S_{\text{SM}_i} = (1 - \eta) S_{\text{SM}_i}^0, \quad (3.2b)$$

with S_{SM}^0 being the rating of a given SM in the original model (with no GFCs, *i.e.*, $\eta = 0$). For $\eta = 0$ (resp. $\eta = 1$), the GFCs (resp. the SMs) are disconnected from the model. The inertia time constant H and the turbine time constant τ are kept constant regardless of the rating, as for a hydro-power plant it is more a function of the type of governor and turbine rather than the size[62, Section 9.1]. Moreover, the original model delivered by Hydro-Quebec specifies identical parameter values for all the plants regardless of the size.

3.3 Results

We start by defining the contingencies that will be considered. It is expected that, as SMs are being replaced by GFCs, the size of the worst contingency (typically the rated power of the largest SM in the grid) will become smaller, as generation becomes less coarse and more distributed. In our particular case study, this implies the worst contingency is the loss of the largest SM for low penetration levels (SM 1 or 6), and the HVDC link trip for high penetration levels. Nonetheless, for a fair comparison across different integration levels, we always consider the same contingency value for all values of η . Therefore, the worst contingency is chosen to be the simultaneous loss of the combined generation unit SM-GFC 1 (namely, the loss of 5.5 GW generation). For completeness, the disconnection of the HVDC link in the model will be considered as well in Sections 3.3.3 and 3.3.5.

3.3.1 PSS retuning for high penetration levels

It has been conjectured that the generation transition from a SM-dominated grid to a GFC-dominated one is challenging [72], [97], [98]. Indeed, we have observed in our initial results that, starting at 80% GFC penetration, stability is lost. However, we found that re-tuning of the PSSs renders the system stable, at least from a frequency perspective. For $\eta \leq 0.7$, the system is stable under the original PSS structure (multiband PSS4B) and parameters, where all PSS blocks have the same parameters for all units. Roughly speaking, this type of PSS structure defines 3 different frequency bands and their corresponding lead-lag compensators. For the original PSS, these 3 frequency bands are set around 0.2Hz, 0.9Hz, and 12Hz, aimed at global, inter-area and local modes, respectively. For $0.8 \leq \eta \leq 0.9$, the PSSs have been modified as follows: the second frequency range has been shifted to 1.2Hz, and the high frequency branch has been completely

removed, to avoid having the corresponding lead-lag compensator acting on the existing GFC fast dynamics. Likewise, the gains of each branch have been reduced by a factor of 5. Based on this successful retuning, it can then be conjectured that, under the massive presence of GFCs, two aspects need to be considered: the PSS action might need to be reduced accordingly (but not fully removed); the PSS effect on high frequencies, where the response of GFCs is significant, can destabilize the system. Further analysis is needed to derive a more formal conclusion. We emphasize that there should be other re-tuning strategies that successfully stabilize the system, including the more natural choice of different PSS parameters for each SM.

Previous works [72], [95] already pointed at AVR and PSS regulators as the possible cause for instability at high values of η . Note that the modified PSS tuning does not stabilize the system for $\eta \leq 0.7$. Finding a unique set of PSS parameters stabilizing the system for all penetration levels is a challenging task. Indeed, it is unclear whether such settings exist, as the system dynamics and oscillation modes drastically vary depending on the amount of GFCs present in the grid. In practice, it is undesirable to continuously retune the existing PSS controllers in a grid depending on the penetration level. Moreover, the real-time ratio of converter-based generation (and its location) is not accurately known at the plant level, unless the transmission system operators disclose this information. Therefore, either novel robust, adaptive or more centralized PSS structures would be required to guarantee stability independently of the amount of converter-based generation present in the grid.

3.3.2 Frequency performance under the worst contingency

Figure 3.4 illustrates the frequency time series of the SM 2 (the closest unit to the event) for the loss of the largest unit i.e., the SM-GFC 1 (see Figure 3.1). The increasing integration of GFCs significantly improves the frequency nadir, but it degrades the RoCoF, when computed over a short time window (more on this topic in the next section). Moreover, the time at which nadir occurs also is shortened. Although converters do not possess any significant inertia, their fast response curbs the impact of generator trip on the grid frequency. The behavior for 80% and 90% is qualitatively different from the rest, due to the PSS retuning. The case of a pure converter-based grid is covered later in Section 3.3.5. Note that a similar behavior has been observed under the other aforementioned grid-forming techniques.

Remark 3. *By enforcing a slow frequency response for the GFCs - mimicking the slow turbine dynamics - GFCs can be made fully compatible with the time-scales of the SMs and their corresponding PSSs (i.e., reducing the time-scale separation of different generation units [72, Figure 4]). However, fully mimicking the response of a SM would require to slow down the GFC frequency response artificially as well as significantly oversizing the GFCs. A much more viable solution is to adapt the PSS parameters according to*

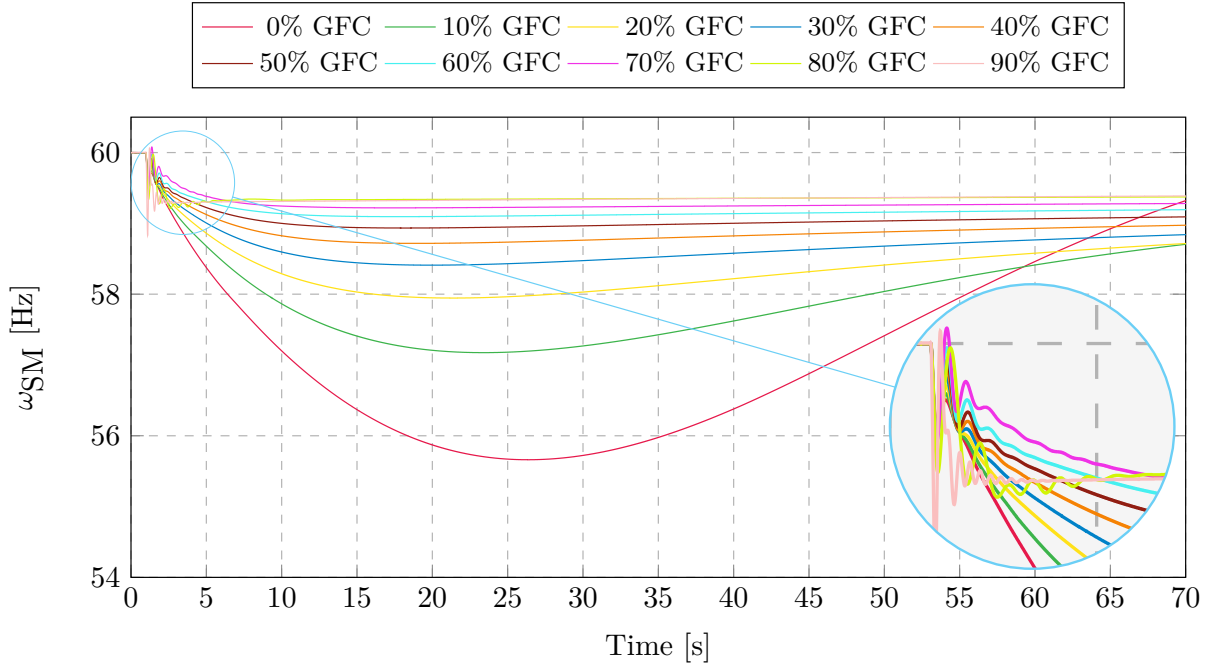


Figure 3.4: Frequency evolution of the SM 2 following the loss of SM-GFC 1. When the GFC integration level is set to 80% and 90%, the PSS controllers for the remaining SMs have been identically retuned.

the penetration level.

The time series in Figure 3.4 correspond to the mechanical frequencies of the SM 2. For low values of η , these signals are expected to be representative of the bus frequencies across the grid. However, for a GFC-dominated grid, the GFC internal frequencies - being well-defined also in transients - might be more descriptive of the frequencies across the grid. Figure 3.5 illustrates the post-contingency frequency time series of SMs and GFCs, for the integration levels $\eta = 0.1$ and $\eta = 0.9$. As expected, the SM-GFCs 2-4 in the Northwest region (see Figure 3.1), which are closer to the event, exhibit the largest RoCoF values. Interestingly, at low penetration levels large oscillations appear at the GFCs before they synchronize with the SMs. At high integration levels we observe larger oscillations at the SMs. Further analyses are needed to conclude which set of signals is more relevant to describe the frequency behavior for different integration levels. In any case - regardless of the integration level - the SMs mechanical frequencies are still needed to evaluate potential RoCoF-related issues associated with conventional generation.

3.3.3 Evolution of the frequency metrics

While appropriate retuning of the PSS stabilizes the system, the results presented in the previous section suggest that the system dynamics drastically change depending on the GFCs integration level. To analyze and characterize this effect, we resort to

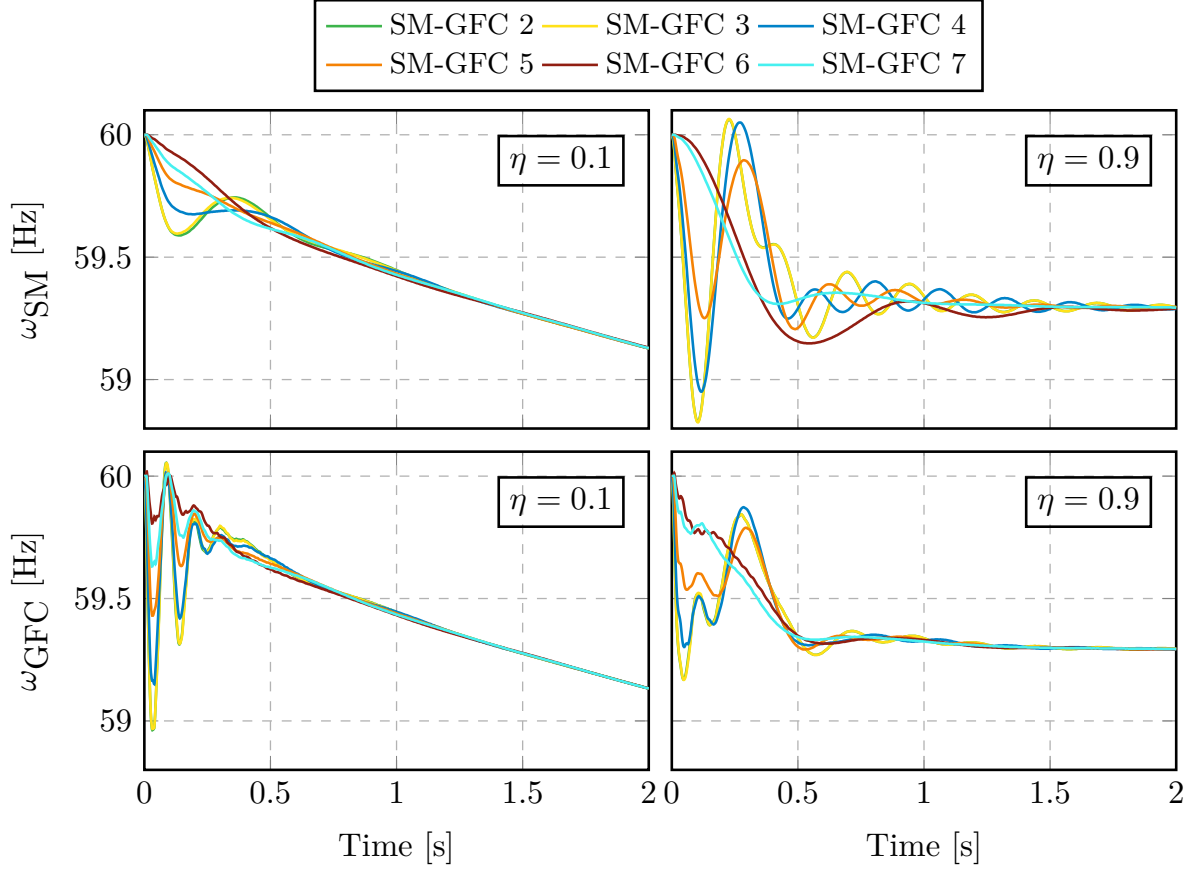


Figure 3.5: The SM and GFC frequencies for two extreme integration levels, across the grid, following the loss of SM-GFC 1. Regardless of the integration level and the source of frequency signal (i.e., SM or GFC), units in the Northwest region - where contingency occurs - exhibit the largest oscillation.

the standard frequency stability metrics e.g., frequency nadir or maximum frequency deviation $\|\Delta\omega\|_\infty$ and $\text{RoCoF}(T) |\dot{\omega}|$, formally defined for the generation unit i as:

$$\|\Delta\omega_i^\eta\|_\infty := \max_{t \geq t_0} |\omega_i^\eta(t_0) - \omega_i^\eta(t)|, \quad (3.3a)$$

$$|\dot{\omega}_i^\eta| := \frac{|\omega_i^\eta(t_0 + T) - \omega_i^\eta(t_0)|}{T}, \quad (3.3b)$$

where t_0 is the time when the event occurs, ω_i^η the mechanical frequency at unit i under penetration ratio η , and T is the RoCoF calculation window. For ease of exposition, we consider in this subsection the HVDC link trip (see Figure 3.1), and evaluate these metrics based on the SMs frequencies across the grid. Figure 3.6 depicts the frequency metrics evolution for SM 1, 5 and 6 (representatives of each area in the grid) following the loss of 2 GW generation caused by the HVDC link trip, for different values of η . We consider two RoCoF computation windows, namely $T_1 = 0.1\text{s}$ and $T_2 = 0.5\text{s}$ (i.e., computing RoCoF using different time windows), denoted as $\text{RoCoF}(0.1)$ and $\text{RoCoF}(0.5)$.

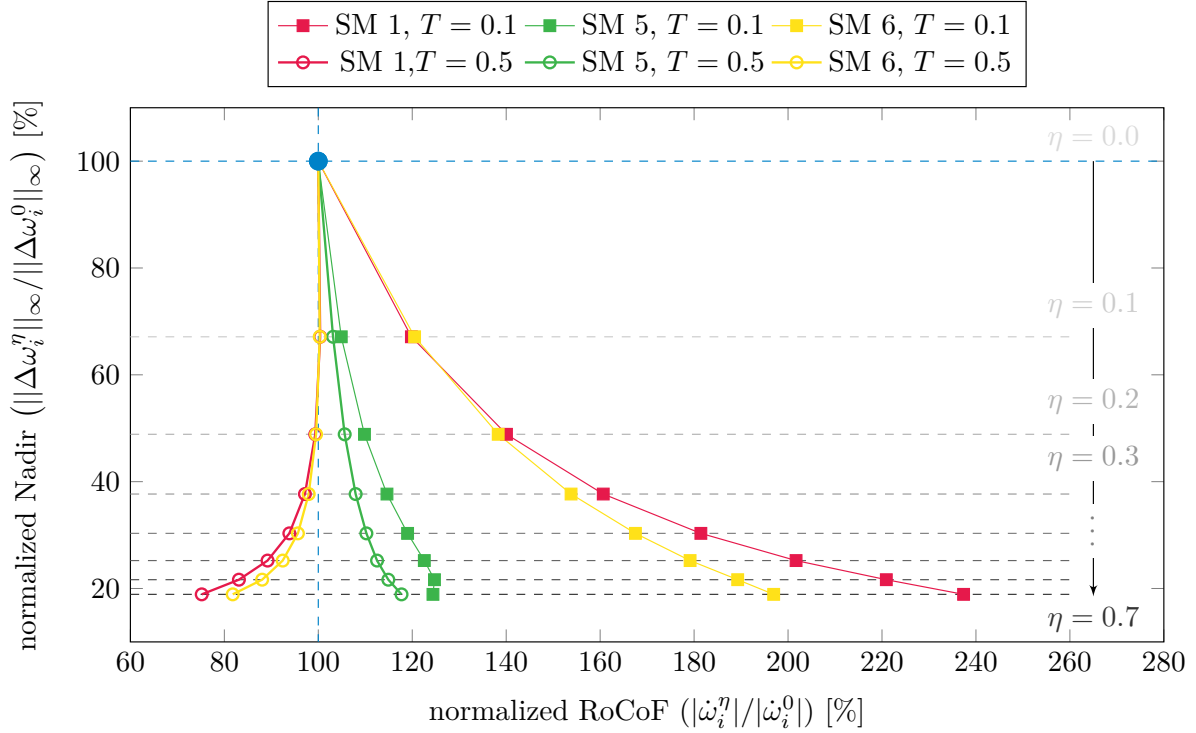


Figure 3.6: Normalized frequency nadir vs RoCoF (calculated over two distinct time window) for different integration levels for all the SMs across the grid. The event corresponds to the loss of 2 GW generation due to the disconnection of the HVDC link in Figure 3.1. All data points are normalized against the corresponding metric values of the baseline all-SMs system.

Furthermore, the nadir and RoCoF values corresponding to a particular choice of $(\eta, T_{1,2})$ are normalized with respect to the metrics of the all-SMs system with the same RoCoF windows (i.e., $\eta = 0$ and $T_{1,2}$). This removes the effect that RoCoF decreases when computed over a longer horizon. From Figure 3.6, the following conclusions can be drawn:

- * For the units SM 1 and 6 (the units far from the event), RoCoF(0.1) deteriorates as η increases, but RoCoF(0.5) improves with respect to the all-SM system.
- * For the SM 5 - adjacent to the event - the RoCoF is less sensitive with respect to the integration level, since the collocated GFC reacts fast enough and comparable to the SM in the short term.
- * In terms of absolute RoCoF values, i.e., not normalized against the all-SMs system's RoCoF, SM 5 is the one experiencing the largest RoCoF(0.1) values, as expected (not shown here for space reasons).
- * Similar observations were obtained in the previous subsection for the loss of SM-GFC 1, where the SMs in the same region (SM 2,3 and 4) exhibit the largest RoCoF(0.1) values (see Figure 3.5).

In other words, as inertia homogeneously decreases across the network, frequency decays faster right after a contingency, leading to larger $\text{RoCoF}(0.1)$ values. The GFCs respond slower than the instantaneous inertial response from SMs, but fast enough to arrest the frequency decay rate before $T = 0.5s$, leading to smaller $\text{RoCoF}(0.5)$ values.

Remark 4. *A similar analysis can be carried out using the GFC frequencies. There is no clear pattern on the evolution of the $\text{RoCoF}(0.1)$ for low values of η , since there are large oscillations within this time scale. In this case, the $\text{RoCoF}(0.1)$ metric is no longer insightful, and low values might hide large swings. It has been observed that $\text{RoCoF}(0.5)$ clearly decreases as η increases.*

3.3.4 Discussion on the frequency metrics

The presented results emphasize the relevance of the choice of the RoCoF window T , typically chosen to properly reflect frequency evolution, filter out noise and ignore fast transients, according to the characteristics of a grid [99]. The presence of GFCs leads to new, fast dynamics and therefore the value of T has to be reconsidered for the low-inertia systems. A natural reaction is to reduce the current choices for T (typically between 500ms and 1s) to accommodate for the fast response of GFCs, but, as explained before, it can lead to misleading conclusions. On the other hand, large values of T might be ineffective for protection devices, as dynamics are much faster under high values of η . High RoCoF values represent a challenge for existing settings of RoCoF relays, some load-shedding schemes, and conventional generation, that in general are not able to withstand sudden changes in speed and might disconnect to avoid damage. Nonetheless, fast transients vanishing in less than 200ms are not expected to be meaningful for the SM or RoCoF relays. Nonetheless, their influence on the grid-following converters can be significant, depending on the PLL implementations.

Notice as well how nadir is no longer uniform for all SMs under high penetration levels (e.g., see the time series corresponding to $\eta = 0.9$ in Figure 3.5), caused by fast oscillations appearing adjacent to the event location and prior to the GFCs synchronization. For such a system, it might be needed to redefine the nadir metric to filter out these oscillations to obtain a meaningful metric which effectively reflects the severity of the grid contingency. Whether these fast dynamics need to be fully captured, ignored or just partially encapsulated in the metrics requires further in-depth investigations. This would depend on the effect of those fast dynamics across different components in the grid (grid-following devices, conventional generation, industrial loads, etc.).

3.3.5 All-GFC grid

We also explore a possible 100% GFC scenario, without the presence of any SM. The controllers are tuned as in the previous section, that is, no modification has been carried

out to stabilize the system. We compare in this case the trip of the HVDC link and the disconnection of generator 1. As shown in Figure 3.7, after a very quick transient all converters synchronize under both contingencies, reaching a steady state before 300ms. Once again, similar results have been observed under other grid-forming techniques, and combinations thereof.

Nadir is largely reduced in comparison to the all-SM grid, as the GFCs are orders of magnitude faster than the hydropower plants. For the case of the disconnection of generation unit 1, all generators in that area (2, 3 and 4) experience the largest values of short time-window RoCoF. On the other hand, for the other generators the response is nearly overdamped, and the nadir is equal to the steady state frequency deviation. This implies that the nadir, as defined in (3.2), is much larger for those units close to the event. Unlike in SM-dominated grids, in all-GFC grids nadir can be reached before the generation units synchronize. Therefore, values are not uniform across all units in the grid, and depend largely on the location of the event. Similar conclusions can be reached for the disconnection of the HVDC link, as the RoCoF and nadir values for generator 5 are much larger than for the rest of the generators.

These results question again the adequacy of the metrics in (3.2) for converter-dominated grids. On one hand, large values of T can render RoCoF useless as a metric, since the system might have reached a steady state², and hence RoCoF would just be proportional to the droop coefficient of the grid. On the other hand, small values of T that capture the first swing (around 50ms for both events) are very impractical and sensitive to noise. Overall, it is unclear whether a metric is required to characterize these fast dynamics, whose effect in the grid might be questionable.

3.4 Conclusions and outlook

While GFCs have already been used at a microgrid scale, there exist serious doubts on the stability of large systems as GFCs replace SMs, especially at high penetration levels. This paper has explored the massive deployment of grid-forming converters and its effects on frequency behavior. The presented results suggest that, under proper controller tuning, it is possible to guarantee frequency stability. Nonetheless, the grid dynamics change drastically, reaching steady state in the sub-second time range, orders of magnitude faster than the original pure-SM system. This has clear implications in terms of nadir and RoCoF, which might imply rethinking tuning of protection devices and load shedding schemes. There is also a need for PSS structures that can deal with a time-varying amount of inverter-based generation. To the best of our knowledge, no guidelines can be found for PSS tuning under high penetration scenarios.

Although in this work we have only covered the penetration of converters controlled

²Assuming no secondary control or similar frequency-recovery scheme is implemented.

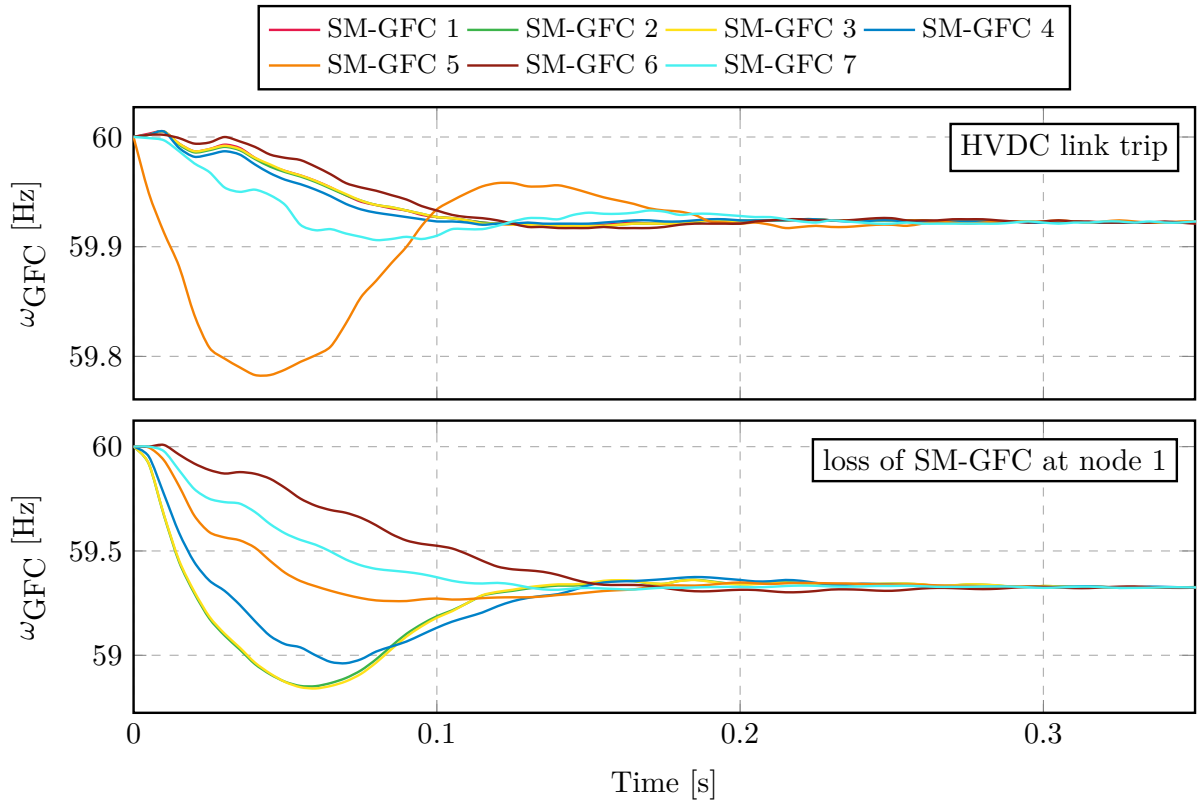


Figure 3.7: Frequency time series for all units in an all-GFC grid.

as grid-forming units, it is expected that a large number of devices will be operated as grid-following units. Large values of short time-window RoCoF might not be meaningful for frequency ride-through schemes in conventional generators or for RoCoF relays. However, grid following devices will try to synchronize to those fast transients, potentially creating large power transients.

Part III

Grid-forming hybrid angle control

Grid-forming hybrid angle control and almost global stability of the DC-AC power converter

Published in the IEEE Transactions on Automatic Control 2022.

Authors – Ali Tayyebi, Adolfo Anta, and Florian Dörfler.

Abstract – This paper introduces a new grid-forming control for a grid-connected dc-ac power converter, termed HAC that combines the dc-based matching control with a novel nonlinear angle feedback reminiscent of (though not identical to) classic droop control. The synthesis of HAC is inspired by the complementary benefits of the dc-based matching and ac-based grid-forming controls as well as ideas from direct angle control and nonlinear damping assignment. The proposed HAC is applied to a nonlinear converter model that is connected to an infinite bus or a center-of-inertia dynamic grid models. We provide parametric sufficient existence, uniqueness, stability, and boundedness conditions that are met by appropriate choice of control parameters. Next, we take into account the safety constraints of power converter, and synthesize a new current-limiting control that is compatible with HAC. Last, we present details on the practical implementation of HAC that are followed by a robustness analysis (which showcases a theory-practice gap), uncover the intrinsic droop behavior of the HAC, derive a feedforward-like ac voltage and power control, and illustrate the behavior of the closed-loop system with simulation case studies.

4.1 Introduction

The generation technology in power system has been drastically changing in recent years. The increasing replacement of bulk synchronous machines (SMs) with converter-interfaced generation is transforming the power system to a so-called *low-inertia* system. The stability aftermath of this transition is highlighted by significant inertia reduction, volatile generation, and the potential adverse interactions due to the presence of adjacent

timescales [1], [2], [33], [70], [100]–[102], among others. The *grid-forming* control concept is envisioned to address the aforementioned stability challenges, whereby the converter features frequency and voltage control, black-start, and load-sharing capabilities.

Several grid-forming control techniques have been recently proposed. *Droop control* mimics the speed droop of synchronous generators (SG), controls the converter modulation angle proportional to the active power imbalance, and is widely recognized as the baseline solution [34], [35]. As a natural extension of droop control, the emulation of SG dynamics and control led to *virtual synchronous machine* (VSM) strategies [38], [64], [103], [104]. The recently proposed *matching* control exploits structural similarities of the converter and SG; and matches their dynamics by controlling the modulation angle according to the dc voltage [40], [41], [43], [44], [65]. Furthermore, *virtual oscillator control* (VOC) mimics the dynamical behavior of Liénard-type oscillators and *globally* synchronizes a converter-based network [46], [49]. Recently, *dispatchable virtual oscillator control* (dVOC) is proposed that ensures *almost global* synchronization of a homogeneous network of oscillator-controlled converters to pre-specified set-points consistent with the power flow equations [45], [47], [50].

Inspired by recent studies [1], [55], [105] two distinct controller classes are identified: 1) *ac-based* techniques (e.g., droop control, VSM, VOC, and dVOC) that shape the converter frequency based on the ac quantities e.g., ac voltage and current, or power flows, and 2) *dc-based* controls (e.g., matching control) that synthesize the converter frequency based on the dc quantities e.g., dc voltage. The ac-based strategies improve the system-level small-signal frequency stability e.g., see [1, Subsection IV-C]. In contrast, the dc-based controls exhibit superior robustness [1, Subsection IV-D][105][55].

We leverage the aforementioned benefits and design a *hybrid angle control* (HAC) which combines a matching control variant and a nonlinear angle feedback (reminiscent of, though not identical to, droop control and dVOC) and is inspired by ideas from direct angle control [40] and sign-indefinite nonlinear damping assignment [106], [107]. Our proposed controller *almost globally* stabilizes the closed-loop converter dynamics when interfaced to either an IB or a dynamic COI grid model through a transmission line. We provide parametric conditions for the existence, uniqueness, and *almost global stability* of closed-loop equilibria. Last, we take into account the converter *safety constraints*, design a new *current-limiting* control, and investigate its stability in combination with HAC¹. Note that similar to other techniques (e.g., [2], [9], [35], [40], [45], [64], [65], [70]) HAC is a candidate for applications on different voltage levels in either grid-connected or islanded configuration.

¹A preliminary version of part of the results presented in this paper can be found in [8]. This paper improves the results in [8] by including 1) more realistic converter and grid models, 2) several theoretical extensions and practical remarks, 3) unified stability and instability conditions, 4) a compatible current-limiting control design, 5) detailed discussions on the HAC implementation, control robustness, complementary feedforward schemes, power-frequency droop behavior, and last 6) various numerical case studies to validate the performance and explore the control tuning trade-offs.

We consider a high-fidelity converter model including an explicit representation of energy source dynamics, dc-link, LC output filter, transmission line, COI grid dynamics, and the converter set-points. Further, the presented stability condition does not demand strong physical damping and is met by appropriate choice of control parameters.

Moreover, our choice of the angle dependent terms in the LaSalle/Lyapunov function and in the HAC formulation overcomes the analysis obstacles arising from lack of damping in angle state. Finally, we conclude this paper with some extensions, namely: a practical implementation and droop behavior of the HAC is described, a feedforward ac voltage and power control is discussed, and the control performance are explored with publicly available case studies [71]. In addition, as an interesting technical contribution in its own right, this paper introduces an offbeat manifold space—the boundary of a *Möbius strip*—for studying the evolution of angle trajectories. A theoretical limitation of all (continuous control) systems with angles evolving on the circle is that they can at best achieve AGAS due to the topological obstruction of the circle [108], which is a recurring theme in many of the aforementioned papers, e.g., see [109]. Here we establish AGAS of the angles on the boundary of a Möbius strip which results in *global* asymptotic stability of the desired equilibrium when projected on the circle.

The remainder of this paper is structured as follows. Section 4.2 describes the model of a converter connected to an IB and introduces the HAC. Section 4.3 presents the closed-loop analysis and the main result of this work. Section 4.4 discusses two theoretical extensions: dynamic COI grid model consideration and the design of a current-limiting control for grid-forming converters. Section 4.5 presents details on practical HAC implementations, robustness analysis of HAC, a complementary feedforward control, and HAC droop behavior. Next, we verify the performance of our controller via numerical examples in Section 4.6. Last, a summary and outlook on future work are given in Section 4.7.

4.2 Model description

4.2.1 Preliminaries and notation

In this paper, \mathbb{R} denotes the set of real numbers, $\mathbb{R}_{>0}$ denotes the set of strictly positive real numbers and $\mathbb{R}_{[a,b]} := \{x \in \mathbb{R} : a \leq x \leq b\}$. The unit circle i.e., one-dimensional torus is denoted by \mathbb{S}^1 . For the column vectors $x \in \mathbb{R}^n$ and $y \in \mathbb{R}^m$, $(x, y) := \begin{bmatrix} x^\top & y^\top \end{bmatrix}^\top \in \mathbb{R}^{n+m}$ denotes the stacked vector, and I is the two-dimensional identity matrix. The vector and matrix of zeros are respectively denoted by 0_n and $0_{n \times m}$. The block diagonal matrix is denoted by $\text{blkdiag}(A_1, \dots, A_n)$. Furthermore, $\|\cdot\|$ denotes the Euclidean norm operator. next, given $\varphi \in \mathbb{S}^1$ we define $\psi(\varphi) := (\cos(\varphi), \sin(\varphi))$. Last, for $x \in \mathbb{R}^2$, $\angle x$ denotes the absolute angle associated with the vector x in the polar coordinates; see

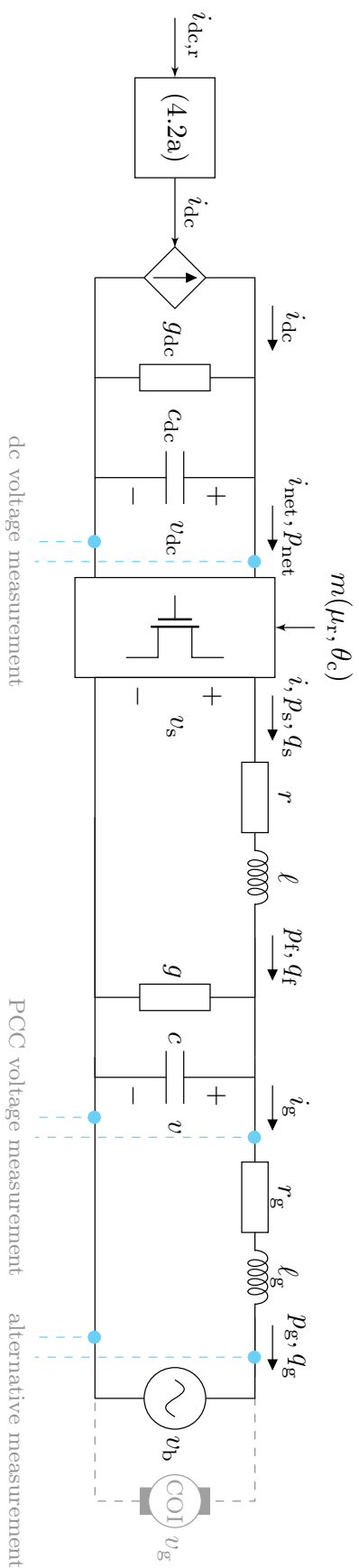


Figure 4.1: Schematic of the closed-loop system (4.7); see Figure 4.5 for the control diagram defining $i_{dc,r}$ and $m(\mu_r, \theta)$, and the Section 4.4.1 for the description of the closed-loop system with the COI grid model.

Appendix 4.9 for details.

In this work, similar to [1], [64], [65], [100] among others, we consider symmetric three-phase electric circuitry assuming identical electrical parameters for all three phases and that all three-phase quantities $z_{\text{abc}} := (z_a, z_b, z_c) \in \mathbb{R}^3$ are balanced i.e., $z_a + z_b + z_c = 0$. Under the latter assumption, a three-phase quantity z_{abc} is transformed to the stationary $\alpha\beta$ -frame via magnitude preserving Clarke transformation i.e., $z_{\alpha\beta} = \mathbf{C}z_{\text{abc}}$ (see Appendix 4.9.1 for details). Moreover, the image of $z_{\alpha\beta}$ in direct-quadrature (dq) coordinates that rotate with constant frequency $\omega_f \in \mathbb{R}_{>0}$ and the angle $\theta_f = \omega_f t + \theta_f(0) \in \mathbb{S}^1$ is given by $z = \mathbf{R}(\theta_f)z_{\alpha\beta}$ with

$$\mathbf{R}(\theta_f) := \begin{pmatrix} \cos \theta_f & -\sin \theta_f \\ \sin \theta_f & \cos \theta_f \end{pmatrix}.$$

4.2.2 Modeling the connection of converter and stiff grid

The IB three-phase voltage is defined by

$$v_{\text{b,abc}} := v_r \left(\sin(\theta_b), \sin\left(\theta_b - \frac{2\pi}{3}\right), \sin\left(\theta_b + \frac{2\pi}{3}\right) \right),$$

where $v_r \in \mathbb{R}_{>0}$ is the nominal ac voltage magnitude, and

$$\theta_b := \omega_0 t + \theta_b(0) \in \mathbb{S}^1 \tag{4.1}$$

is the IB absolute angle with the nominal frequency $\omega_0 \in \mathbb{R}_{>0}$.

We consider an average model of a three-phase two-level dc-ac converter [73, Chapter 5] and model the dc energy source by a first-order system that provides the input for a controlled dc current source. This is a reasonable coarse-grained model of the dc energy source e.g., see [1, Section II.A][110, Section 6.4]. The ac filter is modeled by an LC element. Moreover, the converter is interfaced to the IB with an inductive line (that can also be seen as a low-voltage to medium voltage transformer model); Figure 4.1 presents a schematic of the overall model.

The model of the converter-IB system in $\alpha\beta$ -frame is described by (see [65, Section II][73, Chapter 5] for details)

$$\tau_{\text{dc}} \dot{i}_{\text{dc}} = i_{\text{dc,r}} - i_{\text{dc}}, \tag{4.2a}$$

$$c_{\text{dc}} \dot{v}_{\text{dc}} = i_{\text{dc}} - g_{\text{dc}} v_{\text{dc}} - m_{\alpha\beta}(\mu_r, \theta_c)^\top i_{\alpha\beta}, \tag{4.2b}$$

$$\ell \dot{i}_{\alpha\beta} = v_{\text{dc}} m_{\alpha\beta}(\mu_r, \theta_c) - r i_{\alpha\beta} - v_{\alpha\beta}, \tag{4.2c}$$

$$c \dot{v}_{\alpha\beta} = i_{\alpha\beta} - g v_{\alpha\beta} - i_{\text{g},\alpha\beta}, \tag{4.2d}$$

$$\ell_{\text{g}} \dot{i}_{\text{g},\alpha\beta} = v_{\alpha\beta} - r_{\text{g}} i_{\text{g},\alpha\beta} - v_{\text{b},\alpha\beta}, \tag{4.2e}$$

where τ_{dc} is the source time constant, $i_{\text{dc}} \in \mathbb{R}$ is the dc source current, $c_{\text{dc}}, v_{\text{dc}} \in \mathbb{R}$, and g_{dc} respectively denote the dc-link capacitance, voltage, and the dc conductance (that models the dc-side losses).

Furthermore, $i_{\alpha\beta}, v_{\alpha\beta}$, and $i_{g,\alpha\beta}$ all take values in \mathbb{R}^2 and denote the current flowing through the filter inductance ℓ , the voltage across the filter capacitance c , and the current through the line inductance ℓ_g . Lastly, r, g , and r_g model switching and conduction losses associated with the elements ℓ, c , and ℓ_g , respectively. We do not explicitly model a local impedance load attached to the converter since it can be absorbed into the filter admittance. Due to the three-phase symmetry all parameters take positive and scalar values.

The modulation vector is defined as $m_{\alpha\beta}(\mu_r, \theta_c) := \mu_r \psi(\theta_c) \in \mathbb{R}_{[-1/2, 1/2]}$ with reference magnitude $\mu_r \in \mathbb{R}_{[0, 1/2]}$ and angle $\theta_c \in \mathbb{S}^1$ where θ_c denotes the converter absolute phase angle. In what follows, we will use the shorthand m for $m_{\alpha\beta}(\theta_c, \mu_r)$. The reference dc current in (4.2a) is defined as

$$i_{\text{dc},r} := i_r - \kappa(v_{\text{dc}} - v_{\text{dc},r}), \quad (4.3)$$

where $i_r \in \mathbb{R}$ denotes the open-loop dc current reference, $\kappa \in \mathbb{R}_{>0}$ is the dc voltage control gain, and $v_{\text{dc},r}$ is the reference dc voltage. If the dc source is connected to a dc-dc converter (e.g., as in PV systems), $i_{\text{dc},r}$ in (4.3) represents the reference current for the dc-dc converter. Note that the forthcoming analysis also applies to the case with energy source being modeled as a stiff voltage source i.e., $\tau_{\text{dc}} \rightarrow 0$ and $\kappa \rightarrow \infty$.

4.2.3 Hybrid angle control and closed-loop dynamics

We synthesize a new grid-forming strategy —hybrid angle control (HAC)— by combining the dc-based matching control (see e.g., [41, Equation 25]) and a nonlinear angle feedback reminiscent of —though not identical to— droop control and dVOC (see e.g., [34], [50] and Remark 7 for details). Defining the converter relative angle w.r.t the IB as

$$\theta := \theta_c - \theta_b, \quad (4.4)$$

the HAC takes the form

$$\dot{\theta}_c = \omega_c := \omega_0 + \eta(v_{\text{dc}} - v_{\text{dc},r}) - \gamma \sin\left(\frac{\theta - \theta_r}{2}\right), \quad (4.5)$$

where $\eta \in \mathbb{R}_{\geq 0}, \gamma \in \mathbb{R}_{>0}$ are the control parameters and θ_r denotes the control reference for the relative angle in (4.4) (see Proposition 7 for how to choose θ_r based on given voltage and power set-points). Since the angle term in the right-hand side (RHS) of (4.5) is 4π -periodic, the state θ_c evolves on the set $\mathbb{M} := [-2\pi, 2\pi]$ with -2π and 2π

glued together (i.e., $-2\pi \equiv 2\pi$). The terminology is due to \mathbb{M} being the boundary of the Möbius strip; see Remark 5 and Figure 4.2. This geometric curiosity leads to profound insights later on.

We transform the ac quantities in (4.2c)-(4.2e) to the dq-frame aligned with the IB angle θ_b . Next, state vector is defined as

$$x := (\theta, i_{dc}, v_{dc}, i, v, i_g) \in \mathbb{X} := \mathbb{M} \times \mathbb{R}^8 \quad (4.6)$$

and the overall closed-loop dynamics (4.2)-(4.5) is described by

$$\dot{\theta} = \omega_c - \omega_0 = \eta(v_{dc} - v_{dc,r}) - \gamma \sin\left(\frac{\theta - \theta_r}{2}\right), \quad (4.7a)$$

$$\tau_{dc} \dot{i}_{dc} = i_r - \kappa(v_{dc} - v_{dc,r}) - i_{dc}, \quad (4.7b)$$

$$c_{dc} \dot{v}_{dc} = i_{dc} - g_{dc} v_{dc} - m^\top i, \quad (4.7c)$$

$$\ell \dot{i} = v_{dc} m - Z i - v, \quad (4.7d)$$

$$c \dot{v} = i - Y v - i_g, \quad (4.7e)$$

$$\ell_g \dot{i}_g = v - Z_g i_g - v_b. \quad (4.7f)$$

Here $m = \mu_r \psi(\theta)$, $Z := rI - \ell\omega_0 J$ denotes the filter impedance matrix with $J := \begin{pmatrix} 0 & 1 \\ -1 & 0 \end{pmatrix}$, $Y := gI - c\omega_0 J$ is the shunt admittance matrix, $Z_g := r_g I - \ell_g \omega_0 J$ is the grid impedance matrix, and $v_b := (v_r, 0)$.

For notational convenience we respectively define the net dc current and power transferred to the converter ac-side as $i_{net} := m^\top i$ and $p_{net} := v_{dc} i_{net}$. The ac active and reactive power injections at the switching node, the filter capacitance, and IB nodes in Figure 4.1 are respectively defined by $p_s := i^\top v_s$ with $v_s := v_{dc} m$, $q_s := i^\top J v_s$, $p_f := i^\top v$, $q_f := i^\top J v$ and $p_g := i_g^\top v_b$, $q_g := i_g^\top J v_b$ [73, Section 4.6]. Last, note that the RHS of (4.7) is continuously differentiable in \mathbb{X} and the main nonlinearity aside (4.7a) is represented by the modulated terms in (4.7c) and (4.7d) with their power-preserving structure (assuming lossless dc-ac conversion) i.e., $p_{net} = p_s$ [40]. We close this section with remarks on \mathbb{M} and the HAC.

Remark 5 (Möbius strip). *The angle term in (4.5) is 4π -periodic and thus multi-valued on \mathbb{S}^1 . Hence, we study the evolution of angle trajectories in \mathbb{M} . One representation of \mathbb{M} is the compact boundary of Möbius strip parametrized in \mathbb{R}^3 by $\sigma(w, \varphi)$ with coordinates*

$$\sigma_1(w, \varphi) := \left(\rho - w \cos \frac{\varphi}{2} \right) \cos \varphi,$$

$$\sigma_2(w, \varphi) := \left(\rho - w \cos \frac{\varphi}{2} \right) \sin \varphi,$$

$$\sigma_3(w, \varphi) := w \sin \frac{\varphi}{2},$$

where $\rho \in \mathbb{R}_{>0}$ is the middle circle radius, w denotes the half-width with $|w| \leq 1/2$, and $\varphi \in \mathbb{S}^1$. Figure 4.2 illustrates a parametrization of $\sigma(w, \varphi)$ such that $|\partial\sigma(w, \varphi)| = 4\pi$ where $\partial\sigma(w, \varphi)$ denotes the boundary of Möbius strip.

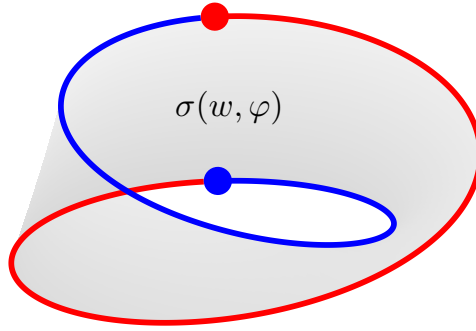


Figure 4.2: The boundary of the Möbius strip represents the angle space of (4.7). The arcs contained in the boundary segments colored in blue and red respectively represent the angles in $[-2\pi, 0]$ and $[0, 2\pi]$.

Remark 6 (Design rationale and control synthesis). *The design rationale for HAC is to blend the dc and ac information in the converter frequency definition. Thus, HAC is expected to inherit the enhanced performance and robustness of the ac and dc-based controls (see Section 4.1 and Subsection 4.6.3 for a numerical confirmation of these hypotheses). Furthermore, the benefits of hybrid control structures are also reported in [55]. On the other hand, HAC is inspired by a direct angle control approach [40]. The angle feedback in (4.5) is an odd function and injects angle damping i.e., it provides dissipation for the angle in (4.7a) unlike the other controls, where the angle variable acts as a mere integrator e.g., [65].*

Remark 7 (Hybrid angle control variants). *With particular parameter choices in (4.5), HAC recovers several existing controls. For instance, $\eta = 0$ in (4.5) leads to a pure angle feedback control i.e., $\omega_c = \omega_0 - \gamma \sin((\theta - \theta_r)/2)$ reminiscent of the droop control [1, Section III-C][34]. Indeed, droop control is described by $\omega_c := \omega_0 + d_{p-\omega}(p_r - p)$, with the droop gain $d_{p-\omega} \in \mathbb{R}_{>0}$ (see Proposition 6 for a definition), power reference p_r , and $p := i_g^\top v$ being the measured power that (with the assumptions in [34]) is proportional to $\sin(\theta)$. Likewise, HAC relates to dVOC dynamics (in polar coordinates) that locally resembles droop control [48], [50]. Furthermore, the HAC's dc term with $\eta = \omega_0/v_{dc,r}$ recovers the standard matching control [65] combined with the angle term i.e., $\omega_c = \eta v_{dc} - \gamma \sin((\theta - \theta_r)/2)$. Last, if $\eta \neq \omega_0/v_{dc,r}$ the dc term in (4.5) is identical to the matching variant in [41].*

4.3 Closed-loop analysis

In this section, we analyze the closed-loop system (4.7) and provide sufficient parametric conditions for the existence, uniqueness, and global stability of the closed-loop equilibria.

4.3.1 Existence of equilibria

Provided that the dc voltage meets its reference in steady state, we will establish that the closed-loop system (4.7) admits a unique equilibrium set containing two disjoint equilibria

$$\Omega^* := \{x_s^* := (\theta_1^*, y^*), x_u^* := (\theta_2^*, y^*)\}, \quad (4.9)$$

where $\theta_1^* := \theta_r$, $\theta_2^* := \theta_r + 2\pi$, and $y^* := (i_{dc}^*, v_{dc}^*, i^*, v^*, i_g^*)$ is the unique equilibrium of the states evolving in \mathbb{R}^8 .

Theorem 1 (Existence of equilibria). *The closed-loop system (4.7) admits two equilibria if there exist a consistent reference $i_r = i_{dc}^*$ in (4.7b) such that $v_{dc}^* = v_{dc,r}$. These disjoint equilibria only differ by their equilibrium angles being equal to θ_r or $\theta_r + 2\pi$, i.e., they are of the form (4.9).*

Proof. We begin by setting the RHS of (4.7) to zero

$$\eta(v_{dc}^* - v_{dc,r}) - \gamma \sin\left(\frac{\theta^* - \theta_r}{2}\right) = 0, \quad (4.10a)$$

$$i_r - \kappa(v_{dc}^* - v_{dc,r}) - i_{dc}^* = 0, \quad (4.10b)$$

$$i_{dc}^* - g_{dc}v_{dc}^* - m(\theta^*)^\top i^* = 0, \quad (4.10c)$$

$$v_{dc}^* m(\theta^*) - Zi^* - v^* = 0_2, \quad (4.10d)$$

$$i^* - Yv^* - i_g^* = 0_2, \quad (4.10e)$$

$$v^* - Z_g i_g^* - v_b = 0_2. \quad (4.10f)$$

If the condition of the theorem is met and thus $v_{dc}^* = v_{dc,r}$, (4.10b) implies that $i_{dc}^* = i_r$ and (4.10a) reduces to $\gamma \sin((\theta^* - \theta_r)/2) = 0$. Hence the angle equilibria are

$$\theta_1^* = \theta_r \quad \text{and} \quad \theta_2^* = \theta_r + 2\pi. \quad (4.11)$$

It remains to show (4.10d)-(4.10f) admits a unique solution. Rearrange (4.10d)-(4.10f) to $A(i^*, v^*, i_g^*) = b$ with

$$A := \begin{pmatrix} -Z & -I & 0_{2 \times 2} \\ I & -Y & -I \\ 0_{2 \times 2} & I & -Z_g \end{pmatrix}$$

and $b := (-v_{\text{dc}}^* m(\theta^*), 0_2, v_b)$. It can be easily computed that symmetric part of A , that is, $(1/2)(A + A^\top) \prec 0$. Hence, A^{-1} exists and $(i^*, v^*, i_g^*) := A^{-1}b$ is unique. \blacksquare

Remark 8 (Equilibria and the existence condition). *Theorem 1 identifies two equilibria in (4.9) conditioned on a consistent reference i_r that ensures $v_{\text{dc}}^* = v_{\text{dc},r}$. This condition is possibly enforced through appropriate feedforward or a proportional-integral control, and it can be entirely omitted if $\eta = 0$ in (4.5). In Subsection 4.3.2, we will prove that the system (4.7) is AGAS w.r.t x_s^* under a mild parametric condition. Thus, if x_s^* exists then no other relevant (i.e., stable) equilibria co-exist. Last, next to x_s^* being AGAS on $\mathbb{M} \times \mathbb{R}^8$, we will establish instability of x_u^* . In fact, when viewing the angle state not as element of \mathbb{M} but more conventionally evolving on \mathbb{S}^1 (i.e., picture projecting Figure 4.2 downwards to a circle), then the two equilibria $\{x_s^*, x_u^*\}$ represent an identical point on \mathbb{S}^1 . Thus, by working on \mathbb{M} rather than \mathbb{S}^1 we by-passed the topological obstruction to continuous stabilization on \mathbb{S}^1 [108].*

4.3.2 Stability analysis

In the sequel, we establish the AGAS of the system (4.7) w.r.t the equilibrium x_s^* characterized in Theorem 1. This finding relies on the basis of intermediate results, namely, 1) global convergence of the trajectories to Ω^* in (4.9), 2) local asymptotic stability of x_s^* , and 3) instability of x_u^* . We begin by restating the definition of AGAS [45, Definition 5].

Definition 1 (AGAS). *An equilibrium of a dynamical system is almost globally asymptotically stable if it is asymptotically stable and for all initial conditions, except those contained in a Lebesgue zero-measure set, the trajectories converge to that equilibrium.*

Theorem 2 below demonstrates the global attractivity of the equilibria (4.9) under a parametric condition that can be satisfied by an appropriate choice of the control gains η and γ in (4.5).

Theorem 2 (Global attractivity). *Consider the closed-loop system (4.7) and the equilibria Ω^* characterized in Theorem 1. If the system parameters satisfy*

$$\frac{\eta}{g_{\text{dc}}} + \frac{\eta(\mu_r \|i^*\|)^2}{g_{\text{dc}}} + \frac{\eta(\mu_r v_{\text{dc}}^*)^2}{r} < \gamma, \quad (4.12)$$

then all trajectories of (4.7) globally converge to Ω^ .*

Proof. Define the error coordinates $\tilde{x} = (\tilde{\theta}, \tilde{i}_{\text{dc}}, \tilde{v}_{\text{dc}}, \tilde{i}, \tilde{v}, \tilde{i}_g)$ w.r.t x_s^* – with the equilibrium angle θ_1^* – in (4.9) as

$$\tilde{x} := (\theta - \theta_1^*, i_{\text{dc}} - i_{\text{dc}}^*, v_{\text{dc}} - v_{\text{dc}}^*, i - i^*, v - v^*, i_g - i_g^*). \quad (4.13)$$

The error dynamics associated with (4.7) are described by

$$\dot{\tilde{\theta}} = \eta \tilde{v}_{\text{dc}} - \gamma \sin \frac{\tilde{\theta}}{2}, \quad (4.14a)$$

$$\tau_{\text{dc}} \dot{\tilde{i}}_{\text{dc}} = -\kappa \tilde{v}_{\text{dc}} - \tilde{i}_{\text{dc}}, \quad (4.14b)$$

$$c_{\text{dc}} \dot{\tilde{v}}_{\text{dc}} = \tilde{i}_{\text{dc}} - g_{\text{dc}} \tilde{v}_{\text{dc}} - \mu_{\text{r}} e_{\psi}^{\top} \tilde{i}^{\star} - m(\mu_{\text{r}}, \theta)^{\top} \tilde{i}, \quad (4.14c)$$

$$\ell \dot{\tilde{i}} = m(\mu_{\text{r}}, \theta) \tilde{v}_{\text{dc}} + \mu_{\text{r}} e_{\psi} v_{\text{dc}}^{\star} - Z \tilde{i} - \tilde{v}, \quad (4.14d)$$

$$c \dot{\tilde{v}} = \tilde{i} - Y \tilde{v} - \tilde{i}_{\text{g}}, \quad (4.14e)$$

$$\ell_{\text{g}} \dot{\tilde{i}} = \tilde{v} - Z_{\text{g}} \tilde{i}_{\text{g}}, \quad (4.14f)$$

where $e_{\psi} := \psi(\theta) - \psi(\theta_1^{\star})$. Let $\tilde{y} := (\tilde{i}_{\text{dc}}, \tilde{v}_{\text{dc}}, \tilde{i}, \tilde{v}, \tilde{i}_{\text{g}})$ and consider the composite parametric LaSalle/Lyapunov function

$$\mathcal{V}(\tilde{x}) := \mathcal{H}(\tilde{y}) + \lambda \mathcal{S}(\tilde{\theta}) = \frac{1}{2} \left(\tilde{y}^{\top} P \tilde{y} \right) + 2\lambda \left(1 - \cos \frac{\tilde{\theta}}{2} \right) \quad (4.15)$$

where $P := \text{blkdiag}(\tau_{\text{dc}}/\kappa, c_{\text{dc}}, \ell I, cI, \ell_{\text{g}} I)$, $\lambda \in \mathbb{R}_{>0}$, and $\mathcal{V}(\tilde{x}) > 0$ for all $\tilde{x} \neq 0_{\text{g}}$; see Figure 4.3 for an illustration of $\mathcal{V}(\tilde{x})$.

Evaluating $\dot{\mathcal{V}}(\tilde{x})$ along trajectories of (4.14) yields

$$\begin{aligned} \dot{\mathcal{V}}(\tilde{x}) = & -g_{\text{dc}} \tilde{v}_{\text{dc}}^2 - \frac{1}{\kappa} \tilde{i}_{\text{dc}}^2 - r \|\tilde{i}\|^2 - g \|\tilde{v}\|^2 - r_{\text{g}} \|\tilde{i}_{\text{g}}\|^2 + \lambda \eta \tilde{v}_{\text{dc}} \sin \frac{\tilde{\theta}}{2} - \lambda \gamma \sin^2 \frac{\tilde{\theta}}{2} \\ & - \mu_{\text{r}} \tilde{v}_{\text{dc}} e_{\psi}^{\top} \tilde{i}^{\star} + \mu_{\text{r}} v_{\text{dc}}^{\star} \tilde{i}^{\top} e_{\psi}, \end{aligned} \quad (4.16)$$

where we exploited the skew symmetry of J in Z , Y , and Z_{g} i.e., $\tilde{i}^{\top} (\ell \omega_0 J) \tilde{i} = \tilde{v}^{\top} (c \omega_0 J) \tilde{v} = \tilde{i}_{\text{g}}^{\top} (\ell_{\text{g}} \omega_0 J) \tilde{i}_{\text{g}} = 0$. We apply the identity (4.71) to the e_{ψ} -dependent terms in (4.16):

$$-\mu_{\text{r}} \tilde{v}_{\text{dc}} e_{\psi}^{\top} \tilde{i}^{\star} \leq (\epsilon_1 \mu_{\text{r}} \|\tilde{i}^{\star}\|)^2 \tilde{v}_{\text{dc}}^2 + \frac{1}{4\epsilon_1^2} \|e_{\psi}\|^2, \quad (4.17a)$$

$$\mu_{\text{r}} v_{\text{dc}}^{\star} \tilde{i}^{\top} e_{\psi} \leq \epsilon_2^2 \|\tilde{i}\|^2 + \frac{(\mu_{\text{r}} v_{\text{dc}}^{\star})^2}{4\epsilon_2^2} \|e_{\psi}\|^2, \quad (4.17b)$$

with $\epsilon_1, \epsilon_2 \in \mathbb{R}_{>0}$. Next, by applying identities (4.72) and (4.75), $\|e_{\psi}\|^2$ is expressed in terms of $\sin(\tilde{\theta}/2)$:

$$\begin{aligned} \|e_{\psi}\|^2 &= (\cos \theta - \cos \theta_1^{\star})^2 + (\sin \theta - \sin \theta_1^{\star})^2 = +2(1 - \cos \theta \cos \theta_1^{\star} - \sin \theta \sin \theta_1^{\star}) \\ &= 2(1 - \cos(\theta - \theta_1^{\star})) = 2\left(1 - \cos \tilde{\theta}\right) = 4 \sin^2 \frac{\tilde{\theta}}{2}. \end{aligned}$$

Replace $\|e_\psi\|^2$ by $4 \sin^2(\tilde{\theta}/2)$ in (4.17), then $\dot{\mathcal{V}}(\tilde{x})$ in (4.16) is upper-bounded by

$$\begin{aligned} \dot{\mathcal{V}}(\tilde{x}) \leq & \lambda \eta \tilde{v}_{\text{dc}} \sin \frac{\tilde{\theta}}{2} - \left(\lambda \gamma - \frac{1}{\epsilon_1^2} - \frac{(\mu_{\text{r}} v_{\text{dc}}^*)^2}{\epsilon_2^2} \right) \sin^2 \frac{\tilde{\theta}}{2} - \left(g_{\text{dc}} - (\epsilon_1 \mu_{\text{r}} \|i^*\|)^2 \right) \tilde{v}_{\text{dc}}^2 \\ & - (r - \epsilon_2^2) \|\tilde{i}\|^2 - \frac{1}{\kappa} \tilde{i}_{\text{dc}}^2 - g \|\tilde{v}\|^2 - r_{\text{g}} \|\tilde{i}_{\text{g}}\|^2 = -\tilde{\zeta}^\top \mathbf{Q} \tilde{\zeta}, \end{aligned} \quad (4.18)$$

where $\tilde{\zeta} := \left(\sin(\tilde{\theta}/2), \tilde{y} \right)$ and $\mathbf{Q} := \begin{pmatrix} \mathbf{Q}_{11} & \mathbf{0}_{3 \times 6} \\ \mathbf{0}_{6 \times 3} & \mathbf{Q}_{22} \end{pmatrix}$ with

$$\mathbf{Q}_{11} := \begin{pmatrix} \gamma \lambda - \frac{1}{\epsilon_1^2} - \frac{(\mu_{\text{r}} v_{\text{dc}}^*)^2}{\epsilon_2^2} & 0 & -\frac{\eta \lambda}{2} \\ 0 & \frac{1}{\kappa} & 0 \\ -\frac{\eta \lambda}{2} & 0 & g_{\text{dc}} - (\epsilon_1 \mu_{\text{r}} \|i^*\|)^2 \end{pmatrix} \quad (4.19)$$

and $\mathbf{Q}_{22} := \text{blkdiag}\left((r - \epsilon_2^2) \mathbf{I}, g \mathbf{I}, r_{\text{g}} \mathbf{I}\right)$. By standard Schur complement analysis, $\mathbf{Q} \succ 0$ iff

$$\epsilon_1^2 < \frac{g_{\text{dc}}}{(\mu_{\text{r}} \|i^*\|)^2} := \alpha \quad \text{and} \quad \epsilon_2^2 < r, \quad (4.20a)$$

$$\left(\frac{\lambda \eta}{2 \sqrt{g_{\text{dc}}}} \right)^2 < \left(\gamma \lambda - \frac{1}{\epsilon_1^2} - \frac{(\mu_{\text{r}} v_{\text{dc}}^*)^2}{\epsilon_2^2} \right) \left(1 - \frac{\epsilon_1^2}{\alpha} \right). \quad (4.20b)$$

These bounds can be optimized over the parameters ϵ_1, ϵ_2 , and λ to obtain the least conservative or most compact condition.

To continue assume for now that $\eta > 0$. The simple and favorable choice $\epsilon_1 = \sqrt{\alpha/2}$, $\epsilon_2 = \sqrt{r/2}$, and $\lambda = 2/\eta$ yields that conditions (4.20) are satisfied and $\mathbf{Q} \succ 0$ iff the bound (4.12) is met. Accordingly, $\dot{\mathcal{V}}(\tilde{x}) < 0$ for all $\tilde{\zeta} \neq 0_{\text{g}}$. For $\eta = 0$, the off-diagonal elements of \mathbf{Q}_{11} in (4.19) vanish. With the same choice of $\epsilon_1 = \sqrt{\alpha/2}$ and $\epsilon_2 = \sqrt{r/2}$, condition (4.20b) reduces to

$$\frac{2(\mu_{\text{r}} \|i^*\|)^2}{\lambda g_{\text{dc}}} + \frac{2(\mu_{\text{r}} v_{\text{dc}}^*)^2}{\lambda r} < \gamma. \quad (4.21)$$

For any $\gamma > 0$, (4.21) is met by a sufficiently large $\lambda > 0$, which is consistent with condition (4.12) for $\eta = 0$.

Recall the boundedness of $\tilde{\theta}$ in \mathbb{M} and radial unboundedness of $\mathcal{H}(\tilde{y})$. Since $\dot{\mathcal{V}}(\tilde{x}) \leq 0$, for any $\tilde{x}(0) \in \mathbb{X}$, the set $\mathcal{L}_{\mathcal{V}(\tilde{x}(0))} = \{\tilde{x} \in \mathbb{X} : \mathcal{V}(\tilde{x}) \leq \mathcal{V}(\tilde{x}(0))\}$ is compact and forward invariant. Thus, by LaSalle's invariance [111, Theorem 4.4], all trajectories of (4.14) converge to the largest invariant set in $\Omega = \{\tilde{x} \in \mathbb{X} : \dot{\mathcal{V}}(\tilde{x}) = 0\}$.

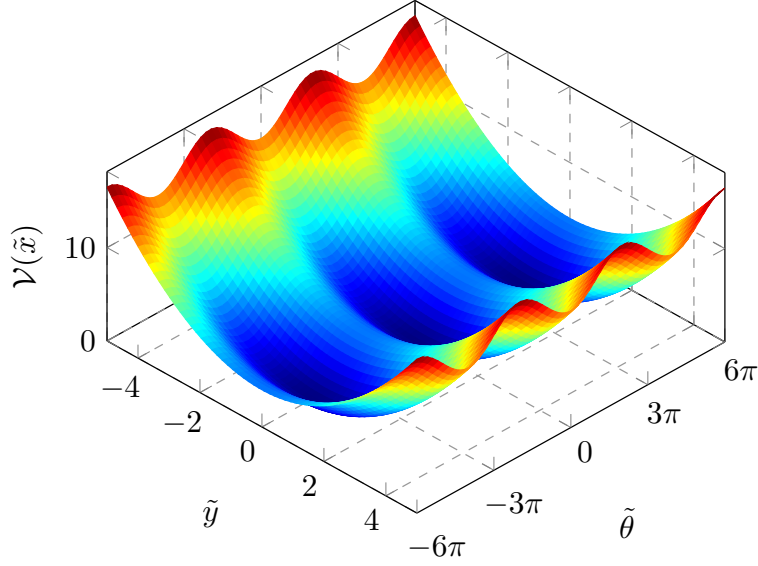


Figure 4.3: Illustration of the Lyapunov function (4.15) under the simplifying assumption that $\tilde{y}, \tilde{\theta} \in \mathbb{R}$, $P = 1$, and $\lambda = 1$.

Since $Q \succ 0$, $\dot{V}(\tilde{x}) = 0$ iff $\tilde{\zeta} = 0_9$ which holds iff $\sin(\tilde{\theta}/2) = 0$ and $\tilde{y} = 0_8$ that means either $\tilde{\theta} = 0$ or $\tilde{\theta} = 2\pi$ in Ω proving that $\Omega = \Omega^*$. ■

Proposition 1 below reveals the local asymptotic stability of the equilibrium x_s^* in (4.9) under the condition (4.12).

Proposition 1 (Local asymptotic stability). *Consider (4.7) and assume that (4.12) holds. Then the equilibrium x_s^* in (4.9) is locally asymptotically stable.*

The proof is provided in Appendix 4.8. Proposition 2 reveals instability of x_u^* in (4.9) and characterizes its region of attraction as a Lebesgue zero-measure set.

Proposition 2 (Unstable equilibrium point). *Consider (4.7) and assume that (4.12) holds. The x_u^* in (4.9) is unstable with a zero-Lebesgue-measure region of attraction.*

The proof is provided in Appendix 4.8. On the basis of the intermediate results, the next theorem presents our main result.

Theorem 3 (Main result: AGAS). *Consider the closed-loop system (4.7). If condition (4.12) is satisfied, x_s^* in (4.9) is almost globally asymptotically stable.*

Remark 9 (Feasibility and interpretations). *First, condition (4.12) is met for sufficiently large $\gamma > 0$ and it is possible to arbitrarily scale the left-hand side (LHS) terms via $\eta \geq 0$. Condition (4.12) implies that for small g_{dc} and r , a large ratio γ/η is required. Also, for high $\|i^*\|$, v_{dc}^* , and μ_r , the ratio γ/η must be increased. Finally, for pure angle feedback, i.e., $\eta = 0$ and $\gamma > 0$ in (4.5), condition (4.12) is always met regardless of the*

system equilibria and parameters. Second, condition (4.12) does not demand a minimum physical damping and is met by a large enough ratio of gains γ/η . An interpretation is that with large enough virtual angle damping, the inherent converter passivity stabilizes the dc and ac quantities [65]. Third, condition (4.12) does not depend on the dc source time constant τ_{dc} and control gain κ . Thus, (4.12) also unveils the robustness of HAC w.r.t delays in source actuation that suggests the compatibility of HAC with different energy sources on distinct timescales. Furthermore, κ can still be freely chosen to optimize the dc voltage performance. Last, although HAC dominantly relies on ac dynamics (by recommendation for large γ/η), stabilization does not require the conventional timescale separation of angle, dc, and ac dynamics [112], [113]. Last, the Propositions 1 and 2 highlight that (4.12) is sufficient simultaneously for the local stability of x_s^* and the instability of x_v^* . Hence, (4.12) is a unified condition whereas the conditions in [8] impose different bounds on γ in (4.5).

4.4 Dynamic grid and current-limiting control

In this section, we construct two practically relevant theoretic extensions on the basis of the analysis presented in the Section 4.3. First, we consider the connection of the converter to a dynamic grid represented by a COI model and investigate the closed-loop stability. Thus, extending the results of Theorem 2 to a more realistic class of power grid models; see Theorem 4. Second, we tackle an open problem that is associated with grid-forming power converters i.e., we account for the converter current constraint and design a new current-limiting control that is compatible with HAC. Proving the overall stability while augmenting the closed-loop dynamics with the current-limiting mechanism relies on the analysis presented in the Section 4.3; see Propositions 3 and 4.

4.4.1 Modeling the connection of converter and dynamic grid

Under the slow coherency assumptions [114, Chapter 2][115], an interconnected network of SGs can be represented with an equivalent COI model that relies on the aggregation of swing dynamics [61, Section 6.10][116, Section 3.2]. The angle and frequency dynamics of the COI grid model are described by

$$\dot{\theta}_g = \omega, \quad (4.22a)$$

$$J\dot{\omega} = T_m - D\omega - T_e, \quad (4.22b)$$

where $J \in \mathbb{R}_{>0}$ is the moment of inertia and it is defined (in terms of the base power $S_{r,g}$ and the inertia constant H) by $J := 2HS_{r,g}/\omega_0^2$ [117, Equation 5.10]. Moreover, $T_m \in \mathbb{R}$ denotes the mechanical torque, $D \in \mathbb{R}_{>0}$ denotes the aggregated damping and droop coefficient that models the aggregated governor action, and $T_e \in \mathbb{R}$ is the electrical

torque. Considering the structural similarity of (4.22) and the full SM dynamics [109], we define the dynamic grid voltage as

$$v_{g,abc} := b\omega \left(\sin \theta_g, \sin \left(\theta_g - \frac{2\pi}{3} \right), \sin \left(\theta_g + \frac{2\pi}{3} \right) \right), \quad (4.23)$$

where $b \in \mathbb{R}_{>0}$ is constant [109, Equation 9]. Thus, T_e in (4.22b) in terms of grid voltage and current is [109, Equation 10]

$$T_e = \frac{i_{g,abc}^\top v_{g,abc}}{\omega}. \quad (4.24)$$

Note that if $J \rightarrow \infty$ and b is chosen such that $\|v_g\| \rightarrow v_r$ as $\omega \rightarrow \omega_0$, (4.22)-(4.24) recovers the IB grid model with constant frequency and voltage magnitude (see Section 4.2.2).

Consider a converter controlled by HAC and connected to the COI grid model via an inductive line; see Figure 4.1. Combining (4.2), (4.3), (4.5), and (4.22)-(4.24) the overall closed-loop dynamics in a dq-frame aligned with θ_g is

$$\dot{\underline{\theta}} = \omega_0 + \eta(v_{dc} - v_{dc,r}) - \gamma \sin \left(\frac{\underline{\theta} - \underline{\theta}_r}{2} \right) - \omega, \quad (4.25a)$$

$$\tau_{dc} \dot{i}_{dc} = i_r - \kappa(v_{dc} - v_{dc,r}) - i_{dc}, \quad (4.25b)$$

$$c_{dc} \dot{v}_{dc} = i_{dc} - g_{dc} v_{dc} - m^\top i, \quad (4.25c)$$

$$\ell \dot{i} = v_{dc} m - Z(\omega) i - v, \quad (4.25d)$$

$$c \dot{v} = i - Y(\omega) v - i_g, \quad (4.25e)$$

$$\ell_g \dot{i}_g = v - Z_g(\omega) i_g - b\omega e_1, \quad (4.25f)$$

$$J \dot{\omega} = T_m - D\omega + b e_1^\top i_g. \quad (4.25g)$$

Here $\underline{\theta} := \theta_c - \theta_g$ denotes the relative converter-COI angle, $\underline{\theta}_r$ is the reference for $\underline{\theta}$, and $e_1 := (1, 0)$. Note the impedance and admittance matrices in (4.25d)-(4.25f) are ω -dependent (cf. constant matrices in (4.7d)-(4.7f)).

4.4.2 Equilibria characterization and closed-loop stability

To begin with, define the augmented closed-loop state vector

$$\underline{x} := (\underline{\theta}, i_{dc}, v_{dc}, \omega, i, v, i_g) \in \underline{\mathbb{X}} := \mathbb{M} \times \mathbb{R}^9. \quad (4.26)$$

Assume that the reference dc current and mechanical torque in (4.25b) and (4.25g) are set such that the equilibrium dc voltage and frequency coincide with $v_{dc,r}$ and ω_0 . Following the same procedure as in the proof Theorem 1, dynamical system (4.25) admits two

equilibria with the same structure as Ω^* in (4.9) i.e.,

$$\underline{\Omega}^* := \{ \underline{x}_s^* := (\theta_1^*, \underline{y}^*), \underline{x}_u^* := (\theta_2^*, \underline{y}^*) \}, \quad (4.27)$$

with $\theta_1^* := \underline{\theta}_r$, $\theta_2^* := \underline{\theta}_r + 2\pi$, and $\underline{y}^* := (i_{dc}^*, v_{dc}^*, \omega^*, i^*, v^*, i_g^*)$ denoting the unique equilibrium associated with states evolving in \mathbb{R}^9 . Theorem 4 delivers the same result as Theorem 2 i.e., global stability of $\underline{\Omega}^*$ under the flow defined by (4.25).

Theorem 4 (Global stability with dynamic grid model). *Consider the closed-loop system (4.25) and the equilibria $\underline{\Omega}^*$ defined in (4.27). If the system and control parameters satisfy*

$$D > D_{\min} := \frac{(\ell \|i^*\|)^2}{r} + \frac{(c \|v^*\|)^2}{g} + \frac{(\ell_g \|i_g^*\|)^2}{r_g}, \quad (4.28a)$$

$$\gamma > \frac{\eta}{g_{dc}} + \frac{\eta (\mu_r \|i^*\|)^2}{g_{dc}} + \frac{\eta (\mu_r v_{dc}^*)^2}{r} + \frac{1}{2(D - D_{\min})}, \quad (4.28b)$$

then all trajectories of (4.25) globally converge to $\underline{\Omega}^*$.

The proof is provided in Appendix 4.8.

Remark 10 (Extended stability conditions). *Condition (4.28a) is met if the COI model is sufficiently damped (see [106], [109], [118] for discussions on the critical damping requirement) and with large enough γ condition (4.28b) is satisfied (see Remark 9). The conditions in (4.28) almost decouple into the condition (4.12) (cf. (4.28b)) and the damping requirement (4.28a). The latter can be perceived as characterization of the grid types to which the converter can be interfaced. For $D \gg D_{\min}$ conditions (4.28) reduce to (4.12). An interpretation of the trade-off between γ and D is that with large D the timescale of COI model approaches that of the converter. Thus, synchronization demands less virtual angle damping due to more coherent converter-COI frequency dynamics.*

Akin to the relation between Theorem 2 and 4, following analogous arguments, one can extend Propositions 1, 2, and Theorem 3 to (4.25) under (4.28). For brevity of presentation, we omit the straightforward albeit lengthy calculations.

4.4.3 Compatible current-limiting control synthesis

In practice, power converters have tight state constraints for safety: in particular, their filter current magnitude needs to be constrained to a prescribed limit for protecting the semiconductor switches. There are ad hoc current-limiting techniques (without theoretical certificates e.g., see [86]) for *grid-following* converters (see [33] for a definition). The design of current limitation strategies for grid-forming (i.e., voltage source) converters

is an active research topic [1], [70], [81], [87]. To this date, a universally satisfactory solution that safeguards the converter against various contingencies (e.g., load-induced over-current and balanced / unbalanced faults) is not known. In what follows, we propose a new current-limiting control and highlight its compatibility with the HAC.

To begin with, by viewing the current dynamics in isolation, we derive the magnitude dynamics associated with (4.7d) by means of polar coordinates transformation (see Appendix 4.9.2 for details). First, expand the current dynamics in (4.7d) i.e.,

$$\ell \dot{i}_d = \mu_r v_{dc} \cos(\theta) - r i_d + \ell \omega_0 i_q - v_d, \quad (4.29a)$$

$$\ell \dot{i}_q = \mu_r v_{dc} \sin(\theta) - r i_q - \ell \omega_0 i_d - v_q. \quad (4.29b)$$

Consider that $\|i\| = \sqrt{i_d^2 + i_q^2}$ and thus

$$\frac{d}{dt} \|i\|^2 = 2 \|i\| \frac{d}{dt} \|i\| = \frac{d}{dt} (i_d^2 + i_q^2) = 2 (i_d \dot{i}_d + i_q \dot{i}_q). \quad (4.30)$$

Replace i_d and i_q with $\|i\| \cos(\theta_i)$ and $\|i\| \sin(\theta_i)$ where $\theta_i := \tan^{-1}(i_q/i_d)$ and multiply (4.30) with $\ell/2\|i\|$:

$$\ell \frac{d}{dt} \|i\| = \ell \cos(\theta_i) \dot{i}_d + \ell \sin(\theta_i) \dot{i}_q. \quad (4.31)$$

Substitute v_d and v_q in (4.29) with $\|v\| \cos(\theta_v)$ and $\|v\| \sin(\theta_v)$ where $\theta_v := \tan^{-1}(v_q/v_d)$. Replacing \dot{i}_d and \dot{i}_q in (4.31) with the RHS of (4.29) and exploiting (4.75) results in

$$\ell \frac{d}{dt} \|i\| = \mu_r v_{dc} \cos(\theta - \theta_i) - r \|i\| - \|v\| \cos(\theta_v - \theta_i). \quad (4.32)$$

So far μ_r in (4.32) was assumed to be a positive constant; see the definition of $m_{\alpha\beta}(\mu_r, \theta_c)$ in (4.2). We now re-parametrize the to-be-controlled modulation magnitude as

$$\mu := (1 - \Delta_\mu) \mu_r, \quad (4.33)$$

where $\Delta_\mu : \mathbb{X} \rightarrow \mathbb{R}_{(0,1)}$ is a locally Lipschitz function. Observe that $\Delta_\mu \in \mathbb{R}_{(0,1)}$ is required since μ in (4.33) has to be positive. Replacing μ_r in (4.32) with (4.33) results in

$$\ell \frac{d}{dt} \|i\| = \mathcal{A} (1 - \mathcal{D} - \Delta_\mu) - r \|i\|, \quad (4.34)$$

where

$$\mathcal{A} := \mu_r v_{dc} \cos(\theta - \theta_i) \quad \text{and} \quad \mathcal{D} := \frac{\|v\| \cos(\theta_v - \theta_i)}{\mu_r v_{dc} \cos(\theta - \theta_i)}. \quad (4.35)$$

Note that \mathcal{D} takes value in $\mathbb{R}_{(0,1)}$ under normal operation. Furthermore, since the computation of \mathcal{D} in (4.35) is computationally cumbersome, thus, a mere knowledge of its lower bound might be the only available information on \mathcal{D} . Therefore, we assume that \mathcal{D} admits a constant lower bound \mathcal{D}_{\min} such that $0 < \mathcal{D}_{\min} \leq \mathcal{D} < 1$. In practice, \mathcal{D}_{\min}

is chosen by estimating \mathcal{D} for the worst-case scenario (i.e., the contingency that results in the most severe over-current behavior).

In the sequel, we treat \mathcal{D} in (4.34) (and accordingly \mathcal{D}_{\min}) as a fictitious disturbance that captures the influence of other states in the current magnitude dynamics (4.34). Consider a threshold current $i_{\text{th}} \in \mathbb{R}_{>0}$ that $\|i\|$ should not exceed. We aim to design a Δ_μ such that 1) the RHS of (4.34) is strictly negative for all $\|i\| > i_{\text{th}}$ and 2) ideally (i.e., not necessarily) $\Delta_\mu = 0$ for $\|i\| \leq i_{\text{th}}$. The design of Δ_μ in Proposition 3 is inspired by ideas from feedback linearization [111, Chapter 13] and disturbance decoupling techniques.

Proposition 3 (Current-limiting control). *Consider the current magnitude dynamics (4.34) and assume that $|\theta - \theta_i| < \pi/2$ and $\mathcal{D} \in \mathbb{R}_{[\mathcal{D}_{\min}, 1]}$. Define*

$$\Delta_\mu := \frac{(1 - \mathcal{D}_{\min}) e^{\beta(\|i\| - i_{\text{th}})}}{1 + (1 - \mathcal{D}_{\min}) (e^{\beta(\|i\| - i_{\text{th}})} - 1)}, \quad (4.36)$$

with $\beta \in \mathbb{R}_{>0}$, then $\|i\|$ is strictly decreasing in the state space characterized by $\|i\| > i_{\text{th}}$.

The proof is provided in Appendix 4.8. It remains to be shown that tampering with the current magnitude in (4.34) does not jeopardize the overall system stability. Proposition 4 gives an affirmative answer: under (4.12) and with current-limiting control (4.33) the desired closed-loop equilibrium of (4.7) remains locally asymptotically stable.

Proposition 4 (HAC and current-limiting control). *Consider the closed-loop system (4.7) where μ_r is replaced by the bounded μ in (4.33). Assume that the modified dynamics admits equilibria of the form (4.9) and condition (4.12) holds. Then the equilibrium x_s^* is locally asymptotically stable.*

Proof. By replicating the proof of Theorem 1 it follows that

$$\begin{aligned} \dot{\mathcal{V}}(\tilde{x}) \leq & - \left(\lambda\gamma - \frac{1}{\epsilon_1^2} - \frac{(\mu v_{\text{dc}}^*)^2}{\epsilon_2^2} \right) \sin^2 \frac{\tilde{\theta}}{2} - \frac{1}{\kappa} \tilde{i}_{\text{dc}}^2 - \left(g_{\text{dc}} - (\epsilon_1 \mu \|i^*\|)^2 \right) \tilde{v}_{\text{dc}}^2 - (r - \epsilon_2^2) \|\tilde{i}\|^2 \\ & - g \|\tilde{v}\|^2 - r_g \|\tilde{i}_g\|^2 + \lambda\eta \tilde{v}_{\text{dc}} \sin \frac{\tilde{\theta}}{2}. \end{aligned} \quad (4.37)$$

Since $\mu < \mu_r$, the RHS of (4.37) is smaller than the bound in (4.18), therefore $\dot{\mathcal{V}}(\tilde{x}) \leq -\tilde{\zeta}^\top \mathbf{Q} \tilde{\zeta}$ as in (4.18). Note that $\mathcal{V}(0_9) = 0$, $\mathcal{V}(\tilde{x}) > 0$ for all $\tilde{x} \neq 0_9$. By the proof of Theorem 2 if (4.12) holds, $\dot{\mathcal{V}}(\tilde{x}) < 0$ for all $\tilde{x} \neq 0_9$ in a sufficiently small neighborhood of the origin. The local asymptotic stability of x_s^* immediately follows from Lyapunov's direct method [111, Theorem 3.1] as in the proof of Proposition 1. \blacksquare

The assumptions in Proposition 3 (i.e., bounded angle and disturbance) are standard in small-signal stability and protection design. To further elaborate on the assumption

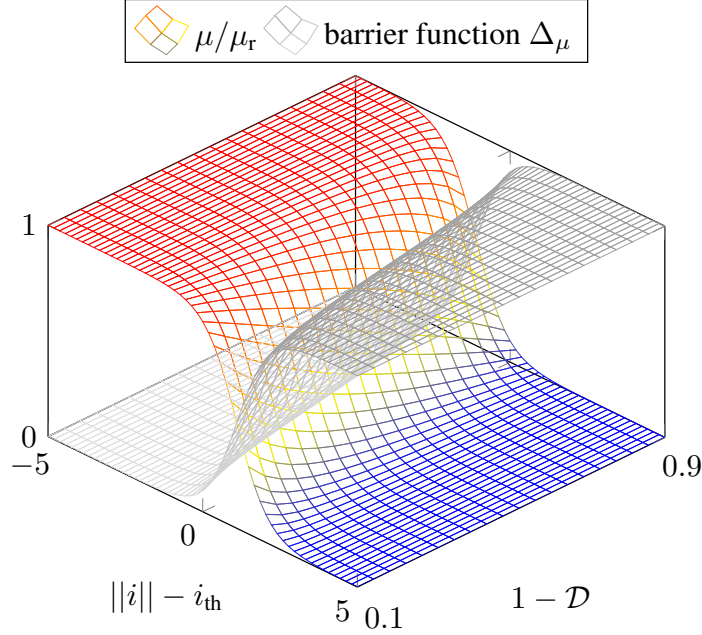


Figure 4.4: Illustration of normalized μ in (4.33) and Δ_μ in (4.36). For clarity of presentation, here $\beta = 2$ and $\mathcal{D} \in \mathbb{R}_{(0.1,0.9)}$. For small \mathcal{D} (i.e., a severe event) Δ_μ results in the modulation magnitude decay at a lower current compared to a scenario with large \mathcal{D} .

$\mathcal{D} \in \mathbb{R}_{[\mathcal{D}_{\min},1)}$, for now assume that $\mu = \mu_r$, then multiplying the nominator and denominator (4.35) with $\|i\|$ results in $\mathcal{D} = p_f/p_s$ (see Figure 4.1). Thus, $\mathcal{D} < 1$ means $p_f < p_s$ that highlights the power injection into the grid (while considering the filter loss). Last but not least, the case $\mathcal{D} < 0$ (while assuming normal operation i.e., $\mu = \mu_r$) means different power flow directions for p_f and p_s which is an extremely unlikely case. Moreover, the upper-bound on the disturbance feasible set i.e., $\mathcal{D} \in \mathbb{R}_{[\mathcal{D}_{\min},1)}$ can actually be relaxed i.e., $\mathcal{D} \in \mathbb{R}_{[\mathcal{D}_{\min},+\infty)}$. To make this idea clear for now assume that $\mu = \mu_r$, then multiplying the nominator and denominator (4.35) with $\|i\|$ gives $\mathcal{D} = p_f/p_s$ (see Figure 4.1). Thus, $\mathcal{D} > 1$ equals $p_f > p_s$ corresponding to the less critical scenario in which converter absorbs power from grid, e.g., after loss of load. Observe that in the relaxed case $-\infty < 1 - \mathcal{D} \leq 1 - \mathcal{D}_{\min}$. Subsequently, based on the proof of Proposition 3, $\Delta_\mu > 1 - \mathcal{D}_{\min}$ for all $\|i\| > i_{\text{th}}$. Thus, under (4.33) it is guaranteed that the RHS of (4.34) is strictly negative for $\mathcal{D} \in \mathbb{R}_{[\mathcal{D}_{\min},+\infty)}$ and $\|i\| > i_{\text{th}}$.

Remark 11 (Comments on the current-limiting control). *The function Δ_μ in (4.36) should be perceived as a barrier-type function (observe the influence of Δ_μ on μ in Figure 4.4) that smoothly reduces μ in (4.33) and thus the voltage magnitude $\|v_s\|$ (see Figure 4.1) when $\|i\| > i_{\text{th}}$; see Subsection 4.6.2 for a numerical verification. Next, parameter β controls the curvature and the exponential decay rate of μ in $\|i\|$. Note that $\Delta_\mu \rightarrow 0$ as $\beta \rightarrow +\infty$ for $\|i\| < i_{\text{th}}$ and for any \mathcal{D} , however large β results in an aggressive controller resembling a sign function. Last, the result of the Proposition 3 can be improved when augmenting \mathcal{D} with the dissipation term $r\|i\|$ in (4.34). Although, in practice $r\|i\|$ is*

negligible compared to the denominator of (4.35) (because of insignificant resistance).

Remark 12 (Comments on the existence of equilibria). *In order to verify the assumption of Proposition 3 i.e., the existence of equilibria, let us firstly highlight a side information about x_s^* in (4.9). Practically speaking, if x_s^* exists it is reasonably expected to be strictly contained within the state constraints. Next, one can always select β in (4.36) to be sufficiently large such that $\Delta_\mu \approx 0$ in $\mathcal{L}_{i_{th}} := \{x \in \mathbb{X} : \|i\| \ll i_{th}\}$ (due to the exponential decay of Δ_μ). Therefore, μ in (4.33) is approximately equal to μ_r in $\mathcal{L}_{i_{th}}$. Subsequently, this means in $\mathcal{L}_{i_{th}}$ the vector b that includes $m(\theta^*) = \mu\psi(\theta^*)$ and denotes the RHS of linear system of equations associated with (4.10d)-(4.10f) remains identical in the proof of the Theorem 1. Hence, the existence and uniqueness of the closed-loop equilibria of the form (4.9) that is contained in $\mathcal{L}_{i_{th}}$ is established with a similar interlacing argument. This coincides with our a priori knowledge of x_s^* . Next, if the assumptions of the Proposition 3 hold, it yields that $\mathcal{U}_{i_{th}} := \{x \in \mathbb{X} : \|i\| > i_{th}\}$ contains no disjoint or continuum of equilibrium points (by the strict monotonicity of $\|i\|$ in $\mathcal{U}_{i_{th}}$). The reader is referred to Subsection 4.6.2 for a case study confirming that during an event (e.g., an active fault condition), the control (4.33) steers the equilibrium into the set $\mathbb{X} - \{\mathcal{L}_{i_{th}} \cup \mathcal{U}_{i_{th}}\}$. Last, a complete characterization of the equilibria will be addressed in our future work.*

Finally, it is worth mentioning that the current-limiting control (4.33) is agnostic to the HAC. Hence, it is expected that (4.33) is practically compatible with different grid-forming controls in [1] (although possibly without any stability guarantees). The performance of control (4.33) for a three-phase-to-ground fault scenario is verified in the Subsection 4.6.2.

4.5 Implementation, robustness, practical aspects

In this section, we discuss the implementation of HAC that is followed by a formal robustness analysis, and highlight several practical aspects of the HAC. The forthcoming arguments showcase the gap between the theoretic proposals/analysis in Sections 4.2-4.4 and simulation test cases in Section 4.6.

4.5.1 The exact hybrid angle control implementation

The HAC in (4.5) relies on the relative angle measurement (4.4) that is not available in practice. Hence, we seek an alternative implementation based on the dc and ac measurements. The dc term in (4.5) is constructed by measuring the dc voltage; see Figure 4.1. Assume that the IB voltage is measured and transformed to $\alpha\beta$ -frame (see Appendix 4.9.2 for details). Then, an implicit IB angle measurement is obtained by $\psi(\theta_b) = v_{b,\alpha\beta}/\|v_{b,\alpha\beta}\|$. Further, $\psi(\theta_c)$ is internally available from the modulation signal

$m(\mu_r, \theta_c)$. Thus, by the means of (4.74) and (4.75), the relative angle measurement $\psi(\theta)$ is derived

$$\psi(\theta) = \left(\psi(\theta_c)^\top \psi(\theta_b), \psi(\theta_c)^\top J\psi(\theta_b) \right). \quad (4.38)$$

Given $\psi(\theta_r)$ (see Proposition 7) and $\psi(\theta)$ in (4.38) that respectively encapsulate the relative angle reference and measurement, Proposition 5 explains derivation of the ac term in (4.5).

Proposition 5 (Angle feedback implementation). *Given $\psi(\theta_r)$ and $\psi(\theta)$ derived in (4.38), if $|\theta - \theta_r| < \pi$ then*

$$\sin\left(\frac{\theta - \theta_r}{2}\right) = \frac{\psi(\theta_r)^\top J\psi(\theta)}{\sqrt{2(1 + \psi(\theta_r)^\top \psi(\theta))}}. \quad (4.39)$$

Proof. Consider $\psi(\theta_r)^\top J\psi(\theta)$ and apply (4.74):

$$\psi(\theta_r)^\top J\psi(\theta) = \sin\theta \cos\theta_r - \sin\theta_r \cos\theta = \sin\tilde{\theta} = 2 \sin\frac{\tilde{\theta}}{2} \cos\frac{\tilde{\theta}}{2},$$

where $\tilde{\theta} := \theta - \theta_r$. Next, consider $\psi(\theta_r)^\top \psi(\theta)$ and apply (4.75):

$$\psi(\theta_r)^\top \psi(\theta) = \cos\theta \cos\theta_r + \sin\theta \sin\theta_r = \cos\tilde{\theta}.$$

Subsequently, applying identity (4.73) results in

$$\sqrt{2(1 + \psi(\theta_r)^\top \psi(\theta))} = \sqrt{2(1 + \cos\tilde{\theta})} = 2 \left| \cos\frac{\tilde{\theta}}{2} \right|.$$

Hence, the RHS of (4.39) is equal to

$$\frac{\cos\frac{\tilde{\theta}}{2} \sin\frac{\tilde{\theta}}{2}}{\left| \cos\frac{\tilde{\theta}}{2} \right|} = \operatorname{sgn}\left(\cos\frac{\tilde{\theta}}{2}\right) \sin\frac{\tilde{\theta}}{2}. \quad (4.40)$$

Thus, if $|\tilde{\theta}| < \pi$ then $\operatorname{sgn}\left(\cos\left(\tilde{\theta}/2\right)\right) = 1$ and (4.39) holds. ■

The stability analysis under the assumption of Proposition 5 is analogous to the proof of Proposition 1. In this case, the sublevel set of the Lyapunov function must be chosen such that angle is constrained according to the bound in Proposition 5.

4.5.2 The alternative hybrid angle control implementation

The derivation in (4.38) and implementation (4.39) rely on the IB voltage measurement; see Figure 4.1. However, this information is typically not available. In what follows, we introduce an alternative implementation approach and show how certain properties still hold under such implementations.

Consider a pronounced timescale separation between the slow converter and fast line dynamics (see [45], [47] for details) that are written in a dq-frame that is aligned with the arbitrary angle θ_f and frequency ω_0 . Therefore, the line model takes a quasi-steady-state algebraic form, i.e.,

$$\ell_g \dot{i}_g = v - Z_g i_g - v_b \approx 0. \quad (4.41)$$

Hence, an IB voltage approximation is given by $v_b \approx \hat{v}_b := v - Z_g i_g$ based on (4.41). We remark that the line parameter Z_g might be subject to uncertainty, thus, one can employ an estimation technique, e.g., see [119]. Note that the timescale separation can be enforced by an appropriate choice of control parameters to slow down the converter dynamics w.r.t the line dynamics [113]. On the other hand, if Z_g is negligible, then $\hat{v}_b \approx v$ which is a weak albeit practically available approximation for v_b ; see Figure 4.1. For the sake of consistency with the discussions in Subsection 4.5.1, we transform \hat{v}_b to the $\alpha\beta$ -frame i.e., $\hat{v}_{b,\alpha\beta} = \mathbf{R}^{-1}(\theta_f) \hat{v}_b$.

Note that either due to the potential violation of the timescale separation assumption, parameter uncertainty, estimation error, or measurement noise $\hat{v}_{b,\alpha\beta}$ takes the form

$$\hat{v}_{b,\alpha\beta} = (v_r + e_v) \psi(\theta_b + e_\theta), \quad (4.42)$$

where e_v and e_θ denote the time-varying magnitude and phase angle errors. Deriving an approximation of $\psi(\theta)$ in (4.38) only requires $\psi(\theta_b + e_\theta)$ which is obtained by normalizing $\hat{v}_{b,\alpha\beta}$. The next subsection presents a formal robustness analysis.

4.5.3 Perturbed system dynamics and robustness analysis

Replacing $\psi(\theta)$ in (4.38) with $\psi(\theta_b + e_\theta)$ obtained from (4.42), applying Proposition 5, and substituting the resulting angle feedback in (4.7a) leads to the perturbed relative angle dynamics

$$\dot{\theta} = \eta(v_{dc} - v_{dc,r}) - \gamma \sin\left(\frac{\theta - \theta_r - e_\theta}{2}\right). \quad (4.43)$$

Hence, the perturbed system is described by (4.43) and (4.7b)-(4.7f).

Theorem 5 (Boundedness of the perturbed dynamics). *Consider the perturbed system consisting of (4.43) and (4.7b)-(4.7f). Assume that the time-varying disturbance e_θ is*

bounded by a constant angle \bar{e}_θ , i.e., $0 \leq |e_\theta| \leq \bar{e}_\theta < \pi$ such that

$$\sin \frac{\bar{e}_\theta}{2} < \frac{8\sigma_{\min}(\mathbf{Q})}{\gamma \max \left\{ \sigma_{\max}(\mathbf{P}), \frac{2}{\eta} \right\}}, \quad (4.44)$$

where $\sigma_{\min}(\mathbf{Q})$ and $\sigma_{\max}(\mathbf{P})$ denote the smallest and largest eigenvalue of \mathbf{Q} in (4.18) and \mathbf{P} in (4.15), respectively. Subsequently, if the following modified stability condition

$$\gamma \cos \frac{\bar{e}_\theta}{2} > \frac{\eta}{g_{\text{dc}}} + \frac{\eta (\mu_{\text{r}} \|i^*\|)^2}{g_{\text{dc}}} + \frac{\eta (\mu_{\text{r}} v_{\text{dc}}^*)^2}{r} \quad (4.45)$$

holds, then the solutions of perturbed system that are initially sufficiently close² to x_s^* in (4.9), are ultimately bounded.

Proof. Considering (4.43), the error dynamics are described by

$$\dot{\tilde{\theta}} = \eta \tilde{v}_{\text{dc}} - \gamma \sin \left(\frac{\tilde{\theta} - e_\theta}{2} \right), \quad (4.46)$$

and (4.14b)-(4.14f). Next, employing the identity (4.74) yields an expansion of the angle term in the RHS of (4.46), i.e.,

$$\sin \left(\frac{\tilde{\theta} - e_\theta}{2} \right) = \sin \frac{\tilde{\theta}}{2} \cos \frac{e_\theta}{2} - \cos \frac{\tilde{\theta}}{2} \sin \frac{e_\theta}{2}. \quad (4.47)$$

Substituting (4.47) in (4.46), adopting the Lyapunov function (4.15), and evaluating $\dot{\mathcal{V}}(\tilde{x})$ along the solutions of the perturbed dynamics (4.46) and (4.14b)-(4.14f) leads to $\dot{\mathcal{V}}(\tilde{x}) =$

$$\dot{\mathcal{H}}(\tilde{y}) + \lambda \eta \tilde{v}_{\text{dc}} \sin \frac{\tilde{\theta}}{2} - \lambda \gamma \left(\sin^2 \frac{\tilde{\theta}}{2} \cos \frac{e_\theta}{2} - \sin \frac{\tilde{\theta}}{2} \cos \frac{\tilde{\theta}}{2} \sin \frac{e_\theta}{2} \right).$$

Considering the assumption $0 \leq |e_\theta| \leq \bar{e}_\theta < \pi$, double-angle identity, and exploiting $|\sin \tilde{\theta}| \leq 1$ imply that $\dot{\mathcal{V}}(\tilde{x}) \leq$

$$\dot{\mathcal{H}}(\tilde{y}) + \lambda \eta \tilde{v}_{\text{dc}} \sin \frac{\tilde{\theta}}{2} - \lambda \gamma \sin^2 \frac{\tilde{\theta}}{2} \cos \frac{\bar{e}_\theta}{2} + \frac{\lambda \gamma}{2} \sin \frac{\bar{e}_\theta}{2}. \quad (4.48)$$

As in the proof of Theorem 2, if (4.45) holds, then for $\lambda = 2/\eta$,

$$\dot{\mathcal{H}}(\tilde{y}) + \lambda \eta \tilde{v}_{\text{dc}} \sin \frac{\tilde{\theta}}{2} - \lambda \gamma \sin^2 \frac{\tilde{\theta}}{2} \cos \frac{\bar{e}_\theta}{2} \leq -\tilde{\zeta}^\top \mathbf{Q} \tilde{\zeta} \leq -\sigma_{\min} \|\tilde{\zeta}\|^2.$$

²A quantitative bound on the initial conditions is contained in the proof.

Therefore, the bound on $\dot{\mathcal{V}}(\tilde{x})$ in (4.48) can be written as

$$\dot{\mathcal{V}}(\tilde{x}) \leq -\sigma_{\min}(\mathbf{Q})\|\tilde{\zeta}\|^2 + \frac{\gamma}{\eta} \sin \frac{\bar{e}_\theta}{2}. \quad (4.49)$$

Hence, if $\|\tilde{\zeta}\| \geq \epsilon_1 := \sqrt{\gamma \sin(\bar{e}_\theta/2) / (\eta \sigma_{\min}(\mathbf{Q}))}$ then $\dot{\mathcal{V}}(\tilde{x}) \leq 0$. Next, since $|\sin(\tilde{\theta}/2)| \leq |\tilde{\theta}|$, then $\|\tilde{\zeta}\| \geq \epsilon_1$ implies that $\|\tilde{x}\| \geq \epsilon_1$. To sum up, if $\|\tilde{\zeta}\| \geq \epsilon_1$ then $\|\tilde{x}\| \geq \epsilon_1$ and $\dot{\mathcal{V}}(\tilde{x}) \leq 0$.

To conclude the boundedness of $\|\tilde{x}\|$, one must ensure that the set defined by $\|\tilde{x}\| < \epsilon_1$ lies within a sublevel set of $\mathcal{V}(\tilde{x})$. Such a sublevel set is then forward invariant since $\mathcal{V}(\tilde{x})$ is non-increasing along its boundary, and thus the dynamics are ultimately bounded. Note that the angle term in (4.15) is upper-bounded i.e., $\mathcal{S}(\tilde{\theta}) \leq \tilde{\theta}^2/4$. Thus,

$$\mathcal{V}(\tilde{x}) \leq \sigma_{\max}(\mathbf{P})\|\tilde{y}\|^2 + \left(\frac{1}{2\eta}\right)\tilde{\theta}^2 \leq \alpha\|\tilde{x}\|^2 =: \mathcal{W}(\tilde{x}), \quad (4.50)$$

where $\alpha := \max\{\sigma_{\max}(\mathbf{P}), 1/(2\eta)\}$. Define the sublevel sets $\mathcal{L}_{k,\mathcal{W}(\tilde{x})} := \{\tilde{x} : \mathcal{W}(\tilde{x}) \leq k\}$ and $\mathcal{L}_{k,\mathcal{V}(\tilde{x})} := \{\tilde{x} : \mathcal{V}(\tilde{x}) \leq k\}$ where $k > 0$ is constant. Thus, (4.50) implies that $\mathcal{L}_{k,\mathcal{W}(\tilde{x})} \subset \mathcal{L}_{k,\mathcal{V}(\tilde{x})}$ for all k . Consider $k \leq \lambda \max(\mathcal{S}(\tilde{\theta})) = 8/\eta$ such that $\mathcal{L}_{k,\mathcal{V}(\tilde{x})}$ is a union of compact sets due to the radial unboundedness of $\mathcal{H}(\tilde{y})$ and the periodicity of $\mathcal{S}(\tilde{\theta})$. In this case, $\mathcal{L}_{k,\mathcal{V}(\tilde{x})}$ is characterized by $\|\tilde{x}\| \leq \epsilon_2 := \sqrt{8/(\eta\alpha)}$ and is contained in $\mathcal{L}_{k,\mathcal{V}(\tilde{x})}$. Finally, if $\epsilon_1 < \epsilon_2$ —that is satisfied under (4.44)—the set characterized by $\|\tilde{\zeta}\| < \epsilon_1$ is strictly contained in $\mathcal{L}_{k,\mathcal{V}(\tilde{x})}$. Thus, the solutions of (4.7) originating in $\mathcal{L}_{k,\mathcal{V}(\tilde{x})}$ (i.e., that are initially sufficiently close to x_s^*) are bounded and remain in $\mathcal{L}_{k,\mathcal{V}(\tilde{x})}$ for all time. \blacksquare

Remark 13 (Comments on the robustness analysis). *Theorem 5 establishes the boundedness of the perturbed dynamics (4.43) and (4.7b)-(4.7f) w.r.t bounded disturbances. The condition (4.45) reflects the effect of the disturbance, i.e., if $\bar{e}_\theta \rightarrow \pi$ and $\cos(\bar{e}_\theta/2) \rightarrow 0$, then γ must be increased to ensure the boundedness. Next, if e_θ in (4.42) is constant, with a similar analysis as in Theorem 1, one can prove that the equilibria in (4.9) are unique and uniformly shifted by e_θ . Thus, based on Theorem 3, it is possible to establish the AGAS of the shifted equilibrium point. Further, considering erroneous frequency or angle references i.e., when the IB frequency is not equal to ω_0 in (4.5) or $\theta_r \neq \theta_s^*$, an analogous analysis as in Theorem 5 delivers the boundedness result. Last, Theorem 5 strongly relies on Theorem 2. Hence, based on the global attractivity result in Theorem 4, one can derive the boundedness result for the perturbed converter-COI dynamics.*

4.5.4 HAC behavior and tuning recommendations

Grid-forming behavior

If the v_{dc} is sufficiently regulated to $v_{dc,r}$ by the control (4.3). Then, HAC (4.5) modifies the modulation angle θ_c such that $\theta = \angle v_s - \angle v_b$ (see Figure 4.1) settles at the reference θ_r . For instance, droop control (see Remark 7) achieves an implicit relative angle synchronization through active power control (i.e., $p \rightarrow p_r$ implies $\theta \rightarrow \theta_r$). Unlike PLL-based grid-following controls [33], HAC and droop control realize relative angle control without introducing auxiliary dynamics. Thus, they achieve a favorable control objective with minimal design complexity.

Tuning recommendations

HAC offers two degrees of freedom for optimal frequency tuning. The gain γ in (4.5) strongly influences the frequency timescale, thus, the impact of γ is similar to that of $d_{p-\omega}$ on droop control (see Remark 7). In contrast, η determines the extent of frequency dependency on the dc voltage. Further, for large enough η , HAC preserves the robustness of matching controls; see Subsection 4.6.3. Last, high γ/η ratios imply fast convergence, but as in the standard control approaches, we suggest avoiding aggressive tuning.

4.5.5 Intrinsic active power-frequency droop behavior

Consider the converter-COI system (4.25) that allows frequency droop which is hindered when considering the IB grid model. Recall that the existence of equilibria $\underline{\Omega}^*$ in (4.27) is guaranteed if $v_{dc}^* = v_{dc,r}$ and $\omega^* = \omega_0$. These assumptions can be met by appropriate choice of i_r and T_m in (4.25b) and (4.25g). For the sake of argument, assume that i_r and T_m are not consistent with the assumptions or the system is subject to disturbances, then the dc voltage and frequency converge to different equilibria $v_{dc,x}$ and ω_x . Hence, by (4.25a) the relative angle settles at a different equilibrium $\theta_x \neq \theta_r$. The drift from desired references is also reflected in other ac quantities.

In proposition 6, we presents a derivation of the droop slope that relates the active power and frequency at an arbitrary equilibrium. More precisely, for an operating frequency $\omega_x \in \mathbb{R}_{>0}$, the power-frequency linear sensitivity factor (i.e., *droop*) is defined by $d_{p-\omega} := \partial p_{net,x} / \partial \omega_x$; see Figure 4.1 and the Subsection 4.2.3 for the definition of $p_{net,x}$.

Proposition 6 (Power–frequency droop slope). *Consider system (4.25), the power-frequency droop slope at an equilibrium with frequency ω_x and dc voltage $v_{dc,x}$ equals*

$$d_{p-\omega} = - \left(\frac{2G_{dc}}{\eta^2} \right) \omega_x + \left(\frac{\eta i_0 + 2G_{dc} \beta_{\theta_x}}{\eta^2} \right), \quad (4.51)$$

where $G_{\text{dc}} := \kappa + g_{\text{dc}}$, $i_0 := i_r + \kappa v_{\text{dc},r}$, $\beta_{\theta_x} := \omega_0 - \eta v_{\text{dc},r} - \gamma \sin((\theta_x - \theta_r)/2)$, and θ_x is equilibrium relative angle.

The proof is given in Appendix 4.8.

4.5.6 Feedforward power and voltage set-points inclusion

As well as $\psi(\theta_r)$ in Proposition 5, the reference modulation magnitude μ_r (see Figure 4.1) is not explicitly available in practice. Rather power references $p_{g,r}$ and $q_{g,r}$ (associated with p_g and q_g in Figure 4.1) are specified. In what follows, we describe consistent definitions for $\psi(\theta_r)$ and μ_r that rely on the steady-state dc voltage, ac voltage magnitude, and power flows (see (4.64) and [45, Definition 2] for a definition).

Proposition 7 (Consistent definition of $\psi(\theta_r)$ and μ_r). *Given the voltages v_{dc}^* , $\|v^*\|$, and the references $p_{g,r}$ and $q_{g,r}$ consistent with the equilibrium values i.e., $p_{g,r} = p_g^*$ and $q_{g,r} = q_g^*$, the consistent references are defined by*

$$\psi(\theta_r) := \mathbf{R}(\delta)^\top \left(\hat{s}_g^{*\top} \begin{pmatrix} +1 & 0 \\ 0 & -1 \end{pmatrix} \hat{s}_f^*, \hat{s}_g^{*\top} \begin{pmatrix} 0 & +1 \\ +1 & 0 \end{pmatrix} \hat{s}_f^* \right), \quad (4.52)$$

$$\mu_r := \frac{\sqrt{(p_f^{*2} + q_f^{*2}) (r^2 + (\ell\omega_0)^2)}}{v_{\text{dc}}^* \|v^*\|}, \quad (4.53)$$

with $\delta := \tan^{-1}(\ell_g\omega_0/r_g) + \tan^{-1}(\ell\omega_0/r)$, $s_g^* := (p_g^*, q_g^*)$ and $\hat{s}_g^* := s_g^*/\|s_g^*\|$, $s_f^* := (p_f^*, q_f^*)$ and $\hat{s}_f^* := s_f^*/\|s_f^*\|$.

The proof is given in Appendix 4.8. Observe that the consistent reference specifications (4.52)-(4.53) can conceptually also be used as feedforward ac voltage and power control. Figure 4.5 represents the overall block diagram of the feedback controls (4.3), (4.5), and the feedforward controls (4.52) and (4.53).

4.6 Numerical examples

We firstly consider the system (4.25) with parameters adopted from [1]; also see Table 4.1. We explore the impact of HAC tuning on frequency behavior and verify the performance of current-limiting control (4.33). Next, we present a system-level case study that highlights the merits of HAC compared to its precursors i.e., droop and matching controls. For simplicity of exposition the converter model includes an average dc-ac conversion stage. However, similar behavior is observed when considering a switching converter model. For the latter, low-pass filtering the measurements is recommended for safeguarding the control against high-frequency harmonics [51]. The case study models

Table 4.1: The parameters of converter-COI system (4.25).

Converter model parameters and nominal values		
$S_{r,c} = 0.5$ [MVA]	$v_r = 816.4$ [V]	$\omega_0 = 2\pi 50$ [rad/s]
$c_{dc} = 8$ [mF]	$\ell = \ell_g = 0.2$ [mH]	$c = 0.3$ [mF]
$r = r_g = 1$ [m Ω]	$g_{dc} = g = 1$ [m Ω^{-1}]	$\tau_{dc} = 50$ [ms]
Center of inertia model parameters		
$S_{r,g} = 5$ [MVA]	$H = 5$ [s]	$D = 100$
Control parameters and reference values		
$\theta_r = 0$	$i_{dc,r} = 0$	$v_{dc,r} = 3v_r$
$\eta = 0.01$	$\gamma = 10000$	$\kappa = 2$
$\mu_r = 2v_r/v_{dc,r}$	$b = v_r/\omega_0$	$T_m = D\omega_0$

in MATLAB/Simulink environment are available [71]. We remark that the phase portrait of (4.7) that verifies the results of Theorem 2 is presented in the preliminary version of this work [8].

4.6.1 The influence of HAC Tuning on frequency performance

Consider the converter-COI system (4.25) with $\eta = \omega_0/v_{dc,r} = 0.128$ which renders the dc term in HAC identical to that of the standard matching control (see Remark 7 and [65]). Initially, it is assumed that $\gamma = 0$. We select $\kappa = 5$ in (4.25b) and $D = 300$ (4.25g) such that the converter and COI grid model exhibit equal post-contingency load-sharing. In this example, the contingency is an active power load disturbance that is sized to $0.5S_{r,c}$ (where $S_{r,c}$ denotes the converter power rating) and is modeled by connecting a constant conductance g_{load} in parallel connection with the filter capacitance c in Figure 4.1. Figure 4.6 illustrates the post-contingency evolution of COI frequency for different γ values. Figure 4.6 suggests that HAC by the means of its angle feedback in (4.5) improves the frequency response of the standard matching control [65] that is identical to (4.5) with $\eta = \omega_0/v_{dc,r}$ and $\gamma = 0$. This improvement is more tangible in the rate of change of frequency (RoCoF) performance metric $\hat{\omega}$ [70, Section III-A][1, Figure 10] corresponding to the COI frequency ω i.e.,

$$|\hat{\omega}| := \frac{|\omega(t_0 + \Delta t) - \omega(t_0)|}{\Delta t}, \quad (4.54)$$

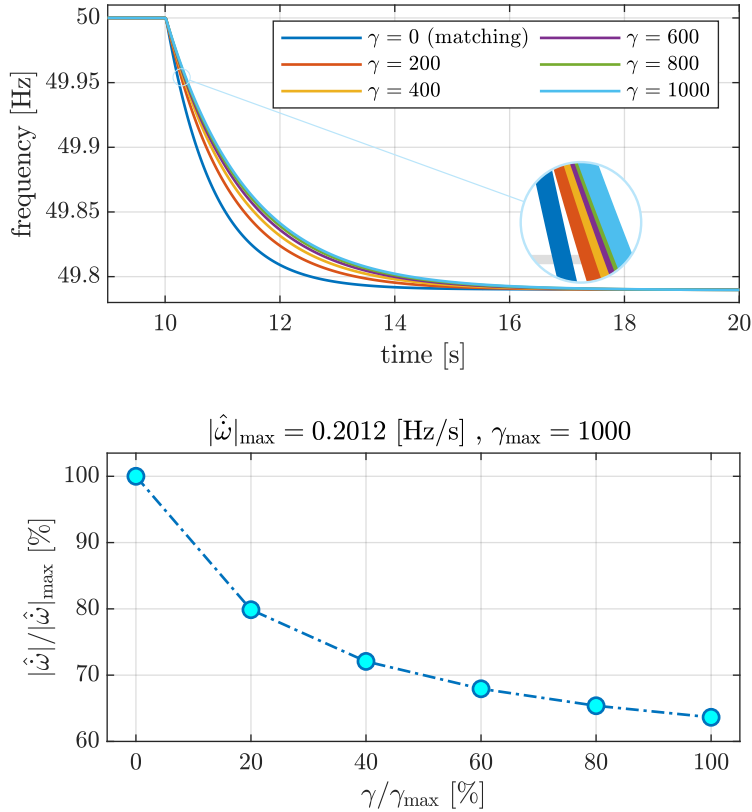


Figure 4.6: Post-event frequency of the system (4.25) under different HAC tuning (top), corresponding normalized RoCoF values (bottom).

where t_0 denotes the time when the disturbance is applied and Δt denotes the approximation time horizon. Figure 4.6 shows that the RoCoF (with $\Delta t = 100$ [ms]) clearly decreases as γ increases. In other word, the angle feedback of the HAC (4.5) serves as a remedy for the suboptimal matching control RoCoF performance (see [1, Figure 11] for a comparison). The pure matching control senses the load disturbance (and accordingly modifies the angle dynamics) once its aftermath is propagated to the dc voltage dynamics via the filter current in (4.25b). However, HAC with its multi-variable dc-ac nature reacts to the disturbance on a slightly faster timescale that, in our opinion, explains its enhanced frequency response.

4.6.2 Current-limiting control performance

Consider the system in the previous example combined with the current-limiting control (4.33) with Δ_μ as in Proposition 3 where $\beta = 0.25$, $i_{\text{th}} = 1.25$ per-unit (pu), and $\mathcal{D}_{\min} = 0.01$ (see Remark 11). We consider a low-impedance three-phase-to-ground fault (see [62, Section 3.7] on fault modeling) at the filter capacitance node in Figure 4.1 driving $\|v\| \rightarrow 0^+$ thus $\mathcal{D} \rightarrow 0^+$ and $\Delta_\mu \rightarrow 1^-$. Figure 4.7 shows that the current-

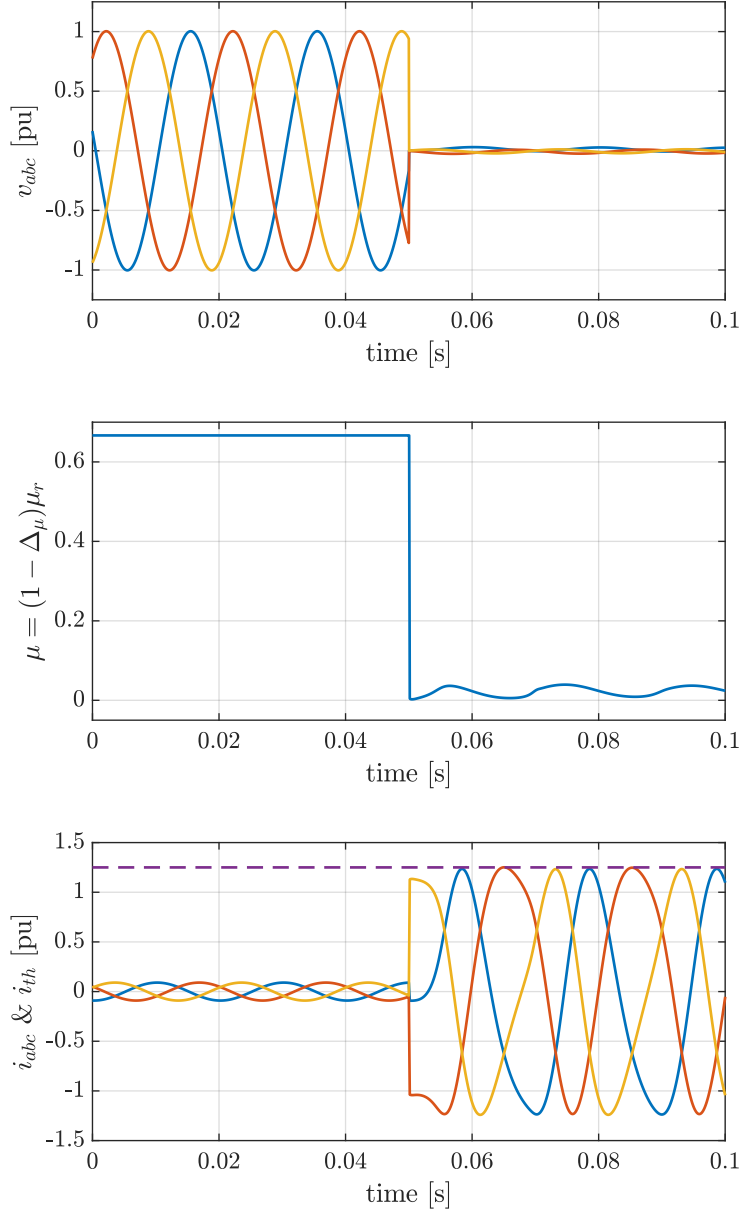


Figure 4.7: Current-limiting control performance w.r.t a three-phase-to-ground fault; output/fault node voltage (top), modulation magnitude (middle), and filter current (bottom).

limiting control (4.33) limits the post-fault current magnitude $\|i\|$ to i_{th} . This is obtained by an immediate reduction of μ and subsequently $\|v_s\| = \mu|v_{dc}|$ (note that v_{dc} is stiffly regulated to $v_{dc,r}$ by (4.3)). In addition, although Δ_μ in (4.36) is strongly nonlinear in $\|i\|$, it is an algebraic controller and modifies the modulation magnitude on the same timescale as that of the filter current. As a result, we do not see a sudden spike in the current waveforms shown in Figure 4.7 (as in e.g., [70, Figure 6]). Last, same limiting performance is observed when considering a load-induced over-current scenario.

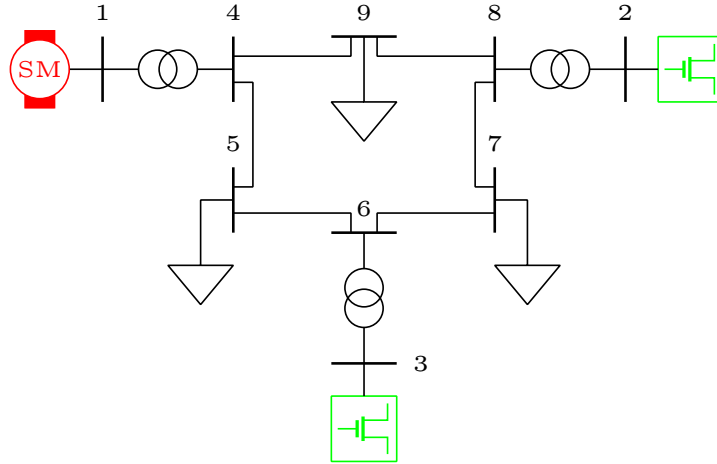


Figure 4.8: IEEE 9-bus test system including SM and power converters.

4.6.3 Comparative system-level performance evaluation

We consider the IEEE 9-bus system model that includes a mixture of the SM and power converters as in the Figure 4.8. The reader is referred to [1, Section II] for the benchmark description and [71] for the case study models. to begin with, we consider three different network configurations; one SM and two converters (as in Figure 4.8) in which the converters are identical and controlled by either droop control [1, Subsection III-C], matching control [1, Subsection III-E], or HAC. In all configurations, the governor and converter controls are tuned such that the generation units exhibit equal load-sharing (i.e., the droop gains are identical); see [1, Appendix]. The SM and converters equally supply the total network load of 2.25 pu (i.e., 75 megawatts (MW) by each unit) that is distributed across the system (resting at a stable equilibrium at $t = 0$ [s]). We resort to the SM mechanical and internal converter frequencies to avoid using an explicit measurement device (that introduces excess delays and might partially distort the intrinsic frequency dynamics); see [1, Section IV] for further details. The dc energy source models are constrained via a saturation function that represents the current limits of such systems (see [1, Subsection II-A][105]). Last, we remark that the HAC implementation in the IEEE 9-bus system only relies on its dc and output ac voltage.

Transient frequency performance

Figure 4.9 illustrates the SM frequency following an identical 0.75 pu load-disturbance (defined such that the converters do not exceed their current limits) in the aforementioned network configurations. Figure 4.9 suggests that when the converters are controlled by an ac-based technique e.g., droop control or HAC, the SM experiences significantly smaller RoCoF values. In contrast, when the converters are controlled by the dc-based matching control, the SM's RoCoF performance is relatively weak. This finding verifies our first

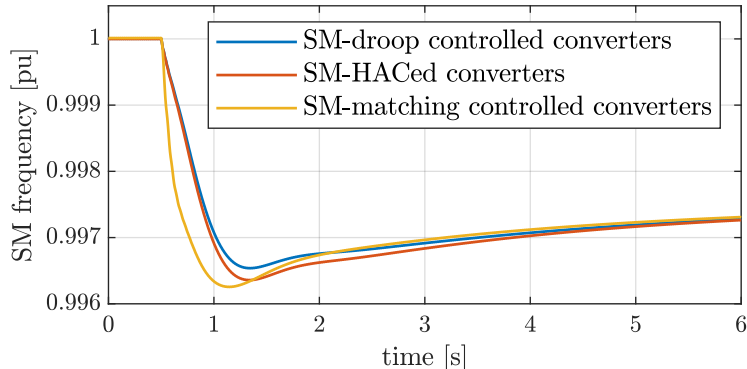


Figure 4.9: Post-disturbance SM frequency evolution in IEEE 9-bus test system with power converters under different control strategies.

hypothesis (see Remark 7) i.e., HAC enhances the frequency stability (similar to other ac-based techniques); see [1, Subsection IV-C] for a similar observation.

Response to a large load disturbance

In this scenario, the load-disturbance is increased to 0.9 pu such that the converters' post-disturbance transient currents exceed their protection limits i.e., demanding excessive current from the dc sources (see [1, Subsection IV-D] for further details). Figure 4.10 illustrates the post-disturbance SM and converters' frequencies. Observe that the pure ac-based droop controlled converters exhibits instability and loss of synchronism that subsequently destabilize the SM. This behavior has also been reported in [1], [105]. In contrast, the pure dc-based matching control and HAC exhibit robustness and remain stable under active dc current constraints. This is underpinned by an implicit mode-switching behavior from grid-forming to grid-following; see the frequency re-synchronization at $t \approx 1$ and $t \approx 1.5$ [s] respectively for matching controlled and HACed converters. This is primarily due to the inclusion of a dc term in the converter frequency. Thus, verifying our second hypothesis (see Remark 7) i.e., HAC inherits the robustness of matching control. Note that the robustness of matching control in presence of the state constraints is formally investigated in [105] and further explored in [55]. Last but not least, compared to the matching control, the converters' frequency oscillations are significantly reduced under HAC resulting in better frequency nadir performance (see [1, Figure 10]). We close by referring the reader to [5] for an extensive numerical exploration of the HAC system-level performance and [4] for a theoretic investigation of the HAC applicability and scalability in hybrid ac/dc power grids.

4.7 Summary and outlook

In this paper, we introduced a new grid-forming control termed hybrid angle control (HAC). We established the existence, uniqueness, and almost global stability of the closed-loop equilibria under mild parametric conditions. We extended the stability guarantees of HAC by considering grid dynamics and synthesized a new current-limiting control to account for the converter's safety constraints. Moreover, practical imple-

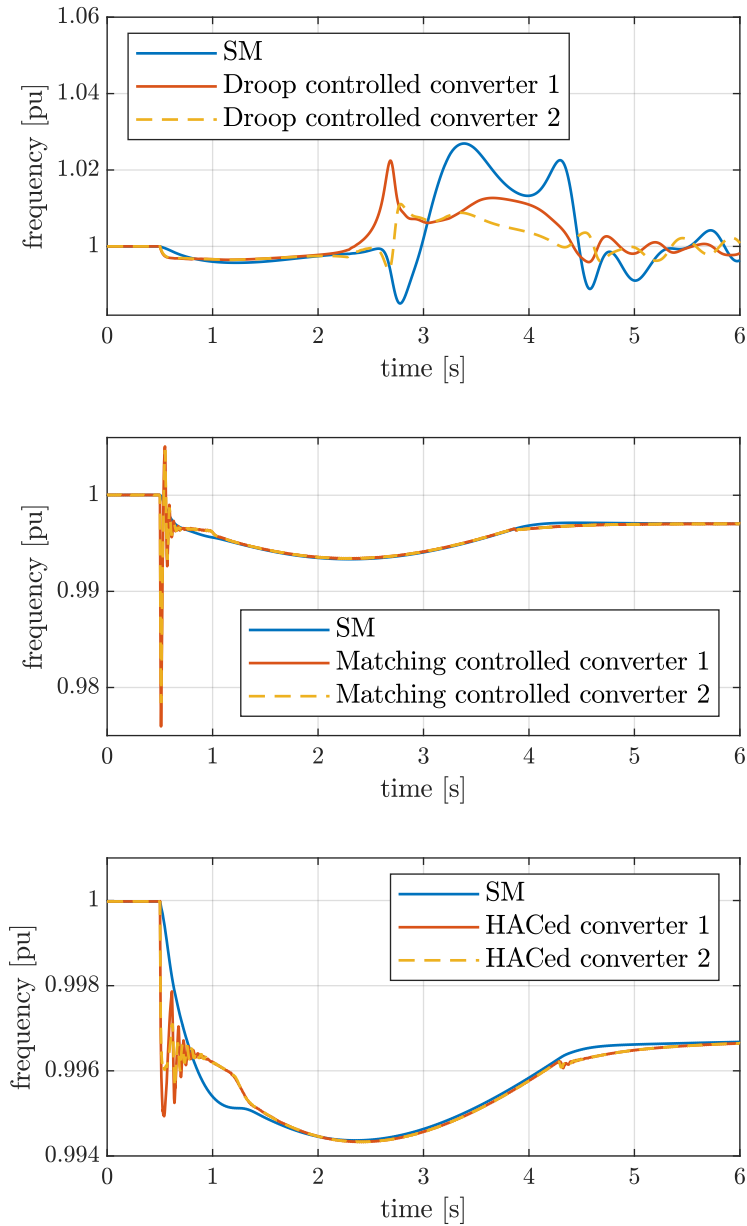


Figure 4.10: SM and converters' frequency evolution (for three different SM-converter pairs) following a large load disturbance that stresses the converters beyond their current limits.

mentations of HAC and their robustness analysis, the intrinsic power-frequency droop behavior, and a complementary feedforward ac voltage and power control were discussed. Last, the performance of controls (4.5) and (4.36) was investigated with numerical examples. Avenues for future work include: 1) stability analysis of the HAC constructed based on the output voltage, 2) stability and performance analysis in interconnected multi-converter systems, 3) the inclusion of robust high-level power controls, 4) the performance of current-limiting control w.r.t asymmetric faults and further practical explorations, and 5) concept validation on hardware setups.

4.8 Appendix A: proof of the technical results

Proof of Proposition 1. Consider the error dynamics (4.14) and the Lyapunov function (4.15) that satisfies $\mathcal{V}(0_g) = 0$ and $\mathcal{V}(\tilde{x}) > 0$ for all $\tilde{x} \neq 0_g$. Furthermore, if (4.12) holds, $\dot{\mathcal{V}}(\tilde{x}) < 0$ for all $\tilde{x} \neq 0_g$ in a sufficiently small neighborhood of the origin. Consider a c -sublevel set of $\mathcal{V}(\tilde{x})$ i.e., $\mathcal{L}_c := \{\tilde{x} \in \mathbb{X} : \mathcal{V}(\tilde{x}) \leq c, c \in \mathbb{R}_{>0}\}$, which is forward invariant under the flow (4.7) since $\dot{\mathcal{V}}(\tilde{x}) \leq 0$. Take c to be sufficiently small such that the origin is the only equilibrium in \mathcal{L}_c (recall that the equilibria in (4.9) are disjoint). Thus, by Lyapunov's direct method [111, Theorem 3.1] the origin is a locally asymptotically stable for (4.14). ■

Proof of Proposition 2. Consider the shorthand $\dot{x} = f(x)$ for (4.7) and let $J_f(x)$ be the Jacobian of $f(x)$, then $\det(J_f(x)) = \det(H(x))/\tau_{dc}c_{dc}(\ell c \ell_g)^2$ where

$$H(x) = \begin{pmatrix} H_{11} & H_{12} \\ H_{21} & H_{22} \end{pmatrix} := \left(\begin{array}{cc|cccc} -\frac{\gamma}{2} \cos\left(\frac{\theta - \theta_r}{2}\right) & 0 & \eta & 0_2^\top & 0_2^\top & 0_2^\top \\ 0 & -1 & -\kappa & 0_2^\top & 0_2^\top & 0_2^\top \\ \hline -\frac{\partial m(\theta)}{\partial \theta} i & 1 & -g_{dc} & -m(\theta)^\top & 0_2^\top & 0_2^\top \\ v_{dc} \frac{\partial m(\theta)}{\partial \theta} & 0_2 & m(\theta) & -Z & -I & 0_{2 \times 2} \\ 0_2 & 0_2 & 0_2 & I & -Y & -I \\ 0_2 & 0_2 & 0_2 & 0_{2 \times 2} & I & -Z_g \end{array} \right).$$

Evaluating H_{11} at x_u^* in (4.9) results in $H_{11} = \begin{pmatrix} \gamma/2 & 0 \\ 0 & -1 \end{pmatrix}$ which is invertible for $\gamma > 0$. Thus, the overall determinant is

$$\det(H(x_u^*)) = \det(H_{11}) \det(H_{22} - H_{21}H_{11}^{-1}H_{12}). \quad (4.55)$$

Define

$$K := H_{22} - H_{21}H_{11}^{-1}H_{12} = \begin{pmatrix} -G_{\text{dc}} + \left(\frac{2\eta}{\gamma}\right) \frac{\partial m(\theta)}{\partial \theta} \Big|_{\theta=\theta_r}^\top i^* & -m(\theta_r)^\top & 0_2^\top & 0_2^\top \\ m(\theta_r) - \left(\frac{2\eta v_{\text{dc}}^*}{\gamma}\right) \frac{\partial m(\theta)}{\partial \theta} \Big|_{\theta=\theta_r} & -Z & -I & 0_{2 \times 2} \\ 0_2 & I & -Y & -I \\ 0_2 & 0_{2 \times 2} & I & -Z_g \end{pmatrix}$$

where $G_{\text{dc}} := g_{\text{dc}} + \kappa$ and consider the symmetric part of K i.e., $K_S := (1/2)(K + K^\top)$. Next, we show that $K_S \prec 0$ under (4.12). Schur complements analysis yields that $K_S \prec 0$ iff

$$\frac{2\eta\mu_r\gamma \frac{\partial \psi(\theta)}{\partial \theta} \Big|_{\theta=\theta_r}^\top i^*}{G_{\text{dc}}} + \frac{(\eta\mu_r v_{\text{dc}}^*)^2}{rG_{\text{dc}}} < \gamma^2. \quad (4.56)$$

We apply the identity (4.71) to the first term on the RHS of (4.56)

$$2\mu_r \frac{\partial \psi(\theta)}{\partial \theta} \Big|_{\theta=\theta_r}^\top i^* \leq \left\| \frac{\partial \psi(\theta)}{\partial \theta} \Big|_{\theta=\theta_r} \right\|^2 + (\mu_r \|i^*\|)^2 = 1 + (\mu_r \|i^*\|)^2. \quad (4.57)$$

Subsequently, taking into account the bound in (4.57), if

$$\frac{\eta\gamma}{G_{\text{dc}}} + \frac{\eta\gamma(\mu_r \|i^*\|)^2}{G_{\text{dc}}} + \frac{(\eta\mu_r v_{\text{dc}}^*)^2}{rG_{\text{dc}}} < \gamma^2, \quad (4.58)$$

then (4.56) is satisfied. Next, dividing (4.58) by γ results in

$$\frac{\eta}{\bar{\beta}g_{\text{dc}}} + \frac{\eta(\mu_r \|i^*\|)^2}{\bar{\beta}g_{\text{dc}}} + \frac{\eta(\mu_r v_{\text{dc}}^*)^2}{\bar{\alpha}r} < \gamma \quad (4.59)$$

where $\bar{\alpha} := \gamma G_{\text{dc}}/\eta$ and $\bar{\beta} := G_{\text{dc}}/g_{\text{dc}}$. Since $\bar{\beta} > 1$ by definition (recall that $G_{\text{dc}} = \kappa + g_{\text{dc}}$), if $\bar{\alpha} > 1$ then the LHS of (4.59) is strictly smaller than the LHS of (4.12). That means if $\bar{\alpha} > 1$ then (4.12) implies (4.59). To show that $\bar{\alpha} > 1$ that equals $\gamma > \eta/\bar{\beta}g_{\text{dc}}$ consider that if (4.12) holds then $\gamma > \eta/g_{\text{dc}} > \eta/\bar{\beta}g_{\text{dc}}$ hence $\bar{\alpha} > 1$.

To sum up, under (4.12), $K_S \prec 0$. Thus, K has all eigenvalues in the open left half-plane. Since $\dim(K) = 7$, then $\det(K) < 0$ and by (4.55) $\det(H(x_u^*)) = -\gamma \det(K)/2 > 0$ which means $\det(J_f(x_u^*)) > 0$. Since $\dim(J_f(x)) = 9$, then $J_f(x_u^*)$ has at least one positive real eigenvalue. Instability of x_u^* follows from Lyapunov's indirect method [111, Theorem 4.7] and its global inset has zero Lebesgue measure invoking [120, Proposition 11]. ■

Proof of Theorem 4. Define the error coordinates as $\tilde{x} := \underline{x} - \underline{x}_s^*$. The error dynamics

associated with (4.25) are described by

$$\begin{aligned}
\dot{\tilde{\theta}} &= \eta \tilde{v}_{\text{dc}} - \gamma \sin \frac{\tilde{\theta}}{2} - \tilde{\omega}, \\
\tau_{\text{dc}} \dot{\tilde{i}}_{\text{dc}} &= -\kappa \tilde{v}_{\text{dc}} - \tilde{i}_{\text{dc}}, \\
c_{\text{dc}} \dot{\tilde{v}}_{\text{dc}} &= \tilde{i}_{\text{dc}} - g_{\text{dc}} \tilde{v}_{\text{dc}} - \mu_{\text{r}} \underline{e}_{\psi}^{\top} i^{\star} - m(\mu_{\text{r}}, \underline{\theta})^{\top} \tilde{i} \\
\dot{\tilde{i}} &= \tilde{v}_{\text{dc}} m(\mu_{\text{r}}, \underline{\theta}) + \mu_{\text{r}} v_{\text{dc}}^{\star} \underline{e}_{\psi} - r \tilde{i} - \ell \omega \tilde{J} \tilde{i} - \ell \tilde{\omega} \tilde{J} i^{\star} - \tilde{v}, \\
\dot{\tilde{v}} &= \tilde{i} - g \tilde{v} - c \omega \tilde{J} \tilde{v} - c \tilde{\omega} \tilde{J} v^{\star} - \tilde{i}_{\text{g}}, \\
\dot{\tilde{i}}_{\text{g}} &= \tilde{v} - r_{\text{g}} \tilde{i}_{\text{g}} - \ell_{\text{g}} \omega \tilde{J} \tilde{i}_{\text{g}} - \ell_{\text{g}} \tilde{\omega} \tilde{J} i_{\text{g}}^{\star} - b e_1 \tilde{\omega}, \\
\dot{\tilde{\omega}} &= -D \tilde{\omega} + b e_1^{\top} \tilde{i}_{\text{g}}.
\end{aligned}$$

where $\underline{e}_{\psi} := \psi(\underline{\theta}) - \psi(\underline{\theta}_1^{\star})$. Define $\tilde{\underline{y}} := (\tilde{i}_{\text{dc}}, \tilde{v}_{\text{dc}}, \tilde{\omega}, \tilde{i}, \tilde{v}, \tilde{i}_{\text{g}}) \in \mathbb{R}^9$, and consider the following Lyapunov function

$$\underline{\mathcal{V}}(\tilde{\underline{x}}) := \frac{1}{2} \left(\tilde{\underline{y}}^{\top} \underline{\mathbf{P}} \tilde{\underline{y}} \right) + 2\lambda \left(1 - \cos \frac{\tilde{\theta}}{2} \right)$$

where $\underline{\mathbf{P}} := \text{blkdiag}(\tau_{\text{dc}}/\kappa, c_{\text{dc}}, J, \ell \mathbf{I}, c \mathbf{I}, \ell_{\text{g}} \mathbf{I})$ and $\lambda \in \mathbb{R}_{>0}$. Evaluating $\dot{\underline{\mathcal{V}}}(\tilde{\underline{x}})$ along the error trajectories yields

$$\begin{aligned}
\dot{\underline{\mathcal{V}}}(\tilde{\underline{x}}) &= -\frac{1}{\kappa} \tilde{i}_{\text{dc}}^2 - g_{\text{dc}} \tilde{v}_{\text{dc}}^2 - D \tilde{\omega}^2 - r \|\tilde{i}\|^2 - g \|\tilde{v}\|^2 - r_{\text{g}} \|\tilde{i}_{\text{g}}\|^2 - \lambda \gamma \sin^2 \frac{\tilde{\theta}}{2} + \lambda (\eta \tilde{v}_{\text{dc}} - \tilde{\omega}) \sin \frac{\tilde{\theta}}{2} \\
&\quad - \tilde{i}^{\top} (\ell \tilde{J} i^{\star}) \tilde{\omega} - \tilde{v}^{\top} (c \tilde{J} v^{\star}) \tilde{\omega} - \tilde{i}_{\text{g}}^{\top} (\ell_{\text{g}} \tilde{J} i_{\text{g}}^{\star}) \tilde{\omega} - \mu_{\text{r}} \underline{e}_{\psi}^{\top} i^{\star} \tilde{v}_{\text{dc}} + \mu_{\text{r}} v_{\text{dc}}^{\star} \tilde{i}^{\top} \underline{e}_{\psi}. \tag{4.61}
\end{aligned}$$

From the proof of Theorem 2 recall that $\|\underline{e}_{\psi}\|^2 = 4 \sin^2(\tilde{\theta}/2)$ and apply (4.71) to the cross-terms in (4.61) that depend on v_{dc}^{\star} , i^{\star} , v^{\star} , and i_{g}^{\star} . Then $\dot{\underline{\mathcal{V}}}(\tilde{\underline{x}})$ is upper-bounded by

$$\begin{aligned}
\dot{\underline{\mathcal{V}}}(\tilde{\underline{x}}) &\leq -\frac{1}{\kappa} \tilde{i}_{\text{dc}}^2 - \left(g_{\text{dc}} - (\underline{\epsilon}_1 \mu_{\text{r}} \|i^{\star}\|)^2 \right) \tilde{v}_{\text{dc}}^2 - (D - \underline{\alpha}) \tilde{\omega}^2 \\
&\quad - (r - \underline{\epsilon}_2^2 - \underline{\epsilon}_3^2) \|\tilde{i}\|^2 - (g - \underline{\epsilon}_4^2) \|\tilde{v}\|^2 - (r_{\text{g}} - \underline{\epsilon}_5^2) \|\tilde{i}_{\text{g}}\|^2 \\
&\quad - \left(\gamma \lambda - \frac{1}{\underline{\epsilon}_1^2} - \frac{(\mu_{\text{r}} v_{\text{dc}}^{\star})^2}{\underline{\epsilon}_2^2} \right) \sin^2 \frac{\tilde{\theta}}{2} - \lambda \tilde{\omega} \sin \frac{\tilde{\theta}}{2} + \lambda \eta \tilde{v}_{\text{dc}} \sin \frac{\tilde{\theta}}{2} \tag{4.62}
\end{aligned}$$

where $\underline{\epsilon}_j \in \mathbb{R}_{>0}$ for $j = 1, \dots, 5$ and

$$\underline{\alpha} := \left(\frac{\ell \|i^{\star}\|}{2 \underline{\epsilon}_3} \right)^2 + \left(\frac{c \|v^{\star}\|}{2 \underline{\epsilon}_4} \right)^2 + \left(\frac{\ell_{\text{g}} \|i_{\text{g}}^{\star}\|}{2 \underline{\epsilon}_5} \right)^2.$$

Defining $\underline{\zeta} := \left(\sin(\tilde{\theta}/2), \tilde{\underline{y}} \right)$ the bound in (4.62) takes the quadratic form i.e., $\dot{\underline{\mathcal{V}}}(\tilde{\underline{x}}) \leq$

$-\underline{\zeta}^\top \underline{Q} \underline{\zeta}$, where $\underline{Q} = \text{blkdiag}(\underline{Q}_{11}, \underline{Q}_{22})$ with

$$\underline{Q}_{11} := \begin{pmatrix} \gamma \underline{\lambda} - \frac{1}{\underline{\epsilon}_1^2} - \frac{(\mu_r v_{\text{dc}}^*)^2}{\underline{\epsilon}_2^2} & 0 & -\frac{\eta \underline{\lambda}}{2} & \frac{\underline{\lambda}}{2} \\ 0 & \frac{1}{\kappa} & 0 & 0 \\ -\frac{\eta \underline{\lambda}}{2} & 0 & g_{\text{dc}} - (\underline{\epsilon}_1 \mu_r \|i^*\|)^2 & 0 \\ \frac{\underline{\lambda}}{2} & 0 & 0 & D - \underline{\alpha} \end{pmatrix},$$

and $\underline{Q}_{22} := \text{blkdiag}((r - \underline{\epsilon}_2^2 - \underline{\epsilon}_3^2)\mathbf{I}, (g - \underline{\epsilon}_4^2)\mathbf{I}, (r_g - \underline{\epsilon}_5^2)\mathbf{I})$. Choosing the free parameters as $\underline{\lambda} = 2/\eta$, $\underline{\epsilon}_1 = \sqrt{g_{\text{dc}}}/(\sqrt{2}\mu_r\|i^*\|)$, $\underline{\epsilon}_2 = \sqrt{r/2}$, $\underline{\epsilon}_3 = \sqrt{r}/2$, $\underline{\epsilon}_4 = \sqrt{g}/2$ and $\underline{\epsilon}_5 = \sqrt{r_g}/2$ renders $\underline{Q}_{22} \succ 0$. Under this favorable choice of parameters, $\underline{Q}_{11} \succ 0$ if and only if (4.28) is satisfied. Thus, $\underline{Q} \succ 0$ and $\dot{\mathcal{V}}(\tilde{x}) < 0$ for all $\underline{\zeta} \neq 0_{10}$. Following the LaSalle's invariance argument in the proof of Theorem 2, it is straightforward to show that the trajectories of (4.60) globally converge to the largest invariant set contained in $\underline{\Omega} := \{\tilde{x} \in \underline{\mathbb{X}} : \dot{\mathcal{V}}(\tilde{x}) = 0\}$ and $\underline{\Omega} = \underline{\Omega}^*$. ■

Proof of Proposition 3. Let $\mathcal{C} := 1 - \mathcal{D}_{\min}$ where $0 < \mathcal{C} < 1$, and observe that

$$\lim_{\|i\| \rightarrow i_{\text{th}}^+} \Delta_\mu = \mathcal{C} \quad \text{and} \quad \lim_{\|i\| \rightarrow +\infty} \Delta_\mu = 1.$$

Moreover, Δ_μ is strictly increasing i.e.,

$$\frac{\partial \Delta_\mu}{\partial \|i\|} = \frac{\beta \mathcal{C} (1 - \mathcal{C}) e^{\beta(\|i\| - i_{\text{th}})}}{\left(1 + \mathcal{C} (e^{\beta(\|i\| - i_{\text{th}})} - 1)\right)^2} > 0, \quad (4.63)$$

Since Δ_μ is strictly monotone and continuous with finite limits, it is bounded by its left and right limits i.e., $\Delta_\mu \in (\mathcal{C}, 1)$ for all $\|i\| > i_{\text{th}}$. In addition, since $\mathcal{D}_{\min} \leq \mathcal{D}$ and due to the monotonicity of Δ_μ , we establish that $1 - \mathcal{D} \leq \mathcal{C} < \Delta_\mu$ for all $\|i\| > i_{\text{th}}$ (i.e., Δ_μ dominates $1 - \mathcal{D}$).

Furthermore, the assumptions on $\theta - \theta_i$ and positiveness of v_{dc} yields that $\mathcal{A} > 0$ in (4.34). Hence, with Δ_μ as in (4.36), the RHS of (4.34) is strictly negative for $\|i\| > i_{\text{th}}$. Nagumo's theorem [121, Theorem 3.1] yields that $\|i(t)\|$ (with slight abuse of the notation) is strictly decreasing whenever $\|i(t)\| > i_{\text{th}}$. ■

Proof of Proposition 7. The power injection to the IB at equilibrium [45, Definition 2]

can be expressed as

$$p_g^* = -\frac{\|v^*\|v_r \left(r_g \cos(\delta_{bv}^*) + \ell_g \omega_0 \sin(\delta_{bv}^*) \right)}{r_g^2 + (\ell_g \omega_0)^2}, \quad (4.64a)$$

$$q_g^* = -\frac{\|v^*\|v_r \left(\ell_g \omega_0 \cos(\delta_{bv}^*) - r_g \sin(\delta_{bv}^*) \right)}{r_g^2 + (\ell_g \omega_0)^2}, \quad (4.64b)$$

where $\delta_{bv}^* := \theta_b^* - \theta_v^*$ and $\theta_v^* = \tan^{-1}(v_q^*/v_d^*)$. Taking into account the line loss and the power associated with the shunt element, we can compute p_f^* and q_f^* (see Figure 4.1) by

$$p_f^* = p_g^* + \left(\frac{r_g}{r_g^2 + (\ell_g \omega_0)^2} + g \right) \|v^*\|^2,$$

$$q_f^* = q_g^* + \left(\frac{\ell_g \omega_0}{r_g^2 + (\ell_g \omega_0)^2} - c\omega_0 \right) \|v^*\|^2.$$

Note that p_f^* and q_f^* are also expressed by

$$p_f^* = -\frac{\|v_s^*\| \|v^*\| \left(r \cos(\delta_{vc}) + \ell \omega_0 \sin(\delta_{vc}) \right)}{r^2 + (\ell \omega_0)^2}, \quad (4.65a)$$

$$q_f^* = -\frac{\|v_s^*\| \|v^*\| \left(\ell \omega_0 \cos(\delta_{vc}) - r \sin(\delta_{vc}) \right)}{r^2 + (\ell \omega_0)^2}, \quad (4.65b)$$

where $\delta_{vc} := \theta_v^* - \theta_c^*$ and $\|v_s^*\| := \mu^* v_{dc}^*$ denotes the equilibrium voltage magnitude before the filter inductor.

Consider the shorthand $\det(Z_g) = r_g^2 + (\ell_g \omega_0)^2$, and let us define $\vartheta_g := \tan^{-1}(\ell_g \omega_0 / r_g)$, $\sin(\vartheta_g) := \ell_g \omega_0 / \sqrt{\det(Z_g)}$, and $\cos(\vartheta_g) := r_g / \sqrt{\det(Z_g)}$. Then, (4.64) is equivalent to

$$s_g^* = -\|s_g^*\| \mathbf{R}(\vartheta_g) \psi(\theta_v^* - \theta_b^*) = -\|s_g^*\| \psi(\theta_v^* + \vartheta_g - \theta_b^*),$$

where $\|s_g^*\| = v_r \|v^*\| / \sqrt{\det(Z_g)}$ and subsequently, $\hat{s}_g^* = -\psi(\theta_v^* + \vartheta_g - \theta_b^*)$. Similarly, define $\vartheta_f := \tan^{-1}(\ell \omega_0 / r)$, then (4.65) is equivalent to

$$s_f^* = -\|s_f^*\| \mathbf{R}(\vartheta) \psi(\theta_c^* - \theta_v^*) = -\|s_f^*\| \psi(\theta_c^* + \vartheta - \theta_v^*),$$

where $\|s_f^*\| = \|v_s^*\| \|v^*\| / \sqrt{\det(Z)}$. Thus, $\hat{s}_f^* = -\psi(\theta_c^* + \vartheta - \theta_v^*)$. By the means of (4.74) and (4.75)

$$\left(\hat{s}_g^{*\top} \begin{pmatrix} +1 & 0 \\ 0 & -1 \end{pmatrix} \hat{s}_f^*, \hat{s}_g^{*\top} \begin{pmatrix} 0 & +1 \\ +1 & 0 \end{pmatrix} \hat{s}_f^* \right) = \psi(\theta_c^* - \theta_b^* + \delta)$$

and subsequently, $R(\delta)^\top \psi(\theta_c^* - \theta_b^* + \delta) = \psi(\theta^*)$.

Thus, $\psi(\theta_r)$ that is uniquely defined by (4.52) coincides with the solution of power flow equations, i.e., $\psi(\theta_r) = \psi(\theta^*)$. To prove the second statement (4.53), μ^* is derived from the expression of $\|s_f^*\|$ i.e., $\mu^* = \|s_f^*\| \sqrt{\det(\mathbf{Z})}/v_{dc}^* \|v^*\|$, which shows μ_r defined by (4.53) is consistent with μ^* . ■

Proof of Proposition 6. Note that by the relative angle dynamics (4.25a) at equilibrium $\omega_{c,x} = \omega_x$. Multiply (4.25c) at equilibrium by $v_{dc,x}$

$$i_{dc,x} v_{dc,x} - g_{dc} v_{dc,x}^2 - p_{net,x} = 0,$$

and replace $v_{dc,x}$ with the expression from (4.5), that is, $v_{dc,x} = (\omega_x - \beta_{\theta_x})/\eta$ which results in

$$p_{net,x} = \frac{i_{dc,x}(\omega_x - \beta_{\theta_x})}{\eta} - \frac{g_{dc}(\omega_x - \beta_{\theta_x})^2}{\eta^2}. \quad (4.66)$$

Replacing $i_{dc,x}$ from (4.7b) at equilibrium results in

$$p_{net,x} = \frac{i_0(\omega_x - \beta_{\theta_x})}{\eta} - \frac{(\kappa + g_{dc})(\omega_x - \beta_{\theta_x})^2}{\eta^2}. \quad (4.67)$$

Hence, (4.51) directly follows by linearizing (4.67) w.r.t ω_x . ■

4.9 Appendix B: transformations and identities

4.9.1 $\alpha\beta$ -coordinates

For a three-phase quantity $z_{abc} := (z_a, z_b, z_c) \in \mathbb{R}^3$ that is balanced i.e., $z_a + z_b + z_c = 0$ the magnitude preserving Clarke transformation is defined by

$$z_{\alpha\beta} = (z_\alpha, z_\beta) := \mathbf{C}z_{abc} = \frac{2}{3} \begin{pmatrix} 1 & -\frac{1}{2} & -\frac{1}{2} \\ 0 & \frac{\sqrt{3}}{2} & -\frac{\sqrt{3}}{2} \end{pmatrix} z_{abc}. \quad (4.68)$$

4.9.2 Polar coordinates

The transformation from Cartesian to polar coordinates i.e., $\mathcal{P} : \mathbb{R}^2 \setminus \{0\} \rightarrow \mathbb{R}_{>0} \times \mathbb{S}^1$ is

$$(\|z\|, \theta_z) = \mathcal{P}(z) := \left(\sqrt{z_1^2 + z_2^2}, \tan^{-1} \frac{z_2}{z_1} \right). \quad (4.69)$$

Moreover, the inverse transformation is given by

$$(z_1, z_2) = \mathcal{P}^{-1}(\|z\|, \theta_z) := \|z\|\psi(\theta_z). \quad (4.70)$$

Note that the polar coordinates are well-defined for the entire Cartesian space except the origin since $\mathcal{P}(0)$ is not unique.

Lemma 1 (Algebraic and trigonometric identities). *For $a, b \in \mathbb{R}^2$, $\epsilon \in \mathbb{R}_{>0}$ and $\varphi, \phi \in \mathbb{S}^1$ the followings hold*

$$\pm a^\top b \leq \epsilon^2 \|a\|^2 + \frac{1}{4\epsilon^2} \|b\|^2, \quad (4.71)$$

$$\sin^2 \frac{\varphi}{2} = \frac{1 - \cos \varphi}{2}, \quad (4.72)$$

$$\cos^2 \frac{\varphi}{2} = \frac{1 + \cos \varphi}{2}, \quad (4.73)$$

$$\sin(\varphi \pm \phi) = \sin \varphi \cos \phi \pm \cos \varphi \sin \phi, \quad (4.74)$$

$$\cos(\varphi \pm \phi) = \cos \varphi \cos \phi \mp \sin \varphi \sin \phi. \quad (4.75)$$

Hybrid angle control and almost global stability of non-synchronous hybrid AC/DC power grids

Presented at the IEEE Conference on Decision and Control (CDC) 2022.

Authors – Ali Tayyebi and Florian Dörfler.

Abstract – This paper explores the stability of non-synchronous hybrid ac/dc power grids under the hybrid angle control strategy. We formulate detailed dynamical models for the ac grids and transmission lines, interlinking converters, and dc generations and interconnections. Next, we establish the existence and uniqueness of the closed-loop equilibria and demonstrate global attractivity of the equilibria, local asymptotic stability of the desired equilibrium point, and instability and zero-Lebesgue-measure region of attraction for other equilibria. The theoretic results are derived under mild, parametric, and unified stability/instability conditions. Further, we conclude the almost global asymptotic stability of the hybrid ac/dc power grids under the hybrid angle control. Last, we present a numerical verification of the theoretical results.

5.1 Introduction

The global paradigm shift toward harvesting energy from renewable sources has recently led to the emergence of hybrid ac/dc power grids. Such systems are typically comprised of several non-synchronous ac power grids that interact with each other through dc/ac ILCs that are interconnected by a dc transmission network [56], [122]–[124]. For instance, Figure 5.1 illustrates an abstraction of the meshed hybrid ac/dc grids that have been recently evolving in Europe.

The complex nonlinear dynamics of the hybrid ac/dc power grids with multiple timescales and interactions between the dc network, renewable generations, and ac grids renders the control of interlinking converters a daunting task. It has been recently reported that the grid-forming converter control techniques [1] are viable candidates for

RGs: Nordic | Baltic | Continental Europe | United Kingdom | Ireland

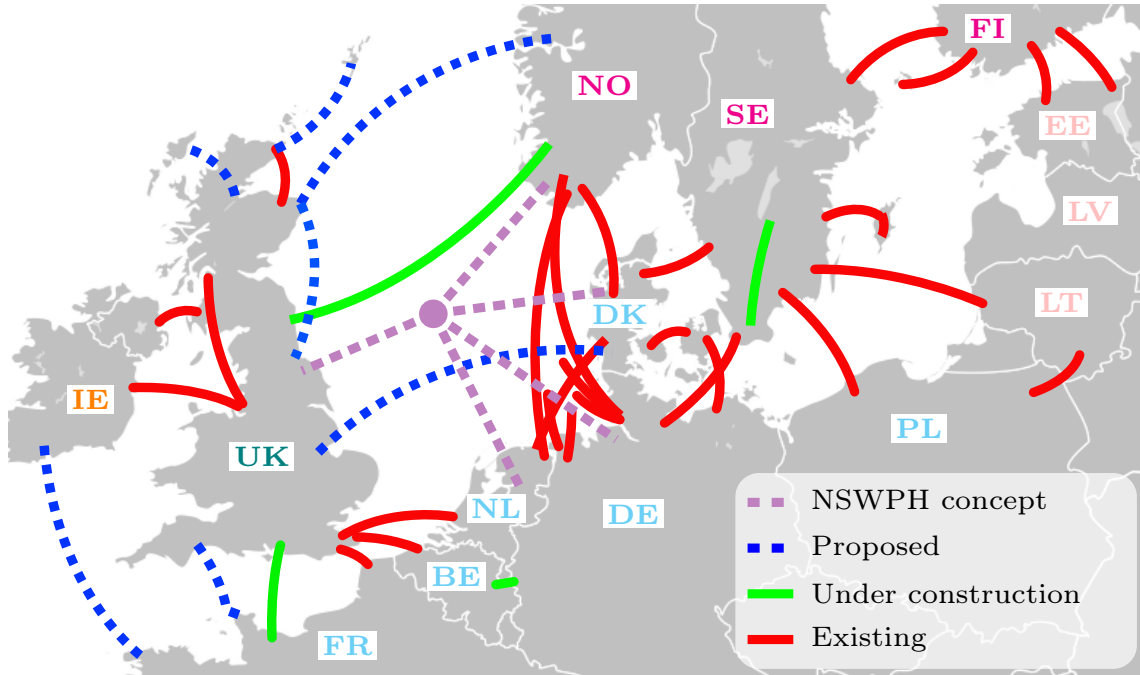


Figure 5.1: The overview of the high voltage dc (HVDC) links and North Sea wind power hub (NSWPH) concept that connect the regional groups (RGs) in the Northern Europe and Baltic regions [124].

controlling the ILCs in hybrid ac/dc power grids [125]. In particular, [125] suggests that the matching control [65], [126] exhibits superior dynamic performance in hybrid ac/dc grids compared to classic control schemes for the interlinking converters, e.g., dual-droop control among others [125]. Inspired by this intriguing observation, this work explores the stability certificates of the HAC [3] for multiple ILCs. We provide detailed linear/nonlinear dynamical models for the ac grids and transmission lines, ILCs, dc generations and interconnections. Next, we prove the existence and uniqueness of equilibria for the closed-loop dynamics under a verifiable assumption. Further, we prove the AGAS of hybrid ac/dc power grids with ILCs under the HAC. Last, we present a numerical verification of the presented results.

5.2 Hybrid AC/DC grid model description

In this section, we describe a dynamical model of the hybrid ac/dc grids. We consider $n \in \mathbb{Z}_{>0}$ ac grids, n ILCs, and define $\mathcal{N}_{ac} \triangleq \{1, \dots, n\}$ that collects the labels of the ac systems. Further, it is envisioned that the ILCs are interconnected via $m \in \mathbb{Z}_{>0}$ dc lines; see Figure 5.2 for the overall configuration.

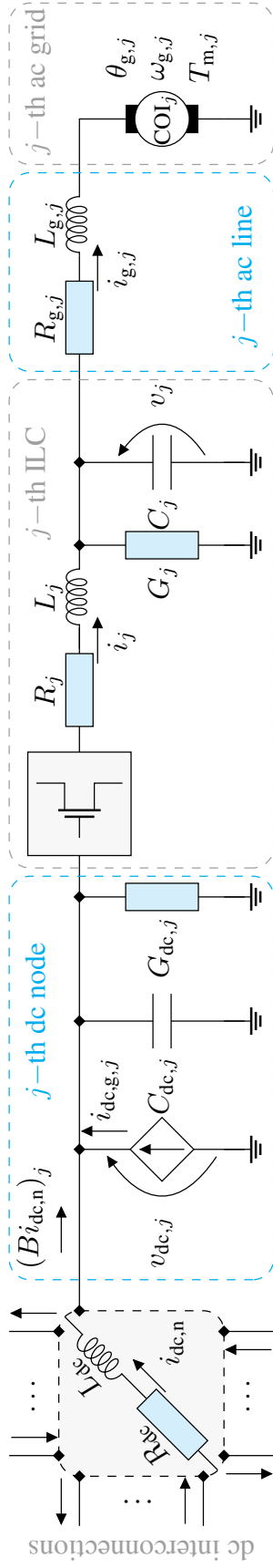


Figure 5.2: The hybrid ac/dc grid model comprised of the dynamic dc interconnections, j -th dc node, ILC, transmission line, and ac grid.

AC grids

We model the ac grids by aggregated dynamic COI models [3], [127], i.e.,

$$\dot{\theta}_g = \omega_g, \quad (5.1a)$$

$$\dot{\omega}_g = J^{-1} (T_m - D_f \omega_g - D_d (\omega_g - \omega_r) - T_e), \quad (5.1b)$$

$$\dot{T}_m = \tau_g^{-1} (T_r - \kappa_g (\omega_g - \omega_r) - T_m), \quad (5.1c)$$

where $\theta_g \triangleq (\theta_{g,1}, \dots, \theta_{g,n}) \in \mathbb{S}^n$ denotes the stacked vector of the absolute phase angles of the ac grids, $\omega_g \triangleq (\omega_{g,1}, \dots, \omega_{g,n}) \in \mathbb{R}^n$ denotes the vector of angular frequencies, $J \triangleq \text{diag}(\{J_j\}_{j=1}^n) \in \mathbb{R}_{>0}^{n \times n}$ denotes the diagonal matrix of the moment of inertia constants, $T_m \triangleq (T_{m,1}, \dots, T_{m,n}) \in \mathbb{R}^n$ denotes the vector of mechanical torques, $D_f \triangleq \text{diag}(\{D_{f,j}\}_{j=1}^n) \in \mathbb{R}_{>0}^{n \times n}$ denotes the diagonal matrix of the aggregated damping constants associated with the friction torques that are proportional to the absolute frequencies, $D_d \triangleq \text{diag}(\{D_{d,j}\}_{j=1}^n) \in \mathbb{R}_{>0}^{n \times n}$ denotes the diagonal matrix of the aggregated damping constants associated with the damper windings that are proportional to the frequency deviations, and $T_e \triangleq (T_{e,1}, \dots, T_{e,n}) \in \mathbb{R}^n$ denotes the vector of electrical torques.

Further, $\tau_g \triangleq \text{diag}(\{\tau_{g,j}\}_{j=1}^n) \in \mathbb{R}_{>0}^{n \times n}$ captures the aggregated turbine time constants, $T_r \triangleq (T_{r,1}, \dots, T_{r,n}) \in \mathbb{R}^n$ collects the reference mechanical torque inputs for the turbines, $\kappa_g \triangleq \text{diag}(\{\kappa_{g,j}\}_{j=1}^n)$ is the diagonal matrix of governor proportional control gains, and finally $\omega_r \triangleq (\omega_{r,1}, \dots, \omega_{r,n}) \in \mathbb{R}_{>0}^n$ denotes the nominal frequencies of the ac grids (that are not necessarily identical). The damping terms in (5.1b) can be seen as a representation of the primary and fast frequency controls that are respectively associated with the underlying synchronous machines and power converters in the aggregated COI model.

In Subsection 5.3.2, the connection of (5.1) to the other system dynamics is characterized. We emphasize that, in the sequel, all three-phase quantities are transformed to dq-coordinates aligned with θ_g in (5.1a), hence, the ac impedance and admittance matrices are dynamic and depend on ω_g .

AC transmission lines

The lines that couple the ac grid models (5.1) to the ILCs' (see Figure 5.2) are modeled by [3]

$$\dot{i}_g = L_g^{-1} \left(v - (R_g - \underline{L}_g \omega_g \otimes J_2) i_g - v_g \right), \quad (5.2)$$

where $i_g \triangleq (i_{g,1}, \dots, i_{g,n}) \in \mathbb{R}^{2n}$ denotes line currents in the respective dq-frames that are aligned with the COI angles θ_g and $L_g \triangleq \text{diag}(\{L_{g,j} \otimes I_2\}_{j=1}^n) \in \mathbb{R}^{2n \times 2n}$ denotes

the augmented inductance matrix associated with transmission lines, and \otimes , I_2 , and J_2 denotes the Kronecker product, 2-D identity matrix and rotation by $\pi/2$, respectively. Further, $v \triangleq (v_1, \dots, v_n) \in \mathbb{R}^{2n}$ denotes the ac output voltages of the ILCs, $R_g \triangleq \text{diag} \left(\{R_{g,j} \otimes I_2\}_{j=1}^n \right) \in \mathbb{R}^{2n \times 2n}$ is the augmented diagonal resistance matrix of the line impedance, and $\underline{L}_g \triangleq \text{diag} \left(\{L_{g,j}\}_{j=1}^n \right) \in \mathbb{R}^{n \times n}$ is the n -D diagonal reduction of L_g . Last, $v_g \triangleq (v_{g,1}, \dots, v_{g,n}) \in \mathbb{R}^{2n}$ denotes the dynamic grid voltages.

Interlinking converters

The ILCs dynamics in dq-frames aligned with the COI angles in (5.1a) are given by [1], [125]

$$\dot{\theta}_c = \omega_c, \quad (5.3a)$$

$$\dot{i}_{\text{dc},g} = \tau_{\text{dc}}^{-1} (i_{\text{dc},r} - \kappa_{\text{dc}}(v_{\text{dc}} - v_{\text{dc},r}) - i_{\text{dc},g}), \quad (5.3b)$$

$$\dot{v}_{\text{dc}} = C_{\text{dc}}^{-1} \left(B i_{\text{dc},n} + i_{\text{dc},g} - G_{\text{dc}} v_{\text{dc}} - m(\delta)^\top i \right), \quad (5.3c)$$

$$\dot{i} = L^{-1} (m(\delta) v_{\text{dc}} - (R - \underline{L} \omega_g \otimes J_2) i - v), \quad (5.3d)$$

$$\dot{v} = C^{-1} (i - (G - \underline{C} \omega_g \otimes J_2) v - i_g), \quad (5.3e)$$

where $\theta_c \triangleq (\theta_{c,1}, \dots, \theta_{c,n}) \in \mathbb{S}^n$ denotes the ILCs modulation angles evolving on the n -D torus and $\omega_c \triangleq (\omega_{c,1}, \dots, \omega_{c,n}) \in \mathbb{R}^n$ denotes the converter frequency. The time constants associated with the first-order dc generation models are denoted by $\tau_{\text{dc}} \triangleq \text{diag} \left(\{\tau_{\text{dc},j}\}_{j=1}^n \right) \in \mathbb{R}^{n \times n}$ and $i_{\text{dc},g} \triangleq (i_{\text{dc},g,1}, \dots, i_{\text{dc},g,n}) \in \mathbb{R}^n$ denotes the currents flowing out of the dc current sources that are collocated with the ILCs dc-sides, $i_{\text{dc},r} \triangleq (i_{\text{dc},r,1}, \dots, i_{\text{dc},r,n}) \in \mathbb{R}^n$ denotes the reference currents for the dc sources, and $\kappa_{\text{dc}} \triangleq \text{diag} \left(\{\kappa_{\text{dc},j}\}_{j=1}^n \right) \in \mathbb{R}^{n \times n}$ denotes the matrix of proportional dc voltage control gains.

The dc-link capacitances are denoted by the diagonal matrix $C_{\text{dc}} \triangleq \text{diag} \left(\{C_{\text{dc},j}\}_{j=1}^n \right) \in \mathbb{R}^{n \times n}$, the signed incidence matrix associated with the directed graph of the dc interconnections is denoted by $B \in \mathbb{R}^{n \times m}$, $i_{\text{dc},n} \triangleq (i_{\text{dc},n,1}, \dots, i_{\text{dc},n,m}) \in \mathbb{R}^m$ collects the dc edge currents, and $G_{\text{dc}} \triangleq \text{diag} \left(\{G_{\text{dc},j}\}_{j=1}^n \right) \in \mathbb{R}^{n \times n}$ denotes the nodal dc conductances that models the ILCs dc-losses and/or the resistive dc loads. The ILCs modulation signals are captured by $m(\delta) \triangleq (m_1(\delta_1), \dots, m_n(\delta_n)) \in \mathbb{R}^{2n \times n}$ with $m_j(\delta_j) = \mu_j r(\delta_j) \otimes e_j \in \mathbb{R}^{2n}$ where e_j denotes the j -th orthonormal basis of \mathbb{R}^n , $r(\delta_j) \triangleq (\cos(\delta_j), \sin(\delta_j))$, and $\mu_j \in \mathbb{R}_{[0,1/2]}$ denotes the j -th modulation signal magnitude. Last, $i \triangleq (i_1, \dots, i_n) \in \mathbb{R}^{2n}$ is the vector of the currents flowing through the ILCs output filters. Furthermore, $L \triangleq \text{diag} \left(\{L_j \otimes I_2\}_{j=1}^n \right) \in \mathbb{R}^{2n \times 2n}$ denotes the augmented diagonal matrix of ILCs filter inductances, $R \triangleq \text{diag} \left(\{R_j \otimes I_2\}_{j=1}^n \right) \in \mathbb{R}^{2n \times 2n}$ denotes the resistance matrix associated with the filter impedance, and $\underline{L} \triangleq \text{diag} \left(\{L_j\}_{j=1}^n \right) \in \mathbb{R}^{n \times n}$ is the reduced version

of L , $C \triangleq \text{diag}(\{C_j \otimes I_2\}_{j=1}^n) \in \mathbb{R}^{2n \times 2n}$ denotes the augmented diagonal matrix of filter capacitance, $G \triangleq \text{diag}(\{G_j \otimes I_2\}_{j=1}^n) \in \mathbb{R}^{2n \times 2n}$ is the filter conductance, and $\underline{C} \triangleq \text{diag}(\{C_j\}_{j=1}^n) \in \mathbb{R}^{n \times n}$ is the reduced version of C .

DC interconnections

We model the dc lines with RL dynamics that [128], i.e.,

$$\dot{i}_{\text{dc},n} = L_{\text{dc}}^{-1} \left(-B^\top v_{\text{dc}} - R_{\text{dc}} i_{\text{dc},n} \right), \quad (5.4)$$

where $L_{\text{dc}} \triangleq \text{diag}(\{L_{\text{dc},j}\}_{j=1}^m) \in \mathbb{R}^{m \times m}$ and $R_{\text{dc}} \triangleq \text{diag}(\{R_{\text{dc},j}\}_{j=1}^m) \in \mathbb{R}^{m \times m}$ respectively denote the diagonal inductance and resistance matrices associated with the dc lines. Note that we do not make any assumption on the sparsity of the underlying graph¹ associated with the dc interconnections.

5.3 Hybrid angle control and stability analysis

In this section, we equip the ILCs with the HAC, formulate the closed-loop dynamics, and present our stability analysis.

5.3.1 Hybrid angle control for interlinking converters

We define the frequency of the ILCs in (5.3a) according to the multi-variable grid-forming HAC [3], i.e.,

$$\omega_c \triangleq \omega_r + \eta(v_{\text{dc}} - v_{\text{dc},r}) - \gamma \mathbf{sin} \left(\frac{\delta - \delta_r}{2} \right), \quad (5.5)$$

where $\eta \triangleq \text{diag}(\{\eta_j\}_{j=1}^n) \in \mathbb{R}^{n \times n}$ and $\gamma \triangleq \text{diag}(\{\gamma_j\}_{j=1}^n) \in \mathbb{R}^{n \times n}$ respectively denote the diagonal matrix of the dc and ac gains associated with HAC. Further, for any $z \in \mathbb{R}^n$, $\mathbf{sin}(z) \triangleq (\sin(z_1), \dots, \sin(z_n))$. Last, $\delta \triangleq \theta_c - \theta_g$ denotes the vector of relative ILC-COI angles and $\delta_r \triangleq (\delta_{r,1}, \dots, \delta_{r,n}) \in \mathbb{S}^n$ collects the reference relative angles. We consider that all angular quantities evolve on the boundary of a Möbius strip, i.e., $\mathbb{M} \triangleq]-2\pi, 2\pi[$ where $-2\pi \equiv 2\pi$ [3], hence, $\delta \in \mathbb{M}^n$; see Figure 5.3 for a geometrical representation of \mathbb{M}^2 .

The HAC (5.5) resembles the hybrid control laws, e.g., see [9], [56]. Unlike the classic techniques, e.g., [34], [125], [128], the hybrid strategies unify the dc and ac feedback in

¹If the dc interconnections includes disconnected subgraphs, the stability result in Section 5.3 holds for the individual hybrid ac/dc subsystems.

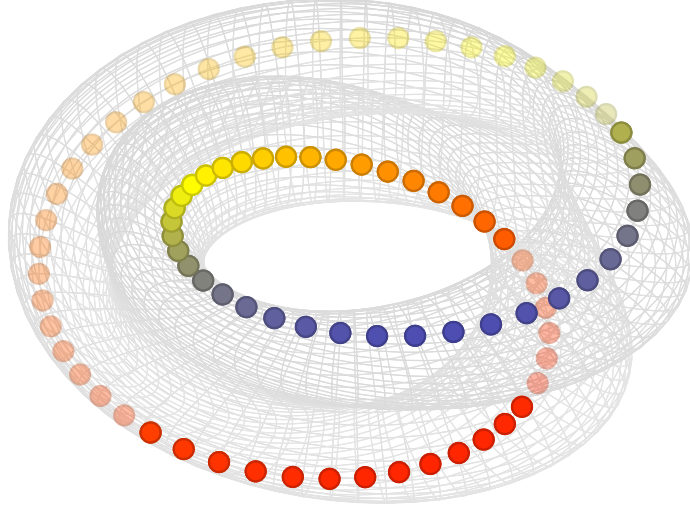


Figure 5.3: The figure-8 immersion of the Klein bottle [129]. The Klein bottle can be decomposed into two Möbius strips (e.g., the ones above and below the colored path) with identical compact boundaries representing \mathbb{M} [3]. The merged boundaries of the underlying Möbius strips (e.g., the colored closed curve) represents the angle manifold $\mathbb{M}^2 =] - 2\pi, 2\pi[\times] - 2\pi, 2\pi[$ where $-2\pi \equiv 2\pi$.

a single controller. In particular, HAC encodes trade-off between the dc voltages (that relate to the dc energies) and the ac angles (that relate to the ac power flows) deviations.

5.3.2 Closed-loop analysis

In order to combine the models introduced in Section 5.2, we first define the aggregated electrical torque and the voltage associated with (5.1). Similar to the modeling approach in [3], [109] we define the j -th stiff COI voltage (that resembles the synchronous generator electromagnetic force) as

$$v_{g,abc,j} \triangleq b_j \omega_{g,j} \left(\sin \theta_{g,j}, \sin \left(\theta_{g,j} - \frac{2\pi}{3} \right), \sin \left(\theta_{g,j} - \frac{4\pi}{3} \right) \right), \quad (5.6)$$

where $v_{g,abc,j}$ is the three-phase representation of $v_{g,j}$ in (5.2) and $b_j \in \mathbb{R}_{>0}$ is a constant. Note that we can alternatively simplify the frequency-dependent magnitude in (5.6) to a constant reference $v_{r,j}$. The implicit assumption in (5.6) is that $b_j \triangleq v_{r,j} / \omega_{g,j}^*$ realizes the desired magnitude at the equilibrium frequency $\omega_{g,j}^*$ for the j -th ac grid. Subsequently, the j -th electrical torque in (5.1b) is defined by [3], [109]

$$T_{e,j} \triangleq \omega_{g,j}^{-1} v_{g,abc,j}^\top i_{g,abc,j}, \quad (5.7)$$

where $i_{g,abc,j}$ is the three-phase representation of $i_{g,j}$ in (5.2). Finally, combining (5.1)-(5.7) yields the overall dynamics, i.e.,

$$\dot{x} = K^{-1}f(x), \quad (5.8)$$

where

$$\begin{aligned} x &\triangleq (\delta, i_{dc,n}, i_{dc,g}, v_{dc}, i, v, i_g, \omega_g, T_m), \\ K &\triangleq \text{diag}(I_n, L_{dc}, \tau_{dc}, C_{dc}, L, C, L_g, J, \tau_g), \end{aligned}$$

and

$$f(x) \triangleq \begin{pmatrix} \omega_r + \eta(v_{dc} - v_{dc,r}) - \gamma \mathbf{sin}\left(\frac{\delta - \delta_r}{2}\right) - \omega_g \\ -B^\top v_{dc} - R_{dc} i_{dc,n} \\ i_{dc,r} - \kappa_{dc}(v_{dc} - v_{dc,r}) - i_{dc,g} \\ B i_{dc,n} + i_{dc,g} - G_{dc} v_{dc} - m(\delta)^\top i \\ m(\delta) v_{dc} - (R - \underline{L}\omega_g \otimes J_2) i - v \\ i - (G - \underline{C}\omega_g \otimes J_2) v - i_g \\ v - (R_g - \underline{L}_g \omega_g \otimes J_2) i_g - \psi \omega_g \\ T_m - D_f \omega_g - D_d(\omega_g - \omega_r) + \psi^\top i_g \\ T_r - \kappa_g(\omega_g - \omega_r) - T_m \end{pmatrix},$$

in which the three-phase quantities in (5.6) and (5.7) are transformed to the dq-frames aligned with $\theta_{g,j}$ and written in terms of $\psi \triangleq (\psi_1, \dots, \psi_n) \in \mathbb{R}^{2n \times n}$ with $\psi_j \triangleq b_j r(0) \otimes e_j \in \mathbb{R}^{2n}$ (here $r(0)$ is used since the dq-frame is aligned with the COI angle). We partition the state vector as $x \triangleq (\delta, y) \in \mathbb{X} \triangleq \mathbb{M}^n \times \mathbb{R}^{10n+m}$ where $y \triangleq (i_{dc,n}, i_{dc,g}, v_{dc}, i, v, i_g, \omega_g, T_m)$ and remark that $f(x)$ is smooth in \mathbb{X} . Last, we define $D \triangleq D_f + D_d$.

Assumption 1 (Frequency and dc voltage regulation). *Assume that the equilibrium frequency ω_g^* and dc voltage v_{dc}^* of (5.8) coincide with respective references ω_r and $v_{dc,r}$.*

Assumption 1 implies requirements for frequency and dc voltage balancing across the ac/dc grids. This is met by an appropriate choice of reference-parameter pairs (T_r, κ_g) and $(i_{dc,r}, \kappa_{dc})$ in (5.1c) and (5.3b), respectively [3]. Note that considering secondary integral-type controllers in (5.1c) and (5.3b) also ensures that Assumption 1 holds, but, the integral control hinders the frequency and dc voltage droop mechanisms that are crucial for load-sharing [125]. Thus, the blend of consistent references and adequately tuned proportional controllers is recommended for verification of Assumption 1. Last, Assumption 1 is conceptually similar to a widely recognized assumption in control of power systems that requires the given set-points to be consistent with (feasible) solutions of power flows equations, e.g., see [45] among others.

Theorem 6 (Existence and uniqueness). *Under Assumption 1, the closed-loop dynamics (5.8) admits a unique equilibrium set that is described by*

$$\Omega^* \triangleq \left\{ (\delta^*, y^*) \mid \delta_j^* \in \{\delta_{r,j}, \delta_{r,j} + 2\pi\}, \forall j \in \mathcal{N}_{ac} \right\}, \quad (5.9)$$

where y^* is unique w.r.t $(\delta_r, v_{dc,r}, \omega_{g,r})$ and Ω^* only contains disjoint points that only differ in their angles.

The proof is provided in the Appendix 5.6. Among all the points in Ω^* , $x_s^* \triangleq (\delta_r, y^*)$ has a different stability nature (more on this later). Last, we define $\Omega_u^* \triangleq \Omega^* \setminus x_s^*$.

Theorem 7 (Decentralized certificates for global attractivity). *The equilibria of system (5.8) as in (5.9) are globally attractive if the following decentralized conditions hold for all $j \in \mathcal{N}_{ac}$:*

$$D_j > D_{\min,j} \quad \text{and} \quad \gamma_j > \gamma_{\min,j}, \quad (5.10)$$

where the critical COI damping, i.e., $D_{\min,j}$ is defined by

$$\frac{\left(L_j \|i_j^*\right)^2}{R_j} + \frac{\left(C_j \|v_j^*\right)^2}{G_j} + \frac{\left(L_{g,j} \|i_{g,j}^*\right)^2}{R_{g,j}},$$

and the critical ILC angle damping, i.e., $\gamma_{\min,j}$ is defined by

$$\frac{\eta_j \left(1 + \left(\mu_j \|i_j^*\right)^2\right)}{G_{dc,j}} + \frac{\eta_j \left(\mu_j \|v_{dc,j}^*\right)^2}{R_j} + \frac{1}{2(D_j - D_{\min,j})}.$$

The proof is provided in the Appendix 5.6. Next, we employ the function in (5.14), and leverage the Lyapunov's direct method to establish the local asymptotic stability of $x_s^* \in \Omega^*$.

Corollary 1 (Local asymptotic stability of x_s^*). *Consider the closed-loop system (5.8) and the equilibrium point $x_s^* = (\theta_r, y^*)$, then x_s^* is locally asymptotically stable if the stability conditions (5.10) are satisfied for all $j \in \mathcal{N}_{ac}$.*

The proof is provided in the Appendix 5.6.

Corollary 2 (Instability and region of attraction of Ω_u^*). *Consider the closed-loop system (5.8), if the conditions (5.10) are satisfied for all $j \in \mathcal{N}_{ac}$ then all equilibria in Ω_u^* are unstable with zero-Lebesgue-measure region of attractions.*

Proof is skipped due to the lack of space but it follows from a standard albeit lengthy Schur complement analysis as in [3]. More precisely, the Jacobian of (5.8) admits at least one eigenvalue with positive real part when evaluated over Ω_u^* . Subsequently, by

invoking the results of [45], [109], [120] one can show that the union of the regions of attraction of the equilibria in Ω_u^* is a zero-Lebesgue-measure set. Intuitively speaking, Ω_u^* contains the saddle points of the LaSalle function (5.14) since $\mathcal{H}(\hat{x})$ is globally convex and $\mathcal{S}(\hat{\delta})$ attains its local maxima on Ω_u^* ; see [3]. Theorem 8 below combines the results of Theorem 7, Corollaries 1, and 2.

Theorem 8 (Main result: AGAS). *The closed-loop system (5.8) is almost globally asymptotically stable with respect to the equilibrium x_s^* if the unified stability/instability conditions (5.10) are satisfied for all $j \in \mathcal{N}_{ac}$.*

Remark 14 (Features, conditions, and implementations). *First, HAC (5.5) provides two degrees of freedom for an optimal frequency tuning. Further, HAC integrates the complementary benefits of purely ac or dc-based grid-forming frequency control laws, i.e., the enhanced performance and robustness; see [1], [5] for a comparison. In addition, the AGAS result is obtained without requiring an assumption on the connectivity/sparsity of the dc interconnections. Second, conditions (5.10) are fully decentralized (i.e., they do not require non-local parameters) and confirm that the stability certificate of HAC for a single converter system is fully scalable; see [3]. Third, the damping requirement for the ILCs i.e., $\gamma_j > \gamma_{\min,j}$ does not require large physical damping but is met by an appropriate choice of the control parameters γ_j and η_j . Next, the COIs damping requirements i.e., $D_j > D_{\min,j}$ is a reoccurring theme in related works; see [3] for details. Forth, conditions in (5.10) does not rely on the control of the dc energy sources. Thus, such generation units can be distributed within the dc network. Finally, the reader is referred to [3] for discussions on the implementation of the HAC (5.5). Note that under the dc power flow assumption and when reducing the ILCs' filters to resistive-inductive elements, HAC is approximated by $\omega_c \approx \omega_r + \eta(v_{dc} - v_{dc,r}) - \gamma \sin((p - p_r)/2)$, where p and p_r respectively denote the active power flows between the ILCs and COIs and the associated references.*

5.4 Numerical verification

In this section, the qualitative behavior of the closed-loop dynamics (5.8) is presented. We consider two ILCs that interconnect two ac grids via a dc transmission line, i.e., we set $n = 2$ and $m = 1$ in (5.8); see Figure 5.2 for an illustration. The model and control parameters of the first subsystem are: $\omega_{r,1} \approx 314$ [rad/s] (i.e., 50 Hz), $\eta_1 = 0.01$, $v_{dc,r,1} = 3.168 \times 10^3$ [V], $\gamma_1 = 10^6$, $\delta_{r,1} = -0.1$ [rad], $L_{dc,1} = L_1 = L_{g,1} = 0.001$ [H], $R_{dc,1} = R_1 = R_{g,1} = 0.001$ [Ω], $\tau_{dc,1} = 0.05$ [s], $i_{dc,r,1} = 0$, $\kappa_{dc,1} = 10^3$, $C_{dc,1} = 0.005$ [F], $G_{dc,1} = G_1 = 0.001$ [Ω^{-1}], $\mu_1 = 0.25$, $C_1 = 0.002$ [F], $b_1 = 2.59$, $v_{r,1} = 816.4$ [V], $J_1 = 500$ [s], $D_{f,1} = 0$, $D_{d,1} = 5 \times 10^3$, $\kappa_{g,1} = 5 \times 10^3$, and $\tau_{g,1} = 5$ [s]. The parameters of the second subsystem are identical to those of the first subsystem except $\omega_{r,2} \approx 377$ [rad/s] (i.e., 60 Hz), $v_{dc,r,2} = 2.59 \times 10^3$ [V], $\delta_{r,2} = 0.1$ [rad], $\mu_2 = 0.31$, and $b_2 = 2.16$. Figure 5.4 illustrates the convergence of state pairs $(\delta_1 - \delta_{r,1}, \delta_2 - \delta_{r,2})$ and $(\omega_{g,1} - \omega_{r,1}, \omega_{g,2} - \omega_{r,2})$

starting from random initial conditions in \mathbb{X} . Since $\delta_{r,1} = -0.1$, the first ILC absorbs power from the first ac grid. In contrast, the second ILC injects power into the second ac grid, since $\delta_{r,2} = 0.1$. The power transfer over the dc interconnection is realized by $v_{dc,1}^* \rightarrow v_{dc,r,1} > v_{dc,2}^* \rightarrow v_{dc,r,2}$; presentation is skipped due to lack of space. It is noteworthy, that even if the dc voltage references are not selected appropriately the drooping mechanism of the HAC [3] shifts the equilibrium dc voltages such that the power transfer is realized. Further, this behavior is achieved while coupling ac grids with significantly different angular frequencies. Figure 5.4 also qualitatively highlights the region of attraction of the stable equilibrium point characterized by $\hat{\delta}_1 = \hat{\delta}_2 = 0$ and instability of other angle equilibria in \mathbb{M}^2 . We close by remarking that the presented results are preliminary and numerical verification of HAC performance in hybrid AC/DC grids requires further in-depth investigations.

5.5 Outlook

In this work, we presented a dynamical modeling of hybrid ac/dc grids and derived fully decentralized conditions for the existence, uniqueness, and global stability of the closed-loop equilibria. Our future work includes: 1) the stability analysis of the hybrid AC/DC grids under HAC while incorporating nonlinear constant power sources/loads, 2) revisiting and extending the analysis by considering the port-Hamiltonian representation, 3) deriving stability certificates for the systems that incorporate high-fidelity dc energy source models, e.g., wind generators, 4) stability analysis when decomposing the ac grid models into distributed generators, and 5) an extensive numerical verification of the control performance.

5.6 Appendix A: proof of the technical results

Proof of Theorem 6. Setting the RHS of (5.8) to zero, by Assumption (1), angle dynamics (5.8) at the equilibrium, i.e.,

$$\omega_r + \eta(v_{dc}^* - v_{dc,r}) - \gamma \mathbf{sin} \left(\frac{\delta^* - \delta_r}{2} \right) - \omega_g^* = 0, \quad (5.11)$$

reduces to $\mathbf{sin}((\delta^* - \delta_r)/2) = 0$. This implies that the elements of the angle equilibrium δ^* , i.e., $\delta_j^* \in \{\delta_{r,j}, \delta_{r,j} + 2\pi\}$ for all $j \in \mathcal{N}_{ac}$. Further, Assumption 1 implies the existence of dc voltage and frequency equilibria, thus, their respective dynamics in (5.8) vanish at the equilibrium. Hence, $i_{dc,n}^* = -R^{-1}B^\top v_{dc,r}$, $i_{dc,g}^* = i_{dc,r}$, and $T_r^* = T_r$ that follow from the dc edge, dc generation, and torque dynamics in (5.8) at the equilibrium, respectively.

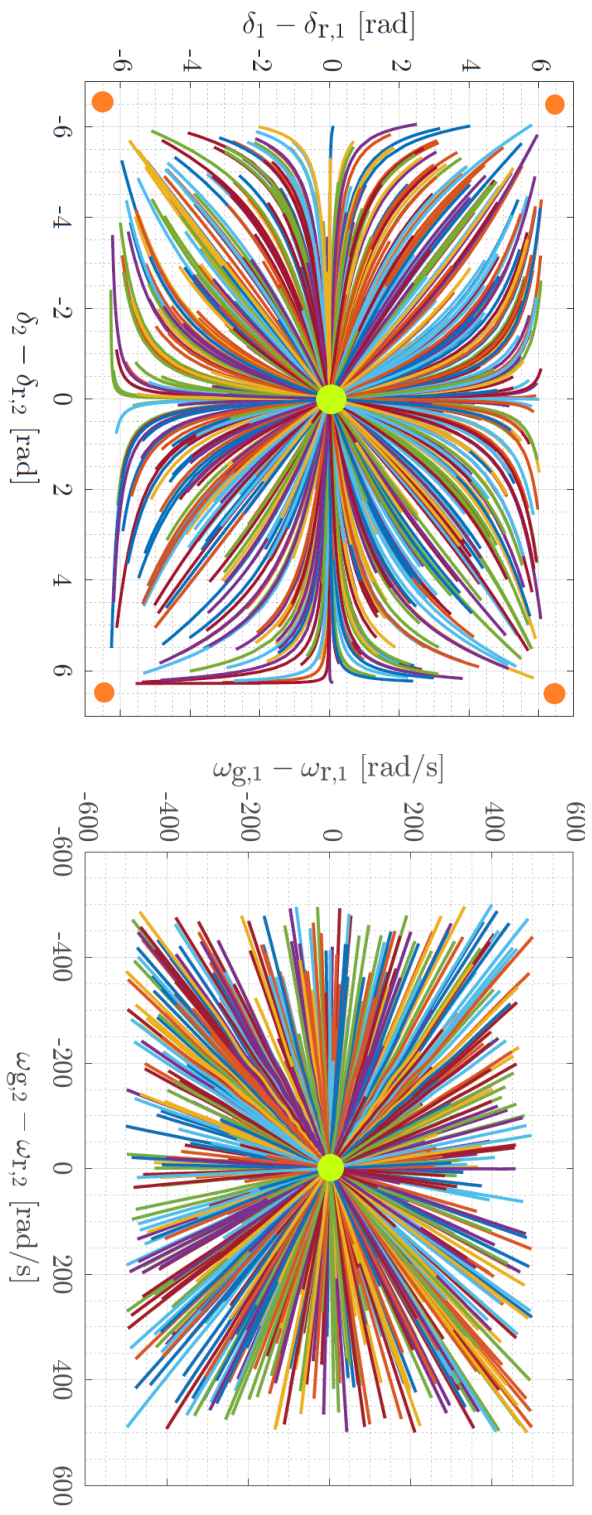


Figure 5.4: The phase portrait of relative angle errors ($\hat{\delta}_1, \hat{\delta}_2$) (left) and angular frequency errors ($\hat{\omega}_{g,1}, \hat{\omega}_{g,2}$) (right).

Next, the ILCs' filter and transmission dynamics can be written as $F\underline{y}^* = h$ where

$$F \triangleq \begin{pmatrix} -(R - \underline{L}\omega_g \otimes J_2) & -I_{2n} & 0 \\ I_{2n} & -(G - \underline{C}\omega_g \otimes J_2) & -I_{2n} \\ 0 & I_{2n} & -(R_g - \underline{L}_g\omega_g \otimes J_2) \end{pmatrix},$$

$\underline{y}^* \triangleq (i^*, v^*, i_g^*)$, and $h \triangleq (-m(\delta^*)v_{dc}^*, 0, \psi\omega_g^*)$. Note that as in [3], the symmetric part of F , i.e., $(1/2)(F + F^\top) \prec 0$ that means F is invertible and \underline{y}^* is unique. Thus, the \underline{y}^* in (5.9) is uniquely given by $\underline{y}^* = (i_{dc,n}^*, i_{dc,g}^*, v_{dc}^*, i^*, v^*, i_g^*, \omega_g^*, T_m^*)$ that completes the proof. \blacksquare

Proof of Theorem 7. Define the error coordinates $\hat{x} \in \mathbb{X}$ w.r.t $x_s^* = (\delta_r^*, \underline{y}^*)$ (as defined in Subsection (5.3.2)), i.e.,

$$\hat{x} \triangleq \begin{pmatrix} \hat{\delta}, \hat{y} \end{pmatrix} \triangleq \begin{pmatrix} \delta - \delta_r, i_{dc,n} - i_{dc,n}^*, i_{dc,g} - i_{dc,g}^*, v_{dc} - v_{dc}^*, i - i^*, v - v^*, i_g - i_g^*, \omega_g - \omega_g^*, T_m - T_m^* \end{pmatrix}. \quad (5.12)$$

Subsequently, the translation of the closed-loop dynamics (5.8) to the coordinates (5.12) results in the error dynamics, i.e.,

$$\dot{\hat{x}} = K^{-1}\hat{f}(\hat{x}), \quad (5.13)$$

where

$$\hat{f}(\hat{x}) \triangleq f(\hat{x} + x_s^*) = \begin{pmatrix} \eta\hat{v}_{dc} - \gamma \mathbf{sin} \frac{\hat{\delta}}{2} - \hat{\omega}_g \\ -B^\top \hat{v}_{dc} - R_{dc}\hat{i}_{dc,n} \\ -\kappa_{dc}\hat{v}_{dc} - \hat{i}_{dc,g} \\ \underline{B}\hat{i}_{dc,n} + \hat{i}_{dc,g} - G_{dc}\hat{v}_{dc} - \hat{m}(\delta)^\top i^* - \underline{m}(\delta)^\top \hat{i} \\ \underline{m}(\delta)\hat{v}_{dc} + \hat{m}(\delta)v_{dc}^* - R\hat{i} - \underline{L}\omega_g \otimes J_2\hat{i} - \underline{L}\hat{\omega}_g \otimes J_2i^* - \hat{v} \\ \hat{i} - G\hat{v} - \underline{C}\omega_g \otimes J_2\hat{v} - \underline{C}\hat{\omega}_g \otimes J_2v^* - \hat{i}_g \\ \hat{v} - R_g\hat{i}_g - \underline{L}_g\omega_g \otimes J_2\hat{i}_g - \underline{L}_g\hat{\omega}_g \otimes J_2i_g^* - \psi\hat{\omega}_g \\ \underline{T}_m - D\hat{\omega}_g + \psi^\top \hat{i}_g \\ -\kappa_g\hat{\omega}_g - \underline{T}_m \end{pmatrix},$$

where we exploited the fact that $f(x_s^*) = 0$ and $\hat{m}(\delta) \triangleq m(\delta) - m(\delta^*)$ denotes the vector

of the trigonometric modulation errors. Consider the LaSalle function candidate:

$$\mathcal{V}(\hat{x}) \triangleq \mathcal{S}(\hat{\delta}) + \mathcal{H}(\hat{y}) = 2 \sum_{j \in \mathcal{N}_{ac}} \lambda_j \left(1 - \cos \frac{\hat{\delta}_j}{2} \right) + \frac{1}{2} \left(\hat{y}^\top P \hat{y} \right), \quad (5.14)$$

where for all $j \in \mathcal{N}_{ac}$, $\lambda_j \in \mathbb{R}_{>0}$ is a free parameter and

$$P =: \text{diag} \left(L_{dc}, \tau_{dc} \kappa_{dc}^{-1}, C, L, L_g, J, \tau_g \kappa_g^{-1} \right) \succ 0$$

with the well-defined model and control parameters. Note that $\mathcal{V}(\hat{x}) > 0$ for all $\hat{x} \neq 0$ (modulo 4π). For notational convenience we collect all λ_j in $\lambda \triangleq \text{diag} \left(\{\lambda_j\}_{j=1}^n \right)$. We evaluate the time derivative of $\mathcal{V}(\hat{x})$ along the solutions of (5.13), that is,

$$\begin{aligned} \dot{\mathcal{V}}(\hat{x}) = & \left(\mathbf{sin} \frac{\hat{\delta}}{2} \right)^\top \left(\lambda \eta \hat{v}_{dc} - \lambda \gamma \mathbf{sin} \frac{\hat{\delta}}{2} - \lambda \hat{\omega}_g \right) - \hat{i}_{dc,n}^\top R_{dc} \hat{i}_{dc,n} - \hat{i}_{dc,g}^\top \kappa_{dc}^{-1} \hat{i}_{dc,g} - \hat{v}_{dc}^\top G_{dc} \hat{v}_{dc} \\ & - \hat{i}^\top R \hat{i} - \hat{v}^\top G \hat{v} - \hat{i}_g^\top R_g \hat{i}_g - \hat{\omega}_g^\top D \hat{\omega}_g - \hat{T}_m^\top \kappa_g^{-1} \hat{T}_m - \hat{v}_{dc}^\top \hat{m}(\delta)^\top i^* + \hat{i}^\top \hat{m}(\delta) v_{dc}^* \\ & - \hat{i}^\top \underline{L} \hat{\omega}_g \otimes J_2 i^* - \hat{v}^\top \underline{C} \hat{\omega}_g \otimes J_2 v^* - \hat{i}_g^\top \underline{L}_g \hat{\omega}_g \otimes J_2 i_g^* \end{aligned} \quad (5.15)$$

where due to the quadratic structure of $\mathcal{H}(\hat{y})$ and choice of P in (5.14), skew-symmetric coupling terms and skew symmetry of J_2 in (5.13) (see the underlined terms), certain terms in $\dot{\mathcal{V}}(\hat{x}) = (\partial \mathcal{V}(\hat{x}) / \partial \hat{x})^\top \hat{\dot{x}}$ either cancel out each other or vanish (see [3] for detailed computations). Next, we derive decoupled bounds on the $\hat{m}(\delta)$ -cross-terms in (5.15), e.g., consider that

$$-\hat{v}_{dc}^\top \hat{m}(\delta)^\top i^* = - \sum_{j \in \mathcal{N}_{ac}} \hat{v}_{dc,j} \mu_j \left(r(\delta_j) - r(\delta_j^*) \right)^\top i_j^*, \quad (5.16)$$

with $r(\delta_j) - r(\delta_j^*) = (\cos(\delta_j) - \cos(\delta_{r,j}), \sin(\delta_j) - \sin(\delta_{r,j}))$.

Rearranging the summand in the RHS of (5.16) and applying the bounding scheme (5.26) results in

$$\left(r(\delta) - r(\delta^*) \right)^\top \left(\hat{v}_{dc,j} \mu_j i_j^* \right) \leq \epsilon_{1,j}^2 \left(\hat{v}_{dc,j} \mu_j \|i_j^*\| \right)^2 + \left(\frac{1}{4\epsilon_{1,j}^2} \right) \left\| r(\delta_j) - r(\delta_j^*) \right\|^2.$$

Applying the trigonometric angle difference and half-angle identities (5.27) and (5.28) yields that

$$\left\| r(\delta_j) - r(\delta_j^*) \right\|^2 = 2 \left(1 - \cos \hat{\delta}_j \right) = 4 \sin^2 \frac{\hat{\delta}_j}{2},$$

and subsequently,

$$(5.16) \leq \sum_{j \in \mathcal{N}_{ac}} \left(\epsilon_{1,j} \mu_j \|i_j^*\| \right)^2 \hat{v}_{dc,j}^2 + \sum_{j \in \mathcal{N}_{ac}} \frac{1}{\epsilon_{1,j}^2} \sin^2 \frac{\hat{\delta}_j}{2}, \quad (5.17)$$

where $\epsilon_{1,j} \in \mathbb{R}_{>0}^n$ for all $j \in \mathcal{N}_{\text{ac}}$ is a constant. The bound in (5.17) takes the alternative form

$$-\hat{v}_{\text{dc}}^\top \hat{m}(\delta)^\top i^\star \leq \hat{v}_{\text{dc}}^\top \varphi_1 \hat{v}_{\text{dc}} + \left(\mathbf{sin} \frac{\hat{\delta}}{2} \right)^\top \varphi_2 \mathbf{sin} \frac{\hat{\delta}}{2}, \quad (5.18)$$

$$\varphi_1 \triangleq \text{diag} \left(\left\{ \left(\epsilon_{1,j} \mu_j \|i_j^\star\| \right)^2 \right\}_{j=1}^n \right), \text{ and } \varphi_2 \triangleq \text{diag} \left(\left\{ \frac{1}{\epsilon_{1,j}^2} \right\}_{j=1}^n \right).$$

By following similar procedure, the other $\hat{m}(\delta)$ -cross-term in (5.15) is bounded as

$$\hat{i}^\top \hat{m}(\delta) v_{\text{dc}}^\star \leq \sum_{j \in \mathcal{N}_{\text{ac}}} \epsilon_{2,j}^2 \|\hat{i}_j\|^2 + \sum_{j \in \mathcal{N}_{\text{ac}}} \left(\frac{\mu_j v_{\text{dc},j}^\star}{\epsilon_{2,j}} \right)^2 \sin^2 \frac{\hat{\delta}_j}{2},$$

where $\epsilon_{2,j} \in \mathbb{R}_{>0}^n$ for all $j \in \mathcal{N}_{\text{ac}}$ is a constant and the bound takes the alternative form

$$\hat{i}^\top \hat{m}(\delta) v_{\text{dc}}^\star \leq \hat{i}^\top \varphi_3 \hat{i} + \left(\mathbf{sin} \frac{\hat{\delta}}{2} \right)^\top \varphi_4 \mathbf{sin} \frac{\hat{\delta}}{2}, \quad (5.19)$$

$$\varphi_3 \triangleq \text{diag} \left(\left\{ \epsilon_{2,j}^2 \otimes I_2 \right\}_{j=1}^n \right), \text{ and } \varphi_4 \triangleq \text{diag} \left(\left\{ \left(\frac{\mu_j v_{\text{dc},j}^\star}{\epsilon_{2,j}} \right)^2 \right\}_{j=1}^n \right).$$

Next, we derive the upper-bounds on the cross-terms in (5.15) that depend on $\hat{\omega}_{\text{g}}$ and either \hat{i} , \hat{v} , or \hat{i}_{g} . These terms arise due to the time-varying angular frequency of the dq-coordinates in (5.8), i.e., ω_{g} . To this end, we employ the identity (5.26) that results in

$$\begin{aligned} -\hat{i}^\top \underline{L} \hat{\omega}_{\text{g}} \otimes J_2 i^\star &\leq \sum_{j \in \mathcal{N}_{\text{ac}}} \epsilon_{3,j}^2 \|\hat{i}_j\|^2 + \sum_{j \in \mathcal{N}_{\text{ac}}} \left(\frac{L_j \|i_j^\star\|}{2\epsilon_{3,j}} \right)^2 \hat{\omega}_{\text{g},j}^2, \\ -\hat{v}^\top \underline{C} \hat{\omega}_{\text{g}} \otimes J_2 v^\star &\leq \sum_{j \in \mathcal{N}_{\text{ac}}} \epsilon_{4,j}^2 \|\hat{v}_j\|^2 + \sum_{j \in \mathcal{N}_{\text{ac}}} \left(\frac{C_j \|v_j^\star\|}{2\epsilon_{4,j}} \right)^2 \hat{\omega}_{\text{g},j}^2, \\ -\hat{i}_{\text{g}}^\top \underline{L}_{\text{g}} \hat{\omega}_{\text{g}} \otimes J_2 i_{\text{g}}^\star &\leq \sum_{j \in \mathcal{N}_{\text{ac}}} \epsilon_{5,j}^2 \|\hat{i}_{\text{g},j}\|^2 + \sum_{j \in \mathcal{N}_{\text{ac}}} \left(\frac{L_{\text{g},j} \|i_{\text{g},j}^\star\|}{2\epsilon_{5,j}} \right)^2 \hat{\omega}_{\text{g},j}^2, \end{aligned}$$

where $\epsilon_{3,j}$, $\epsilon_{4,j}$, and $\epsilon_{5,j} \in \mathbb{R}_{>0}^n$ for all $j \in \mathcal{N}_{\text{ac}}$ are constant and the bounds take the form

$$-\hat{i}^\top \underline{L} \hat{\omega}_{\text{g}} \otimes J_2 i^\star \leq \hat{i}^\top \varphi_5 \hat{i} + \hat{\omega}_{\text{g}}^\top \varphi_6 \hat{\omega}_{\text{g}}, \quad (5.20)$$

$$\varphi_5 \triangleq \text{diag} \left(\left\{ \epsilon_{3,j}^2 \otimes I_2 \right\}_{j=1}^n \right), \text{ and } \varphi_6 \triangleq \text{diag} \left(\left\{ \left(\frac{L_j \|i_j^*\|}{2\epsilon_{3,j}} \right)^2 \right\}_{j=1}^n \right),$$

$$-\hat{v}^\top \underline{C} \hat{\omega}_g \otimes J_2 v^* \leq \hat{v}^\top \varphi_7 \hat{v} + \hat{\omega}_g^\top \varphi_8 \hat{\omega}_g, \quad (5.21)$$

$$\varphi_7 \triangleq \text{diag} \left(\left\{ \epsilon_{4,j}^2 \otimes I_2 \right\}_{j=1}^n \right), \text{ and } \varphi_8 \triangleq \text{diag} \left(\left\{ \left(\frac{C_j \|v_j^*\|}{2\epsilon_{4,j}} \right)^2 \right\}_{j=1}^n \right),$$

$$-\hat{i}_g^\top \underline{L}_g \hat{\omega}_g \otimes J_2 i_g^* \leq \hat{i}_g^\top \varphi_9 \hat{i}_g + \hat{\omega}_g^\top \varphi_{10} \hat{\omega}_g, \quad (5.22)$$

$$\varphi_9 \triangleq \text{diag} \left(\left\{ \epsilon_{5,j}^2 \otimes I_2 \right\}_{j=1}^n \right), \text{ and } \varphi_{10} \triangleq \text{diag} \left(\left\{ \left(\frac{L_{g,j} \|i_{g,j}^*\|}{2\epsilon_{5,j}} \right)^2 \right\}_{j=1}^n \right).$$

Taking into account (5.18)-(5.22), we evaluate an upper-bound on $\dot{\mathcal{V}}(\hat{x})$ in (5.15), i.e.,

$$\begin{aligned} \dot{\mathcal{V}}(\hat{x}) \leq & \left(\mathbf{sin} \frac{\hat{\delta}}{2} \right)^\top \left(\lambda \eta \hat{v}_{\text{dc}} - (\lambda \gamma - \varphi_2 - \varphi_4) \mathbf{sin} \frac{\hat{\delta}}{2} - \lambda \hat{\omega}_g \right) \\ & - \hat{i}_{\text{dc},n}^\top R_{\text{dc}} \hat{i}_{\text{dc},n} - \hat{i}_{\text{dc},g}^\top \kappa_{\text{dc}}^{-1} \hat{i}_{\text{dc},g} - \hat{v}_{\text{dc}}^\top (G_{\text{dc}} - \varphi_1) \hat{v}_{\text{dc}} \\ & - \hat{i}^\top (R - \varphi_3 - \varphi_5) \hat{i} - \hat{v}^\top (G - \varphi_7) \hat{v} - \hat{i}_g^\top (R_g - \varphi_9) \hat{i}_g \\ & - \hat{\omega}_g^\top (D - \varphi_6 - \varphi_8 - \varphi_{10}) \hat{\omega}_g - \hat{T}_m^\top \kappa_g^{-1} \hat{T}_m. \end{aligned} \quad (5.23)$$

Consider the alternative coordinates partitioning $\hat{x} \triangleq (\hat{x}_1, \hat{x}_2)$ that, compared to \hat{x} in (5.12), replaces $\hat{\delta}$ with its nonlinear counterpart $\mathbf{sin} \left(\frac{\hat{\delta}}{2} \right)$ and reshuffles the elements of \hat{x} as

$$\begin{aligned} \hat{x}_1 & \triangleq \left(\sin \frac{\hat{\delta}_1}{2}, \hat{v}_{\text{dc},1}, \hat{\omega}_1, \dots, \sin \frac{\hat{\delta}_n}{2}, \hat{v}_{\text{dc},n}, \hat{\omega}_n \right), \\ \hat{x}_2 & \triangleq \left(\hat{i}_{\text{dc},n}, \hat{i}_{\text{dc},g}, \hat{i}, \hat{v}, \hat{i}_g, \hat{T}_m \right). \end{aligned}$$

Hence, the RHS of (5.23) takes a quadratic form in \hat{x} , i.e.,

$$\dot{\mathcal{V}}(\hat{x}) \leq -\hat{x}^\top Q \hat{x} = -\left(\hat{x}_1^\top Q_{11} \hat{x}_1 + \hat{x}_2^\top Q_{22} \hat{x}_2 \right) \quad (5.24)$$

where $Q_{11} \triangleq \text{diag} \left(\{Q_{11,j}\}_{j=1}^n \right)$ with

$$Q_{11,j} \triangleq \begin{pmatrix} \lambda_j \gamma_j - \frac{1}{\epsilon_{1,j}^2} - \left(\frac{\mu_j v_{\text{dc},j}^*}{\epsilon_{2,j}} \right)^2 & -\frac{\lambda_j \eta_j}{2} & \frac{\lambda_j}{2} \\ -\frac{\lambda_j \eta_j}{2} & G_{\text{dc},j} - \left(\epsilon_{1,j} \mu_j \|i_j^*\| \right)^2 & 0 \\ \frac{\lambda_j}{2} & 0 & Q_{1133,j} \end{pmatrix}, \quad (5.25)$$

where

$$Q_{1133,j} = D_j - \left(\frac{L_j \|i_j^*\|}{2\epsilon_{3,j}} \right)^2 - \left(\frac{C_j \|v_j^*\|}{2\epsilon_{4,j}} \right)^2 - \left(\frac{L_{g,j} \|i_{g,j}^*\|}{2\epsilon_{5,j}} \right)^2,$$

and

$$Q_{22} \triangleq \text{diag} \left(R_{\text{dc}}, \kappa_{\text{dc}}^{-1}, R - \varphi_3 - \varphi_5, G - \varphi_7, R_g - \varphi_9, \kappa_g^{-1} \right).$$

Now, let us assign the free parameters as $\lambda_j = 2/\eta_j$, $\epsilon_{1,j} = \sqrt{G_{\text{dc},j}} / (\sqrt{2}\mu_j \|i_j^*\|)$, $\epsilon_{2,j} = \sqrt{R_j}/2$, $\epsilon_{3,j} = \sqrt{R_j}/2$, $\epsilon_{4,j} = \sqrt{G_j}/2$, and $\epsilon_{5,j} = \sqrt{R_{g,j}}/2$ for all $j \in \mathcal{N}_{\text{ac}}$. This set of parameters directly implies the positive definiteness of Q_{22} . Next, standard Schur complement analysis yields that Q_{11} is positive definite if and only if (5.10) is satisfied.

Since $\dot{\mathcal{V}}(\hat{x}) \leq 0$ for any $\hat{x}(0) \in \mathbb{X}$, then the c -sublevel sets of $\mathcal{V}(\hat{x})$, i.e., $\mathcal{L}_c \triangleq \{\hat{x} \in \mathbb{X} : \mathcal{V}(\hat{x}) \leq c\}$ with $c \triangleq \mathcal{V}(\hat{x}(0))$, is a forward invariant and compact due to the boundedness of $\hat{\delta}$ in \mathbb{M}^n (that is the union of n compact Möbius strip boundaries) and the radial unboundedness of $\mathcal{H}(\hat{y})$. Hence, by invoking the LaSalle's invariance principle, the solutions of (5.13) globally converge to the largest invariant set $\mathcal{M} \subset \Omega \triangleq \{\hat{x} \in \mathbb{X} : \dot{\mathcal{V}}(\hat{x}) = 0\}$. Under the conditions (5.10), $Q \succ 0$ in (5.24). Thus, $\dot{\mathcal{V}}(\hat{x}) = 0$ iff $\hat{x} = 0$. Finally, $\hat{x} = 0$ characterizes a set that is identical to Ω^* in (5.9), i.e., $\Omega = \Omega^*$. ■

Proof of Corollary 1. Consider the coordinates (5.12) (that are written w.r.t x_s^*) and dynamics (5.13). Note that $\mathcal{V}(\hat{x})$ vanishes at the origin and $\mathcal{V}(\hat{x}) > 0$ otherwise in \mathbb{X} . By Theorem 8, if (5.10) is satisfied, $\dot{\mathcal{V}}(\hat{x}) < 0$ in a sufficiently small open neighborhood of x_s^* (that excludes any other equilibria in Ω^*). The existence of such an open neighborhood is guaranteed since all equilibria in Ω^* are disjoint. Consider a sufficiently small \underline{c} -sublevel set of $\mathcal{V}(\hat{x})$ i.e., $\mathcal{L}_{\underline{c}} \triangleq \{\hat{x} \in \mathbb{X} : \mathcal{V}(\hat{x}) \leq \underline{c}, \underline{c} \in \mathbb{R}_{>0}\}$ such that it excludes all the equilibria in Ω^* except x_s^* . Note that for sufficiently small \underline{c} , $\dot{\mathcal{V}}(\hat{x}) \leq 0$ for all \hat{x} in $\mathcal{L}_{\underline{c}}$. Thus, $\mathcal{L}_{\underline{c}}$ is positively invariant w.r.t (5.13). Last, applying the Lyapunov's direct method concludes the asymptotic stability of $x_s^* \in \Omega^*$. ■

5.7 Appendix B: mathematical identities

Lemma 2 (Algebraic and trigonometric identities). *For $u, w \in \mathbb{R}^2$, $\epsilon \in \mathbb{R}_{>0}$ and $\vartheta, \varrho \in \mathbb{S}^1$ the followings hold*

$$\pm u^\top w \leq \epsilon^2 \|u\|^2 + \left(\frac{1}{4\epsilon^2}\right) \|w\|^2, \quad (5.26)$$

$$\cos(\vartheta \pm \varrho) = \cos \vartheta \cos \varrho \mp \sin \vartheta \sin \varrho, \quad (5.27)$$

$$\sin^2 \frac{\vartheta}{2} = \frac{1 - \cos \vartheta}{2}. \quad (5.28)$$

System-level performance and robustness of the grid-forming hybrid angle control

Presented at the Power System Computation Conference (PSCC) 2022 and published in the Elsevier Electric Power System Research Journal.

Authors – Ali Tayyebi, Alan Magdaleno, Denis Vettoretti, Meng Chen, Eduardo Prieto-Araujo, Adolfo Anta, and Florian Dörfler.

Abstract – This paper investigates the implementation and application of the multi-variable grid-forming HAC for high-power converters in transmission grids. We explore the system-level performance and robustness of HAC concept in contrast to other grid-forming schemes i.e., power-frequency droop and matching controls. Our findings suggests that, similar to the ac-based droop control, HAC enhances the small-signal frequency stability in low-inertia power grids, and akin to the dc-based matching control, HAC exhibits robustness when accounting for the practical limits of the converter systems. Thus, HAC combines the aforementioned complementary advantageous. Furthermore, we show how retuning certain control parameters of the grid-forming controls improves the frequency performance. Last, as separate contributions, we introduce an alternative control augmentation that enhances the robustness and provides theoretical guidelines on extending the stability certificates of HAC to multi-converter systems.

6.1 Introduction

The ambitious targets that are set to globally reduce the carbon footprint require revolutionizing the foundations of legacy power systems. In other words, the SM-based energy generation from fossil fuels must be replaced with green and sustainable energy sources. The majority of clean energy sources interface the power grids via dc-ac power converters. Although, in contrast to the bulk SMs, power converters are fast, modular, and highly controllable, they are subject to volatile energy resources and lack the necessary robustness and maturity to ensure adequate and reliable power delivery. It is envisioned that the advanced control architectures for power converters can possibly address the

aforementioned concerns [25]–[27], [33].

The so-called *grid-following* converter controls that exploit an explicit synchronizing mechanism are widely utilized [7], [130], [131]. However, the grid-following converters exhibit robustness and stability issues in the converter-dominated grids that are highlighted by a significant reduction of rotational inertia i.e., *low-inertia* grids; see [2], [100], [132] among others. Subsequently, the concept of *grid-forming converter (GFC)* is introduced that provides fast and robust frequency and voltage regulation to address the stability challenges associated with the low-inertia systems [1], [24].

Several grid-forming control techniques have been proposed in recent years. Restricting the focus to converter frequency definition under these controls, one can highlight fundamental differences. The vast majority of grid-forming techniques e.g., droop control, virtual synchronous machine (VSM), and oscillator-based schemes shape the converter frequency based on the ac quantities such as current, voltage, and power flows e.g., [34]–[36], [38], [45], [46], [49], [52], [64], [104], [133], [134]. Recently, a class of controllers have been proposed that define the converter frequency in proportion to a linear/nonlinear dc voltage feedback [40], [41], [43], [44], [65], [125], [126]. Most recently, the emerging multi-variable control trend is to combine dc and ac information in designing the GFC frequency [3], [4], [8]–[10], [55], [57].

In this work, we focus on the grid-forming hybrid angle control (HAC) that blends linear dc and nonlinear ac feedback for defining converter frequency [3], [4], [8]. We provide:

- * detailed guidelines for a system-level implementation of the HAC [3], [4], [8] accompanied by several practical remarks on the properties and behavior of the HAC,
- * HAC performance evaluation in contrast to other grid-forming controls via various simulation case studies involving single/two-area power grid models,
- * insights concerning the influence of appropriately tuned local converter control parameters on the global system frequency performance and findings on the PSS-free operation of the converter-dominated grids,
- * a high-level stability analysis that presents guidelines on extending the stability certificates of HAC (as in [3], [4], [8]) to an interconnected system of converters,
- * and finally, a complementary dynamic inverse droop control augmentation for enhancing the HAC robustness.

The remainder of this paper is structured as follows: Section 6.2 presents our modeling approach for low-inertia power grids, Section 6.3 describes three different grid-forming controls and highlights their dominant features. Furthermore, it provides practical details on the implementation of HAC. Section 6.4 presents several comparative case studies.

Last, the Appendix introduces a variant of HAC with enhanced robustness and includes a high-level stability investigation for multi-converter systems under HAC.

6.2 Modeling description

In this paper, we consider a transmission power grid that is fed by a mixture of SM and converter-based generation units. For the sake of completeness, we briefly review the SM, network, and converter modeling; the reader is referred to [1] for further elaborations.

6.2.1 Synchronous machine

In this work, we consider a detailed nonlinear SM model that incorporates second-order mechanical dynamics (associated with angle and frequency) and sixth-order electrical dynamics (associated with the stator, damper, and field winding fluxes). Furthermore, the SM is combined with a first-order dynamic turbine model. The reader is referred to [1, Section II-B][62] for a detailed description of the SM modeling. It is noteworthy that we include the standard SM control mechanisms such as automatic voltage regulator (AVR), PSS, and turbine governor control; see [1] for details. Furthermore, the governor gain in [1, Equation 5] is exploited to realize coordinated load-sharing with other generation units across the system; see [1, Appendix] for a tuning criteria recommendation.

6.2.2 Power network

The generation units are considered to interface the transmission lines via identical medium-to-high voltage (MV/HV) transformers. We consider dynamic transmission lines represented with standard π -section models [1], [62]. Furthermore, the network loads are modeled by constant impedances. We emphasize that the load models are voltage-dependent and restrict our focus to the active power loads that primarily influence the frequency dynamics in transmission grids. Note that due to the fast timescales of the GFCs and potential adverse interactions with line dynamics, the quasi-steady-state algebraic network model assumption is not valid [45, Subsection III-A], hence it is necessary to consider dynamic line models for low-inertia power systems [47], [100].

6.2.3 High-power DC-AC converter

The power converter model in this work includes an explicit first-order representation of the dc energy source dynamics, dc-link capacitance, power-preserving (i.e., lossless) average model of the two-level dc-ac conversion stage, and the LC output filter. Furthermore, we consider the current limits of the dc energy source that in practice corresponds to the

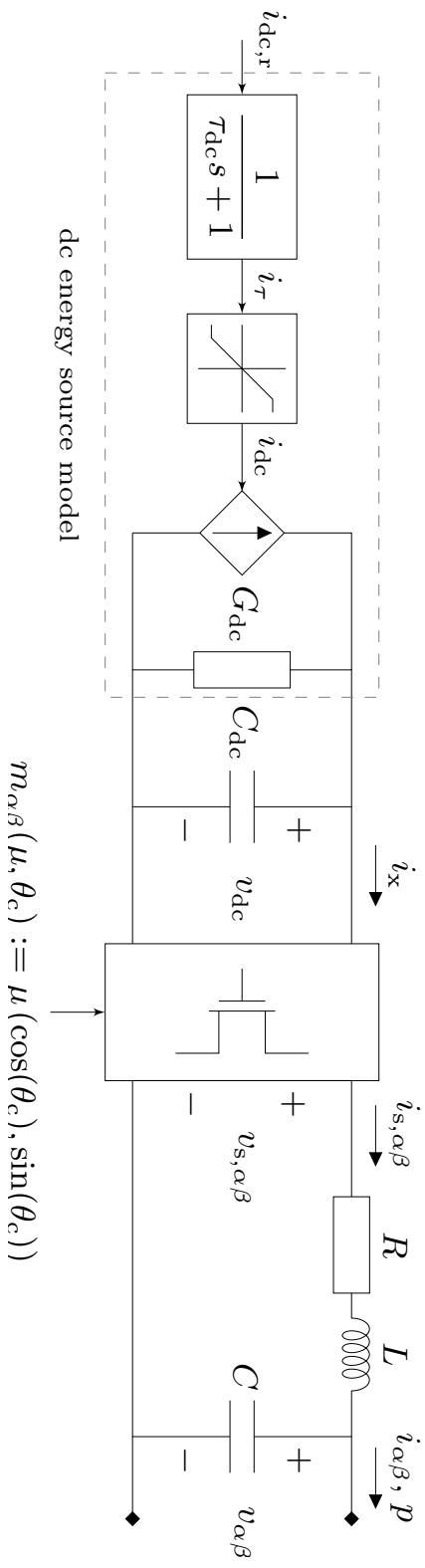


Figure 6.1: DC-AC power converter model schematic with ac quantities represented in stationary $\alpha\beta$ -coordinates [1], [73].

current limits of the PV, battery, or wind generator systems. It is worth mentioning that in this work the dc source model represents an aggregation of several energy sources that supply a modular high-power converter; see Section 6.4 for further details. Figure 6.1 present the schematic of the converter model; see [1, Subsection II-A] for further details and the differential equations corresponding to the Figure 6.1.

The converter model illustrated in Figure 6.1 provides three control degrees of freedom, namely: 1) the dc source current reference $i_{\text{dc,r}}$, 2) the modulation signal magnitude i.e., $\mu = \|m_{\alpha\beta}(\mu, \theta_c)\|$, and the modulation signal angle i.e., $\theta_c = \angle m_{\alpha\beta}(\mu, \theta_c)$. In Section 6.3, we elaborate on the definition of these control inputs under three different grid-forming control strategies.

6.3 Grid-forming frequency controls

The vast literature on grid-forming control schemes can be distinctly assigned into three categories:

- * ac-based control techniques that define the converter frequency based on ac measurements e.g., see [34]–[36], [38], [45], [46], [49], [64], [104], [133], [134],
- * dc-based model-matching inspired techniques that relate the converter frequency to the dc measurements e.g., see [40], [41], [43], [44], [65], [125], [126], and
- * multi-variable hybrid control structures that exploit both dc and ac measurements for a grid-forming frequency synthesis e.g., see [3], [8], [9], [55], [57].

In what follows, we review a candidate from each control category and highlight their dominant features.

6.3.1 AC-based power-frequency droop control

The baseline power-frequency droop control that is inspired by the frequency droop behavior of the SM, serves as a powerful yet simple control solution for grid-forming converter applications [34]–[36], [134]. The power-frequency droop control in its simplest form is described by

$$\dot{\theta}_c = \omega_c := \omega_0 + d_{p-\omega}(p_r - p), \quad (6.1)$$

where θ_c denotes the phase angle of the converter modulation signal $m_{\alpha\beta}(\mu, \theta_c)$ in Figure 6.1, ω_c denotes the converter angular frequency, ω_0 denotes the nominal system frequency, $d_{p-\omega}$ is the power-frequency droop gain, p_r is the control reference for the active power flowing out of the converter’s ac-side terminal that is defined by $p := v_{\alpha\beta}^\top i_{\alpha\beta}$. The ac-based nature of the droop control can be observed in (6.1) that highlights the

frequency dependency on the ac active power feedback. It is worth mentioning that low-pass filtering the active power feedback in (6.1) is a common practice to safeguard the converter control against measurement imperfections and high-frequency harmonics [51, Section I]. Section 6.4 presents a case study that unveils the strong influence of such low-pass filtering in reshaping the system-level post-contingency frequency evolution.

Remark 15 (Enhanced small-signal frequency stability). *Recent explorations [1], [2], [7] uncover that the ac-based grid-forming control strategies e.g., droop control, VSM, and dispatchable virtual oscillator control (dVOC) clearly improve the small-signal frequency stability (in terms of the RoCoF and nadir performance metrics) of the low-inertia system compared to the all-SMs conventional system. This is primarily underpinned by the fast response timescale of the GFCs that enables fast frequency regulation. Furthermore, it has been observed that the ac-based grid-forming schemes exhibit slightly better frequency response compared to the dc-based counterparts e.g., the matching control (presented in the next Subsection); see [1, Subsection IV-C] for details. This behavior is due to the fact that following a network contingency/disturbance, the ac feedback (e.g., p in (6.1)) quickly reflects the grid conditions in the converter frequency definition and enables fast frequency regulation.*

6.3.2 DC-based model-matching control

Inspired by the structural similarities of the SM and converter dynamical models, a family of model-matching control techniques have been proposed [40], [41], [43], [44], [65], [125], [126]. These control structures establish strong duality between the converter and SM dynamical structure; see [40] for a detailed derivation. Matching control in its original form is described by [65]

$$\dot{\theta}_c = \omega_c := \eta v_{dc}, \quad (6.2)$$

where $\eta := \omega_0/v_{dc,r}$ in which $v_{dc,r}$ denotes the reference for the dc voltage v_{dc} . Note that (6.2) highlights the dc-based nature of the matching strategy. Similar to droop control, it might be necessary to low-pass filter the dc feedback in (6.2) to safeguard the angle dynamics against potential dc-link voltage ripples.

Remark 16 (Enhanced robustness). *Recall that the SMs can be operated with either flexible or constant mechanical input torque, and regardless of this degree of freedom, the SMs achieve robust synchronization with the power grid (thanks to their inherent self-synchronizing feature [40], [43], [65], [109]). Under the strong converter-SM duality induced by matching control, the converter can be operated with either constant or flexible input dc current that is injected by the dc energy source in Figure 6.1. This property of*

the matching control comes strongly into the picture when considering the safety current constraints of the dc energy source; see the saturation function in Figure 6.1. Recent works [1], [55], [105] formally and numerically demonstrate that the matching controls (unlike the ac-based schemes) preserve the closed-loop stability under active dc current constraint. This behavior can be perceived as a built-in mode-switching feature that simultaneously changes the converter operation mode from voltage (i.e., grid-forming) to current (i.e., grid-following) source when the dc constraint is activated; e.g., see [1, Figure 15]. To our knowledge this is the most dominant feature of the dc-based controls i.e., superior robustness.

6.3.3 Hybrid angle control

The hybrid ac/dc grid-forming control architecture appears as a natural extension and the promising solution for combining the aforementioned complementary benefits of the ac/dc-based control schemes [3], [8], [55], [57]; see Remarks 15 and 16. In what follows, we restrict our focus to the recently proposed HAC that blends linear dc voltage and nonlinear ac angle error terms for defining the converter frequency [3], [8]. The grid-forming HAC is described by

$$\dot{\theta}_c = \omega_c := \omega_0 + \underbrace{\gamma_{dc} (v_{dc} - v_{dc,r})}_{\text{dc model-matching}} - \underbrace{\gamma_{ac} \sin\left(\frac{\delta - \delta_r}{2}\right)}_{\text{ac angle synchronization}}, \quad (6.3)$$

where γ_{dc} and γ_{ac} respectively denote the dc and ac control gains, and $\delta := \angle v_{s,\alpha\beta} - \angle v_{\alpha\beta} = \theta_c - \theta_v$ denotes the phase angle difference (i.e., the relative angle) of the voltage before the filter and the output voltage in Figure 6.1, and δ_r denotes the control reference for δ . Note that the dc term in (6.3) is identical to the matching control variant proposed in [41] and the nonlinear ac term in (6.3) resembles the Kuramoto-like angle synchronizing term associated with the classic droop control (6.1) under certain assumptions [3, Remark 3][34]. The practical implementation of (6.3) will be explored in the next section. The reader is referred to [3], [8] for details on the design and properties of the HAC. However, the following presents a brief summary:

- * HAC (6.3) incorporates an inherent dc-ac power-balancing behavior i.e., assuming $\omega_c \rightarrow \omega_0$ then $\gamma_{dc} (v_{dc} - v_{dc,r}) - \gamma_{ac} \sin(\delta - \delta_r/2) \rightarrow 0$. For instance, this means that if $v_{dc} > v_{dc,r}$ then $\delta > \delta_r$ that allows for increased power injection into the ac-side and subsequently stabilizes the dc voltage.
- * The dc gain γ_{dc} predominantly reinforces the frequency dependency on the dc dynamics. It is expected that a nonzero dc gain enables HAC to exhibit the

robustness of dc-based controls (see Remark 16 for details and Section 6.4 for a numerical justification of this hypothesis.)

- * The ac gain γ_{ac} strongly influences the timescale associated with the ac-side power flows. Therefore, it resembles the influence of the droop gain on the performance of the droop control.

6.3.4 DC and AC voltage control schemes

The grid-forming droop, matching and hybrid angle controls (6.1)-(6.3) define the phase angle that enters the converter modulation signal $m_{\alpha\beta}(\mu, \theta_c)$ in Figure 6.1. It remains to close the loop by assigning the remaining control inputs i.e., the dc energy source reference current $i_{dc,r}$ and modulation signal magnitude μ . For the sake of fairness in the forthcoming comparative investigation, we consider identical complementary dc and ac voltage controls (that respectively define $i_{dc,r}$ and μ) for the aforementioned grid-forming strategies.

Concerning the dc voltage control, we adopt the scheme that is proposed in [1] (see [40] for a similar approach) i.e.,

$$i_{dc,r} := \underbrace{\kappa_{dc} (v_{dc,r} - v_{dc})}_{\text{proportional control}} + \underbrace{\frac{p_r}{v_{dc,r}} + \left(G_{dc} v_{dc} + \frac{v_{dc} i_x - p}{v_{dc,r}} \right)}_{\text{power injection and loss feedforward}} \quad (6.4)$$

where κ_{dc} denotes the proportional dc voltage control gain and $i_x := m_{\alpha\beta}^\top i_{\alpha\beta}$ denotes the net dc current injection to the ac-side; see Figure 6.1. Note that the power injection and loss compensation terms¹ in (6.4) are not necessary but improve the dynamic response and power set-point tracking [1], [40].

Next, inspired by the AVR mechanism of the SMs, we augment the grid-forming strategies with a proportional-integral (PI) ac voltage magnitude control [1], [135] that is (with slight abuse of the notation) given by

$$\mu := \kappa_p (v_r - \|v_{\alpha\beta}(t)\|) + \kappa_i \int_0^t (v_r - \|v_{\alpha\beta}(s)\|) ds, \quad (6.5)$$

where κ_p and κ_i respectively denote the proportional and integral ac voltage control gains, and v_r denotes the reference ac voltage amplitude. We remark that the robust ac voltage regulation under (6.5) is favorable for a GFC (particularly in islanded/microgrid applications). However, one can alternatively consider a classic reactive power-voltage

¹The compensation scheme in (6.4) is conventionally known as feedforward control, however due to the presence of the state-dependent quantities (such as v_{dc} , i_x , and p) it technically represents an algebraic state feedback.

droop control as in [100]. Subsequently, the converter modulation signal in Figure 6.1 is defined based the angle in (6.1)-(6.3) and the magnitude prescribed by (6.5). Last, in case studies presented in the Section 6.4 we identically tune the dc and ac voltage controls (6.4) and (6.5) for all grid-forming strategies.

6.3.5 Hybrid angle control implementation

In this subsection, we elaborate on the implementation of the grid-forming HAC. Before embarking upon these discussions, we remark that the implementation of droop control (6.1), matching control (6.2), and voltage controls (6.4) and (6.5) is previously addressed; the reader is referred to [1], [35], [40], [41], [71] for details.

Concerning the implementation of HAC (6.3), previous works [3], [8] establish the theoretical foundations. However, the implementation presented in [3], [8] is not straightforward, thus in what follows, we make the reported ideas clear.

To begin with, the dc component of the HAC (6.3) is easily constructed based on the dc voltage measurement in Figure 6.1; see the the dc feedback control in Figure 6.2.

Prior to describing the implementation of the angle synchronizing term in (6.3), note that $\delta = \theta_c - \theta_v$, thus one has to implicitly/explicitly derive the angle information from the output ac voltage measurement. Assume that the ac voltage control (6.5) is sufficiently fast such that $\|v_{\alpha\beta}\| \approx v_r$ (i.e., $\|v_{abc}\| \approx v_r$ that follows from the magnitude-preserving Clarke transformation [3], [73]).

As it is illustrated in Figure 6.2, $\bar{v}_{abc} := v_{abc}/v_r$ denotes the normalized three-phase ac output voltage (note that \bar{v}_{abc} represents a unity phasor in polar coordinates that rotates with angle θ_v). Next, we transform this quantity to a dq-coordinates that is aligned with the converter modulation angle θ_c . Thus, the image of \bar{v}_{abc} in the dq-rectangular coordinates (i.e., the unit vector rotating with the angle $\theta_v - \theta_c = -\delta$) implicitly contains the relative angle information i.e.,

$$(\bar{v}_d, \bar{v}_q) = (\cos(\theta_v - \theta_c), \sin(\theta_v - \theta_c)) = (\cos \delta, -\sin \delta).$$

Similar to low-pass filtering the active power feedback for the droop control (6.1), we apply a first-order low-pass filter to $(\cos \delta, -\sin \delta)$ where ω_f denotes the cutoff frequency. Subsequently, the filter output represents an approximation of the $(\cos \delta, -\sin \delta)$ that is $(\widetilde{\cos \delta}, -\widetilde{\sin \delta})^2$.

On the other hand, we process a given relative angle reference δ_r that is consistent with desired power flows by the trigonometric functions that results in $(\cos \delta_r, -\sin \delta_r)$ (see [3] which shows how δ_r relates to the power and voltage set-points). Finally, by exploiting the angle difference trigonometric identities and the half-angle sine formula

²Note that the LPF can be alternatively applied to v_{abc} in Figure 6.2.

[3, Lemma 1 and Proposition 5] an approximation of the angle term in (6.3) is obtained

$$-\sin\left(\frac{\delta - \delta_r}{2}\right) \approx \frac{\sin \delta_r \widetilde{\cos \delta} - \widetilde{\sin \delta} \cos \delta_r}{\sqrt{2\left(1 + \widetilde{\cos \delta} \cos \delta_r + \widetilde{\sin \delta} \sin \delta_r\right)}}. \quad (6.6)$$

Respective multiplication of (6.6) and the dc voltage error with the gains γ_{ac} and γ_{dc} provides the necessary ingredients for implementing HAC (6.3).

The reader is referred to [3, Section V] for further discussions.

6.4 Numerical case studies

In this section, we employ the standard IEEE 9-bus test system as described in [1], [71], [100]; see Figure 6.3 and Table 6.1 for the model and control parameters. This system represents a transmission grid in which the SMs are rated at 100 [MVA]. Thus, in order to study the system-level influence of the GFCs, it is ideally desired to consider a roughly similar rating for the GFCs as that of the SMs. Therefore, we employ the dynamic aggregation technique proposed in [136] that provides appropriate scaling laws for deriving the aggregated parameters of a high-power converter system based on the parameters of a smaller module.

To this end, we consider a GFC module rated at 500 [kVA] that corresponds to a commercially available system; see [1, Table 1] for the parameters. Next, we envision a parallel connection of 200×500 [kVA] units that is represented with a 100 [MVA] aggregated model with the same structure as in Figure 6.1. The reader is referred to [1, Figure 2 and Remark 1][2], [136] for further details and similar model aggregation approaches. In what follows, the system-level performance of the grid-forming hybrid angle control is explored in various case studies. Note that the employed simulation model in the MATLAB/Simulink environment is publicly available [71].

6.4.1 Purely converter-based system

In this scenario, we remove the SMs from the grid model shown in Figure 6.3 and consider three identical GFCs at nodes 1-3. We implement the HAC strategy (as in Figure 6.2) for all the GFCs and identically tune the controllers (resulting in equal load-sharing). Figure 6.4 illustrates the frequency and active power evolution at the generation nodes following a 0.75 [pu] load-disturbance at node 7. Note that we do not implement an explicit frequency measurement mechanism and rather observe the internal frequency of the GFCs i.e., (6.3).

Figure 6.4 firstly verifies the grid-forming nature of HAC technique i.e., the au-

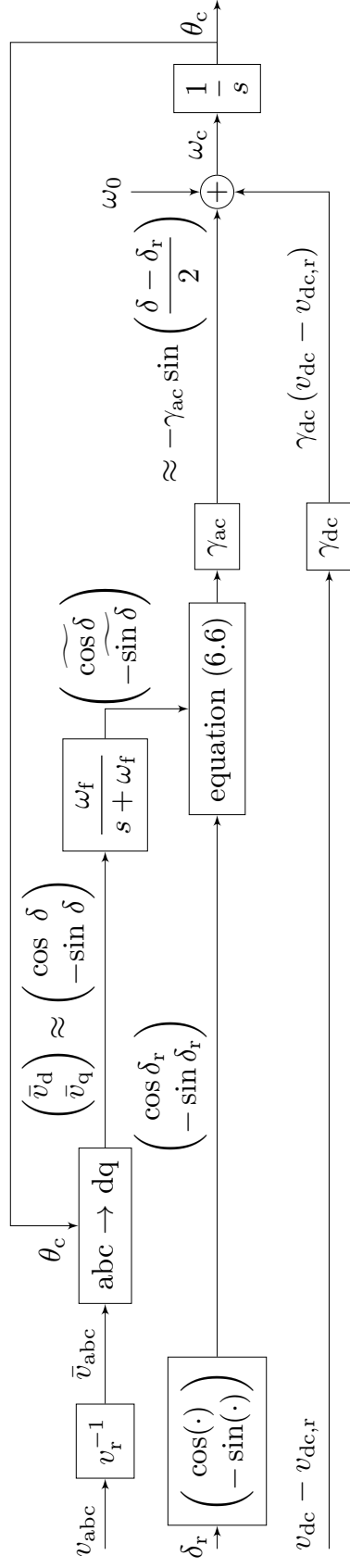


Figure 6.2: Block diagram of the HAC (6.3) based on the dc voltage and the output ac voltage measurements in Figure 6.1.

Table 6.1: Case study model and control parameters [71].

IEEE 9-bus test system base values					
S_b	100 MVA	v_b	230 kV	ω_b	50 Hz
Synchronous machine					
S_r	100 MVA	v_r	13.8 kV	D	0
H	3.7 s	d_p	1%	τ_g	5 s
Single converter module					
S_r	500 kVA	G_{dc}, C_{dc}	0.83, 0.008 Ω^{-1}, F	$v_{dc,r}, v_{ll-rms,r}$	2.44, 1 kV
R	0.001 Ω	L	200 μH	C	300 μF
n	200	τ_{dc}	50 ms	i_{max}^{dc}	1.2 pu
DC and AC voltage controls					
k_{dc}	1.6×10^3	k_p	0.001	k_i	0.5
Droop control, matching control, and HAC					
ω_0	ω_b	$d_{p-\omega}$	1%	η	$\omega_0/v_{dc,r}$
γ_{dc}	0.01η	γ_{ac}	205	δ_r	0.0238

tonomous operation of converters without relying on a reference frequency provided by an external source (as in the case of grid-following devices). Second, note that all GFCs reach the post-contingency equilibrium in approximately 200 [ms]. This fast response timescale is crucial for a satisfactory grid-forming performance [33]. Observe that the units that are electrically closer to the disturbance location i.e., GFCs at node 2 and 3 react on a slightly faster timescale. Last, Figure 6.4 confirms the equal load-sharing of the GFCs. See [1], [2] for similar observations concerning the behavior of other grid-forming schemes in an all-GFCs network.

6.4.2 The influence on the frequency performance metrics

In what follows, we explore the influence of grid-forming architectures (presented in Section 6.3) on the frequency stability of low-inertia configuration associated with the grid model shown in Figure 6.3 i.e., with SM at node 1 and GFCs at nodes 2 and 3. More precisely, we 1) implement identical droop controllers for both GFCs, 2) implement matching control for the GFCs, and finally 3) consider HAC for the converters. Subsequently, for all the 1SM-2GFCs pairs under different controls, we apply five load-

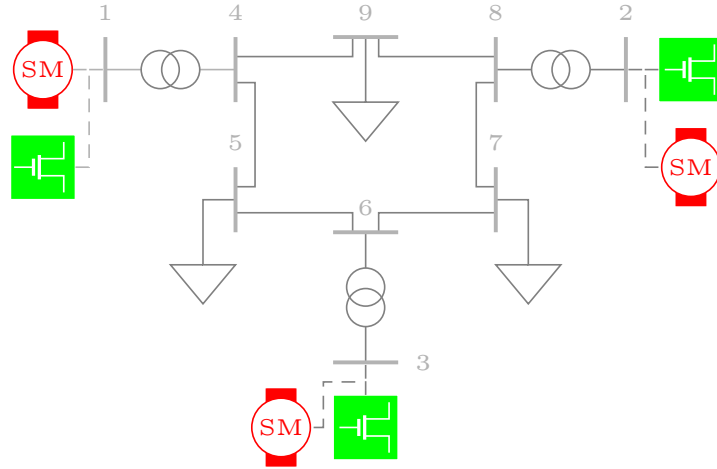


Figure 6.3: IEEE 9-bus test system including SMs and GFCs; depending on the choice of the generation technology at nodes 1, 2, and 3 this network model represents: 1) a conventional system (i.e., all-SMs), 2) a SM-dominated system (2SMs-1GFC), 3) a low-inertia system (i.e., 1SM-2GFCs), and 4) a purely converter-based system (i.e., all-GFCs).

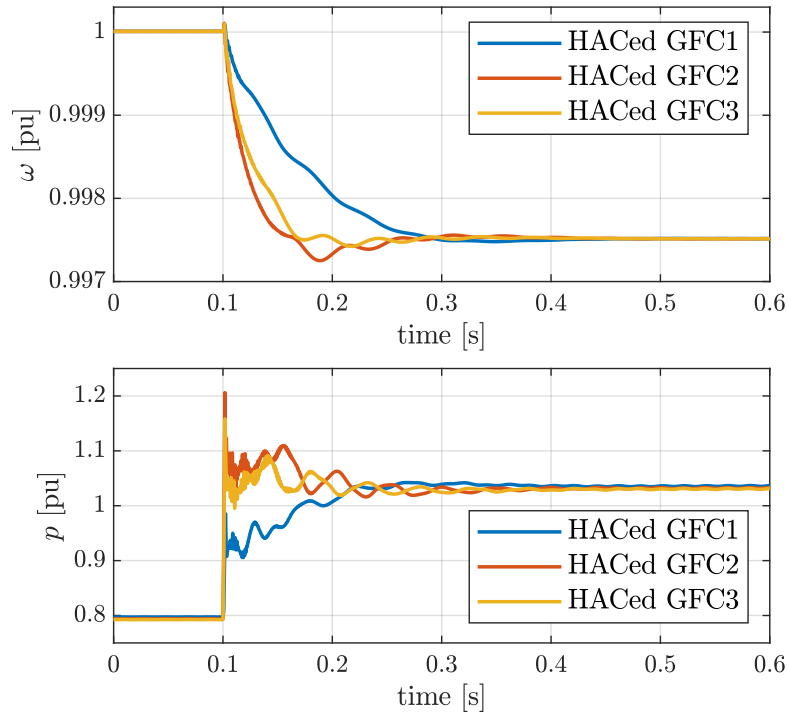


Figure 6.4: Frequency response of the all-GFCs IEEE 9-bus system configuration under HAC strategy following a load disturbance (top), the active power time-evolution associated with the GFCs at node 1, 2, and 3 (bottom).

disturbances at note 7 i.e., $\Delta p_{\ell,k} = 15k$ [MVA] where $k = 1, \dots, 5$. Next, we observe the frequency dynamics via the angular frequency of the SM at node 1; see [1], [2] for similar approaches. We evaluate the standard frequency performance metrics, namely:

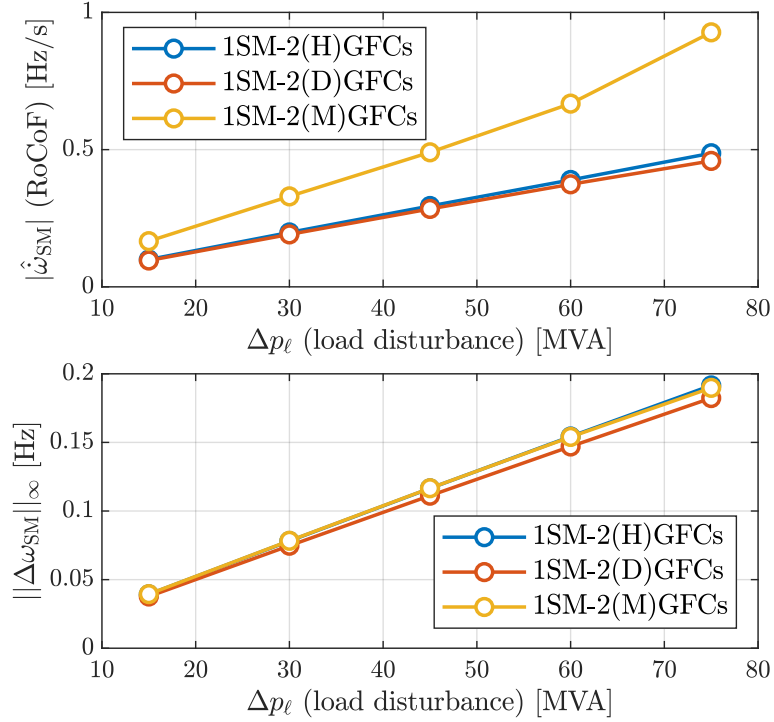


Figure 6.5: RoCoF evolution of the SM at node 1 in 1SM-2GFCs system configuration under different controls and with respect to variations in network load disturbance (top), maximum frequency deviation (bottom).

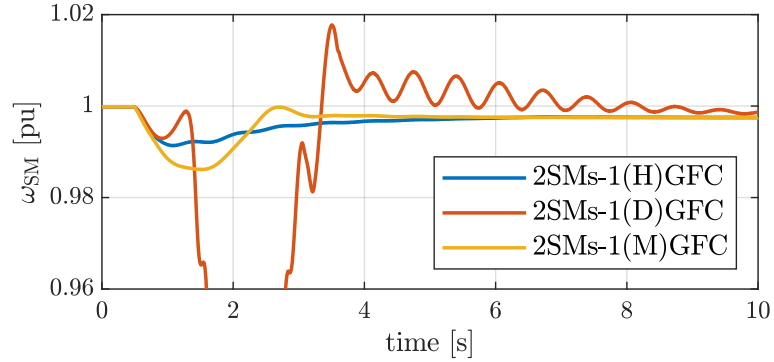


Figure 6.6: The post-event frequency time-evolution of the SM at node 1 in 2SMs-1GFC system configuration under different controls for the GFC.

1) maximum frequency deviation, and 2) RoCoF that are (with slight abuse of notation) defined by [1], [70]

$$\|\Delta\omega_{SM}\|_\infty := \max(\omega_0 - \omega_{SM}(t)), \quad (6.7a)$$

$$|\hat{\omega}_{SM}| := \left| \frac{\omega_{SM}(t_0 + \Delta t) - \omega_{SM}(t_0)}{\Delta t} \right|, \quad (6.7b)$$

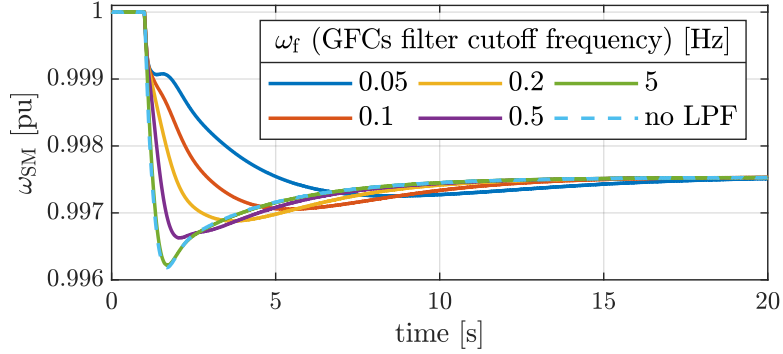


Figure 6.7: Frequency evolution of SM at node 1 when the GFCs are controlled by HAC strategy with 5 different LPF cutoff frequency and without a LPF.

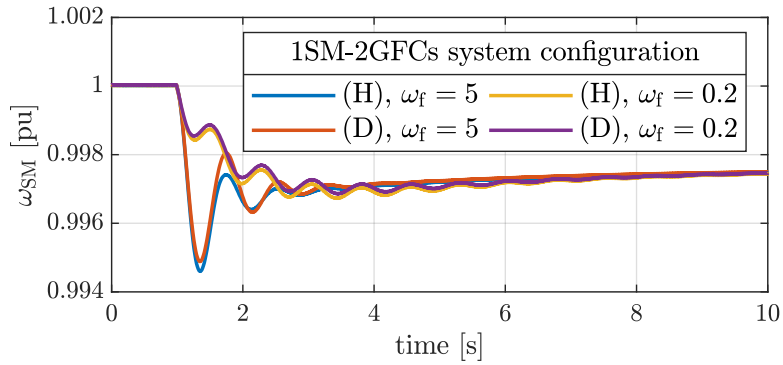


Figure 6.8: The PSS-free response of the SM at node 1 when the GFCs are controlled by either HAC or droop control while considering two different LPF cutoff frequencies.

where ω_{SM} and Δt respectively denote the SM frequency and the RoCoF approximation time horizon. We consider $\Delta t = 150$ [ms] that allows to observe the influence of fast GFCs dynamics on the system frequency; the reader is referred to [2] for a detailed discussion on the choice of RoCoF window.

Figure 6.5 highlights the evolution of metrics (6.7) in 1SM-2GFCs system, under different grid-forming controls, and w.r.t the disturbance variation. Concerning the RoCoF, the techniques incorporating an ac feedback i.e., droop control (6.1) and HAC (6.3) result in better performance compared to the purely dc-based matching control. This is underpinned by their fast disturbance sensing and frequency modification feature. In contrast, matching control (6.2) only reacts when the network disturbance is propagated to the converter dc dynamics.

Figure 6.5 confirms that HAC inherits the advantage of the other ac-based controls e.g., droop control; see Remark 15 and [1] for further details. On the other hand, maximum frequency deviation performance is almost identical when employing different controls. The reader is referred to [1] for a detailed discussion on this aspect. Although Figure 6.5 uncovers a performance variation that depends on the grid-forming controls in

1SM-2GFCs setup, all controls outperform the all-SMs configuration by a clear margin; e.g., see [1, Figures 11 and 12]. The positive influence of the grid-forming controls on frequency stability is also reported in [2], [100].

6.4.3 Synchronous machine dominated system

In this test case, we consider a SM-dominated generation profile by including identical SMs at nodes 1 and 3, and a GFC at node 2 in Figure 6.3 leading to a 2SMs-1GFC system. We consider the same load-disturbance as in Subsection 6.4.1 and enforce equal load-sharing for all units. Figure 6.6 shows the frequency of the SM at node 1 when the GFC is under different controls. The network base load and disturbance are chosen such that the desired post-disturbance GFC’s active power does not result in exceeding the converter dc source current limit; see Figure 6.1. However, due to the presence of slowly reacting SMs (because of large turbine time constants), the GFC dominantly supports the load during the transient that results in violating the dc limit. As it is also reported in [1], [55], [105], under active dc current constraint, droop control exhibits instability by depleting the dc-link energy. This aggressive behavior is because droop control (6.1) is agnostic to the dc dynamics. Subsequently, the converter instability propagates through the network and destabilizes the SMs. This adverse interaction can be counteracted by augmenting droop control with an ac current limiting mechanism e.g., threshold virtual impedance [70]. However, in our experience the limiting performance is fragile and depends on various factors e.g., the disturbance size and location.

In contrast, as it can be observed in Figure 6.6, the controls that exploit dc feedback in their angle dynamics e.g., matching control and HAC exhibit robustness with respect to the dc current constraint. This behavior is numerically and formally explored in [1], [55], [105]. In a nutshell, it is underpinned by an inherent mode-switching behavior that transforms the grid-forming control to a following one and allows injecting constant current while the dc source is saturated. The reader is referred to [1] for a detailed discussion. Interestingly, HAC results in better frequency deviation performance compared to matching control. This is because HAC provides global stability certificates [3], [8] and includes a hybrid ac/dc structure that strikes a balance between robustness and performance.

Remark 17 (Adverse timescales interaction). *In case studies presented in [1], [55], [105], the instability of the purely ac-based grid-forming techniques strongly depends on the disturbance magnitude. However, Figure 6.6 provides an alternative insight. More precisely, the base load and disturbance scenario specification does not derive the converter beyond its limit in all-GFCs or 1SM-2GFCs systems. However, in an SM-dominated system the adverse interplay of the fast GFC and slow SMs results in excessive transient current injection by the converter. Hence, aside the disturbance characteristics, the penetration level of the converter-based generation is an influencing factor for this*

instability mechanism.

6.4.4 The influence of GFC parameters on frequency behavior

Several works e.g., [38], [51], [137] highlight the necessity and benefits of low-pass filtering the ac measurements that are exploited in synthesizing converter control. In the following, we show how an appropriate tuning of the converters' low-pass filters improves the frequency stability and can be perceived as a decentralized frequency shaping strategy.

To begin with, we consider the 1SM-2GFCs configuration as in Subsection 6.4.2. Next, we equip the GFCs at nodes 2 and 3 with HAC and consider different cutoff frequencies for the underlying low-pass filters; see Figure 6.2. Figure 6.7 illustrates the frequency response of the SM with respect to the converters' cutoff frequency variation. Note that this observation suggests that an appropriate tuning of the LPFs can globally reshape the frequency response across the system. This is due to the fact that the LPFs with an appropriate tuning provide a certain amount of virtual inertia and thus enhance the SM frequency response. The reader is referred to [38] for detailed discussion. We remark that the positive influence of ω_f -variation on frequency stability must be compared against the enhancement that is achieved via changing the converters' controls. In particular, the maximum frequency deviation metric is significantly reduced in Figure 6.7 as ω_f is reduced, in contrast, for a fixed ω_f the improvement due to changing grid-forming strategies is minimal; see Figure 6.5. Last, our numerical investigations confirm an almost identical behavior as when the GFCs are controlled by droop control.

6.4.5 The PSS-free behavior of the low-inertia system

It has been recently uncovered that the PSSs of the SMs in a low-inertia system might adversely interact with certain timescales of the converter systems [100]. Moreover, it is highlighted that an adaptive PSS might be a crucial element in ensuring system stability in transitioning to 100% converter-based generation [2], [138], [139]. However, the online/offline modification of the well-established PSS control architectures might be an expensive, challenging, and practically infeasible task. In this subsection, we investigate if the LPF retuning strategy can possibly allow for a PSS-free operation of the SMs in a low-inertia network configuration.

To this end, we consider the 1SM-2GFCs configuration and remove the PSS from the SM model at node 1. Similar to previous cases, we separately consider droop control and HAC for the GFCs. Next, we consider two different cutoff frequencies for the underlying LPFs. Figure 6.8 depicts the frequency response of the SM. It can be seen that under $\omega_f = 5$ [Hz], HAC results in slightly less oscillations compared to droop control. However, when selecting $\omega_f = 0.2$ [Hz], the SM frequency nadir (that might potentially trip the low-frequency protection mechanisms) is almost removed. Although, under $\omega_f =$

0.2 [Hz] the low-frequency oscillation are still present but the appropriate LPF tuning reshapes the envelope on the frequency response and constrains the frequency oscillations within the stability margin. Last, the enhanced response is achieved regardless of the control strategies of the GFCs. We remark that this insight is a result of a preliminary exploration and requires an in-depth analysis.

6.4.6 Performance in a non-uniform synthetic two-area system

We close our numerical investigations by exploring the performance of GFCs under the HAC w.r.t a grid split scenario in a synthetic two-area low-inertia system; see Figure 6.9. To this end, consider two structurally identical 9-bus systems as in Figure 6.3 with SM at node 1 and GFCs at nodes 2 and 3. Assume that the node 9 in the first area, i.e., n_{91} is connected to the node 7 in the second area, i.e., n_{72} through a transmission line that is five times longer than the longest local line, i.e., the line between nodes 5 and 6 in either areas; see Figure 6.9 and [140]. Further, the time constant of the SM's turbine in the second area is twice the SM's turbine time constant in the first area, i.e., $\tau_{g,12} = 2\tau_{g,11} = 10$ [s]. Note that we also remove the PSS of the SM in the second area. Further, we consider non-uniform dc source timescales for the GFCs in the second area, i.e., $\tau_{dc,22} = \tau_{dc,21} = 50$ [ms] while $\tau_{dc,23} = 20\tau_{dc,31} = 1$ [s]. Moreover, we consider a total two-area loading of $p_{total} = 4.5$ [pu] with unequal distribution between the areas, i.e., $p_{area,1} = 0.4p_{total}$ and $p_{area,2} = 0.6p_{total}$. Note that $p_{area,1}$ is equally divided between the loads at nodes n_{51} , n_{71} , and n_{91} . However, $p_{area,2}$ is non-uniformly distributed within the area, i.e., $p_{72} = 3p_{52}$ and $p_{92} = 2p_{52}$. Last, all converters are under the HAC, the controllers are tuned such that all generation units exhibit identical load-sharing, and we do not consider a load disturbance scenario.

With the aforementioned characterization, during the normal operation the first area exports 0.45 [pu] active power to the second area. Figure 6.10 illustrates the evolution of the system frequencies after tripping the interconnecting $n_{91} - n_{72}$ line. As it is expected, the first area experiences over-frequency due to the excess generation. On the other hand, the second area exhibits under-frequency due to the excess loading. It is noteworthy that the HACed GFCs in the second area re-synchronize in presence of such severe event (that not only creates a disturbance but also decouples the system dynamics), low-frequency oscillations due to the lack of SM's PSS, non-uniform generation timescales and load distribution. Last, we remark that this grid split scenario results in the instability of the second area if the GFCs are under droop control.

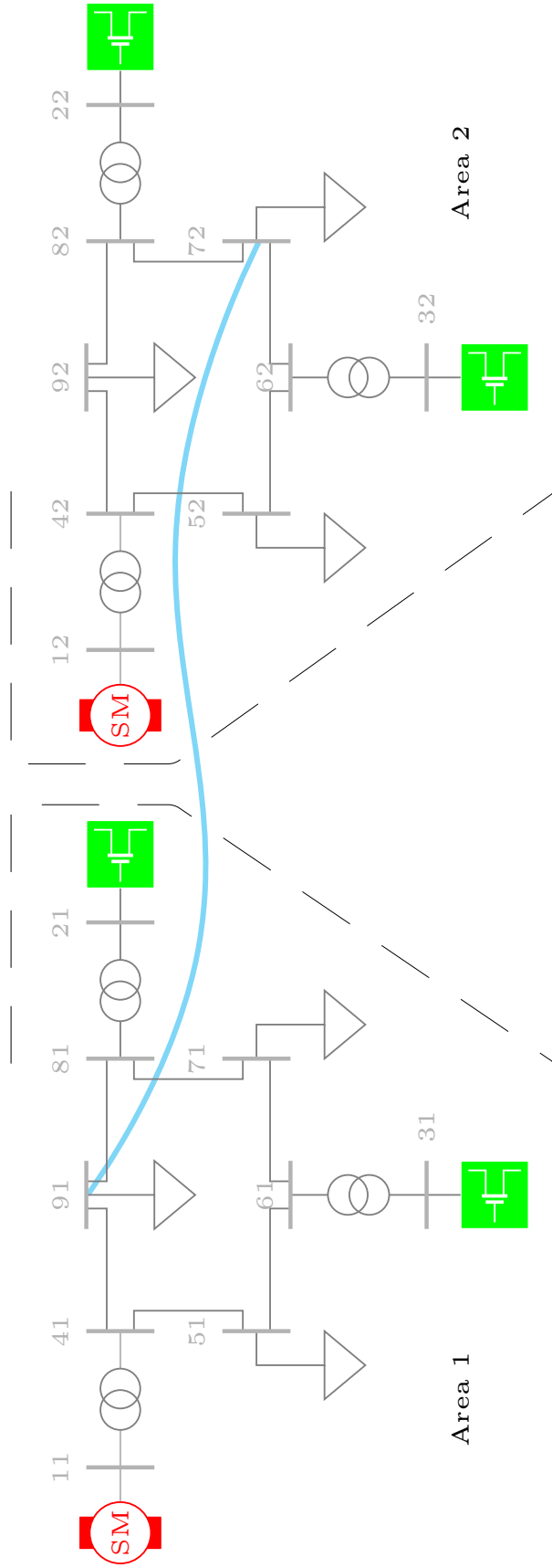


Figure 6.9: Synthetic two-area low-inertia system configuration.

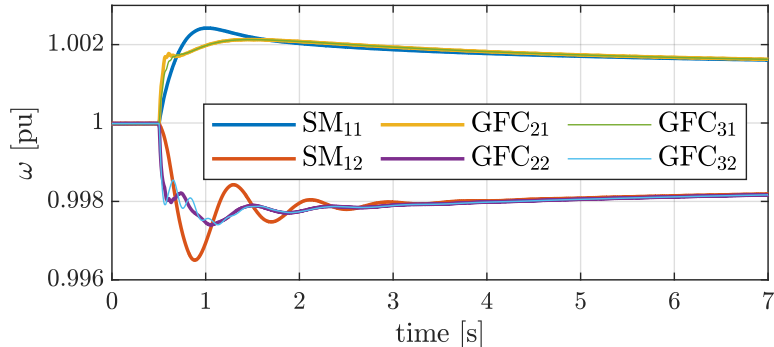


Figure 6.10: Frequencies of the two-area system following a grid split scenario.

6.5 Conclusions and outlook

In this paper, the system-level performance and robustness of grid-forming HAC is explored. We verified that the multi-variable dc-ac HAC inherits the enhanced performance and robustness of ac-based and dc-based controls, respectively. Furthermore, we highlighted how retuning the low-pass filters for grid-forming controls can significantly enhance the frequency performance across the system. Last, an alternative augmented controller is introduced and a simplified stability analysis for a two-converter system is presented. Our future work includes: 1) implementation of HAC for power converters in more complex power grid models, 2) power hardware validation of HAC concept, and 3) detailed stability analysis multi-converter system under HAC.

6.6 Appendix A: dynamic inverse droop control augmentation

The HAC implementation described in the Section 6.3, explicitly relies on the foreknowledge of the relative angle reference δ_r . The reader is referred to [3, Proposition 6] on deriving δ_r based on the power and voltage set-points. However, this technique relies on the system parameters and might exhibit robustness issues. In what follows, we introduce a complementary high-level feedback control mechanism that achieves the same objective with enhanced robustness.

To begin with we introduce an integral control that defines δ_r in relation to the active power mismatch i.e.,

$$\delta_r = \int_0^t \kappa_{p\delta} (p_r - p), \quad (6.8)$$

where $\kappa_{p\delta}$ denotes the integrator gain. It is worth mentioning that augmenting the HAC with (6.8) transforms the grid-forming HAC to a phase locked loop (PLL)-free grid-

following controller that achieves robust active power reference tracking. This is due to the fact that the integrator (6.8) disables the natural $p - \omega$ droop behavior of the HAC [3, Proposition 7].

Although robust reference tracking and disturbance rejection might be desirable for certain applications, drooping behavior that enables load-sharing between generation units in transmission grids is vital. Thus, we combine (6.8) with an inverse $\omega - p$ droop control (reminiscent of the speed droop control of the SM e.g., see [1, Equation 5]) that is

$$p_r := p^* + d_{\omega-p}(\omega_c - \omega_0), \quad (6.9)$$

where p^* denotes the power reference at nominal frequency, $d_{\omega-p}$ is the inverse droop gain, and ω_c is the internal feedback given by HAC (6.3). We emphasize that the combination of (6.3) with the dynamic inverse droop control (6.8) and (6.9) is a heuristic approach, and requires a separate detailed stability analysis as in [3]. However, our numerical investigations confirm that the cascade control structure achieves the aforementioned control specification. Furthermore, as in standard cascaded control systems (e.g., [113]) the controls (6.3), (6.8), and (6.9) must be tuned in harmony while respecting the required timescales separation between the nested loops. Last, we remark that since the main focus of this work is to explore the behavior of the standard HAC (6.3), the presented case studies in the Section 6.4 only incorporates (6.3).

6.7 Appendix B: stability analysis of the interconnected converters

The stability analysis of the HAC in [3], [8] is centered around a model configuration that includes a single converter connected to an infinite bus or a dynamic center of inertia (CoI) grid model. The converter-CoI model abstractly represents the mixed converter-SM configurations of the IEEE 9-bus system shown in Figure 6.3. However, the stability and synchronization analysis of a multi-converter setup requires a separate investigation and is presented as it follows.

To begin with, we consider a simplified two-converter model as in Figure 6.11; see [126] for a similar model configuration. Without loss of generality we assume the line current is flowing out of the converter 1 and into the converter 2. It is noteworthy that the configuration in Figure 6.11 represents two converters with RL output filters that are connected through a RL line section. Thus, the filter elements and the line section are merged into a single RL element.

We equip both converters with HAC (6.3) and thus the overall dynamical model is

given by

$$\dot{\theta}_1 = \omega_0 + \gamma_{dc,1}(v_{dc,1} - v_{dc,r1}) - \gamma_{ac,1} \sin\left(\frac{\delta - \delta_r}{2}\right), \quad (6.10a)$$

$$\dot{v}_{dc,1} = \frac{i_{dc,1} - G_{dc,1}v_{dc,1} - m(\mu_1, \theta_1)^\top i_\ell}{C_{dc,1}}, \quad (6.10b)$$

$$\dot{\theta}_2 = \omega_0 + \gamma_{dc,2}(v_{dc,2} - v_{dc,r2}) + \gamma_{ac,2} \sin\left(\frac{\delta - \delta_r}{2}\right), \quad (6.10c)$$

$$\dot{v}_{dc,2} = \frac{i_{dc,2} - G_{dc,2}v_{dc,2} + m(\mu_2, \theta_2)^\top i_\ell}{C_{dc,2}}, \quad (6.10d)$$

where $\delta := \theta_1 - \theta_2$. In addition, the dc source current and the modulation signal control input pairs are defined as

$$i_{dc,1} := -\kappa_{dc,1}(v_{dc,1} - v_{dc,r1}), \quad (6.11a)$$

$$m(\mu_1, \theta_1) := \mu_1 (\cos \theta_1, \sin \theta_1)^\top, \quad (6.11b)$$

$$i_{dc,2} := -\kappa_{dc,2}(v_{dc,2} - v_{dc,r2}), \quad (6.11c)$$

$$m(\mu_2, \theta_2) := \mu_2 (\cos \theta_2, \sin \theta_2)^\top. \quad (6.11d)$$

Furthermore, for simplicity of exposition we assume quasi-steady-state line dynamics, thus the current in stationary $\alpha\beta$ -coordinates is given by

$$i_\ell := \frac{(v_{dc,1}m(\mu_1, \theta_1) - v_{dc,2}m(\mu_2, \theta_2))}{R}. \quad (6.12)$$

We subsequently 1) combine the absolute angle dynamics (6.10a) and (6.10c) into relative angle dynamics, 2) replace i_ℓ in (6.10b) and (6.10d) with the expression in (6.12), and 3) incorporate the controls (6.11) that results in the overall closed-loop dynamics:

$$\dot{v}_{dc,1} = - \frac{\left(\kappa_{dc,1}(v_{dc,1} - v_{dc,r1}) + (G_{dc,1} + R^{-1}\mu_1^2)v_{dc,1} - R^{-1}\mu_1\mu_2 \cos(\delta)v_{dc,2}\right)}{C_{dc,1}} \quad (6.13a)$$

$$\dot{v}_{dc,2} = - \frac{\left(\kappa_{dc,2}(v_{dc,2} - v_{dc,r2}) + (G_{dc,2} + R^{-1}\mu_2^2)v_{dc,2} - R^{-1}\mu_1\mu_2 \cos(\delta)v_{dc,1}\right)}{C_{dc,2}} \quad (6.13b)$$

$$\dot{\delta} = + \gamma_{dc,1}(v_{dc,1} - v_{dc,r1}) - \gamma_{dc,2}(v_{dc,2} - v_{dc,r2}) - (\gamma_{ac,1} + \gamma_{ac,2}) \sin\left(\frac{\delta - \delta_r}{2}\right). \quad (6.13c)$$

Assume that there exists an equilibrium and it coincides with the desired control references (similar to [3, Theorem 1]) i.e.,

$$\left(\delta^*, v_{dc,1}^*, v_{dc,2}^*\right) := (\delta_r, v_{dc,r1}, v_{dc,r1}). \quad (6.14)$$

Next, we associate an energy function with the closed-loop dynamics (6.13), that is given by

$$\mathcal{V} := \frac{1}{2} \left(C_{\text{dc},1} (v_{\text{dc},1} - v_{\text{dc},r1})^2 + C_{\text{dc},2} (v_{\text{dc},2} - v_{\text{dc},r2})^2 \right) + 2 \left(1 - \cos \left(\frac{\delta - \delta_r}{2} \right) \right). \quad (6.15)$$

Following the analysis recipe as in [3, Theorem 2], it is possible to show that there exists positive lower bounds $\gamma_{\text{ac},\min}$ and $\kappa_{\text{dc},\min}$ such that if $\gamma_{\text{ac},1} + \gamma_{\text{ac},2} > \gamma_{\text{ac},\min}$ and $\kappa_{\text{dc},1}, \kappa_{\text{dc},2} > \kappa_{\text{dc},\min}$ then the energy function $\mathcal{V} \rightarrow 0$ for (almost) all the solutions of (6.13). Note that when $\mathcal{V} \rightarrow 0$ it yields that $(\delta, v_{\text{dc},1}, v_{\text{dc},2}) \rightarrow (\delta_r, v_{\text{dc},r1}, v_{\text{dc},r2})$. This result verifies the asymptotic convergence of converter dynamics to the desired dc voltage and relative angle references.

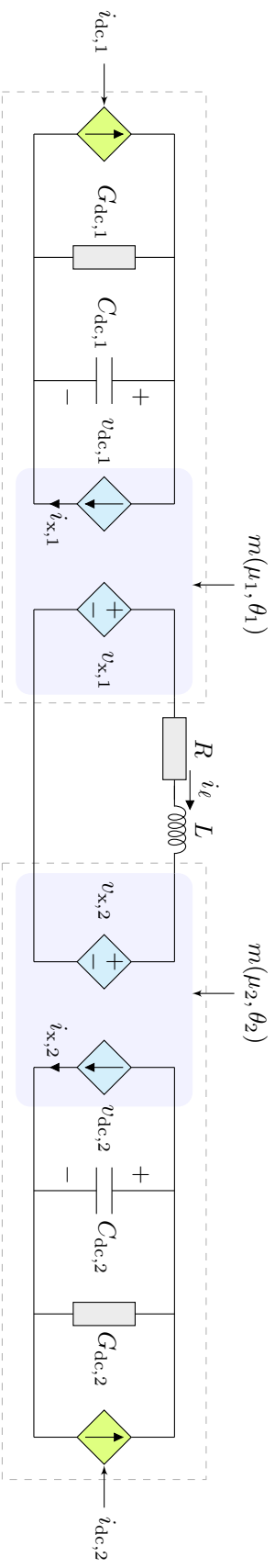


Figure 6.11: The simplified two-converter system configuration where $i_{x,j} := m(\mu_j, \theta_j)^\top i_l$ and $v_{x,j} := m(\mu_j, \theta_j)v_{dc,j}$ for $j = 1$ and 2 .

Grid-forming hybrid angle control: behavior, stability, variants, and verification

Under review in the IEEE Transactions on Smart Grid 2023.

Authors – Ali Tayyebi, Denis Vettoretti, Adolfo Anta, and Florian Dörfler.

Abstract – This work explores the stability, behavior, variants, and a controller-hardware-in-the-loop (C-HiL) verification of the recently proposed grid-forming (GFM) hybrid angle control (HAC). We revisit the foundation of GFM HAC, and highlight its behavioral properties in relation to the conventional SM. Next, we introduce the required complementary controls to be combined with the HAC to realize a GFM behavior. The characterization of the analytical operating point and nonlinear energy-based stability analysis of a grid-connected converter under the HAC is presented. Further, we consider various output filter configurations and derive an approximation for the original control proposal. Moreover, we provide details on the integration of GFM HAC into a complex converter control architecture and introduce several variants of the standard HAC. Finally, the performance of GFM HAC is verified by several test scenarios in a C-HiL setup to test its behavior against real-world effect such as noise and delays.

7.1 Introduction

The global shift toward the massive integration of energy generation from renewable source accompanied by the supply chain concerns associated with conventional energy generation has raised significant interest in converter-based systems. Thus, power converters are perceived as the vital corner stones of the modern power system and are expected to replace the well-established SM technology. However, a robust and reliable control of power converters in a converter-dominated power system is to some extent an open question. The emerging grid-forming (GFM) control synthesis in contrast to the classic grid-following (GFL) converter control concept is envisioned to address the stability challenges in a converter-dominated power grid [1], [2], [32], [33], [100], [141], [142]. On the other hand, it is worth mentioning that the power system operators are

actively designing test procedures and grid code requirements for the GFM converters, as well, e.g., [28], [29].

The broadly recognized droop control serves as a powerful baseline GFM control candidate that mimics the behavior of a SM governor for the power converters [35], [36], [50]. As the natural extension of the droop control, the virtual synchronous machine concept is proposed that emulates the SM dynamics (up to different degrees of accuracy) [64], [143]. On the other hand, the matching-type GFM controllers are proposed that synthesize the converter control based on the structural dynamic similarities with the SM [40], [43]. Along a different design direction, the nonlinear oscillators dynamics are recently exploited for a GFM control design [48], [52], [53]. Finally, the combination of aforementioned techniques has resulted in several hybrid control architectures [3], [9], [55], [56].

The GFM HAC relies on a combination of the dc matching control and ac synchronization term that resembles the droop control and/or Kuramoto oscillator dynamics [34]. The theoretic control design and system-level simulation-based performance investigation of the HAC are previously explored [3]–[5], [8]. Previous works highlight 1) the strong stability properties of the HAC under mild parametric conditions, 2) system-level frequency stability enhancement, 3) stabilizing behavior in complex hybrid ac/dc power grids, and finally, 4) robustness w.r.t the nonlinear phenomena such as current limitation and grid split.

In this paper, we highlight further details on the behavioral properties of the GFM HAC, provide a closed-form characterization of the converter operating point, formulate an intuitive energy-based stability analysis, provide an approximate form of the HAC, and disclose several variants of the standard HAC. Last but not least, the performance of GFM HAC is verified by several test scenarios in a C-HiL setup that utilizes an OPAL-RT simulator and external control cards.

The remainder of this paper is structured as it follows. Section 7.2 describes the dynamic modeling of a grid-connected converter, introduces the HAC, and discusses its behavioral properties. Section 7.3 presents the closed-loop analysis. Section 7.4 provides details on the weak grid connection, HAC approximation, and its variants. Section 7.5 provides C-HiL performance verification, and Section 7.6 concludes the paper.

7.2 Converter connected to a stiff grid

In this section, we present the dynamic modeling of a grid-connected converter, revisit the GFM HAC strategy, and discuss its behavioral properties.

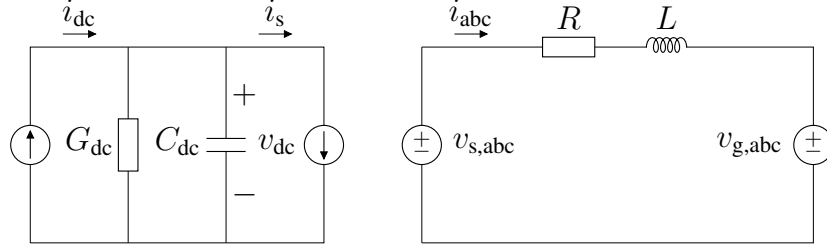


Figure 7.1: The circuit diagram associated with the open-loop dynamics of the grid-connected converter model as in (7.1).

7.2.1 Physical converter system dynamics

Let us consider a two-level dc-ac power converter model that is interfaced to a stiff grid (i.e., with constant frequency and voltage magnitude) through a resistive-inductive element [40]; see Figure 7.1. The open-loop dc voltage and ac current dynamics of such system are described by

$$C_{dc} \frac{dv_{dc}}{dt} = i_{dc} - G_{dc}v_{dc} - i_s, \quad (7.1a)$$

$$L \frac{di_{abc}}{dt} = v_{s,abc} - Ri_{abc} - v_{g,abc}, \quad (7.1b)$$

where C_{dc} denotes the dc-link capacitance, v_{dc} denotes the dc-link voltage, i_{dc} denotes the current flowing out of the dc energy source, G_{dc} denotes the dc conductance that models the dc-side losses, and i_s denotes the dc-side switched current. Further, L denotes the ac-side inductance that models the converter output filter, i_{abc} denotes the converter output current flowing into the grid, $v_{s,abc}$ denotes the ac-side switched voltage, R denotes the equivalent series resistance of the filter inductance, and finally $v_{g,abc}$ denotes the balanced voltage of the stiff ac grid at nominal frequency ω_0 and magnitude v_0 .

7.2.2 Energy source model and control

The dc current source in Figure 7.1 that models the primary dc energy source e.g., a battery, can be controlled in several ways. One can close the loop by considering a proportional controller to increase the dc voltage damping [1]. Further, it is possible to also include integral and derivative terms to enhance the dc voltage reference tracking and dynamic performance. Thus, the i_{dc} in (7.1a) takes generic form

$$i_{dc} = -\kappa_p (v_{dc} - v_{dc,r}) - \kappa_i \int_0^t (v_{dc} - v_{dc,r}) d\tau - \kappa_d \frac{dv_{dc}}{dt}, \quad (7.2)$$

where κ_p , κ_i , and κ_d denote the parameters of the proportional-integral-derivative control. Note that one can implement the derivative term in (7.2) by measuring the dc-link

capacitance current (since they are equivalent up to a constant factor). Previous work investigated the contribution of control (7.2) to the frequency damping and inertial response under the GFM matching control [40], [65]. Finally, if the energy source is not controllable, e.g., battery-integrated system without a dc-dc converter stage, one can fix i_{dc} to a constant reference.

7.2.3 Power-preserving averaged DC-AC converter model

The dc-ac converter (7.1) is represented by the switched current and voltage pair $(i_s, v_{s,abc})$. Let us introduce the balanced three-phase converter modulation signal

$$m_{abc} = \mu \left(\cos \theta, \cos \left(\theta + \frac{2\pi}{3} \right), \cos \left(\theta - \frac{2\pi}{3} \right) \right)^\top, \quad (7.3)$$

where μ and θ respectively denote the modulation signal magnitude and phase angle. Next, the lossless power-preserving averaged model of the two-level converter is given by [73]

$$i_s = m_{abc}^\top i_{abc}, \quad (7.4a)$$

$$v_{s,abc} = v_{dc} m_{abc}. \quad (7.4b)$$

In the sequel, we show how μ and θ are selected. Aside from the nonlinear power-preserving model (7.4), other approaches can be considered.

- * One can assume decoupled dc and ac dynamics that is usually verified by considering a sufficiently fast dc voltage control [35], [64], [143]. In this viewpoint, the converter is seen as an ideal controllable voltage source.
- * Another trend is to model the internal dynamics of the dc-ac converters by oscillator dynamics. This approach is often adopted when studying the stability of interconnected converter-based systems; see [52] for a review and [48], [50] for experimental investigations.
- * Recent works highlight the application of hybrid systems theory in modeling the converter dynamics. These works consider a blend of discontinuous and continuous signals in converter dynamical description, therefore, do not distinguish between the switching and continuous averaged converter models; e.g., see [144], [145].

7.2.4 Grid-forming hybrid angle control strategy

In this subsection, we briefly revisit the design of grid-forming HAC [3]–[5], [8]. Let us begin by defining the converter relative angle w.r.t the grid model in Figure 7.1. The

modulation angle θ in (7.3) enters $v_{s,abc}$ in (7.4) that subsequently appears in (7.1b) (as the voltage behind output filter). Let us define ω as the converter angular frequency that is given by the time-derivative of θ . Similarly, let θ_g and ω_g respectively denote the phase angle and the angular frequency grid voltage $v_{g,abc}$ in (7.1b) and Figure 7.1. Note that $\omega_g = \omega_0$, since we consider a stiff grid. Thus, the converter-grid relative angle and its derivative are given by

$$\delta = \theta - \theta_g, \quad (7.5a)$$

$$\frac{d\delta}{dt} = \frac{d\theta}{dt} - \frac{d\theta_g}{dt} = \omega - \omega_g = \omega - \omega_0. \quad (7.5b)$$

The GFM HAC that defines the converter frequency (hence the modulation angle) takes the form

$$\omega = \omega_0 + \underbrace{\kappa_{dc} (v_{dc} - v_{dc,r})}_{\text{dc matching term}} - \underbrace{\kappa_{ac} \sin\left(\frac{\delta - \delta_r}{2}\right)}_{\text{ac synchronization term}}, \quad (7.6)$$

where $v_{dc,r}$ and δ_r respectively denote the dc voltage and relative angle references. It is worth mentioning that the dc part of (7.6) is similar to the matching control [40], [41], [43]. On the other hand, the ac part of the HAC realizes the frequency synchronization via nonlinear angle damping assignment. The prior works [1], [3], [5] provide detailed discussions on the properties of GFM controls that depend on the ac and/or dc quantities. Nonetheless, in a nutshell, incorporating the dc feedback in the frequency dynamics tends to enhance the robustness and including the ac feedback enhances the dynamic performance; see [5], [55], [105], [146] for theoretic and numerical investigations. The HAC (7.6), while defining the converter frequency, behaves as a synchronization mechanism. To further elaborate, if the converter dc voltage is sufficiently regulated, i.e., $v_{dc} \approx v_{dc,r}$, then the converter-grid relative angle dynamics (7.5b) reduces to

$$\frac{d\delta}{dt} \approx -\kappa_{ac} \sin\left(\frac{\delta - \delta_r}{2}\right). \quad (7.7)$$

This means if $\delta > \delta_r \Rightarrow d\delta/dt < 0 \Rightarrow \delta \downarrow$ and similarly, if $\delta < \delta_r \Rightarrow d\delta/dt > 0 \Rightarrow \delta \uparrow$. The HAC potentially replaces the synchronization mechanism (e.g., phase-locked loop, virtual synchronous machine, active power control sub-systems) in converter control architectures; see Figure 7.5. For instance, HAC is a synchronizing control candidate for

- * high voltage direct current (HVDC) converters in embedded, inter-connector, multi-terminal, and offshore wind farm integration setups,
- * flexible ac transmission system (FACTS) devices,
- * low-voltage photovoltaic (PV) and battery systems,
- * and, utility-scale battery energy storage system (BESS).

7.2.5 DC voltage and AC power flow regulation

The HAC regulates the dc voltage and ac power flow through frequency synchronization. To further elaborate, let us consider two separate cases.

Pure DC feedback control

Assume $\kappa_{dc} \neq 0$ and $\kappa_{ac} = 0$ that reduces (7.6) to

$$\Delta\omega = \omega - \omega_0 = \kappa_{dc} (v_{dc} - v_{dc,r}) = \kappa_{dc}\Delta v_{dc}. \quad (7.8)$$

This controller combination is the reduction of HAC to the matching control [40]. It is established that under the matching control, i.e., when the converter frequency is defined proportional to the dc voltage, the converter dynamics are structurally similar to that of the SM. Therefore, the converter exhibits self-synchronizing behavior of the SM [43] which means

$$\omega \rightarrow \omega_0 \Rightarrow \Delta\omega \rightarrow 0 \Rightarrow \Delta v_{dc} \rightarrow 0 \Rightarrow v_{dc} \rightarrow v_{dc,r}.$$

Thus, the frequency synchronization implies dc voltage regulation, that is achieved by modifying the ac power. This control mode is particularly interesting in weak dc-link applications.

Pure AC feedback control

Consider the gain combination $\kappa_{dc} = 0$ and $\kappa_{ac} \neq 0$. Let us approximate the ac term in (7.6) with the ac power flow deviation, i.e., assume that $\Delta\delta = \delta - \delta_r$ is proportional to $\Delta p = p - p_r$ up to a constant factor $\kappa_{\delta-p}$. Then, (7.6) reduces to

$$\Delta\omega \approx -\kappa_{ac} \sin\left(\frac{\kappa_{\delta-p}\Delta p}{2}\right) \approx -\left(\frac{\kappa_{ac}\kappa_{\delta-p}}{2}\right) \Delta p, \quad (7.9)$$

assuming that Δp is sufficiently small. This variant represents the power-frequency droop control embedded in HAC, thus,

$$\omega \rightarrow \omega_0 \Rightarrow \Delta\omega \rightarrow 0 \Rightarrow \Delta p \rightarrow 0 \Rightarrow p \rightarrow p_r.$$

In this case, frequency synchronization implies ac power flow regulation, that is achieved by the power injection/absorption of the dc-link. This control mode is particularly interesting in stiff dc-link applications. Finally, the hybrid configuration under appropriate tuning provides seamless transition between the aforementioned modes [3], [56].

7.2.6 Behavioral interpretations and connections to the SM

It is possible to interpret the structure of HAC in relation to SM control and behavior. Firstly, the influence of a governor on the SM behavior is perceived as modifying the turbine output mechanical power p_m according to the mechanical frequency ω_m deviation from its reference $\omega_{m,r}$. In other words,

$$p_m = p_{m,r} - \kappa_{\omega-p} (\omega_m - \omega_{m,r}), \quad (7.10)$$

where $p_{m,r}$ and $\kappa_{\omega-p}$ respectively denote the turbine reference power and governor control gain. Observe that if $\omega_m \uparrow \downarrow \Rightarrow p_m \downarrow \uparrow$ to accordingly modify the energy input into the SM such that the frequency is stabilized. One can alternatively rewrite (7.10) as the so-called droop control, i.e.,

$$\omega_m = \omega_{m,r} - \frac{1}{\kappa_{\omega-p}} (p_m - p_{m,r}). \quad (7.11)$$

Now, under the small power-angle assumption, i.e., $\Delta\delta \propto \Delta p$ one can interpret the ac part of the HAC (7.6) as droop control (7.9) which takes the same form as (7.11). Therefore, the ac term in (7.6) mimics the stabilizing influence of the turbine governor.

Next, let us revisit the modeling of SM inertial response [116]. We assume that the mechanical power p_m is flowing into the SM and electrical power p_e is flowing out of its ac terminal. These two quantities are linked through the time-derivative of kinetic energy E_k stored in the SM rotor, i.e.,

$$\frac{dE_k}{dt} = p_m - p_e \quad \text{where} \quad E_k = \frac{1}{2} J \omega^2 \quad (7.12)$$

and J denotes the rotor moment of inertia. A salient feature of the SM is that if there is an imbalance between its mechanical and electrical powers, e.g., due to load variation, the rotating mass acts as an energy buffer and provides/absorbs the excess power to restore the power balance. The resulting influence is the SM frequency variation, i.e.,

$$\text{if } \frac{dE_k}{dt} = J\omega \frac{d\omega}{dt} > 0 \text{ (or } < 0) \Rightarrow \omega \uparrow (\downarrow). \quad (7.13)$$

The dc-ac power converters, by design, incorporate a similar mechanism. To further elaborate, let p_{dc} denote the power that is flown into the converter dc-link and p_{ac} is the power that is flown out of the converter ac terminal. These quantities are linked together through the potential energy E_p that is stored in the converter dc-link, i.e.,

$$\frac{dE_p}{dt} = p_{dc} - p_{ac} \quad \text{where} \quad E_p = \frac{1}{2} C_{dc} v_{dc}^2. \quad (7.14)$$

Similarly, the power imbalance between the converter dc and ac ports is compensated

by the dc-link energy variation, i.e.,

$$\text{if } \frac{dE_p}{dt} = C_{dc}v_{dc} \frac{dv_{dc}}{dt} > 0 \text{ (or } < 0) \Rightarrow v_{dc} \uparrow (\downarrow). \quad (7.15)$$

From this perspective, the dc term in HAC (7.6) that relates the converter frequency to the dc voltage (i.e., $\omega \propto v_{dc}$), resembles the inertial response of the SM and links the converter frequency to the available physical stored energy in the dc-link capacitance.

7.2.7 AC voltage control

The GFM HAC is primarily designed as an active power-frequency controller [3]. Thus, one has to consider complementary ac voltage control. Similar to other grid-forming controls [1], there are different control candidates.

- * One can implement a proportional-integral (PI) (or simply a proportional) ac voltage control that processes the PCC voltage error and provides a reference magnitude for converter modulation in (7.3) [5].
- * Another alternative is to define the modulation signal magnitude based on a reactive power and voltage droop control [100], [142]. In this approach, the converter modulation magnitude is modified if the reactive power deviates from its reference. Thus, the modulation magnitude modification indirectly controls the PCC voltage.
- * The most straightforward, although less robust, approach is to define the reference magnitude for the converter modulation signal according to the desired references for the dc and ac voltages [3].

7.2.8 Control implementation and filtering requirement

The previous work [5], establish that HAC (7.6) can be exactly constructed based on the dc voltage measurement, internal converter modulation angle, and the grid voltage measurement in Figure 7.1. To recapitulate, one should firstly expand the ac term in (7.6), i.e.,

$$\sin\left(\frac{\delta - \delta_r}{2}\right) = \sin\frac{\delta}{2} \cos\frac{\delta_r}{2} - \cos\frac{\delta}{2} \sin\frac{\delta_r}{2}. \quad (7.16)$$

Then, the terms depending on δ_r can be computed according to the prescribed power and voltage set-points [3]. Next, the terms depending on $\delta = \theta - \theta_g$ are constructed based on the sines and cosines of θ and θ_g that can be respectively obtained from the converter modulation signal m_{abc} and the grid voltage $v_{g,abc}$. Note that it is standard practice to low-pass filter the dc voltage feedback in (7.6) and the grid voltage measurement to remove the potential dc ripple and ac noise, respectively.

7.3 Closed-loop stability analysis

In what follows, we select a combination of the controls described in the previous section, construct the closed-loop dynamics, and investigate the overall system stability.

7.3.1 Closed-loop system formulation

Let us begin by transforming the three-phase dynamics (7.1) to the stationary $\alpha\beta$ -coordinates by using the standard Clarke transformation [73] that results in

$$C_{\text{dc}} \frac{dv_{\text{dc}}}{dt} = i_{\text{dc}} - G_{\text{dc}} v_{\text{dc}} - i_{\text{s}}, \quad (7.17\text{a})$$

$$L \frac{di_{\alpha\beta}}{dt} = v_{\text{s},\alpha\beta} - Ri_{\alpha\beta} - v_{\text{g},\alpha\beta}. \quad (7.17\text{b})$$

Next, we select the PI dc voltage control¹ (for an enhanced dynamic performance and robustness) from (7.2), i.e.,

$$\begin{aligned} \frac{d\zeta}{dt} &= v_{\text{dc}} - v_{\text{dc},\text{r}}, \\ i_{\text{dc}} &= -\kappa_{\text{p}} (v_{\text{dc}} - v_{\text{dc},\text{r}}) - \kappa_{\text{i}} \zeta, \end{aligned}$$

where ζ denotes the integrator state, the HAC (7.6), and the feedforward ac voltage control, i.e.,

$$\mu = \frac{v_{\text{r}}}{v_{\text{dc},\text{r}}}. \quad (7.19)$$

Therefore, all three control inputs, i.e., the dc energy source current, modulation magnitude, and angle are well-defined (the latter is obtained by integrating the converter frequency defined by (7.6)). Next, we consider rotating dq-coordinates [73] that are aligned with the grid angle θ_{g} , thus, rotating with the grid frequency ω_{g} . The closed-loop dynamics in rotating dq-coordinates is represented by

$$\frac{d\delta}{dt} = \kappa_{\text{dc}} (v_{\text{dc}} - v_{\text{dc},\text{r}}) - \kappa_{\text{ac}} \sin \left(\frac{\delta - \delta_{\text{r}}}{2} \right), \quad (7.20\text{a})$$

$$\frac{d\zeta}{dt} = v_{\text{dc}} - v_{\text{dc},\text{r}}, \quad (7.20\text{b})$$

$$C_{\text{dc}} \frac{dv_{\text{dc}}}{dt} = -\kappa_{\text{p}} (v_{\text{dc}} - v_{\text{dc},\text{r}}) - \kappa_{\text{i}} \zeta - G_{\text{dc}} v_{\text{dc}} - \mu (i_{\text{d}} \cos \delta + i_{\text{q}} \sin \delta), \quad (7.20\text{c})$$

¹The previous works on HAC [3]–[5], [8] do not include the integral term in their dc voltage controls, therefore, the forthcoming closed-loop system analysis (although conceptually similar) differs from the prior investigations. In particular, the PI dc voltage control consideration omits the previously required assumption to prove the existence and derive a closed-form expression of the closed-loop stationary operating points.

$$L \frac{di_d}{dt} = \mu v_{dc} \cos \delta - Ri_d - L\omega_0 i_q - v_{g,d}, \quad (7.20d)$$

$$L \frac{di_q}{dt} = \mu v_{dc} \sin \delta - Ri_q + L\omega_0 i_d. \quad (7.20e)$$

We remark that $v_{g,d} = v_0$ (i.e., the nominal voltage magnitude of the stiff grid) and $v_{g,q} = 0$ since the d-axis is aligned with θ_g . Moreover, it is important to emphasize that the closed-loop system is nonlinear due to HAC in (7.20a) and modulated trigonometric terms in (7.20c) and (7.20d).

7.3.2 Analytical derivation of equilibria

In order to evaluate the stationary operating points (denoted by star superscript) of the closed-loop system, we begin by setting the RHS of the (7.20) to zero, i.e.,

$$\kappa_{dc} (v_{dc}^* - v_{dc,r}) - \kappa_{ac} \sin \left(\frac{\delta^* - \delta_r}{2} \right) = 0, \quad (7.21a)$$

$$v_{dc}^* - v_{dc,r} = 0, \quad (7.21b)$$

$$-\kappa_p (v_{dc}^* - v_{dc,r}) - \kappa_i \zeta^* - G_{dc} v_{dc}^* - \mu (i_d^* \cos \delta^* + i_q^* \sin \delta^*) = 0, \quad (7.21c)$$

$$\mu v_{dc}^* \cos \delta^* - Ri_d^* - L\omega_0 i_q^* - v_{g,d} = 0, \quad (7.21d)$$

$$\mu v_{dc}^* \sin \delta^* - Ri_q^* + L\omega_0 i_d^* = 0. \quad (7.21e)$$

Hence, one can solve (7.21a) and (7.21b) to evaluate δ^* and v_{dc}^* . Next, it is possible to solve (7.21d) and (7.21e) that result in the closed-form expressions for i_d^* and i_q^* that are the functions of δ^* and v_{dc}^* . Finally, one can solve (7.21c) to find ζ^* . Thus, (letting $k \in \{1, 2\}$) the steady-state system of equations (7.21) yields the following operating points,

$$\delta^* = \delta_r + 2\pi k, \quad (7.22a)$$

$$v_{dc}^* = v_{dc,r}, \quad (7.22b)$$

$$\zeta^* = \frac{-G_{dc} v_{dc}^* - \mu (i_d^* \cos \delta^* - i_q^* \sin \delta^*)}{\kappa_i}, \quad (7.22c)$$

$$i_d^* = \frac{\mu v_{dc}^* (R \cos \delta^* - L\omega_0 \sin \delta^*) - R v_{g,d}}{R^2 + (L\omega_0)^2}, \quad (7.22d)$$

$$i_q^* = \frac{\mu v_{dc}^* (L\omega_0 \cos \delta^* + R \sin \delta^*) - L\omega_0 v_{g,d}}{R^2 + (L\omega_0)^2}. \quad (7.22e)$$

We remark that due to the periodicity of (7.22c)-(7.22e) w.r.t δ , the steady-state quantities ζ^* , i_d^* , and i_q^* are identical for either δ_r or $\delta_r + 2\pi$ [3]. In the next subsection, we investigate the stability of the operating point in (7.22) that is characterized by $\delta^* = \delta_r$,

i.e.,

$$x^* = \left(\delta_r, \zeta^*, v_{dc}^*, i_d^*, i_q^* \right). \quad (7.23)$$

In the sequel, we restrict our focus to a local state space region around the stationary point (7.23) that excludes the other angle equilibrium in (7.22a). The reader is referred to [3] for a global (i.e., large-signal) stability analysis².

7.3.3 Nonlinear energy-based stability analysis

The system (7.20) is characterized by the nonlinearities due to the HAC in (7.20a), and the modulated current and voltage terms in (7.20c)-(7.20e). One potential approach to analyze the stability of the operating point (7.23), is to linearize the (7.20) and investigate the eigenvalues of resulting linear system. However, due to the particular structure of the Jacobian associated with (7.20), it is not straightforward to derive the analytical closed-form expressions for the eigenvalues evaluated at (7.23).

A more comprehensive nonlinear analysis approach is to associate a so-called *energy function* with the closed-loop dynamics (7.20) and study the behavior of this function w.r.t the evolution of states in (7.20). The energy function behavior (under certain conditions) reveals the stability properties of the system. More precisely, let us define an energy function

$$V(\hat{x}) = c_1 \left(1 - \cos \frac{\hat{\delta}}{2} \right) + c_2 \hat{\zeta}^2 + c_3 \hat{v}_{dc}^2 + c_4 \hat{i}_d^2 + c_5 \hat{i}_q^2, \quad (7.24)$$

where $\hat{x} = x - x^*$, $\hat{\delta} = \delta - \delta^*$, $\hat{\zeta} = \zeta - \zeta^*$, $\hat{v}_{dc} = v_{dc} - v_{dc}^*$, $\hat{i}_d = i_d - i_d^*$, and $\hat{i}_q = i_q - i_q^*$ and all the coefficients in (7.24) are positive constants. Let us consider the derivative of (7.24) w.r.t time, i.e.,

$$\begin{aligned} \frac{dV(\hat{x})}{dt} &= \left(\frac{c_1}{2} \sin \frac{\hat{\delta}}{2} \right) \frac{d\hat{\delta}}{dt} + 2 \left(\left(c_2 \hat{\zeta} \right) \frac{d\hat{\zeta}}{dt} + (c_3 \hat{v}_{dc}) \frac{d\hat{v}_{dc}}{dt} + (c_4 \hat{i}_d) \frac{d\hat{i}_d}{dt} + (c_5 \hat{i}_q) \frac{d\hat{i}_q}{dt} \right), \\ &= \left(\frac{c_1}{2} \sin \frac{\delta - \delta^*}{2} \right) \frac{d\delta}{dt} + 2 \left(c_2 (\zeta - \zeta^*) \frac{d\zeta}{dt} + c_3 (v_{dc} - v_{dc}^*) \frac{dv_{dc}}{dt} \right) \\ &\quad + 2 \left(c_4 (i_d - i_d^*) \frac{di_d}{dt} + c_5 (i_q - i_q^*) \frac{di_q}{dt} \right) \end{aligned} \quad (7.25)$$

as in (7.25). The state-dependent function (7.24) can be perceived as a measure of the distance (i.e., error) between the states in (7.20) and the equilibrium point (7.23).

Given that $V(0) = 0$ and $V(\hat{x}) > 0$ for $x \neq x^*$, we can conclude that $V(\hat{x}) \rightarrow 0$

²We remark that the forthcoming analysis can be extended to provide large-signal, i.e., global stability guarantees, as well. However, in this paper, for the sake of brevity, a local analysis is provided.

(thus, $\hat{x} \rightarrow 0$ and $x \rightarrow x^*$) if $dV(\hat{x})/dt < 0$ for all $x \neq x^*$ (i.e., if $V(\hat{x})$ is strictly decreasing). Hence, the convergence of $V(\hat{x})$ to zero implies the stability of (7.20). In order to demonstrate the stability of system (7.20), we seek for a parametric condition that results in $dV(\hat{x})/dt < 0$ for all $x \neq x^*$. Following the procedure in [3, Theorem 2], we set the coefficients in (7.24) as

$$c_1 = \frac{4}{\kappa_{dc}}, c_2 = \frac{\kappa_i}{2}, c_3 = \frac{C_{dc}}{2}, \text{ and } c_4 = c_5 = \frac{L}{2}.$$

Subsequently, lengthy albeit straightforward computation as in [3, Theorem 2][14] shows that if

$$\rho = \frac{\kappa_{ac}}{\kappa_{dc}} > \rho_{\text{critical}}, \quad (7.26)$$

where

$$\rho_{\text{critical}} = \frac{1}{G_{dc} + \kappa_p} + \frac{\mu^2 (i_d^{*2} + i_q^{*2})}{G_{dc} + \kappa_p} + \frac{\mu^2 v_{dc}^{*2}}{R},$$

then $dV(\hat{x})/dt < 0$. We remark that the condition (7.26) is met by choosing a sufficiently large ac synchronization gain in (7.6). Note that the implication of the stability condition (7.26) is the fact that the closed-loop stability is guaranteed solely by an appropriate choice of the HAC ac and dc gains. Further, ρ_{critical} can be reduced by increasing the proportional gain of the dc voltage control, thus, allowing for a less aggressive tuning of the HAC; see [3] for details on the stability condition (7.26). Last, Figure 7.2 provides a conceptual example for the presented energy-based stability analysis where a simplified form of (7.24) is employed. Figure 7.2 shows that how different initial states converge to the desired equilibrium point if the energy decay, i.e., $dV(\hat{x})/dt < 0$ is guaranteed.

7.4 Converter connected to a weak grid

In this section, we consider more complex model configurations in contrast to the model presented in Figure 7.1. Further, an approximate variant of HAC is presented. Next, we show how HAC can be combined with classic cascaded current and voltage controls. Finally, we present several HAC variants.

7.4.1 Grid impedance consideration

A weak grid connection is considered by including an equivalent grid impedance that is represented by a resistive-inductive element as shown in Figure 7.3. The different ratios of L_g and R_g represent connection to the low, medium, and high voltage grids [142]. Since the serial connected filter and grid equivalent impedances can be merged together, the closed-loop dynamics associated with the model in Figure 7.3 takes the same form

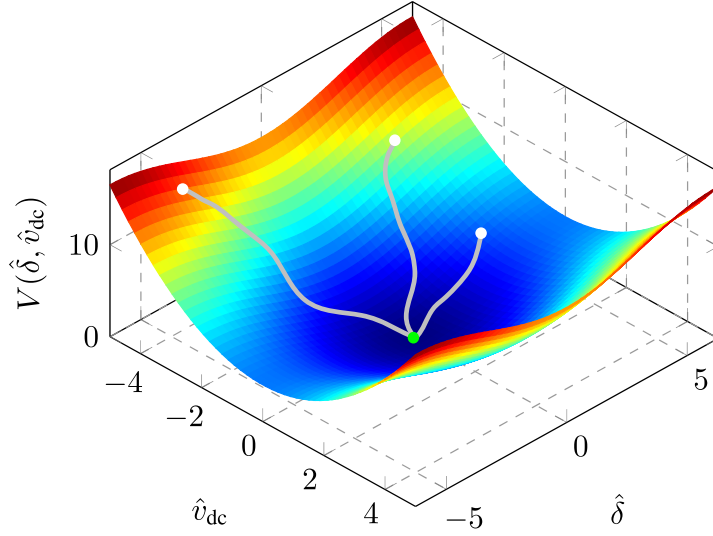


Figure 7.2: Conceptual illustration of the energy-based stability analysis; here it is assumed that the energy function is only function of the relative angle and dc voltage, i.e., $V(\hat{\delta}, \hat{v}_{dc}) = 2(1 - \cos \hat{\delta}/2) + (1/2)\hat{v}_{dc}^2$.

as in (7.20). The main implication of a weak grid connection is the fact that $v_{g,abc}$ (in Figure 7.1) is not available for the control implementation; see subsection 7.2.8 and [3]. Next, we show how leveraging certain assumptions allows to counteract this limitation by deriving an approximation for the HAC based on the ac active power flow.

7.4.2 Power-based control approximation

Consider the model in Figure 7.3 and let us merge the filter and grid equivalent impedance into a unified resistive-inductive element that reduces the ac sub-circuit to a classic coupled voltage sources configuration as in [142, Figure 7]. Subsequently, under dominantly inductive grid and small power angle assumptions [36], [142], the relative angle between

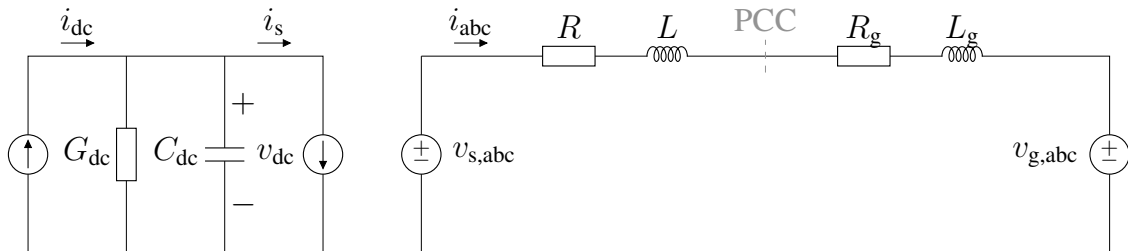


Figure 7.3: The circuit diagram of the converter model connected to a weak grid model in abc-coordinates system.

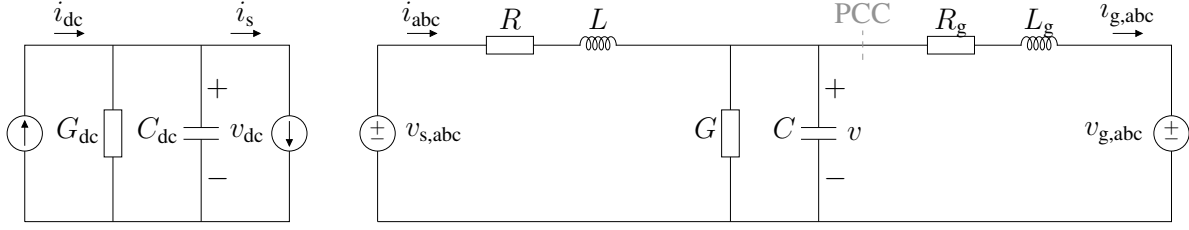


Figure 7.4: The circuit diagram of the converter model with LC output filter connected to a weak grid model in abc-coordinates system; this model also represents the case of a LCL filter consideration in which the grid-side filter inductance is merged with the grid impedance.

$v_{s,abc}$ and $v_{g,abc}$ is linearly approximated by the active power flows, i.e.,

$$\delta \approx \sin(\delta) \approx \left(\frac{(L + L_g) \omega_0}{|v_{s,abc}| |v_{g,abc}|} \right) p, \quad (7.27)$$

where p denotes the power injected by the converter. Further, assuming regulated ac voltages, i.e., constant $|v_{s,abc}|$ and $|v_{g,abc}|$, (7.27) is simplified to

$$\delta \approx \alpha p \quad \text{where} \quad \alpha = \frac{(L + L_g) \omega_0}{|v_{s,abc}| |v_{g,abc}|} \quad \text{is constant.} \quad (7.28)$$

A similar approximation as in (7.28) relates δ_r to the power reference p_r . Thus, the HAC in (7.6) is approximated by

$$\omega \approx \omega_0 + \kappa_{dc} (v_{dc} - v_{dc,r}) - \bar{\kappa}_{ac} (p - p_r), \quad (7.29)$$

where $\bar{\kappa}_{ac} = \alpha \kappa_{ac} / 2$. The approximate HAC (7.29), can be re-written in a trade-off form as

$$\Delta \omega \approx \kappa_{dc} \Delta v_{dc} - \bar{\kappa}_{ac} \Delta p, \quad (7.30)$$

where the converter frequency deviation from the nominal frequency is proportional to the dc voltage and ac power deviations from their respective references. We remark that if the assumptions behind (7.29) hold, the local (i.e., small-signal) stability properties of the original and approximate HAC forms are identical. Finally, note that the approximate HAC (7.30) coincides with the dual-port GFM control [56].

7.4.3 LC filter consideration and cascaded controllers

It is possible to consider LC output filter element which results in the model configuration in Figure 7.4. In this case, one can combine (7.29) with standard PI-based cascaded voltage and current controls [1], [100], [113]. Such control architecture is shown in Figure 7.5 and is briefly described as it follows.

- * The phase angle defined by HAC and a prescribed reference ac voltage magnitude are combined to define the reference PCC voltage in dq-coordinates, i.e., $v_{dq,r}$. Note that the converter frequency and angle defined by integrating (7.29) serves as the reference angle for subsequent controllers implemented in dq0-coordinates.
- * The PI-based ac voltage control (with feedforward terms) [1] processes the reference given by the GFM layer and PCC voltage feedback to define the reference filter current, i.e., $i_{dq,r}$.
- * The PI-based ac current control (with feedforward terms) processes the reference given by the voltage control layer and filter current feedback to define the converter voltage to appear behind the LC filter, i.e., $v_{s,dq,r}$.
- * The reference voltage given by the current control is processed by the modulation algorithm that defines m_{abc} .

We refer the reader to [1], [100], [113] for further details on the structure and tuning of such cascaded control architectures.

7.4.4 Control variants and extensions

On the basis of the GFM HAC, one can construct a few control variants. Let us introduce three different variants.

Fully multivariable variant

The key idea behind the HAC is to include a dc feedback controller into the converter angle dynamics. Along the same direction, one can include an ac feedback controller into the converter dc dynamics. In a generic form, the closed-loop dynamics under such fully multivariable control design takes the form

$$\begin{aligned}\frac{dx_{dc}}{dt} &= f_{dc}(x_{dc}, x_{ac}) + \kappa_{dc}g_{11}(x_{dc}) + \kappa_{ac \rightarrow dc}g_{12}(x_{ac}), \\ \frac{dx_{ac}}{dt} &= f_{ac}(x_{dc}, x_{ac}) + \kappa_{dc \rightarrow ac}g_{21}(x_{dc}) + \kappa_{ac}g_{22}(x_{ac}),\end{aligned}$$

where x_{dc} denotes the dc states, $f_{dc}(x_{dc}, x_{ac})$ describes the physical dc subsystem, κ_{dc} is the dc control gain, $g_{11}(x_{dc})$ is the linear/nonlinear dc controller for the dc states, $\kappa_{ac \rightarrow dc}$ is the gain of ac \rightarrow dc linear/nonlinear coupling control $g_{12}(x_{ac})$. Similarly, the states, physical ac subsystem, coupling controller gain and function, the ac control gain and function of the ac subsystem are respectively denoted by x_{ac} , $f_{ac}(x_{dc}, x_{ac})$, $\kappa_{dc \rightarrow ac}$, $g_{21}(x_{dc})$, κ_{ac} , and $g_{22}(x_{ac})$. Such augmentation of the standard GFM HAC is explored in [14].

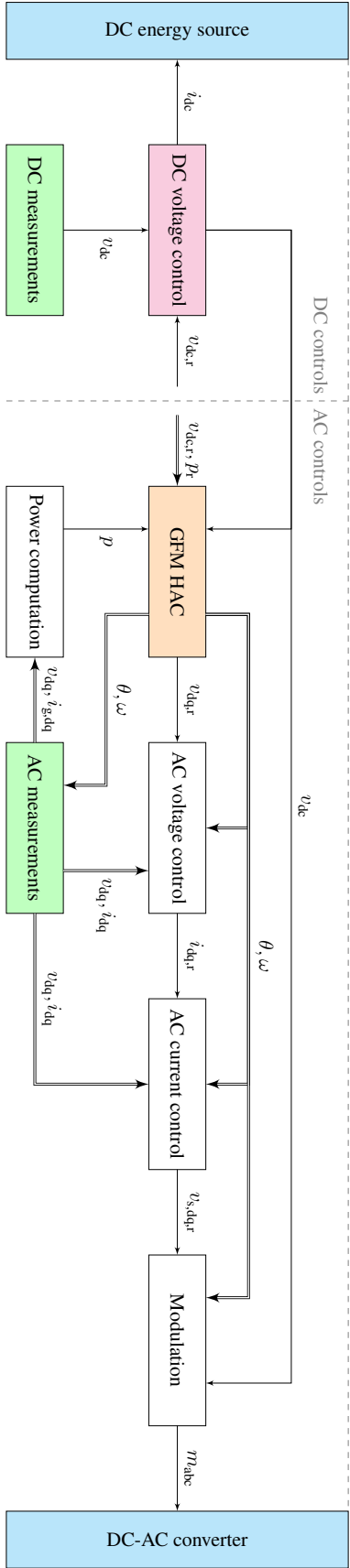


Figure 7.5: The overall control architecture of a grid-connected converter system including the dc-side controls, ac-side GFM, voltage, and current controls.

Inverse tangent variant

One can replace the ac synchronization term in (7.6) by an inverse tangent function, i.e., $\tan^{-1}(\delta - \delta_r)$. Furthermore, one can consider the combination of controls in [36] with [40] to arrive at the hybrid form:

$$\omega = \omega_0 + \kappa_{dc} (v_{dc} - v_{dc,r}) - \kappa_{ac,1} \tan^{-1} (\kappa_{ac,2}(p - p_r)).$$

Note that it is possible to derive strong large-signal (i.e., global) stability guarantees for this control variant as in [3], [14]. Further, [36] highlights the improved dynamic performance of the arctan droop control in contrast to the standard droop control. Thus, one can expect similar improvements for the hybrid arctan variant versus the standard HAC.

Energy-like variant

Finally, one can replace the linear dc term in (7.6) with a nonlinear quadratic term, i.e., $(v_{dc} - v_{dc,r})^2$ that is related to the dc energy and its reference. This control variant is particularly interesting for the modular multilevel converter (MMC) applications.

We remark that our preliminary investigations, e.g., [14], suggest that the aforementioned variants exhibit improved performance and/or lead to more relaxed conditions over the standard HAC, however, a deeper investigation is required.

7.5 Experimental verification

In this section, we describe the employed C-HiL verification approach, and present our test results.

7.5.1 Controller-hardware-in-the-loop verification approach

To verify the proposed GFM HAC strategy under real-world effects such as discretization, delays, measurement noise, etc., we go beyond offline simulations as in [3]–[5], [8] and implement our control algorithm in a control card, in order to run C-HiL simulations. The C-HiL approach represents a good candidate in terms of balancing testing complexity, costs, and fidelity. This setup enables a high degree of automation, thereby facilitating a high coverage of cases and grid conditions, especially those hard to implement in a laboratory setup or in the field. The utilized hardware benchmark is depicted in Figure 7.6, consisting of an Opal-RT OP5700 as real-time simulator, a host PC, and several Texas Instrument (LaunchPad F28379D) control cards in charge of executing the controller. The control cards receive the dc voltage and ac voltage and current as analog

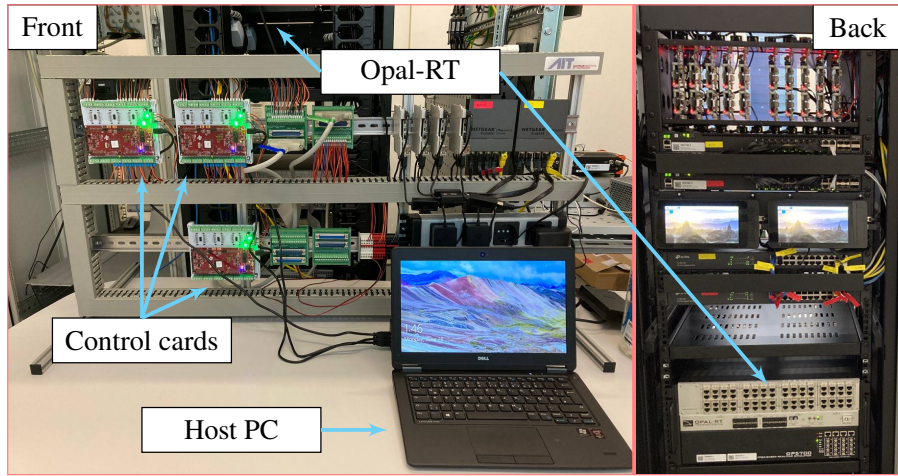


Figure 7.6: C-HiL testbed that includes three external control cards connected to Opal-RT OP5700. The host PC is used to automatically run C-HiL simulations and collect the results.

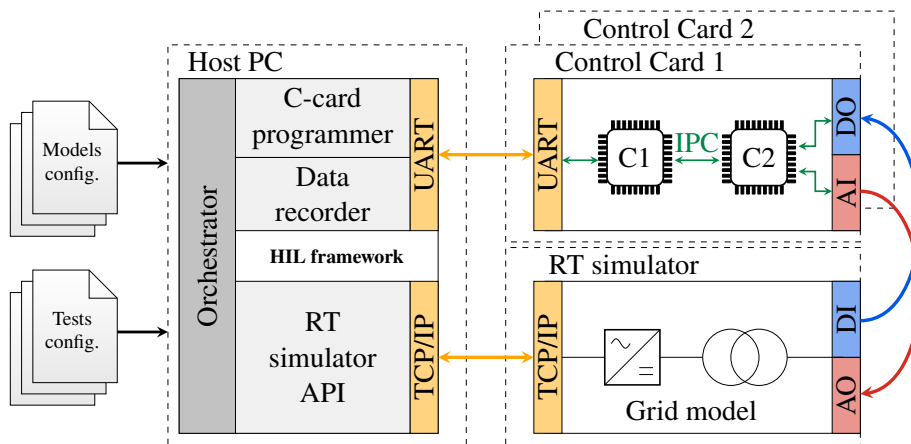


Figure 7.7: C-HiL testbed architecture. The C-HiL framework (on the left side) is developed in Python and its main functionality is to coordinate the RT-simulator and control cards. The control cards (on the right side) are connected to the RT-simulator via physical cables.

signals from Opal-RT, and generate the PWM signals to be sent back to the real-time simulator as digital signals. Switching frequency for the inverter is set to 5kHz, which is the same rate as for the execution of the controller in the control card. The grid-connected converter model and the dc source controller are executed in Opal-RT, using Time-Stamped Bridges to model the inverter IGBTs [147].

The testbed architecture is represented in Figure 7.7. The host PC communicates with the control cards via UART, and with Opal-RT via TCP/IP, thanks to the RT-LAB API. Given that the control cards possess two cores, data recording occurs in an online manner, bypassing memory limitations in the control card. Our setup allows us to measure relevant internal signals from the controllers such as frequency and filtered ac power. By means of configuration files, the tests of interest, set-points, and models to

be used are defined. The tests are completely automatized, including the flashing of the control cards, building the grid models for the Opal-RT, synchronization of the cards and the real-time simulator, and finally the retrieval of all data of interest.

7.5.2 C-HiL verification test scenarios

In what follows, we provide the results of four verification test cases that are performed on the testbed shown in Figure 7.6. Let us begin by highlighting the combination of employed controllers. We consider the PI-based dc and ac voltage control as described in Section 7.2, and the approximate power-based implementation of the HAC presented in Section 7.4. The baseline grid-connected converter model that is implemented in Opal-RT corresponds to the circuit configuration illustrated in Figure 7.4. Finally, the baseline model and control parameters are presented in Table 7.1. Note that the test-specific model and parameters modifications are described case-by-case.

Accuracy verification and islanded GFM operation

In this test scenario, the grid model is removed from the configuration in Figure 7.4. Instead a resistive load is connected at the PCC which at rated ac voltage consumes 0.5 p.u. active power. Figure 7.8 illustrates the behavior of the islanded converter under the HAC in offline and C-HiL simulations. Note that a 0.5 p.u. load increase is applied at $t = 0.1$ s. The results of offline and C-HiL simulations are sufficiently close, thus, verifying the accuracy of C-HiL testbed. Furthermore, the dynamic behavior shown in Figure 7.8 verifies the performances of the HAC control in islanded configuration. Note that, the ac gain (i.e., the droop gain) is selected such that it results in 5% frequency deviation for 1 p.u. active power disturbance. Observe that the 0.5 p.u. results in 2.5% frequency drop in Figure 7.8, thus, verifying the drooping behavior of the approximate HAC (7.29). Finally, the dc voltage is recovered to the reference value due to the integral term.

Grid-connected GFM operation

In this scenario, model configuration is identical to the one showed in Figure 7.4 and HAC behavior is investigated w.r.t a set-point change event in grid-connected mode. Figure 7.9 shows that GFM HAC not only preserves synchronization with the grid under a relatively large active power set-point change, i.e., 0.5 p.u. increase, but also achieves zero post-event steady-state error and stabilizes the converter frequency at the desired reference. We remark that the difference in transient behaviors in Figures 7.8 and 7.9 originates from the natural damping influence of the resistive load in the previous test scenario. Finally, retuning the GFM control parameters and the cut-off frequency of the low-pass filter applied to ac power measurement allows to realize a first-order behavior

Table 7.1: Grid-connected converter model and control parameters.

Symbol	Description	Value
p_b	base power	500 kVA
f_b	base frequency	60 Hz
ω_0	reference angular frequency	$2\pi f_b$
v_0	reference grid voltage magnitude	326.59 V
$v_{dc,r}$	reference dc-link voltage	$3v_0$
G_{dc}	dc-side conductance	$0.01 \text{ m}\Omega^{-1}$
C_{dc}	dc-link capacitance	0.01 F
f_{sw}	switching frequency	5 kHz
L	ac filter inductance	0.12 mH
C	ac filter capacitance	0.13 mF
L_g	grid equivalent inductance	0.56 mH
R_g	grid equivalent resistance	0.064Ω
κ_p	dc voltage control proportional gain	10
κ_i	dc voltage control integral gain	500
$\kappa_{p,ac}$	PCC voltage control proportional gain	0.1
$\kappa_{i,ac}$	PCC voltage control integral gain	20
κ_{dc}	HAC dc gain	0.18
$\bar{\kappa}_{ac}$	HAC ac gain	18.84

following the set-point change event. However, for the sake of consistency the parameters are kept identical.

Grid frequency variation

In this scenario, the grid frequency is increased step-wise by 5%. Figure 7.10 highlights the behavior of grid-connected converter under the HAC. Note that the GFM HAC preserves system stability w.r.t a relatively severe contingency. This is underpinned by the large-signal (i.e., global) stability of the HAC established in [3]. Further, due to the particular choice of the droop gain, the converter active power injection drops by 1 p.u. and reverses the power flow to provide frequency support.

Two-converter load-sharing operation

Finally, we consider a two-converter test scenarios. In this case, the converter models correspond to the model shown in Figure 7.4. However, the grid model is removed and the converters are connected through two RL line models and a resistive load is connected in the middle. Note that the droop gains for the power converters are slightly different, i.e., $0.98\bar{\kappa}_{ac}$ and $1.02\bar{\kappa}_{ac}$. Figure 7.11 illustrates the behavior of the system when a load increase event is applied. Observe that the post-disturbance frequency synchronization is achieved while the converters exhibits slightly different load-sharing according to the prescribed droop gains.

7.6 Conclusion

In this work, we discussed the behavioral properties of the GFM HAC, described required complementary controls, provided a closed-loop analysis involving analytical operating point evaluation and energy-based nonlinear stability analysis, derived an approximation of the HAC, and introduced several extensions of the standard HAC. Last but not least, the control performance was verified by several C-HiL test scenarios. Our agenda of future work includes the stability analysis and performance verification of the HAC variants, and power hardware validation of the control concept.

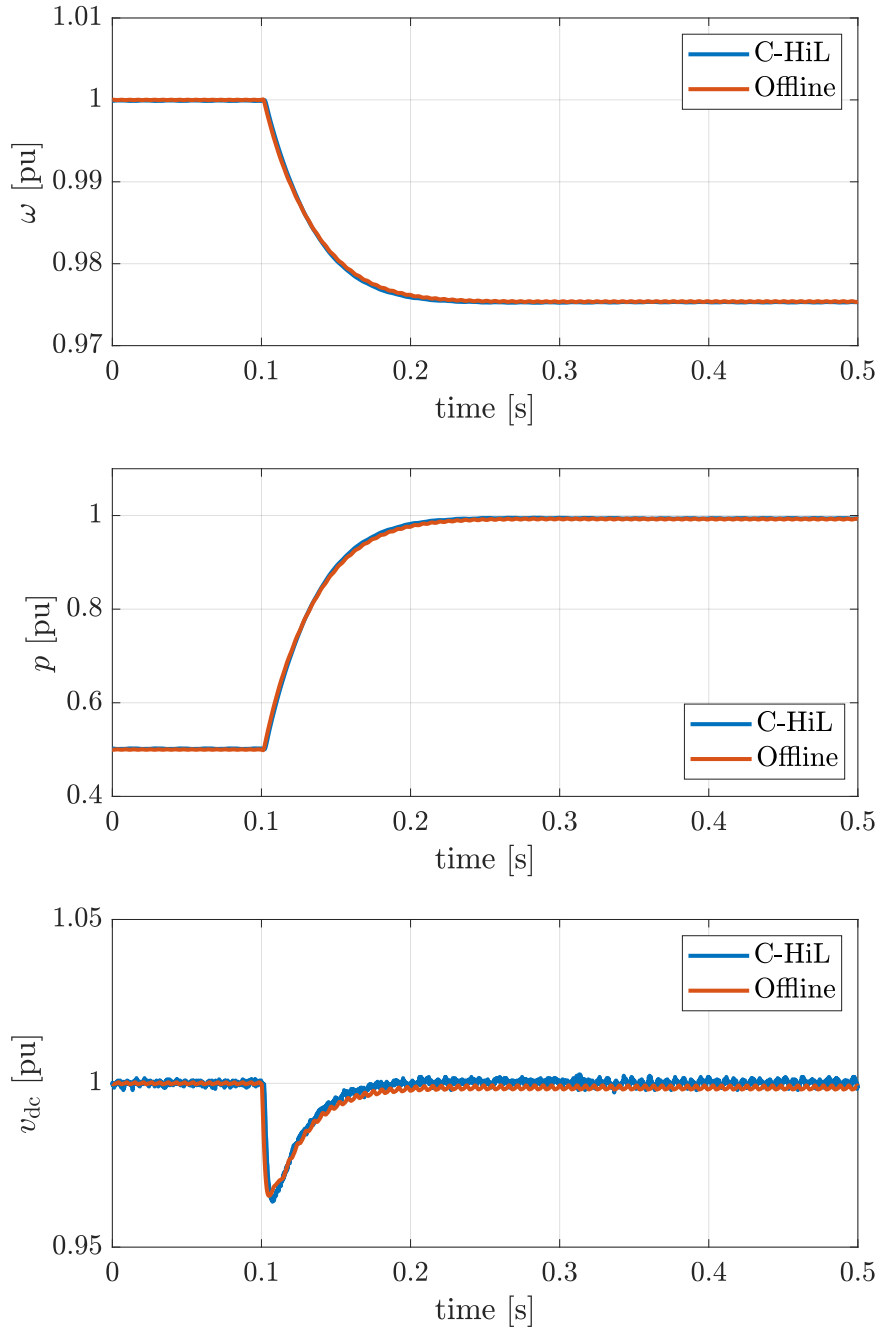


Figure 7.8: The time-evolution of normalized frequency (top), active power (middle), and dc voltage (bottom) of an islanded GFM converter under HAC w.r.t a load disturbance scenario in offline and C-HiL simulations.

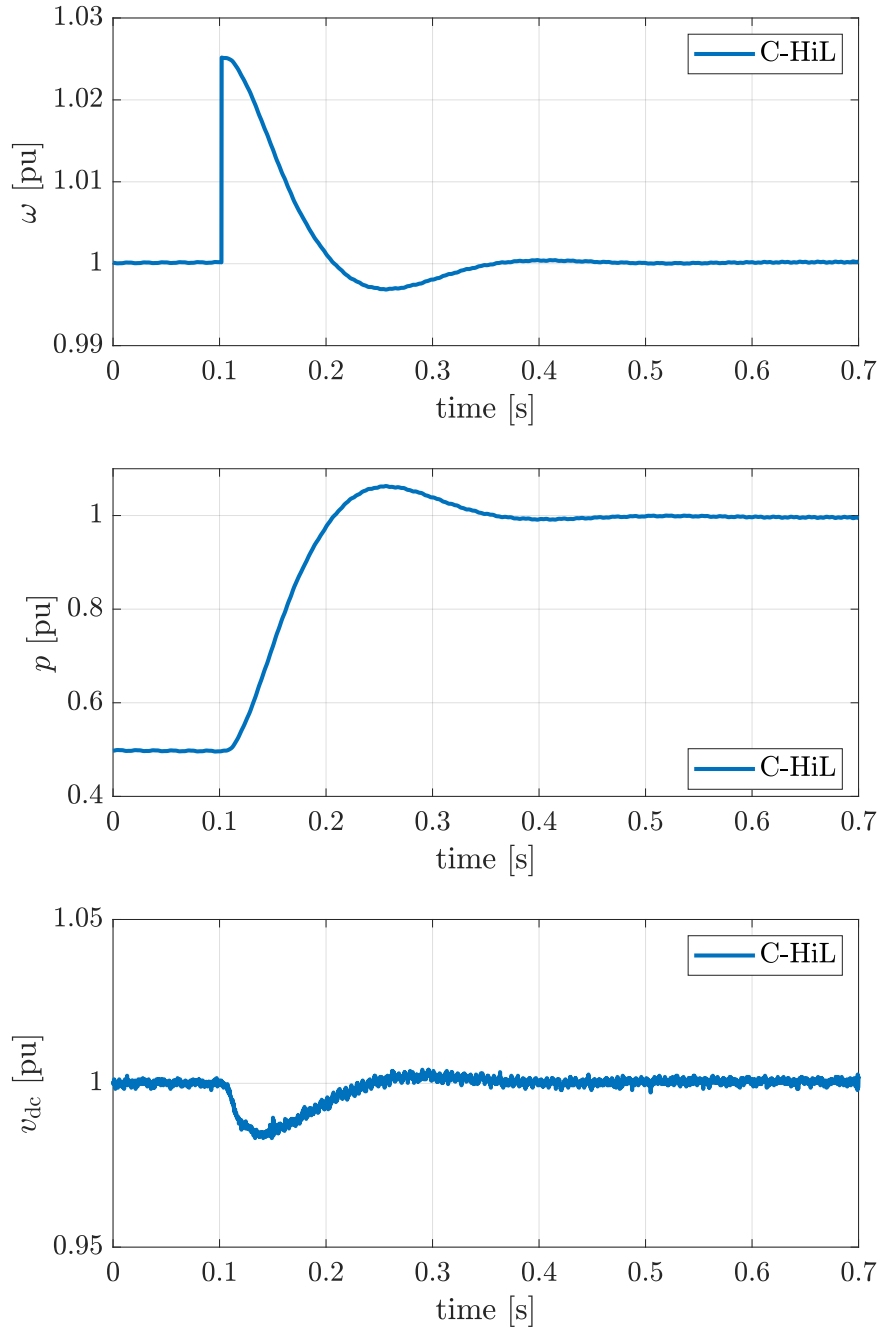


Figure 7.9: The time-evolution of normalized frequency (top), active power (middle), and dc voltage (bottom) of a grid-connected GFM converter under HAC w.r.t a power set-point change scenario in C-HiL simulations.

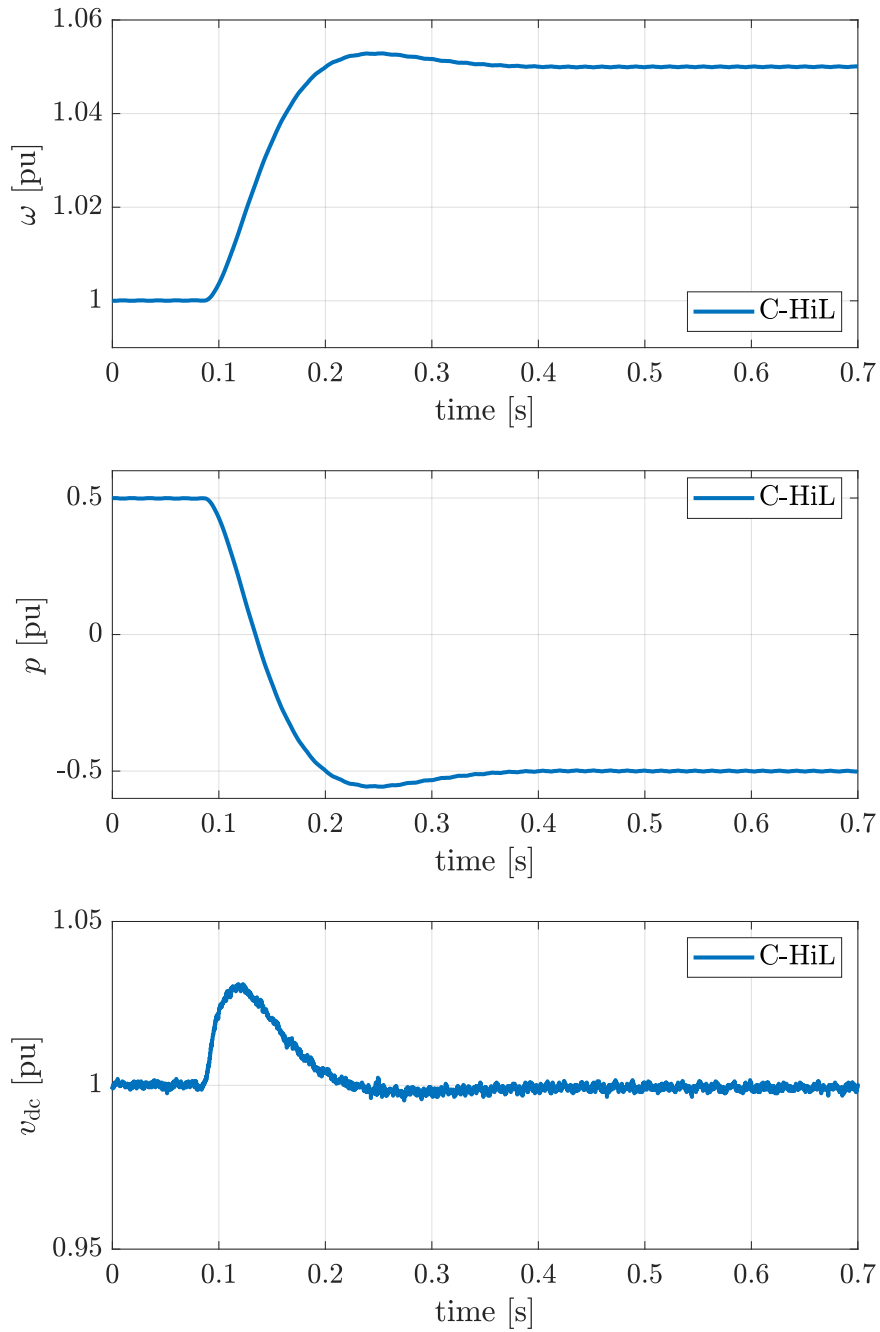


Figure 7.10: The time-evolution of normalized frequency (top), active power (middle), and dc voltage (bottom) of a grid-connected GFM converter under HAC w.r.t a grid frequency variation scenario in C-HiL simulations.

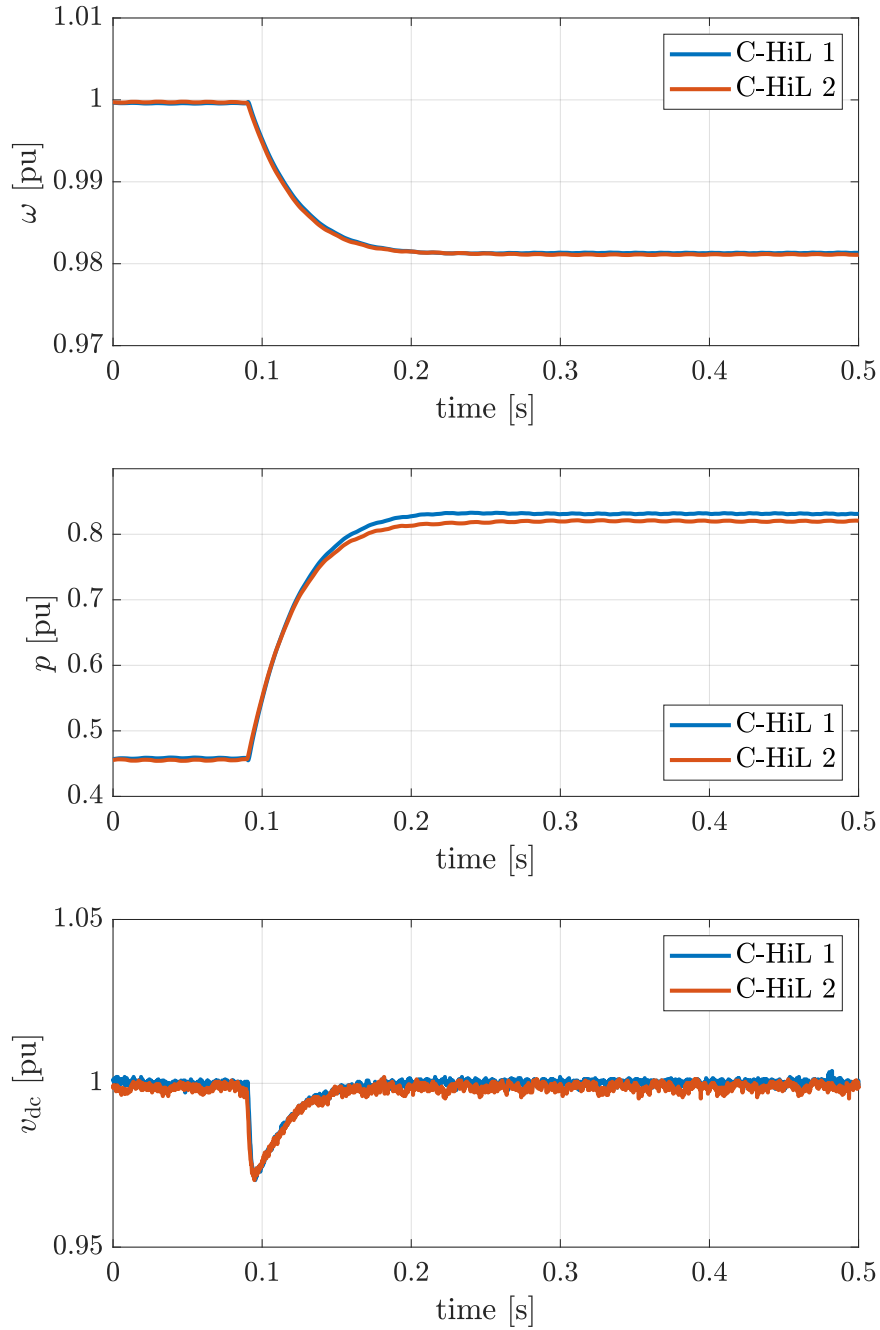


Figure 7.11: The time-evolution of normalized frequency (top), active power (middle), and dc voltage (bottom) of two coupled GFM converters under HAC (with slightly different droop gains) w.r.t a load disturbance scenario in C-HiL simulations.

Part IV

Conclusion

Summary, outlook, and open problems

This chapter concludes this thesis, highlights the future research directions on the basis of the presented results, and describes a few open problems in this research area.

8.1 Summary and outlook

The first part of this thesis, presented the results of extensive EMT simulation-based case studies on different state-of-the-art GFM controls in low-inertia power grid models that are summarized as follows.

- * The GFM control solutions can be classified into distinct classes, namely: dc-based, ac-based, and hybrid controls. The first two classes respectively result in enhanced small-signal frequency stability and robustness w.r.t to nonlinear phenomena, e.g., current limitation. Furthermore, the adverse interaction between the SMs and GFM converter timescales can potentially lead to unstable system-level behaviors.
- * The choice of converter control strategies, i.e., grid-following (GFL) or GFM controls plays a critical role in maximizing the penetration level of the converter-based generation. Further, certain control parameters of the SMs in a low-inertia system must be tuned according to the penetration level of the converter-based generation. Last, the classic frequency stability metrics must be reconsidered (or possibly redefined) to capture the system-level influence of the converter-based generation, especially for high penetration levels.

The second part of this thesis presented the control design, stability analysis, applications, and verification of a new GFM control design, i.e., the hybrid angle control (HAC) that are summarized as it follows:

- * The HAC is designed to integrate the complementary benefits of the dc and ac-based GFL controls. This control proposal results in the existence and almost

global asymptotic stability (AGAS) of the closed-loop equilibrium point of the detailed nonlinear grid-connected converter models under mild parametric stability conditions. Furthermore, a compatible current-limiting control is designed that does not jeopardize the closed-loop stability when combined with the HAC. Finally, a robustness analysis establishes the ultimate boundedness of the closed-loop trajectories in presence of implementation inaccuracies.

- * Although the HAC was originally designed for the two-level power converter applications, it can be applied to interlinking converter (ILC) in hybrid non-synchronous AC/DC power grids. In fact, the stability guarantees of the HAC are fully scalable for the hybrid AC/DC power grids application. Further, the extended AGAS result does not require strong assumptions on the underlying dc interconnections or the ac power flows.
- * Extended EMT simulation case studies verifies the hypothesis behind the HAC design, i.e., HAC combines the complementary benefits of the dc and ac-based GFM controls. Further, it is possible to extend the nonlinear stability analysis to an interconnected system of converter under the HAC.
- * Finally, it is possible to re-design the converter dc voltage control and omit the equilibria existence assumption under the HAC. Further, it is possible to derive an approximate power-based variant of HAC. Next, on the basis of HAC design one can consider several other hybrid control variants. Last, the performance of the control proposal was verified via controller-hardware-in-the-loop (C-HiL) simulation test scenarios.

The practical and theoretical outlooks of this doctoral research is described as follows.

- * A direction to extend the validation of HAC performance is to implement the control strategy on a power hardware. Further, one can also extend the presented controller-hardware-in-the-loop (C-HiL) verification approach by considering more complex network models.
- * A detailed theoretic stability analysis of an interconnected system of converters under the GFM is another direction for future research.
- * One can also follow the presented guidelines on designing a fully multivariable variant of the HAC. Subsequently, the optimization-based tuning methods can be employed for an optimal control parameter tuning.
- * Further detailed theoretic and practical investigation of the proposed current-limiting control and its combination with other GFM strategies is another promising direction.

- * The combination of HAC with the converter models that are derived based on the hybrid system theory (and include both continuous and discontinuous states) is another interesting direction.
- * Finally, a detailed simulation-based investigation of control performance in the hybrid AC/DC power grids is another direction to be explored.

8.2 Open problems

This thesis is closed by listing a few open problems that are directly/indirectly related to this thesis and research area.

- * The performance requirements for the power converters are often diverse and complex. Thus, requiring various complementary control loops to be combined with the classic GFL or GFM controls. A holistic converter control design that considers all performance specifications defined by the system operator is still an open problem. Further, the stability analysis of such a comprehensive control solution is to be explored, as well.
- * A plug-and-play converter control design that is fully agnostic to the power grid behavior and dynamics is also an open problem. This is specially interesting in converter-dominated power grids in which the system modes vary on fast timescales. Further, such plug-and-play control is particularly relevant in multi-vendor power system operation and strongly time-varying RESs integration scenarios.
- * A detailed nonlinear stability analysis of a multi-converter power system while incorporating high-fidelity nonlinear converter models accounting for the dc, modulation, and ac dynamics and dynamic line models is a standing open problem. Similarly, the stability analysis of a multi-machine power system while considering detailed nonlinear SMs models is open.
- * The design of a robust current-limiting strategy for power converters that is suitable for all potential over-current scenarios is open, as well.
- * Finally, the oscillator-based GFM control solutions result in elegant stability results and provide strong global stability certificates. However, the converter modulation and dc dynamics are often neglected in such control design. Thus, an oscillator-based GFM control design that takes into account a detailed nonlinear description of converter dynamics is yet to be explored.

Bibliography

- [1] A. Tayyebi, D. Groß, A. Anta, F. Kupzog, and F. Dörfler, “Frequency stability of synchronous machines and grid-forming power converters”, *IEEE Journal of Emerging and Selected Topics in Power Electronics*, vol. 8, no. 2, pp. 1004–1018, 2020.
- [2] A. Crivellaro, A. Tayyebi, C. Gavriluta, D. Groß, A. Anta, F. Kupzog, and F. Dörfler, “Beyond low-inertia systems: Massive integration of grid-forming power converters in transmission grids”, in *IEEE Power and Energy Society General Meeting (PESGM)*, 2020.
- [3] A. Tayyebi, A. Anta, and F. Dörfler, “Grid-forming hybrid angle control and almost global stability of the DC-AC power converter”, *IEEE Transactions on Automatic Control*, vol. 68, no. 7, pp. 3842–3857, 2022.
- [4] A. Tayyebi and F. Dörfler, “Hybrid angle control and almost global stability of non-synchronous hybrid AC/DC power grids”, in *IEEE Conference on Decision and Control (CDC)*, 2022.
- [5] A. Tayyebi, A. Magdaleno, D. Vettoretti, M. Chen, E. Prieto-Araujo, A. Anta, and F. Dörfler, “System-level performance and robustness of the grid-forming hybrid angle control”, *Electric Power Systems Research*, vol. 212, p. 108 503, 2022.
- [6] A. Tayyebi, D. Vettoretti, A. Anta, and F. Dörfler, “Grid-forming hybrid angle control: Behavior, stability, variants and verification”, *IEEE Transactions on Smart Grid*, 2023, submitted, <https://arxiv.org/abs/2307.09398>.
- [7] A. Tayyebi, F. Dörfler, F. Kupzog, Z. Miletic, and W. Hribernik, “Grid-forming converters – inevitability, control strategies and challenges in future grid applications”, in *International Conference on Electricity Distribution (CIRED)*, 2018.
- [8] A. Tayyebi, A. Anta, and F. Dörfler, “Almost globally stable grid-forming hybrid angle control”, in *IEEE Conference on Decision and Control (CDC)*, 2020.
- [9] M. Chen, D. Zhou, A. Tayyebi, E. Prieto-Araujo, F. Dörfler, and F. Blaabjerg, “Generalized multivariable grid-forming control design for power converters”, *IEEE Transactions on Smart Grid*, vol. 13, no. 4, pp. 2873–2885, 2022.

- [10] M. Chen, D. Zhou, A. Tayyebi, E. Prieto-Araujo, F. Dörfler, and F. Blaabjerg, “Augmentation of generalized multivariable grid-forming control for power converters with cascaded controllers”, in *IEEE International Power Electronics Conference (IPEC)*, 2022.
- [11] V. Häberle, E. Prieto-Araujo, A. Tayyebi, and F. Dörfler, “Grid-forming control design of dynamic virtual power plants”, in *IFAC Conference on Networked Systems (NecSys)*, 2022.
- [12] V. Häberle, A. Tayyebi, X. He, E. Prieto-Araujo, and F. Dörfler, “Grid-forming and spatially distributed control design of dynamic virtual power plants”, *IEEE Transactions on Smart Grid*, 2023, submitted, <https://arxiv.org/abs/2202.02057>.
- [13] M. Chen, D. Zhou, A. Tayyebi, E. Prieto-Araujo, F. Dörfler, and F. Blaabjerg, “On power control of grid-forming converters: Modeling, controllability, and full-state feedback design”, *IEEE Transactions on Sustainable Energy*, pp. 1–12, 2023.
- [14] A. Gattiglio, “Multivariable arctan hybrid angle control and global stability of grid-forming power converters”, 2021.
- [15] A. Magdaleno, “System-level performance evaluation of the hybrid angle control for grid-forming power converters”, 2021.
- [16] C.-C. Jimenez, “Large-scale analysis of massive deployment of converter-based generation equipped with grid-forming strategies”, 2020.
- [17] A. Crivellaro, “Simulation-based study of novel control strategies for inverters in low-inertia system: Grid-forming and followings”, 2019.
- [18] D. Vettoretti, “Validation platform for grid-forming control strategies of power inverters: From component to system-level validation”, 2019.
- [19] “MIGRATE project”, <https://www.h2020-migrate.eu/>.
- [20] “UNIFI project”, <https://sites.google.com/view/unifi-consortium>.
- [21] “AGISTIN project”, <https://www.agistin.eu/>.
- [22] “RESERVE project”, <http://www.re-serve.eu/>.
- [23] R. Musca, A. Vasile, and G. Zizzo, “Grid-forming converters. a critical review of pilot projects and demonstrators”, *Renewable and Sustainable Energy Reviews*, vol. 165, p. 112 551, 2022.
- [24] P. Unruh, M. Nuschke, P. Strauß, and F. Welck, “Overview on grid-forming inverter control methods”, *Energies*, vol. 13, no. 10, p. 2589, 2020.
- [25] R. Rosso, X. Wang, M. Liserre, X. Lu, and S. Engelken, “Grid-forming converters: Control approaches, grid-synchronization, and future trends—a review”, *IEEE Open Journal of Industry Applications*, vol. 2, pp. 93–109, 2021.

- [26] T. Ackermann, T. Prevost, V. Vittal, A. J. Roscoe, J. Matevosyan, and N. Miller, “Paving the way: A future without inertia is closer than you think”, *IEEE Power and Energy Magazine*, vol. 15, no. 6, pp. 61–69, 2017.
- [27] B. Kroposki, B. Johnson, Y. Zhang, V. Gevorgian, P. Denholm, B. M. Hodge, and B. Hannegan, “Achieving a 100% renewable grid: Operating electric power systems with extremely high levels of variable renewable energy”, *IEEE Power Electronics Magazine*, vol. 15, no. 2, pp. 61–73, 2017.
- [28] “Engineering roadmap to 100% renewables”, AEMO, Tech. Rep., 2022.
- [29] “Great Britain grid forming best practice guide”, National Grid ESO, Tech. Rep., 2023.
- [30] “Grid forming functional specifications for BPS-connected battery energy storage systems”, NERC, Tech. Rep., 2023.
- [31] “Grid-forming technology”, NERC, Tech. Rep., 2021.
- [32] Y. Lin, J. H. Eto, B. B. Johnson, J. D. Flicker, R. H. Lasseter, H. N. Villegas Pico, G.-S. Seo, B. J. Pierre, and A. Ellis, “Research roadmap on grid-forming inverters”, NREL, Tech. Rep., 2020.
- [33] F. Milano, F. Dörfler, G. Hug, D. J. Hill, and G. Verbič, “Foundations and challenges of low-inertia systems”, in *Power System Computation Conference (PSCC)*, 2018.
- [34] J. W. Simpson-Porco, F. Dörfler, and F. Bullo, “Synchronization and power sharing for droop-controlled inverters in islanded microgrids”, *Automatica*, vol. 49, no. 9, pp. 2603–2611, 2013.
- [35] M. Chandorkar, D. Divan, and R. Adapa, “Control of parallel connected inverters in standalone AC supply systems”, *IEEE Transactions on Industry Applications*, vol. 29, no. 1, pp. 136–143, 1993.
- [36] C. N. Rowe, T. J. Summers, R. E. Betz, D. J. Cornforth, and T. G. Moore, “Arctan power–frequency droop for improved microgrid stability”, *IEEE transactions on Power Electronics*, vol. 28, no. 8, pp. 3747–3759, 2012.
- [37] E. Mallada, “Idroop: A dynamic droop controller to decouple power grid’s steady-state and dynamic performance”, in *IEEE Conference on Decision and Control (CDC)*, 2016.
- [38] S. D’Arco, J. A. Suul, and O. B. Fosso, “A virtual synchronous machine implementation for distributed control of power converters in smart grid”, *Electric Power Systems Research*, vol. 122, pp. 180–197, 2015.
- [39] Q. Zhong, P. Nguyen, Z. Ma, and W. Sheng, “Self-synchronized synchronverters: Inverters without a dedicated synchronization unit”, *IEEE Transactions on Power Electronics*, vol. 29, no. 2, pp. 617–630, 2014.

- [40] C. Arghir and F. Dörfler, “The electronic realization of synchronous machines: Model matching, angle tracking, and energy shaping techniques”, *IEEE Transactions on Power Electronics*, vol. 35, no. 4, pp. 4398–4410, 2020.
- [41] S. Curi, D. Groß, and F. Dörfler, “Control of low-inertia power grids: A model reduction approach”, in *IEEE Conference on Decision and Control (CDC)*, 2017.
- [42] H. Bevrani, T. Ise, and Y. Miura, “Virtual synchronous generators: A survey and new perspectives”, *International Journal of Electrical Power and Energy Systems*, vol. 54, pp. 244–254, 2014.
- [43] I. Cvetkovic, D. Boroyevich, R. Burgos, C. Li, and P. Mattavelli, “Modeling and control of voltage-source converters emulating isotropic and anisotropic synchronous machines”, in *IEEE Workshop on Control and Modeling for Power Electronics (COMPEL)*, 2015.
- [44] L. Huang, H. Xin, Z. Wang, K. Wu, H. Wang, J. Hu, and C. Lu, “A virtual synchronous control for voltage-source converters utilizing dynamics of DC-link capacitor to realize self-synchronization”, *IEEE Journal of Emerging and Selected Topics in Power Electronics*, vol. 5, no. 4, pp. 1565–1577, 2017.
- [45] M. Colombino, D. Groß, J. Brouillon, and F. Dörfler, “Global phase and magnitude synchronization of coupled oscillators with application to the control of grid-forming power inverters”, *IEEE Transactions on Automatic Control*, vol. 64, no. 11, pp. 4496–4511, 2019.
- [46] M. Sinha, F. Dörfler, B. B. Johnson, and S. V. Dhople, “Uncovering droop control laws embedded within the nonlinear dynamics of van der pol oscillators”, *IEEE Transactions on Control of Network Systems*, vol. 4, no. 2, pp. 347–358, 2017.
- [47] D. Groß, M. Colombino, J. Brouillon, and F. Dörfler, “The effect of transmission-line dynamics on grid-forming dispatchable virtual oscillator control”, *IEEE Transactions on Control of Network Systems*, vol. 6, no. 3, pp. 1148–1160, 2019.
- [48] G. Seo, I. Subotic, B. Johnson, M. Colombino, D. Groß, and F. Dörfler, “Dispatchable virtual oscillator control for decentralized inverter-dominant power systems - analysis of droop characteristic and verification”, in *IEEE Applied Power Electronics Conference (APEC)*, 2019.
- [49] B. B. Johnson, M. Sinha, N. G. Ainsworth, F. Dörfler, and S. V. Dhople, “Synthesizing virtual oscillators to control islanded inverters”, *IEEE Transactions on Power Electronics*, vol. 31, no. 8, pp. 6002–6015, 2015.
- [50] H. Yu, M. Awal, H. Tu, I. Husain, and S. Lukic, “Comparative transient stability assessment of droop and dispatchable virtual oscillator controlled grid-connected inverters”, *IEEE Transactions on Power Electronics*, vol. 36, no. 2, pp. 2119–2130, 2021.

- [51] B. Johnson, M. Rodriguez, M. Sinha, and S. Dhople, “Comparison of virtual oscillator and droop control”, in *IEEE Workshop on Control and Modeling for Power Electronics (COMPEL)*, 2017.
- [52] S. A. Aghdam and M. Agamy, “Virtual oscillator-based methods for grid-forming inverter control: A review”, *IET Renewable Power Generation*, vol. 16, no. 5, pp. 835–855, 2022.
- [53] M. Awal, M. R. K. Rachi, H. Yu, I. Husain, and S. Lukic, “Double synchronous unified virtual oscillator control for asymmetrical fault ride-through in grid-forming voltage source converters”, *IEEE Transactions on Power Electronics*, vol. 38, no. 6, pp. 6759–6763, 2023.
- [54] M. Lu, S. Dhople, and B. Johnson, “Benchmarking nonlinear oscillators for grid-forming inverter control”, *IEEE Transactions on Power Electronics*, vol. 37, no. 9, pp. 10 250–10 266, 2022.
- [55] Y. Gao, H.-P. Ren, and J. Li, “Grid-forming converters control based on DC voltage feedback”, 2020, submitted, <https://arxiv.org/abs/2009.05759>.
- [56] D. Groß, Sánchez-Sánchez, E. Prieto-Araujo, and O. Gomis-Bellmunt, “Dual-port grid-forming control of MMCs and its applications to grids of grids”, *IEEE Transactions on Power Delivery*, vol. 37, no. 6, pp. 4721–4735, 2022.
- [57] I. Subotić and D. Groß, “Power-balancing dual-port grid-forming power converter control for renewable integration and hybrid AC/DC power systems”, *IEEE Transactions on Control of Network Systems*, vol. 9, no. 4, pp. 1949–1961, 2022.
- [58] L. Huang, J. Coulson, J. Lygeros, and F. Dörfler, “Decentralized data-enabled predictive control for power system oscillation damping”, *IEEE Transactions on Control Systems Technology*, vol. 30, no. 3, pp. 1065–1077, 2021.
- [59] O. Stanojev, U. Markovic, P. Aristidou, G. Hug, D. Callaway, and E. Vrettos, “MPC-based fast frequency control of voltage source converters in low-inertia power systems”, *IEEE Transactions on Power Systems*, vol. 37, no. 4, pp. 3209–3220, 2020.
- [60] L. Huang, H. Xin, and F. Dörfler, “ \mathcal{H}_∞ -control of grid-connected converters: Design, objectives and decentralized stability certificates”, *IEEE Transactions on Smart Grid*, vol. 11, no. 5, pp. 3805–3816, 2020.
- [61] P. W. Sauer and M. A. Pai, *Power system dynamics and stability*. Prentice hall, 1998.
- [62] P. Kundur, *Power system stability and control*. McGraw-Hill, 1994.
- [63] “High penetration of power electronic interfaced power sources ENTSO-E guidance document for national implementation for network codes on grid connection”, ENTSO-E, Tech. Rep., 2017.

- [64] Q. C. Zhong and G. Weiss, “Synchronverters: Inverters that mimic synchronous generators”, *IEEE Transactions on Industrial Electronics*, vol. 58, no. 4, pp. 1259–1267, 2011.
- [65] C. Arghir, T. Jouini, and F. Dörfler, “Grid-forming control for power converters based on matching of synchronous machines”, *Automatica*, vol. 95, pp. 273–282, 2018.
- [66] N. Pogaku, M. Prodanovic, and T. C. Green, “Modeling, analysis and testing of autonomous operation of an inverter-based microgrid”, *IEEE Transactions on Power Electronics*, vol. 22, no. 2, pp. 613–625, 2007.
- [67] F. Paganini and E. Mallada, “Global analysis of synchronization performance for power systems: Bridging the theory-practice gap”, *IEEE Transactions on Automatic Control*, vol. 65, no. 7, pp. 3007–3022, 2019.
- [68] M. Pirani, J. W. Simpson-Porco, and B. Fidan, “System-theoretic performance metrics for low-inertia stability of power networks”, in *IEEE Conference on Decision and Control (CDC)*, 2017.
- [69] “Frequency measurement requirements and usage”, ENTSO-E, Tech. Rep., 2018.
- [70] B. K. Poolla, D. Groß, and F. Dörfler, “Placement and implementation of grid-forming and grid-following virtual inertia and fast frequency response”, *IEEE Transactions on Power Systems*, vol. 34, no. 4, pp. 3035–3046, 2019.
- [71] A. Tayyebi, D. Groß, and A. Anta, “GridFormingConverters: Implementation of grid-forming control techniques in IEEE 9-bus system”, *GitHub Repository*, 2019.
- [72] U. Markovic, O. Stanojev, E. Vrettos, P. Aristidou, and G. Hug, “Understanding stability of low-inertia systems”, *IEEE Transactions on Power Systems*, 2019, submitted, <https://engrxiv.org/jwzrq>.
- [73] A. Yazdani and R. Iravani, *Voltage-sourced converters in power systems*. Wiley Online Library, 2010.
- [74] G. Denis, T. Prevost, M. Debry, F. Xavier, X. Guillaud, and A. Menze, “The MIGRATE project: The challenges of operating a transmission grid with only inverter-based generation. A grid-forming control improvement with transient current-limiting control”, *IET Renewable Power Generation*, vol. 12, no. 5, pp. 523–529, 2018.
- [75] “IEEE recommended practice for excitation system models for power system stability studies”, IEEE, Tech. Rep., 2016.
- [76] R. D. Zimmerman, C. E. Murillo-Sanchez, and R. J. Thomas, “MATPOWER: Steady-state operations, planning, and analysis tools for power systems research and education”, *IEEE Transactions on Power Systems*, vol. 26, no. 1, pp. 12–19, 2010.

- [77] P. Vorobev, P. Huang, M. A. Hosani, J. L. Kirtley, and K. Turitsyn, “High-fidelity model order reduction for microgrids stability assessment”, *IEEE Transactions on Power Systems*, vol. 33, no. 1, pp. 874–887, 2018.
- [78] V. Purba, S. V. Dhople, S. Jafarpour, F. Bullo, and B. B. Johnson, “Reduced-order structure-preserving model for parallel-connected three-phase grid-tied inverters”, in *IEEE Workshop on Control and Modeling for Power Electronics (COMPEL)*, 2017.
- [79] M. M. S. Khan, Y. Lin, B. Johnson, V. Purba, M. Sinha, and S. Dhople, “A reduced-order aggregated model for parallel inverter systems with virtual oscillator control”, in *IEEE Workshop on Control and Modeling for Power Electronics (COMPEL)*, 2018.
- [80] V. Purba, B. B. Johnson, M. Rodriguez, S. Jafarpour, F. Bullo, and S. V. Dhople, “Reduced-order aggregate model for parallel-connected single-phase inverters”, *IEEE Transactions on Energy Conversion*, vol. 34, no. 2, pp. 824–837, 2019.
- [81] M. G. Taul, X. Wang, P. Davari, and F. Blaabjerg, “Current limiting control with enhanced dynamics of grid-forming converters during fault conditions”, *IEEE Journal of Emerging and Selected Topics in Power Electronics*, vol. 8, no. 2, pp. 1062–1073, 2020.
- [82] H. Xin, L. Huang, L. Zhang, Z. Wang, and J. Hu, “Synchronous instability mechanism of P-f droop-controlled voltage source converter caused by current saturation”, *IEEE Transactions on Power Systems*, vol. 31, no. 6, pp. 5206–5207, 2016.
- [83] X. Wang, Y. W. Li, F. Blaabjerg, and P. C. Loh, “Virtual-impedance-based control for voltage-source and current-source converters”, *IEEE Transactions on Power Electronics*, vol. 30, no. 12, pp. 7019–7037, 2015.
- [84] Q. Zhong and G. C. Konstantopoulos, “Current-limiting droop control of grid-connected inverters”, *IEEE Transactions on Industrial Electronics*, vol. 64, no. 7, pp. 5963–5973, 2017.
- [85] A. Gkountaras, S. Dieckerhoff, and T. Sezi, “Evaluation of current limiting methods for grid forming inverters in medium voltage microgrids”, in *IEEE Energy Conversion Congress and Exposition (ECCE)*, 2015.
- [86] I. Sadeghkhani, M. E. Hamedani Golshan, J. M. Guerrero, and A. Mehrizi-Sani, “A current limiting strategy to improve fault ride-through of inverter interfaced autonomous microgrids”, *IEEE Transactions on Smart Grid*, vol. 8, no. 5, pp. 2138–2148, 2017.
- [87] A. D. Paquette and D. M. Divan, “Virtual impedance current limiting for inverters microgrids with synchronous generators”, *IEEE Transactions on Industry Applications*, vol. 51, no. 2, pp. 1630–1638, 2015.

- [88] F. Milano and A. Ortega, “Frequency divider”, *IEEE Transactions on Power Systems*, vol. 32, no. 2, pp. 1493–1501, 2017.
- [89] “Final report - Queensland and south Australia system separation on 25 August 2018”, AEMO, Tech. Rep., 2019.
- [90] G. Peponides, P. Kokotovic, and J. Chow, “Singular perturbations and time scales in nonlinear models of power systems”, *IEEE Transactions on Circuits and Systems*, vol. 29, no. 11, pp. 758–767, 1982.
- [91] L. Sigrist, I. Egido, and L. Rouco, “Principles of a centralized UFLS scheme for small isolated power systems”, *IEEE Transactions on Power Systems*, vol. 28, no. 2, pp. 1779–1786, 2013.
- [92] T. Qoria, F. Gruson, F. Colas, X. Guillaud, M. Debry, and T. Prevost, “Tuning of cascaded controllers for robust grid-forming voltage source converter”, in *Power Systems Computation Conference (PSCC)*, 2018.
- [93] “Annual renewable constraint and curtailment report”, EIRGRID, Tech. Rep., 2017.
- [94] A. Tayyebi, D. Groß, A. Anta, F. Kupzog, and F. Dörfler, “Interactions of grid-forming power converters and synchronous machines”, *IEEE Transactions on Power Systems*, 2019, submitted, <https://arxiv.org/abs/1902.10750>.
- [95] Y. Lin, B. Johnson, V. Gevorgian, V. Purba, and S. Dhople, “Stability assessment of a system comprising a single machine and inverter with scalable ratings”, in *North American Power Symposium (NAPS)*, 2017.
- [96] G. Sybille, “Hydro-Quebec 29-bus grid model – Matlab implementation”, *Mathworks Webpage*,
- [97] M.-S. Debry, G. Denis, T. Prevost, F. Xavier, and A. Menze, “Maximizing the penetration of inverter-based generation on large transmission systems: The migrate project”, in *Solar Integration Workshop*, 2017.
- [98] J. Matevosyan, B. Badrzadeh, T. Prevost, E. Quitmann, D. Ramasubramanian, H. Urdal, S. Achilles, J. MacDowell, S. H. Huang, V. Vital, J. O’Sullivan, and R. Quint, “Grid-forming inverters: Are they the key for high renewable penetration?”, *IEEE Power and Energy Magazine*, vol. 17, no. 6, pp. 89–98, 2019.
- [99] “Rate of change of frequency (rocof) withstand capability”, ENTSO-E, Tech. Rep., 2017.
- [100] U. Markovic, O. Stanojev, P. Aristidou, E. Vrettos, D. S. Callaway, and G. Hug, “Understanding small-signal stability of low-inertia systems”, *IEEE Transactions on Power Systems*, vol. 36, no. 5, pp. 3997–4017, 2021.

- [101] Q. Peng, Q. Jiang, Y. Yang, T. Liu, H. Wang, and F. Blaabjerg, “On the stability of power electronics-dominated systems: Challenges and potential solutions”, *IEEE Transactions on Industry Applications*, vol. 55, no. 6, pp. 7657–7670, 2019.
- [102] J. Fang, H. Li, Y. Tang, and F. Blaabjerg, “On the inertia of future more-electronics power systems”, *IEEE Journal of Emerging and Selected Topics in Power Electronics*, vol. 7, no. 4, pp. 2130–2146, 2018.
- [103] V. Natarajan and G. Weiss, “Almost global asymptotic stability of a grid-connected synchronous generator”, *Mathematics of Control, Signals, and Systems*, vol. 30, pp. 1–43, 2018.
- [104] P. Lorenzetti, Z. Kustanovich, S. Shivratri, and G. Weiss, “The equilibrium points and stability of grid-connected synchronverters”, *IEEE Transactions on Power Systems*, vol. 37, no. 2, pp. 1184–1197, 2022.
- [105] S. Samanta and N. R. Chaudhuri, “On stability analysis of power grids with synchronous generators and grid-forming converters under DC-side current limitation”, in *IEEE American Control Conference (ACC)*, 2021.
- [106] R. Ortega, A. van der Schaft, B. Maschke, and G. Escobar, “Interconnection and damping assignment passivity-based control of port-controlled Hamiltonian systems”, *Automatica*, vol. 38, no. 4, pp. 585–596, 2002.
- [107] I. Sarras, R. Ortega, and E. Panteley, “Asymptotic stabilization of nonlinear systems via sign-indefinite damping injection”, in *IEEE Conference on Decision and Control (CDC)*, 2012.
- [108] S. P. Bhat and D. S. Bernstein, “A topological obstruction to continuous global stabilization of rotational motion and the unwinding phenomenon”, *Systems and Control Letters*, vol. 39, no. 1, pp. 63–70, 2000.
- [109] N. Barabanov, J. Schiffer, R. Ortega, and D. Efimov, “Conditions for almost global attractivity of a synchronous generator connected to an infinite bus”, *IEEE Transactions on Automatic Control*, vol. 62, pp. 4905–4916, 2017.
- [110] F. Milano and Á. O. Manjavacas, *Converter-interfaced energy storage systems: Context, modelling and dynamic analysis*. Cambridge University Press, 2019.
- [111] H. Khalil, *Nonlinear systems*. Prentice Hall, 2002.
- [112] S. Baros, C. N. Hadjicostis, and F. O’Sullivan, “Stability analysis of droop-controlled inverter-based power grids via timescale separation”, in *IEEE Conference on Decision and Control (CDC)*, 2020.
- [113] I. Subotić, D. Groß, M. Colombino, and F. Dörfler, “A Lyapunov framework for nested dynamical systems on multiple time scales with application to converter-based power systems”, *IEEE Transactions on Automatic Control*, vol. 66, no. 12, pp. 5909–5924, 2021.

- [114] J. H. Chow, *Power system coherency and model reduction*. Springer, 2013.
- [115] D. Romeres, F. Dörfler, and F. Bullo, “Novel results on slow coherency in consensus and power networks”, in *IEEE European Control Conference (ECC)*, 2013.
- [116] A. Ulbig, T. S. Borsche, and G. Andersson, “Impact of low rotational inertia on power system stability and operation”, *IFAC Proceedings Volumes*, vol. 47, no. 3, pp. 7290–7297, 2014.
- [117] J. Machowski, Z. Lubosny, J. W. Bialek, and J. R. Bumby, *Power system dynamics: Stability and control*. John Wiley and Sons, 2020.
- [118] S. Y. Caliskan and P. Tabuada, “Compositional transient stability analysis of multimachine power networks”, *IEEE Transactions on Control of Network Systems*, vol. 1, no. 1, pp. 4–14, 2014.
- [119] J. Fang, H. Deng, and S. M. Goetz, “Grid impedance estimation through grid-forming power converters”, *IEEE Transactions on Power Electronics*, vol. 36, no. 2, pp. 2094–2104, 2021.
- [120] P. Monzon and R. Potrie, “Local and global aspects of almost global stability”, in *IEEE Conference on Decision and Control (CDC)*, 2006.
- [121] F. Blanchini, “Set invariance in control”, *Automatica*, vol. 35, no. 11, pp. 1747–1767, 1999.
- [122] D. Zonetti, R. Ortega, and A. Benchaib, “A globally asymptotically stable decentralized PI controller for multi-terminal high-voltage DC transmission systems”, in *IEEE European Control Conference (ECC)*, 2014.
- [123] J. D. Watson and I. Lestas, “Frequency and voltage regulation in hybrid ac/dc networks”, *IEEE Transactions on Control Systems Technology*, vol. 29, no. 5, pp. 1839–1849, 2021.
- [124] G. Misyris, A. Tosatto, S. Chatzivasileiadis, and T. Weckesser, “Zero-inertia offshore grids: N-1 security and active power sharing”, *IEEE Transactions on Power Systems*, vol. 37, no. 3, pp. 2052–2062, 2022.
- [125] J. D. Watson and I. Lestas, “Control of interlinking converters in hybrid AC/DC grids: Network stability and scalability”, *IEEE Transactions on Power Systems*, vol. 36, no. 1, pp. 769–780, 2020.
- [126] T. Jouini and F. Dorfler, “Parametric local stability condition of a multi-converter system”, *IEEE Transactions on Automatic Control*, 2020.
- [127] P. Monshizadeh, C. De Persis, N. Monshizadeh, and A. J. van der Schaft, “Non-linear analysis of an improved swing equation”, in *IEEE Conference on Decision and Control (CDC)*, 2016.
- [128] D. Zonetti and R. Ortega, “Control of HVDC transmission systems: From theory to practice and back”, *Control Engineering Practice*, pp. 153–177, 2015.

- [129] C. H. Séquin, “On the number of klein bottle types”, *Journal of Mathematics and the Arts*, vol. 7, no. 2, pp. 51–63, 2013.
- [130] Y. Li, Y. Gu, and T. C. Green, “Rethinking grid-forming and grid-following inverters: A duality theory”, *IEEE Transactions on Power Systems*, vol. 37, no. 6, pp. 4541–4554, 2022.
- [131] D. Pattabiraman, R. H. Lasseter., and T. M. Jahns, “Comparison of grid-following and grid-forming control for a high inverter penetration power system”, in *IEEE Power and Energy Society General Meeting (PESGM)*, 2018.
- [132] D. Pattabiraman, R. H. Lasseter, and T. M. Jahns, “Impact of phase-locked loop control on the stability of a high inverter penetration power system”, in *IEEE Power and Energy Society General Meeting (PESGM)*, 2019.
- [133] M. Chen, D. Zhou, and F. Blaabjerg, “Active power oscillation damping based on acceleration control in paralleled virtual synchronous generators system”, *IEEE Transactions on Power Electronics*, vol. 36, no. 8, pp. 9501–9510, 2021.
- [134] K. Smith, S. Jafarpour, and F. Bullo, “Transient stability of droop-controlled inverter networks with operating constraints”, *IEEE Transactions on Automatic Control*, vol. 67, no. 2, pp. 633–645, 2021.
- [135] A. Sajadi, R. W. Kenyon, M. Bossart, and B.-M. Hodge, “Dynamic interaction of grid-forming and grid-following inverters with synchronous generators in hybrid power plants”, in *IEEE Kansas Power and Energy Conference (KPEC)*, 2021.
- [136] V. Purba, B. B. Johnson, S. Jafarpour, F. Bullo, and S. V. Dhople, “Dynamic aggregation of grid-tied three-phase inverters”, *IEEE Transactions on Power Systems*, vol. 35, no. 2, pp. 1520–1530, 2020.
- [137] M. Raza, E. Prieto-Araujo, and O. Gomis-Bellmunt, “Small-signal stability analysis of offshore AC network having multiple VSC-HVDC systems”, *IEEE Transactions on Power Delivery*, vol. 33, no. 2, pp. 830–839, 2018.
- [138] M. Amer, M. Ulrich, and F. Rolf, “Controller tuning in power systems using singular value optimization”, in *IFAC World Congress*, 2020.
- [139] R. Stanev and K. Nakov, “Power system stabilizers for inverter dominated future power systems”, in *IEEE International symposium on electrical apparatus technologies (SIELA)*, 2020.
- [140] A. Tayyebi, “HybridAngleControl(HAC): Implementation of grid-forming hybrid angle control”, *GitHub repository*, 2020.
- [141] N. Hatziargyriou, J. Milanovic, C. Rahmann, V. Ajjarapu, C. Canizares, I. Erlich, D. Hill, I. Hiskens, I. Kamwa, B. Pal, *et al.*, “Definition and classification of power system stability–revisited and extended”, *IEEE Transactions on Power Systems*, vol. 36, no. 4, pp. 3271–3281, 2020.

- [142] J. Rocabert, A. Luna, F. Blaabjerg, and P. Rodriguez, “Control of power converters in AC microgrids”, *IEEE Transactions on Power Electronics*, vol. 27, no. 11, pp. 4734–4749, 2012.
- [143] M. Chen, D. Zhou, and F. Blaabjerg, “Enhanced transient angle stability control of grid-forming converter based on virtual synchronous generator”, *IEEE Transactions on Industrial Electronics*, vol. 69, no. 9, pp. 9133–9144, 2021.
- [144] G. E. Colon-Reyes, K. C. Stocking, D. S. Callaway, and C. J. Tomlin, “Stability and robustness of a hybrid control law for the half-bridge inverter”, in *IEEE European Control Conference (ECC)*, 2023.
- [145] C. Albea, O. L. Santos, D. Z. Prada, F. Gordillo, and G. Garcia, “Hybrid control scheme for a half-bridge inverter”, *IFAC-PapersOnLine*, vol. 50, no. 1, pp. 9336–9341, 2017.
- [146] S. Samanta, N. R. Chaudhuri, and C. Lagoa, “Fast frequency support from grid-forming converters under dc-and ac-side current limits”, *IEEE Transactions on Power Systems*, vol. 38, no. 4, pp. 3528–3542, 2023.
- [147] C. Dufour and J. Bélanger, “Real-time simulation of a 48-pulse GTO STATCOM compensated power system on a Dual-Xeon PC using RTLAB”, in *International Conference on Power Systems Transients*, 2005.

Curriculum Vitae

Ali Tayyebi, born on 02/12/1987, citizen of Iran.

EDUCATION

M. Sc. in Electrical Engineering (joint degree)

La Sapienza, University of Nottingham, and University of Oviedo
Major: sustainable transportation and electrical power systems
Italy, UK, and Spain, 09/2014 – 09/2016

M. Sc. in Applied Mathematics (joint degree)

University of L'Aquila and University of Hamburg
Major: mathematical modeling in engineering
Italy and Germany, 09/2012 – 07/2014

B. Sc. in Electrical Engineering

University of Tehran
Major: electrical power system
Tehran, Iran, 09/2006 – 09/2011

EMPLOYMENT

Austrian Institute of Technology

Positions: master thesis student, project engineer, and doctoral researcher
Topic: electric energy systems
Vienna, Austria, 03/2016 – 11/2021

Hitachi Energy Research

Position: research scientist
Topic: control of the power systems and electronics
Vasteras, Sweden, 03/2022 – present